

Investigation of the microscopic behavior of Mott insulators by means of the density functional theory and many-body methods

Dissertation zur Erlangung
des Doktorgrades der Naturwissenschaften

vorgelegt beim Fachbereich Physik
der Johann Wolfgang Goethe-Universität
in Frankfurt am Main

VON

Kateryna Foyevtsova

aus Lviv, Ukraine

Frankfurt am Main (2012)

(D 30)

vom Fachbereich Physik der
Johann Wolfgang Goethe-Universität als Dissertation angenommen.

Dekan: Prof. Dr. Michael Huth

1. Gutachter: Prof. Dr. Maria-Roser Valentí

2. Gutachter: Prof. Dr. Peter Kopietz

3. Gutachter: Prof. Dr. Peter Hirschfeld (University of Florida, Gainesville, USA)

Datum der Disputation: 12 Dezember 2011

Zusammenfassung

Diese Arbeit verfolgt ein zweifaches Ziel. Zum einen untersuchen wir die Leistungsfähigkeit der Dichtefunktionaltheorie (DFT) bei der Anwendung auf stark korrelierte Systeme, wie z.B. Verbindungen mit Übergangsmetallen. Wir widmen uns dabei im Besonderen der Entwicklung und Verbesserung von Techniken zur Parametrisierung effektiver Modelle auf der Basis von DFT-Rechnungen. Zum anderen befassen wir uns im Rahmen der DFT mit einer Reihe von Fragestellungen in Bezug auf die Physik der Mott-Isolatoren. Wir betrachten dazu konkrete Systeme, bei deren Untersuchung jeweils verschiedene Aspekte korrelierter elektronischer Systeme im Vordergrund stehen, insbesondere (i) magnetische Frustration und Elektron-Phonon Wechselwirkung (Cs_2CuCl_4 , Cs_2CuBr_4), (ii) Hochtemperatur-Supraleitung ($\text{Bi}_2\text{Sr}_2\text{CaCu}_2\text{O}_{8+\delta}$), sowie (iii) die Dotierung von Mott-Isolatoren (TiOCl).

- (i) (**Magnetische Frustration, Elektron-Phonon Wechselwirkung**) In den frustrierten Antiferromagneten Cs_2CuCl_4 und Cs_2CuBr_4 untersuchen wir das Zusammenspiel von starken elektronischen Korrelationen mit Magnetismus und Elektron-Gitter Kopplung, sowie den Einfluß dieses Zusammenspiels auf die mikroskopischen Modell-Parameter.
- (ii) (**Hochtemperatur-Supraleitung**) Ein weiteres Objekt unserer Untersuchungen ist der mit Sauerstoff dotierte Cuprat-Supraleiter $\text{Bi}_2\text{Sr}_2\text{CaCu}_2\text{O}_{8+\delta}$, in dem durch rastertunnelspektroskopische (STS) Messungen elektronische Inhomogenitäten auf der Nanoskala festgestellt wurden. Unter Verwendung von DFT und Vielteilchenmethoden analysieren wir die Beziehung zwischen strukturellen und elektronischen Inhomogenitäten und die supraleitenden Eigenschaften in diesem Material.
- (iii) (**Dotierung von Mott-Isolatoren**) Wir nutzen DFT und Molekulardynamiksimulationen, um den mikroskopischen Ursprung des Mott-Isolator Zustandes von TiOCl bei beliebigen Natriumdotierungen zu erklären.

Unser Interesse an den frustrierten Antiferromagneten Cs_2CuCl_4 und Cs_2CuBr_4 gründet sich auf das fehlende Verständnis des mikroskopischen Ursprungs der experimentell beobachteten Unterschiede in den magnetischen Eigenschaften dieser beiden isostrukturellen Verbindungen. Die magnetischen Eigenschaften der beiden Antiferromagneten werden typischerweise im Rahmen des zweidimensionalen Heisenberg-Hamiltonians auf dem Dreiecksgitter diskutiert. Die führenden Spinaustausch-Kopplungen J und J' zwischen den lokalisierten magnetischen Kupfermomenten, die sich auf die Bindungen entlang einer Kette bzw. auf die Zick-Zack Verbindungen im Dreiecksgitter beziehen, wurden experimentell wie folgt bestimmt: $J'/J = 0.3$ in Cs_2CuCl_4 sowie $J'/J = 0.7$ in

Cs_2CuBr_4 (was auf höhere magnetische Frustration in Cs_2CuBr_4 hinweist), mit jeweils höheren Werten für J und J' in Cs_2CuBr_4 . Darüber hinaus wurden schwache interplanare Wechselwirkungen sowie eine anisotrope Dzyaloshinskii-Moriya Wechselwirkung gemessen. Es ist jedoch noch nicht geklärt, ob das Heisenberg-Modell ausreicht, um das reichhaltige Phasendiagramm von Cs_2CuCl_4 und Cs_2CuBr_4 erklären zu können: im Fall von Cs_2CuCl_4 lassen sich Signaturen von Spin-Liquids wie z.B. kontinuierliche Anregungsspektren und Bose-Einstein Kondensation von Magnonen finden, während das Phasendiagramm von Cs_2CuBr_4 Phasen mit "up-up-down" Spinkonfigurationen und Plateaus in der Magnetisierung aufweist, die von Quantenfluktuationen stabilisiert werden. Die zwei wichtigsten Ergebnisse unserer DFT Untersuchungen an Cs_2CuCl_4 und Cs_2CuBr_4 sind (1) die Bestimmung der zugehörigen Tight-Binding und Heisenberg-Modelle und (2) das Herausstellen der entscheidenden Bedeutung von elektronischen Korrelationen und Magnetismus für eine akkurate Beschreibung der Kristallstrukturen in DFT. Bei der Strukturoptimierung mit verschiedenen Näherungen für das Austausch-Wechselwirkungs-Funktional erzielen wir eine systematische Verbesserung der sich ergebenden Strukturparameter und eine bessere bereinstimmung der aus DFT ermittelten Modelle mit den experimentellen Ergebnissen, indem wir die Behandlung von Korrelationen und Magnetismus im Rahmen der gegebenen Funktionale verbessern. Die DFT-gestützte Parametrisierung der Heisenberg-Modelle für Cs_2CuCl_4 und Cs_2CuBr_4 erlaubt uns die Identifikation mehrerer bislang unbekannter Spinaustausch-Kopplungen, die für einige der exotischen magnetischen Phasen verantwortlich sein könnten. Wir finden auch einen qualitativen Unterschied zwischen den elektronischen Strukturen von Cs_2CuCl_4 und Cs_2CuBr_4 , nämlich die Relevanz nur eines Cu t_{2g} Bandes für das Hopping der Elektronen in Cs_2CuCl_4 im Vergleich zur Beteiligung aller drei t_{2g} Bänder in Cs_2CuBr_4 .

Die elektronischen Inhomogenitäten im dotierten Cuprat-Supraleiter $\text{Bi}_2\text{Sr}_2\text{CaCu}_2\text{O}_{8+\delta}$ sind jüngst Gegenstand intensiver Forschung mit der Hoffnung, in diesem Phänomen einen Schlüssel zum Verständnis der Hochtemperatur-Supraleitung zu finden. Eine der überzeugendsten Erklärungen der in STS-Experimenten beobachteten Korrelation zwischen der Größe der lokalen supraleitenden Lücke und der Position der Dotierungsatome basiert auf der Annahme, daß die Fremdatome die Supraleitung lokal erhöhen. In unserer Arbeit testen wir diese Annahme im Rahmen des Spin-Fluktuations-Austausch Modells für die Hochtemperatursupraleitung. In einem ersten Schritt parametrisierten wir Tight-Binding Modelle für die Beschreibung des Cu $3d_{x^2-y^2}$ Bands in reinem und mit Sauerstoff dotiertem $\text{Bi}_2\text{Sr}_2\text{CaCu}_2\text{O}_{8+\delta}$. Diese aus den DFT-Ergebnissen abgeleiteten Modelle werden im Anschluß für die Berechnung der Spin-Suszeptibilität und der Stärke der supraleitenden Paarwechselwirkung unter Verwendung der Random Phase Approximation benutzt. Der Vergleich der Ergebnisse für reines und dotiertes $\text{Bi}_2\text{Sr}_2\text{CaCu}_2\text{O}_{8+\delta}$ zeigt, daß

die über den Raum gemittelte Stärke der supraleitenden Paarwechselwirkung durch die Dotierung um ca. 30 % steigt. Das ist in bereinstimmung mit der lokalen Erhöhung der Spinaustausch-Wechselwirkung, die sich aus Modellrechnungen mit einem Band ergibt und über das Spin-Fluktuations-Austausch Modell mit der lokalen supraleitenden Lücke in Beziehung steht. Auf der anderen Seite liefern ähnliche, von uns durchgeführte Rechnungen für einen Hubbard Hamiltonian mit drei Bändern abweichende Ergebnisse, indem dort die durch die Dotierung induzierte lokale Inhomogenität je nach Parameterbereich zur Verstärkung oder Unterdrückung des lokalen Spinaustauschs führen kann. Diese widersprüchlichen Ergebnisse verlangen nach einer sorgfältigen und akkuraten Charakterisierung der durch die Dotierung induzierten Variation der Parameter für das Dreiband-Modell. Die Anwendung der von uns entwickelten Projektions-Methode verspricht hier gute Ergebnisse.

Für den geschichteten Mott-Isolator TiOCl erklären unsere DFT-Rechnungen die mikroskopische Natur seines ungewöhnlichen isolierenden Zustandes, der auch bei Dotierung sowie unter Anwendung von Druck erhalten bleibt. TiOCl – welches ein effektives quasi-1D Spinsystem darstellt – ist bekannt als eine der wenigen anorganischen Verbindungen mit einem Spin-Peierls Phasenübergang. Es ist auch interessant aufgrund seiner strukturellen Ähnlichkeit mit den Cuprat-Supraleitern, was auf eine mögliche Supraleitung hinweist, sofern es gelänge, TiOCl zu metallisieren. Experimente mit Photoemission an mit Na oder K dotiertem TiOCl sowie unter Anwendung von Druck zeigten jedoch keine Signaturen eines metallischen Zustandes. Um dieses überraschende Verhalten zu erklären, führten wir eine DFT-Analyse der elektronischen Strukturen von reinem und dotiertem TiOCl durch. Da keine Strukturdaten für dotiertes TiOCl vorlagen, bestimmten wir mittels Molekular-dynamik-Simulationen die Parameter der Einheitszelle für verschiedene Na-Dotierungen sowie für Substitution mit V, Sc, F und S. Wir stellen fest, dass der isolierende Zustand das Ergebnis eines Zusammenspiels der Hund'schen Regel, die die Besetzung eines neuen Ti 3d Orbitals durch ein dotiertes Elektron fördert, und der durch die Dotierung induzierten Modifikation der Kristallfeld-Aufspaltung für Ti ist, die zum Einfangen des Elektrons durch ein Ti Ion führt. Auf der Basis dieser Ergebnisse schlagen wir Ansätze zur Metallisierung von TiOCl vor. Darüber hinaus zeigen wir mittels Downfolding-Rechnungen, daß dotiertes TiOCl durch ein zweidimensionales ionisches Hubbard Modell mit mehreren Bändern beschrieben werden sollte.

Eine wichtige Errungenschaft dieser Arbeit ist die Entwicklung einer Parametrisierungstechnik für Bandstrukturen, die auf der Projektion von Blochfunktionen aus den Kohn-Sham Gleichungen auf Wannierfunktionen basiert. Wir wenden diese Technik für die Parametrisierung des Tight-Binding Modells für Cs_2CuBr_4 mit drei Bändern an. Perspektivisch kann sie auch für die Parametrisierung eines Dreiband-Modells für die komplizierte Supercell-Bandstruktur von dotiertem $\text{Bi}_2\text{Sr}_2\text{CaCu}_2\text{O}_{8+\delta}$ verwendet werden.

Abstract

The objective of this work is twofold. First, we explore the performance of the density functional theory (DFT) when it is applied to solids with strong electronic correlations, such as transition metal compounds. Along this direction, particular effort is put into the refinement and development of parameterization techniques for deriving effective models on a basis of DFT calculations. Second, within the framework of the DFT, we address a number of questions related to the physics of Mott insulators, such as (i) magnetic frustration and electron-phonon coupling (Cs_2CuCl_4 , Cs_2CuBr_4), (ii) high-temperature (high- T_c) superconductivity ($\text{Bi}_2\text{Sr}_2\text{CaCu}_2\text{O}_{8+\delta}$) and (iii) doping of Mott insulators (TiOCl).

- (i) (**Magnetic frustration and electron-phonon coupling**) In the frustrated antiferromagnets Cs_2CuCl_4 and Cs_2CuBr_4 , we investigate the interplay between strong electronic correlations and magnetism on one hand and electron-lattice coupling on the other as well as the effect of this interplay on the microscopic model parameters.
- (ii) (**High-temperature superconductivity**) Another object of our investigations is the oxygen-doped cuprate superconductor $\text{Bi}_2\text{Sr}_2\text{CaCu}_2\text{O}_{8+\delta}$, where nano-scale electronic inhomogeneities have been observed in scanning tunneling spectroscopy (STS) experiments. By means of DFT and many-body calculations, we analyze the connection between the structural and electronic inhomogeneities and the superconducting properties of $\text{Bi}_2\text{Sr}_2\text{CaCu}_2\text{O}_{8+\delta}$.
- (iii) (**Doping of Mott insulators**) We use the DFT and molecular dynamic simulations to explain the microscopic origin of the persisting under doping Mott insulating state in the layered compound TiOCl .

Our interest in the frustrated antiferromagnets Cs_2CuCl_4 and Cs_2CuBr_4 has been motivated by the lack of understanding of the microscopic origin of the experimentally observed differences in the magnetic properties of these isostructural compounds. Magnetic properties of both antiferromagnets are usually discussed in terms of the Heisenberg Hamiltonian on a 2D triangular lattice. The leading spin exchange couplings between Cu localized magnetic moments J and J' , which correspond to the intrachain and zig-zag bonds of the triangular lattice respectively, have been determined experimentally as follows: $J'/J \approx 0.3$ for Cs_2CuCl_4 and $J'/J \approx 0.7$ for Cs_2CuBr_4 (which indicates that Cs_2CuBr_4 is more frustrated than Cs_2CuCl_4), both J and J' being stronger in Cs_2CuBr_4 . Additionally, weak interlayer interactions as well as an anisotropic Dzyaloshinsky-Moriya

interaction are detected. It is, however, still a matter of debate whether the Heisenberg model alone is sufficient to explain the rich phase diagrams of Cs_2CuCl_4 and Cs_2CuBr_4 , where in the case of Cs_2CuCl_4 one finds signatures of a spin liquid state, such as continuous excitation spectra, and the Bose-Einstein condensation of magnons while in the case of Cs_2CuBr_4 the phase diagram contains phases with quantum-fluctuation-stabilized “up-up-down” spin configurations and magnetization plateaux. The two main results of our DFT studies on Cs_2CuCl_4 and Cs_2CuBr_4 consist in (1) deriving their tight-binding and Heisenberg models and (2) unveiling the importance of electronic correlations and magnetism for an accurate description of the Cs_2CuCl_4 and Cs_2CuBr_4 crystal structures within the DFT. By performing structural optimizations using various approximations for the exchange-correlation functional, we find a systematic improvement of the resulting Cs_2CuCl_4 and Cs_2CuBr_4 structural parameters and better agreement of the DFT-derived models with experimental results as the treatment of correlations and magnetism is being improved within a given functional. The DFT-assisted parameterization of the Cs_2CuCl_4 and Cs_2CuBr_4 Heisenberg models allowed us to identify several so far unknown second-order spin exchange couplings that might be responsible for some of the observed exotic magnetic phases. We also find a qualitative difference between the electronic structures of Cs_2CuCl_4 and Cs_2CuBr_4 , namely, that in Cs_2CuCl_4 only one of the Cu t_{2g} bands participates in electron hopping whereas in Cs_2CuBr_4 all three t_{2g} bands are involved.

The nano-scale electronic inhomogeneities in the doped cuprate superconductor $\text{Bi}_2\text{Sr}_2\text{CaCu}_2\text{O}_{8+\delta}$ have been recently a subject of intense research as one hopes to find in this phenomenon a key to the understanding of the high- T_c superconductivity. One of the most convincing explanations of the correlation between the size of the local superconducting gap and the position of dopant atoms, observed in STS experiments, is based on the assumption that the dopants enhance the superconducting pairing locally. In our work, this assumption was tested in the framework of the spin-fluctuation-exchange model for the high- T_c superconductivity. As a first step, we parameterized the tight-binding models to describe the Cu $3d_{x^2-y^2}$ band of the pure and oxygen-doped $\text{Bi}_2\text{Sr}_2\text{CaCu}_2\text{O}_{8+\delta}$. The DFT-derived models were subsequently used to calculate the spin susceptibility and superconducting pairing strength within the random phase approximation. The comparison between the results for the pure and doped $\text{Bi}_2\text{Sr}_2\text{CaCu}_2\text{O}_{8+\delta}$ reveals that the averaged over the real space superconducting pairing strength increases by about 30% upon doping. This is in agreement with the local enhancement of the spin exchange interaction – which is related with local superconducting gap within the spin-fluctuation-exchange model – as found in single-band model calculations. On the other hand, similar model calculations on a three-band Hubbard Hamiltonian that we perform give a different result, namely, that the dopant-induced

local electronic inhomogeneity can lead both to the enhancement as well as suppression of the local spin exchange, depending on the parameter regime. These contradictory findings call for a more thorough and accurate characterization of the dopant-induced variations of the three-band model parameters. In view of this challenging task, the application of the projection technique which has been developed in this work is expected to give good results.

Concerning the layered Mott insulator TiOCl, our DFT calculations explained the microscopic nature of its unusual insulating state, which survives doping as well as application of pressure. TiOCl – which effectively behaves as a quasi-1D spin system – is known as one of the rare inorganic compounds with a spin-Peierls phase transition. This compound is also interesting due to its structural similarity with cuprate superconductors, which suggests that, once metallized, TiOCl might also become superconducting. However, the doped via K or Na intercalation TiOCl showed no signature of a metallic state, as probed by photoemission experiments. In order to understand this unexpected result, we performed a DFT analysis of the electronic structures of the pure and doped TiOCl. Since structural data on the doped TiOCl had not been available, we performed molecular dynamics simulations to determine unit cell parameters for several Na-doping concentrations as well as for substitutional doping with V, Sc, F and S. We find that the insulating state is a result of the interplay between the Hund’s rule coupling, which makes a doped electron occupy a new Ti $3d$ orbital, and the dopant induced modification of the crystal field splitting of Ti states, which leads to trapping of the doped electron on a Ti ion. Based on these conclusions, we outline possible routes to metallize TiOCl. Also, using the downfolding technique, we established that the doped TiOCl should be described in terms of a 2D multi-band ionic Hubbard model.

An important achievement of this thesis is the development of the bandstructure parameterization technique that is based on projecting Bloch functions of the Kohn-Sham equations onto Wannier functions. We apply this technique to parameterize the three-band tight-binding model for Cs_2CuBr_4 . In perspective, it can also be used to parameterize the complicated bandstructure of the doped $\text{Bi}_2\text{Sr}_2\text{CaCu}_2\text{O}_{8+\delta}$ supercell in terms of a three-band model.

“Whatever is worth doing at all is worth doing well.”

Lord Chesterfield

Contents

List of Figures	xv
List of Tables	xvii
Abbreviations	xix
Symbols	xxi
Introduction	1
1 Physics of Mott insulators	5
1.1 Properties of transition metal compounds	5
1.2 Effective models for Mott insulators	7
1.2.1 Hubbard model	7
1.2.2 Heisenberg, t - J and Kugel-Khomski models	10
1.3 Many-body approaches to study the Hubbard model	12
1.3.1 Hartree-Fock and RPA solutions. Superconductivity	12
2 Electronic properties of solids within the density functional theory	19
2.1 Theoretical foundations	20
2.1.1 Hohenberg-Kohn theorem	21
2.1.2 Kohn-Sham equations	23
2.1.3 Exchange-correlation functional	24
2.1.4 DFT cycle	27
2.2 Application to crystalline materials: variability of basis sets	28
2.2.1 LMTO and NMTO	30
2.2.2 FPLO	31
2.2.3 APW+lo and LAPW	33
2.3 Forces and lattice dynamics	34
2.4 Extensions of DFT for strongly correlated materials	37
2.5 DFT-based derivation of effective models	38
2.5.1 Tight-binding and Hubbard models	38
2.5.2 Heisenberg model	42
3 Strongly correlated materials under study	45
3.1 Low-dimensional frustrated antiferromagnets CsCu_2Cl_4 and Cs_2CuBr_4 . .	45
3.1.1 Magnetic frustration	45

3.1.2	Cs ₂ CuCl ₄ and Cs ₂ CuBr ₄ : experimental background and theoretical description	48
3.2	Oxygen-doped high- T_c superconductor Bi ₂ Sr ₂ CaCu ₂ O ₈	53
3.2.1	Cuprates – unconventional superconductors	53
3.2.2	Doping-induced inhomogeneity of the superconducting gap in the high- T_c cuprate superconductor Bi ₂ Sr ₂ CaCu ₂ O _{8+δ}	57
3.3	Quasi-1D quantum magnet TiOCl	61
4	Cs₂CuCl₄ and Cs₂CuBr₄ microscopic models	65
4.1	Electronic properties	66
4.1.1	Structure optimization schemes	66
4.1.2	Structural analysis	68
4.1.3	Bandstructure and density of states	72
4.2	Derivation of effective models	77
4.2.1	Tight-binding model	77
4.2.2	Heisenberg model	80
4.3	Discussion	82
4.3.1	Analysis of the results	82
4.3.2	Placing the DFT study in the context of our general knoweldege about Cs ₂ CuCl ₄ and Cs ₂ CuBr ₄	84
5	Modulation of pairing interaction in Bi₂Sr₂CaCu₂O_{8+δ} by an oxygen dopant	87
5.1	DFT-assisted TB model parameterization of the oxygen-doped Bi ₂ Sr ₂ CaCu ₂ O ₈	88
5.1.1	Crystal structure of Bi ₂ Sr ₂ CaCu ₂ O _{8+δ}	88
5.1.2	Electronic structures of the parent and oxygen-doped compounds	90
5.1.3	Parameterization of a single-band tight-binding model	92
5.2	RPA susceptibility and spin fluctuation pairing	99
5.2.1	Spin susceptibility	99
5.2.2	Superconducting gap function	102
5.3	One-band <i>versus</i> three-band Hubbard Hamiltonians	105
5.3.1	Three-band Hubbard Hamiltonian in the presence of an oxygen dopant	106
5.3.2	Application of the perturbation expansion	107
5.3.3	Results: Effect of doping on local superexchange	108
5.4	Discussion	112
6	Doped Mott insulator TiOCl	117
6.1	Electronic structure of Na _{x} Ti _{1-y} V _{y} (Sc _{y})O _{1-z} F _{z} Cl _{1-w} S _{w}	119
6.1.1	Na doping	119
6.1.2	V (Sc), F and S doping	122
6.2	Effective microscopic model	123
6.3	Discussion	124
	Summary and outlook	125

A	Additional information for Cs_2CuCl_4 and Cs_2CuBr_4	129
A.1	Computational details of the Cs_2CuCl_4 and Cs_2CuBr_4 crystal structure optimization	129
A.2	Experimental and relaxed crystal structures of Cs_2CuCl_4 and Cs_2CuBr_4 .	129
A.3	Tight-binding model for Cs_2CuBr_4	134
A.4	Calculation of exchange couplings for Cs_2CuCl_4 and Cs_2CuBr_4 : Computational details	135
	Bibliography	139
	Acknowledgements	157
	Curriculum Vitae	159

List of Figures

1.1	$3d$ energy states in an isolated ion and in a solid	6
1.2	Hartree-Fock phase diagram for the 2D Hubbard model	13
1.3	Feynman diagrams: definitions and the Green's function expansion	15
1.4	The Hartree-Fock approximation in terms of Feynman diagrams.	16
1.5	RPA magnetic susceptibility	17
1.6	RPA effective spin-fluctuation-exchange pairing vertex	18
2.1	DFT cycle.	27
3.1	Examples of frustrated lattices	46
3.2	T -dependent susceptibility of a frustrated system	47
3.3	Resonating valence bond state	48
3.4	Cs_2CuCl_4 and Cs_2CuBr_4 crystal structure.	49
3.5	Phase diagrams of Cs_2CuCl_4 and Cs_2CuBr_4	50
3.6	Bose-Einstein condensation of magnons in Cs_2CuCl_4 and magnetization plateaux in Cs_2CuBr_4	51
3.7	Interaction paths for the effective spin model of Cs_2CuCl_4 and Cs_2CuBr_4	52
3.8	Cuprates: the T - n phase diagram, the Cooper pair function symmetry and the CuO_2 plane	55
3.9	$\text{Bi}_2\text{Sr}_2\text{CaCu}_2\text{O}_8$: crystal structure and an STM image of the surface	58
3.10	Spatial modulation of the superconducting gap size in $\text{Bi}_2\text{Sr}_2\text{CaCu}_2\text{O}_{8+\delta}$: an STS scan	59
3.11	TiOCl crystal structure and spin interaction pathways	62
3.12	DOS of TiOCl	63
4.1	Comparison between the GGA[nm], GGA[fm] and GGA+U[fm] DOS for Cs_2CuCl_4 and Cs_2CuBr_4	68
4.2	Definition of the CuX_4 tetrahedron geometrical parameters	69
4.3	CuX_4 tetrahedron geometrical parameters in various experimental and relaxed crystal structures of Cs_2CuX_4	71
4.4	Atomic species resolved and orbital resolved DOS for Cs_2CuX_4	73
4.5	Cs_2CuX_4 : the crystal field splitting, the bandstructure \mathbf{k} path and the local reference frame of the CuX_4 tetrahedron	74
4.6	DOS and bandstructures for various Cs_2CuCl_4 structures	75
4.7	DOS and bandstructures for various Cs_2CuBr_4 structures	76
4.8	Cs_2CuCl_4 interaction pathways considered for the TB model parameter- ization.	79
4.9	The spin exchange coupling constants as a function of $1/U$ for Cs_2CuX_4	81

5.1	$\text{Bi}_2\text{Sr}_2\text{CaCu}_2\text{O}_8$ unit cell <i>versus</i> $\text{Bi}_2\text{Sr}_2\text{CaCu}_2\text{O}_{8+\delta}$ supercell	89
5.2	Bandstructures of $\text{Bi}_2\text{Sr}_2\text{CaCu}_2\text{O}_8$ and $\text{Bi}_2\text{Sr}_2\text{CaCu}_2\text{O}_{8+\delta}$	91
5.3	Tight-binding fits: model 1	95
5.4	Tight-binding fits: model 2	96
5.5	TB model parameters for $\text{Bi}_2\text{Sr}_2\text{CaCu}_2\text{O}_{8+\delta}$	99
5.6	The static spin susceptibility	101
5.7	The pairing strength and the gap function	104
5.8	Notation for the three-band model: the energy level diagram of a Cu_2O_5 cluster	107
5.9	Graphs representing the fourth- and fifth-order spin-exchange processes	109
5.10	A phase diagram for the fourth-order correction to the local exchange coupling	111
5.11	A phase diagram for the fifth-order correction to the local exchange coupling	113
6.1	Superlattices of Na-doped TiOCl	118
6.2	Total DOS for Na-doped TiOCl	120
6.3	Partial DOS for $\text{Na}_{1/8}\text{TiOCl}$, $\text{TiO}_{7/8}\text{F}_{1/8}\text{Cl}$ and $\text{TiOCl}_{7/8}\text{S}_{1/8}$	121
6.4	t_{2g} crystal field splitting energies for Ti ions in TiOCl as well as in $\text{Na}_{1/8}\text{TiOCl}$, $\text{TiO}_{7/8}\text{F}_{1/8}\text{Cl}$, $\text{TiOCl}_{7/8}\text{S}_{1/8}$, $\text{Ti}_{7/8}\text{V}_{1/8}\text{OCl}$ and $\text{Ti}_{7/8}\text{Sc}_{1/8}\text{OCl}$	122
A.1	Antiferromagnetic spin configuration for the GGA+U[afm] structural relaxation	130
A.2	Three-band TB model spectrum for Cs_2CuBr_4	135
A.3	The $2 \times 2 \times 1$ supercell of Cs_2CuX_4 used for evaluating the exchange coupling constants	137

List of Tables

4.1	CuCl ₄ tetrahedron geometrical parameters in various experimental and relaxed crystal structures of Cs ₂ CuCl ₄	70
4.2	CuBr ₄ tetrahedron geometrical parameters in various experimental and relaxed crystal structures of Cs ₂ CuBr ₄	70
4.3	The single-band tight-binding model parameters for Cs ₂ CuCl ₄	78
5.1	Tight-binding parameters for Bi ₂ Sr ₂ CaCu ₂ O ₈ : model 1	93
5.2	Tight-binding parameters for Bi ₂ Sr ₂ CaCu ₂ O ₈ and Bi ₂ Sr ₂ CaCu ₂ O _{8+δ} : model 2	94
A.1	The three-band tight-binding model parameters for Cs ₂ CuBr ₄	136

Abbreviations

1D	One-Dimensional
2D	Two-Dimensional
3D	Three-Dimensional
AL	Atomic Limit
AMF	Around Mean Field
ARPES	Angle-Resolved PhotoEmission Spectroscopy
ASA	Atomic Sphere Approximation
BCS	Bardeen, Cooper and Schrieffer
DFT	Density Functional Theory
DMFT	Dynamical Mean-Field Theory
DOS	Density Of States
FPLO	Full-Potential Local-Orbital
LAPW	Linearized Augmented Plane Waves
LDA	Local Density Approximation
LMTO	Linearized Muffin-Tin Orbitals
LSDA	Local Spin Density Approximation
NMTO	Polynomial Muffin-Tin Orbital
NMR	Nuclear Magnetic Resonance
PAW	Projector-Augmented Wave
RPA	Random Phase Approximation
RVB	Resonating Valence Bond
STM	Scanning Tunneling Microscopy
STS	Scanning Tunneling Spectroscopy
TB	Tight-Binding

Symbols

Vectors

\mathbf{F}_I	force acting on ion I
\mathbf{G}	reciprocal lattice vector
$\mathbf{k}, \mathbf{p}, \mathbf{q}$	wave-vector
\mathbf{R}^T	lattice vector
\mathbf{r}_i	electron spacial coordinate
\mathbf{R}_I	ionic spacial coordinate

Greek symbols

Δ	charge-transfer gap in $\text{Bi}_2\text{Sr}_2\text{CaCu}_2\text{O}_8$
$\Delta_{\mathbf{k}}$	superconducting energy gap
δ_{opt}	optimal doping
δ_l	energy shift for an O atom in $\text{Bi}_2\text{Sr}_2\text{CaCu}_2\text{O}_8$
ε	single-particle energy
ε_d	on-site energy of the Cu $3d_{x^2-y^2}$ orbital in $\text{Bi}_2\text{Sr}_2\text{CaCu}_2\text{O}_8$
\hbar	Planck constant
λ	Cooper pairing strength
μ_{Cu}	Cu magnetic moment
$\mu_{mm'}, \mu$	on-site energy for orbitals m and m'
μ	chemical potential
ψ	single-particle wave-function

ϕ	basis function
σ	spin quantum number
τ	imaginary time
θ_{CW}	Curie-Weiss temperature
θ_{N}	Néel temperature
$ \Psi_0\rangle$	ground state

Operators

$\hat{c}_{im_i\sigma}^\dagger$ ($\hat{c}_{im_i\sigma}$)	creation (annihilation) operator for an electron at site i and orbital m_i and with spin σ
$\hat{d}_{i\sigma}^\dagger$ ($\hat{d}_{i\sigma}$)	creation (annihilation) operator for an electron at Cu site i with spin σ
\hat{H}^{3b}	three-band Hubbard model
\hat{H}^{H}	Heisenberg model
\hat{H}^{Hub}	Hubbard model
$\hat{H}^{\text{multi-Hub}}$	multi-band Hubbard model
$\hat{H}^{J^{\text{H}}}$	intrasite exchange interaction (Hund's rule coupling)
$\hat{n}_{i\sigma}$	number operator for an electron at site i with spin σ
\hat{P}	projector
$\hat{p}_{l\sigma}^\dagger$ ($\hat{p}_{l\sigma}$)	creation (annihilation) operator for an electron at O site l with spin σ
\hat{R}	$= 1 - \hat{P}$
$\hat{\mathbf{S}}_i$	spin operator for an electron at site i
\hat{T}	time ordering operator
\hat{V}_{ext}	external potential operator

Latin symbols

B	magnetic field (induction)
E_l^I	linearization energy for atom I and shell l
E_{xc}	exchange-correlation functional
E_{F}	Fermi energy
E_0	ground state energy
E	total energy
f	frustration factor
$G(t - t')$	zero-temperature Green's function
$\mathcal{G}(\tau - \tau')$	Matsubara Green's function
$g(\mathbf{k})$	Cooper pair wave-function
H	magnetic field
h.c.	hermitian conjugate terms
J^{H}	Hund's rule coupling
J_{ij}	exchange coupling between two spins at sites i and j
$J_{lm}(\mathbf{r})$	regular solution of the Laplace equation
$K_{lm}(\mathbf{r})$	irregular solution of the Laplace equation
k_B	Boltzmann constant
m_e	electron mass
M_I	ionic mass
M_s	saturation magnetization
m	orbital angular momentum quantum number
N_e	total number of electrons
R_{MT}^I	muffin-tin sphere radius on ion I
S	overlap matrix
$t_{ij}^{m_i m_j}$	electron transfer integral between sites i and j and orbitals m_i and m_j
T_c	superconducting transition temperature
T	temperature
U_p	on-site Coulomb repulsion on p orbitals
U, U_d	on-site Coulomb repulsion on d orbitals

V_{BZ}	Brillouin zone volume
$v_{\text{xc}}(\mathbf{r})$	exchange-correlation potential
V_i	energy shift for a Cu atom in $\text{Bi}_2\text{Sr}_2\text{CaCu}_2\text{O}_8$
v_i	$= V_i - \delta_i$
V	unit cell volume
$w_{im_i}(\mathbf{r})$	Wannier function on site i and orbital m_i
$Y_{lm}(\mathbf{r})$	spherical harmonic

To my parents...

Introduction

The *density functional theory* (DFT) is nowadays one of the best tools to study the electronic properties of *real materials* but it runs into difficulties when applied to systems with strong electronic correlations. The application of *many-body methods* which are more suitable to tackle the problem of strong correlations is, on the other hand, limited by the presently available computer power to considering only greatly simplified *model systems*. However, as the material science has been recently entering the era of practical applications based on phenomena driven by strong correlations (see, *e. g.*, Refs. [Ahn03, Dagotto05]), the need for the new approaches within the DFT, which would be as good in their treatment of strong correlations as the many-body methods, becomes more urgent.

Somewhat generalizing, there are currently two ways of considering the DFT for the study of strongly correlated materials. One is to use the DFT for establishing the microscopic model parameters that are specific to a given material and then to apply many-body methods to solve the model system that has been derived within the DFT. A large part of this thesis is dedicated to the improvement and development of the DFT-assisted model parameterization techniques and their application to a number of Mott insulators. For some of them, we also perform model calculations based on the DFT-derived models. The other way to combine the DFT and many-body methods is to improve the DFT-calculated energy spectrum of a material by performing a many-body calculation for the strongly correlated Bloch states of the DFT solution. This is done, for instance, in the LDA+DMFT (local density approximation, dynamical mean-field theory) method, where the Bloch states are projected onto a model basis for strongly correlated electrons and the model Hamiltonian is self-consistently solved within the DMFT. The LDA+DMFT as well as other methods of similar philosophy have been rapidly developing in the recent years and are seen as the most promising adaptation of the DFT designed to handle strong electronic correlations. Although the present thesis does not take advantage of the achievements of the LDA+DMFT method directly, we employ some concepts of the method, namely, Wannier functions and the projection technique, to develop an efficient tool for parameterizing multi-band tight-binding models.

With the methodology outlined above, we address a broad spectrum of questions related to the physics of Mott insulators. Thus, the DFT is used for a comparative study of the frustrated antiferromagnets Cs_2CuCl_4 and Cs_2CuBr_4 , which are Mott insulators in the regime of strong on-site Coulomb interaction and localization of the Cu magnetic moment. The frustrating triangular geometry together with the antiferromagnetic exchange coupling between the localized spins and low dimensionality in these compounds give rise to quite exotic magnetic behavior. For a fundamental theoretical understanding of the observed behavior of Cs_2CuCl_4 and Cs_2CuBr_4 , the knowledge of the spin exchange model parameters is essential, but, as a result of magnetic frustration, their experimental determination is rather complicated. This motivated us to use DFT calculations for an alternative determination of the Cs_2CuCl_4 and Cs_2CuBr_4 model parameters. Along with providing important physical results, the presented DFT study of Cs_2CuCl_4 and Cs_2CuBr_4 illustrates the amount of caution and delicate balancing between various approximations that is sometimes required in order to apply the DFT-based methods to correlated systems, especially when structural optimization is involved.

Strong electronic correlations – which lead to a Mott insulating state in Cs_2CuCl_4 and Cs_2CuBr_4 – are believed to be responsible for the unconventional high- T_c superconductivity in doped copper oxides ($\text{La}_{2-x}\text{Ba}_x\text{CuO}_4$ [Bednorz86], $\text{Nd}_{2-x}\text{Ce}_x\text{CuO}_4$, $\text{La}_{2-x}\text{Sr}_x\text{CuO}_4$, $\text{YBa}_2\text{Cu}_3\text{O}_{7-x}$). The research on the cuprate superconductivity has been profiting from DFT calculations for many years (see, *e. g.*, [Rosner99] and references therein). In our work, we undertake a technically involved task of parameterizing the tight-binding model for an oxygen-doped cuprate superconductor $\text{Bi}_2\text{Sr}_2\text{CaCu}_2\text{O}_{8+\delta}$. The DFT-assisted model parameterization of the pure and oxygen-doped $\text{Bi}_2\text{Sr}_2\text{CaCu}_2\text{O}_{8+\delta}$ allows us to study the crystal and electronic structure inhomogeneities, induced by the dopant atom, and their effect on the superconducting properties of the compound. The analysis of the superconducting properties of $\text{Bi}_2\text{Sr}_2\text{CaCu}_2\text{O}_{8+\delta}$ is performed in the framework of the spin-fluctuation-exchange model for the high- T_c superconductivity and using the random phase approximation.

Another low-dimensional Mott insulator, TiOCl , which due to its structural similarity with the cuprates is often seen as a possible candidate for unconventional superconductivity, is also studied. Despite this similarity, TiOCl demonstrates a rather different behavior upon Na doping remaining in an insulating state at Na concentrations up to ≈ 0.4 . We analyze the microscopic origin of this persistent insulating state and propose an effective model that describes the anomalous behavior of this Mott insulator in terms of crystal field splitting effects and the Hund’s rule coupling.

In short, the structure of the thesis is as follows.

- A general discussion of Mott insulators and their effective models as well as the Hartree-Fock and random phase approximations are presented in **Chapter 1**.
- **Chapter 2** gives an overview of various approaches within the DFT, covering both the fundamental theorems of the DFT and the practical aspects of its application to solids.
- In **Chapter 3**, we present a more detailed discussion of the studied materials Cs_2CuCl_4 , Cs_2CuBr_4 , $\text{Bi}_2\text{Sr}_2\text{CaCu}_2\text{O}_{8+\delta}$ and TiOCl by reviewing the current status of their experimental and theoretical investigations.
- Results of our DFT and many-body studies on $\text{Cs}_2\text{CuCl}_4/\text{Cs}_2\text{CuBr}_4$, $\text{Bi}_2\text{Sr}_2\text{CaCu}_2\text{O}_{8+\delta}$ and TiOCl are discussed in **Chapters 4, 5** and **6**, respectively.
- In the concluding chapter, we summarize the results and highlight possible directions of future research.

Chapter 1

Physics of Mott insulators

1.1 Properties of transition metal compounds

The Mott insulating state has been most extensively explored in transition metal compounds. These materials contain transition atoms, *i. e.*, atoms whose various ionized forms have an incomplete (open) d shell. The studied Ti and Cu based compounds (Cs_2CuCl_4 , Cs_2CuBr_4 , $\text{Bi}_2\text{Sr}_2\text{CaCu}_2\text{O}_8$ and TiOCl) belong to the $3d$ transition element series.

Depending on the d shell filling, transition ions are classified as *light* or *heavy*. In the light transition ions, such as the Ti^{3+} ion with a single $3d$ electron ($3d^1$ configuration) in TiOCl , less than half of the ten $3d$ electron levels are occupied. In the heavy transition ions, such as the Cu^{2+} ion with nine $3d$ electrons ($3d^9$ configuration) in Cs_2CuCl_4 , Cs_2CuBr_4 or $\text{Bi}_2\text{Sr}_2\text{CaCu}_2\text{O}_8$, the situation is the opposite. The two classes of transition metal compounds demonstrate similar properties due to the *electron-hole symmetry*, which implies that, *e. g.*, the nine $3d$ electrons of the Cu^{2+} ion effectively behave as a single hole with charge $+e$ (see, for example, Ref. [Sugano70]).

The ten $3d$ energy levels are degenerate in an isolated atom, with each state $|m, \sigma\rangle$ being distinguished by the orbital angular momentum quantum number $m = -2, -1, 0, 1, 2$ and the spin angular momentum quantum number $\sigma = -\frac{1}{2}, \frac{1}{2}$. Often, it is more convenient to deal with a set of states $|m', \sigma\rangle$ constructed as linear combinations of $|m, \sigma\rangle$, which constitute a basis for the irreducible representation of the real space symmetry operations group. The real-valued functions $\langle \mathbf{r} | m', \sigma \rangle$ are referred to as the d_{z^2} , $d_{x^2-y^2}$, d_{xy} , d_{xz} and d_{yz} orbitals¹, their shapes being schematically shown in Fig. 1.1.

¹One may as well use linear combinations of the d_{z^2} , $d_{x^2-y^2}$, d_{xy} , d_{xz} and d_{yz} orbitals. Eventually, the choice of the most convenient basis depends on the symmetry of the crystal field.

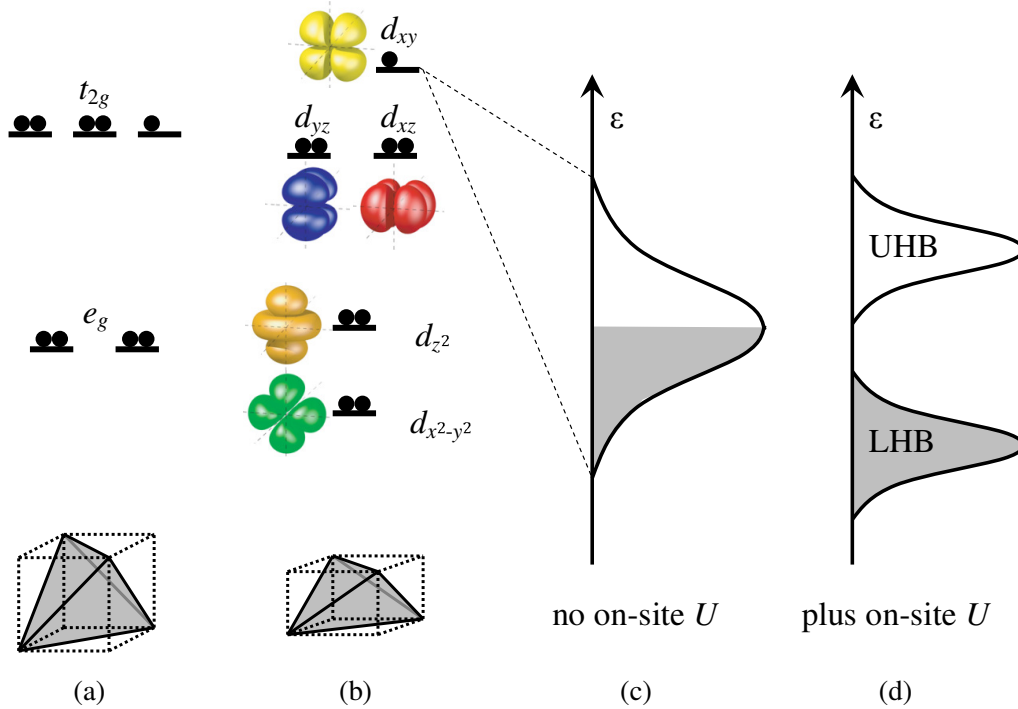


FIGURE 1.1: $3d$ energy states: crystal field splitting of the ionic $3d$ levels (a) in a regular tetrahedral environment as well as (b) in a distorted tetrahedral environment; the half-filled $3d$ energy band in a solid (c) without the on-site electron repulsion U and (d) with the on-site repulsion. “UHB” and “LHB” stand for the upper Hubbard band and the lower Hubbard band, respectively. ϵ denotes the energy.

In a crystal, the transition metal atom gets oxidized by giving away some of its outer electrons. In addition, the electrostatic field created by the neighboring ions, mainly the nearest anions which are called *ligands*, causes redistribution of the transition ion’s energy levels. In particular, the crystal field affects the $3d$ levels by splitting them in various ways depending on the crystal field symmetry. Figures 1.1 (a) and (b) show examples of the $3d$ level splitting in a regular and a distorted tetrahedral ligand environment, respectively. In the regular tetrahedral environment, the $3d$ levels are split into six degenerate t_{2g} levels (d_{xy} , d_{xz} and d_{yz} orbitals) with higher energy and four degenerate e_g levels (d_{z^2} and $d_{x^2-y^2}$ orbitals) with lower energy². The tetragonal distortion in a squeezed tetrahedron of ligands lifts some of the remaining degeneracies in the t_{2g} and e_g levels [Fig. 1.1 (b)]. The $3d$ level splitting illustrated by Fig. 1.1 (b) occurs, for instance, in the Cu^{2+} ion in Cs_2CuCl_4 and Cs_2CuBr_4 (see Chapter 4).

Due to the hybridization between valence states of different atoms in a crystal, their single energy levels develop into energy bands, as illustrated in Fig. 1.1 (c), which reflects the fact that valence electrons occupying the hybridized *partially filled* states can move around with a certain momentum \mathbf{k} . Typically, the $3d$ states of the transition ions are

²The names t_{2g} and e_g stem from the group theory notation.

strongly hybridized with anion p states. In the example considered in Fig. 1.1 (c), which is relevant for Cs_2CuCl_4 or Cs_2CuBr_4 , the $3d_{xy}$ band is half-filled indicating a metallic ground state.

However, Cs_2CuCl_4 and Cs_2CuBr_4 as well as many other transition metal compounds are insulators. The insulating behavior originates from the Coulomb repulsion between the $3d$ electrons of transition metal ions. The special property of the $3d$ electrons is their significant localization at ionic sites, which reduces the electron charge screening and thus makes the Coulomb interaction more pronounced than in the case of completely delocalized conduction s electrons.

Moving around in a crystal, two $3d$ electrons can simultaneously occupy the same transition ion for a short time period, which would have no influence on the electron motion if there were no interaction between electrons. But the presence of the Coulomb repulsion between the two $3d$ electrons on the same ion increases the system's energy and therefore the state with doubly occupied ions becomes energetically unfavorable. This introduces *correlations* between the motions of individual electrons and, with large enough on-site Coulomb repulsion, the electrons may freeze completely thus turning the crystal into an insulator [Fig. 1.1 (d)]. In this case, the energy band splits into two such that the lower band corresponds to each ionic level being occupied by a single electron, which would be the ground state, while the upper band collects states with doubly occupied ions. The two bands are separated by an energy gap of the order of the Coulomb interaction strength U , which corresponds to the energy required to excite the system, *i. e.*, create doubly occupied ionic sites. An insulating state that has been developed through the mechanism described above is referred to as the *Mott insulating state*.

1.2 Effective models for Mott insulators

1.2.1 Hubbard model

It has been early recognized that the Mott metal-insulator transition in transition metal compounds is mainly governed by the behavior of the semi-localized $3d$ electrons. Mott was the first who made use of this fact to simplify the many-body problem of interacting particles in a crystal. He showed [Mott49, Mott56, Mott61] that the metal-insulator transition can be explained already in the framework of an effective model where all particle degrees of freedom except those of the $3d$ electrons in partially filled transition ion outer shells have been neglected.

Mott's idea lies in the foundation of the famous *Hubbard model* [Anderson59, Hubbard63, Hubbard64], which has probably become the most intensively studied model of strongly correlated electronic systems. The Hubbard model considers a case of a single active $3d$ orbital on each transition ion, which can host maximally two electrons. The model is traditionally written in second quantization as

$$\begin{aligned} \hat{H}^{\text{Hub}} &= \mu \sum_{i\sigma} \hat{n}_{i\sigma} \\ &\quad - \sum_{\langle ij \rangle, \sigma} \left(t_{ij} \hat{c}_{i\sigma}^\dagger \hat{c}_{j\sigma} + \text{h.c.} \right) \\ &\quad + \sum_i U \hat{n}_{i\uparrow} \hat{n}_{i\downarrow}, \end{aligned} \tag{1.1}$$

where operators $\hat{c}_{i\sigma}^\dagger$ ($\hat{c}_{i\sigma}$) create (annihilate) an electron with spin σ at ionic site i , $\hat{n}_{i\sigma} \equiv \hat{c}_{i\sigma}^\dagger \hat{c}_{i\sigma}$, μ is the on-site energy, t_{ij} is a parameter characterizing hybridization between orbitals of different ions, and U is the on-site Coulomb repulsion strength, as has already been mentioned.

The Hubbard Hamiltonian (1.1) describes a competition of two processes:

- (1) the kinetic motion of electrons, represented by the second term; t_{ij} is a matrix element of the kinetic energy operator \hat{T} in the basis of Wannier functions $w_i(\mathbf{r})$ (see also Section 2.5.1),

$$t_{ij} = \int d\mathbf{r} w_i^*(\mathbf{r}) \left(-\frac{\hbar^2}{2m_e} \nabla^2 \right) w_j(\mathbf{r}); \tag{1.2}$$

- (2) the Coulomb repulsion between two $3d$ electrons on the same atom, represented by the third term, which hinders free electron hopping between ionic sites.

Of special interest is the case when the number of electrons in the system deviates from the number of ionic sites. Then, one of the two bands that appear upon switching on the on-site Coulomb interaction will be partially filled – in the electron-deficient regime there will be some empty states in the *lower Hubbard band* and in the electron-abundant regime some of the *upper Hubbard band* states will be occupied – so that an insulating state does not occur.

Though metallic, properties of such a *doped* correlated system are, generally, rather different from those of Fermi-liquid metals. Some of the unusual properties of strongly correlated metals are, for instance, the *high-temperature superconductivity* and *spatial*

charge order in doped cuprates (Ref. [Lee06], Section 3.2) or the anomalous *effective mass enhancement* near the boundary with an insulating phase in, *e. g.*, V_2O_3 ³.

Multi-band case

In many transition metal compounds there are several $3d$ orbitals, with close or equal energies, that are involved in the intersite electron hopping. This happens when the crystal field splitting is less than the $3d$ bands' dispersion like, for example, in iron pnictides, where at the Fermi level all five $3d$ bands of Fe are strongly hybridized [Wen11]. Also, sometimes, especially in highly symmetric structures, the partially filled t_{2g} or e_g states remain degenerate, as in the case of the doubly occupied t_{2g} manifold of the V^{3+} ion's $3d$ shell in cubic $SrVO_3$ (see, *e. g.*, Ref. [Aichhorn09]) or in $TiOCl$, where the single Ti $3d$ electron can equally occupy the doubly degenerate $3d_{xz}$ and $3d_{yz}$ bands or the slightly lower in energy $3d_{xy}$ band (Chapter 6).

The presence of additional *orbital degrees of freedom* may have important consequences on the behavior of the multi-band system. Therefore, such systems are better described by the following *multi-band Hubbard model*

$$\begin{aligned} \hat{H}^{\text{multi-Hub}} &= \sum_{i, m_i, m'_i, \sigma} \mu_{m_i m'_i} \hat{c}_{i m_i \sigma}^\dagger \hat{c}_{i m'_i \sigma} \\ &\quad - \sum_{\substack{\langle ij \rangle \\ \sigma, m_i, m_j}} \left(t_{ij}^{m_i m_j} \hat{c}_{i m_i \sigma}^\dagger \hat{c}_{j m_j \sigma} + \text{h.c.} \right) \\ &\quad + \sum_{\substack{i, m_i, m'_i \\ \sigma \sigma'}} (1 - \delta_{\sigma \sigma'} \delta_{m_i m'_i}) U_{m_i m'_i} \hat{n}_{i m_i \sigma} \hat{n}_{i m'_i \sigma'}, \end{aligned} \quad (1.3)$$

where index m_i denotes one of the $3d$ orbitals of ion i . This Hamiltonian allows for the intersite as well as intrasite interorbital electron hopping and differentiates the strengths of the on-site Coulomb repulsion between electrons from different orbitals.

Often, one additionally includes the *intrasite exchange interaction* term \hat{H}^{J^H} ,

$$\begin{aligned} \hat{H}^{J^H} &= - \sum_{\substack{i, m_i, m'_i \\ \sigma \sigma'}} J_{m_i m'_i}^H \left[(1 - \delta_{m_i m'_i}) \hat{c}_{i m_i \sigma}^\dagger \hat{c}_{i m_i \sigma'} \hat{c}_{i m'_i \sigma'}^\dagger \hat{c}_{i m'_i \sigma} \right. \\ &\quad \left. - (1 - \delta_{m_i m'_i}) (1 - \delta_{\sigma \sigma'}) \hat{c}_{i m'_i \sigma'}^\dagger \hat{c}_{i m'_i \sigma} \hat{c}_{i m_i \sigma} \hat{c}_{i m_i \sigma'} \right], \end{aligned} \quad (1.4)$$

into Hamiltonian (1.3). This term models a *Hund's rule coupling* by favoring parallel orientation of electron spins on different atomic orbitals.

³Ref. [Mott90] reviews experiments on this compound.

1.2.2 Heisenberg, t - J and Kugel-Khomski models

In the limit of strong Coulomb repulsion,

$$\frac{U}{t} \gg 1, \quad (1.5)$$

the Hubbard Hamiltonian (1.1) at half-filling, *i. e.*, with one electron per site, can be approximated by an *effective spin Hamiltonian*. Indeed, when the on-site Coulomb repulsion is strong enough, the electron motion around the crystal via interatomic hopping freezes, which results in an insulating state. Yet, *virtual electron hopping* between neighboring atoms, which would lower the system's energy, may still take place provided that the electron spins on neighboring sites are antiparallel, as required by the Pauli exclusion principle. By means of the virtual electron hopping, the electron spins interact with an effective antiferromagnetic⁴ coupling J , which can be expressed in terms of a spin effective model as

$$\hat{H}^H = \sum_{\langle ij \rangle} J_{ij} \hat{\mathbf{S}}_i \hat{\mathbf{S}}_j, \quad (1.6)$$

where $\hat{\mathbf{S}}_i$ is the spin operator acting on a site i electron. The Hamiltonian (1.6) is known as the *Heisenberg model*.

The expression (1.6) can be rigorously derived by performing a perturbation theory expansion of the Hubbard model (1.1) in terms of the kinetic energy term. Then, to the second order, the effective spin exchange coupling is given by

$$J_{ij} = \frac{4t_{ij}^2}{U}, \quad (1.7)$$

while the spin operator $\hat{\mathbf{S}}_i = (\hat{S}_i^x, \hat{S}_i^y, \hat{S}_i^z)$ is related with the electron creation and annihilation operators as

$$\begin{aligned} \hat{S}_i^+ &= \hat{S}_i^x + i\hat{S}_i^y = \hat{c}_{i\uparrow}^\dagger \hat{c}_{i\downarrow}, \\ \hat{S}_i^- &= \hat{S}_i^x - i\hat{S}_i^y = \hat{c}_{i\downarrow}^\dagger \hat{c}_{i\uparrow}, \\ \hat{S}_i^z &= \frac{1}{2} \left(\hat{c}_{i\uparrow}^\dagger \hat{c}_{i\uparrow} - \hat{c}_{i\downarrow}^\dagger \hat{c}_{i\downarrow} \right). \end{aligned} \quad (1.8)$$

In Section 5.3, one can find more technical details on the perturbation expansion applied to derive the spin superexchange in the three-band Hubbard model.

Two special cases of the Heisenberg Hamiltonian are the *Ising model* and the *XY model*, where the x and y spin operator components or, respectively, the z component are

⁴Ferromagnetic spin coupling is, in general, also possible.

neglected. Such models are relevant for real systems with substantial anisotropy of spin coupling.

While the Heisenberg model is defined for Mott insulators in the half-filled regime, the presence of extra charge carriers in doped systems requires an effective model that accounts for their possible motion through empty or singly occupied sites. The t - J model [Gros87, Chao77, Hirsch85a]

$$\hat{H}^{t-J} = - \sum_{\langle ij \rangle, \sigma} \hat{P}_d^\dagger \left(t_{ij} \hat{c}_{i\sigma}^\dagger \hat{c}_{j\sigma} + \text{h.c.} \right) \hat{P}_d + \sum_{\langle ij \rangle} J_{ij} \hat{\mathbf{S}}_i \hat{\mathbf{S}}_j, \quad (1.9)$$

where \hat{P}_d projects away doubly occupied sites, is a good approximation for systems which are slightly under half-filling. The t - J model has been intensively discussed in the context of the high- T_c cuprate superconductivity [Gros87].

In multi-band systems, the interorbital electron hopping results in an effective *orbital exchange coupling* in analogy with the spin exchange coupling (1.6). The corresponding effective model applicable in the strong interaction regime has been derived by Kugel and Khomski [Kugel82]. For the simplest case of a two-band system with only nearest-neighbor interactions, the *Kugel-Khomski model* reads⁵

$$\hat{H}^{\text{KH}(2b)} = \sum_{\langle ij \rangle} \left(J^{(1)} \hat{\mathbf{S}}_i \hat{\mathbf{S}}_j + J^{(2)} \hat{\boldsymbol{\tau}}_i \hat{\boldsymbol{\tau}}_j + 4J^{(3)} \hat{\mathbf{S}}_i \hat{\mathbf{S}}_j \hat{\boldsymbol{\tau}}_i \hat{\boldsymbol{\tau}}_j \right), \quad (1.11)$$

where

$$J^{(1)} = \frac{2t^2}{U} \left(1 - \frac{J^{\text{H}}}{U} \right), \quad J^{(2)} = J^{(3)} = \frac{2t^2}{U} \left(1 + \frac{J^{\text{H}}}{U} \right). \quad (1.12)$$

Operators $\hat{\boldsymbol{\tau}}_i = (\hat{\tau}_i^x, \hat{\tau}_i^y, \hat{\tau}_i^z)$ are given in terms of pseudospin representation as

$$\begin{aligned} \hat{\tau}_i^+ &= \hat{\tau}_i^x + i\hat{\tau}_i^y = \hat{c}_{im_i}^\dagger \hat{c}_{im'_i}, \\ \hat{\tau}_i^- &= \hat{\tau}_i^x - i\hat{\tau}_i^y = \hat{c}_{im'_i}^\dagger \hat{c}_{im_i}, \\ \hat{\tau}_i^z &= \frac{1}{2} \left(\hat{c}_{im_i}^\dagger \hat{c}_{im_i} - \hat{c}_{im'_i}^\dagger \hat{c}_{im'_i} \right). \end{aligned} \quad (1.13)$$

⁵It has also been assumed that

$$\begin{aligned} t_{ij}^{m_i=1, m_j=1} &= t_{ij}^{m_i=2, m_j=2} = t, \quad t_{ij}^{m_i=1, m_j=2} = 0; \\ U_{m_i=1, m'_i=1} &= U_{m_i=2, m'_i=2} = U_{m_i=1, m'_i=2} = U; \\ J_{m_i=1, m'_i=2}^{\text{H}} &= J_{m_i=2, m'_i=1}^{\text{H}} = J^{\text{H}}, \quad J_{m_i=m'_i}^{\text{H}} = 0. \end{aligned} \quad (1.10)$$

1.3 Many-body approaches to study the Hubbard model

The Mott-insulating phase transition is controlled by the strength of the on-site Coulomb repulsion U and the width of the d band W . The transition is to be expected in the intermediate regime, when the two controlling parameters are of the same order of magnitude,

$$\frac{U}{W} \sim 1. \quad (1.14)$$

Therefore, the Hubbard model, Eq. (1.1) or Eq. (1.3), is a minimal model to study the Mott transition. The effective models introduced in the previous section are applicable in the strong coupling regime and are helpful in elucidating collective phenomena in systems with only spin and/or orbital degrees of freedom (see, for instance, Section 3.1.1).

Although the Hubbard model is an enormous simplification to the original many-particle Schrödinger equation for electrons and nuclei in a solid, its general solution is not available. Except for the 1D case, where the Hubbard model can be solved exactly [Lieb68], one has to resort to approximative methods in order to analyze its properties. Imada *et al.* present in Ref. [Imada98] an extensive overview of the methods that have been developed for this purpose. Often, the various mean-field approaches (*e. g.*, Hartree-Fock and random phase approximations [Bohm53], infinite-dimensional approach [Georges96] *etc.*) and numerical methods (*e. g.*, quantum Monte Carlo) are used as complementary many-body tools to study different aspects of the problem at hand and to better control approximation errors.

Here, we will discuss in some detail the Hartree-Fock and random phase approximations (RPA). We pay special attention to the RPA in order to provide a theoretical background for the discussion of the spin-fluctuation-exchange-mediated superconductivity in $\text{Bi}_2\text{Sr}_2\text{CaCu}_2\text{O}_8$, which we present in Section 5.2.

1.3.1 Hartree-Fock and RPA solutions. Superconductivity

In the *Hartree-Fock method*, two-particle correlations are neglected so that the many-body wave-function can be approximated by a single Slater determinant. This approximated wave-function is obtained *self-consistently* by adjusting the particle density $\langle \hat{n}_{i\sigma} \rangle$ and the effective *mean-field* potential it generates. This approach is equivalent to approximating the interaction term of the Hubbard model (1.1) by an interaction with the

mean field as

$$\begin{aligned} \hat{H}^{\text{Hub}} \approx & \mu \sum_{i\sigma} \hat{n}_{i\sigma} \\ & - \sum_{\langle ij \rangle, \sigma} (t_{ij} \hat{c}_{i\sigma}^\dagger \hat{c}_{j\sigma} + \text{h.c.}) \\ & + U \sum_i (\langle \hat{n}_{i\uparrow} \rangle \hat{n}_{i\downarrow} + \hat{n}_{i\uparrow} \langle \hat{n}_{i\downarrow} \rangle + \langle \hat{n}_{i\uparrow} \rangle \langle \hat{n}_{i\downarrow} \rangle). \end{aligned} \quad (1.15)$$

The Hartree-Fock method can already capture the metal-insulator transition upon doping the Hubbard model away from half-filling, as was, for example, demonstrated by Hirsch [Hirsch85b] for a 2D nearest-neighbor Hubbard model (Fig. 1.2).

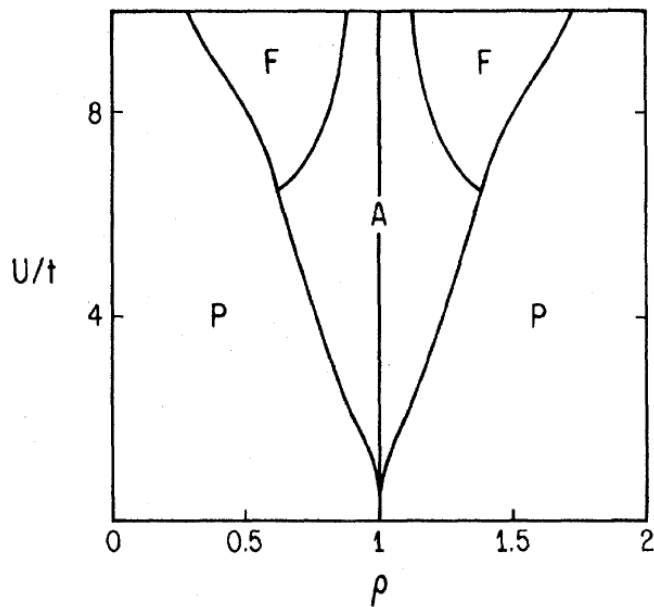


FIGURE 1.2: The Hartree-Fock phase diagram for the 2D nearest-neighbor Hubbard model (taken from Ref. [Hirsch85b]). Here, ρ stands for the filling (n) whereas “P”, “A” and “F” denote, respectively, the paramagnetic, antiferromagnetic and ferromagnetic phases.

The nature of approximations in the Hartree-Fock method can also be expressed in the language of *Green's functions* and *Feynman diagrams*. In fact, the Green's functions formalism is widely used to study many-body problems. The zero-temperature one-electron Green's function is defined as

$$G_\lambda(t-t') = -\frac{i}{\hbar} \langle \Psi_0 | \hat{T} \hat{c}_\lambda(t) \hat{c}_\lambda^\dagger(t') | \Psi_0 \rangle. \quad (1.16)$$

It probes the response of a system in the ground state $|\Psi_0\rangle$ to an electron characterized by the quantum number λ that is created at time t' , then *propagates* through the system, interacting on its way, and is finally destroyed at time t . In Eq. (1.16), the electron

creation and annihilation operators are in the Heisenberg representation and \hat{T} is the time ordering operator. This kind of probing the system's response can provide full information on its equilibrium properties as well.

At finite temperatures, it is convenient to operate with Green's functions defined for imaginary time τ through the thermodynamic average as [Mahan81]

$$\mathcal{G}_\lambda(\tau - \tau') = \text{Tr} \left(e^{-\beta(\hat{H} - \mu\hat{N} - \hat{\Omega})} \hat{T}_\tau e^{\tau(\hat{H} - \mu\hat{N})} \hat{c}_\lambda e^{-(\hat{H} - \mu\hat{N})(\tau - \tau')} \hat{c}_\lambda^\dagger e^{-\tau'(\hat{H} - \mu\hat{N})} \right), \quad (1.17)$$

$$e^{-\beta\hat{\Omega}} = \text{Tr} \left(e^{-\beta(\hat{H} - \mu\hat{N})} \right), \quad (1.18)$$

or, in short notation,

$$\mathcal{G}_\lambda(\tau - \tau') = -\langle \hat{T}_\tau \hat{c}_\lambda(\tau) \hat{c}_\lambda^\dagger(\tau') \rangle. \quad (1.19)$$

In Eq. (1.17), \hat{N} is the total particle number operator, μ plays the role of the chemical potential and $-\beta \leq \tau - \tau' \leq \beta$, with $\beta = \frac{1}{k_B T}$.

The Green's function for a non-interacting (single-band) system $\mathcal{G}_\mathbf{p}^0(\tau - \tau')$, with the quantum number \mathbf{p} being the wavevector, can be easily calculated, and its Matsubara frequency Fourier transform⁶ is

$$\mathcal{G}_\mathbf{p}^0(i\omega_n) = \frac{1}{i\omega_n - \varepsilon(\mathbf{p})}, \quad \mathcal{G}_\mathbf{p}^0(\tau - \tau') = \frac{1}{\beta} \sum_n e^{-i\omega_n(\tau - \tau')} \mathcal{G}_\mathbf{p}^0(i\omega_n), \quad (1.20)$$

where $\varepsilon(\mathbf{p})$ is the spectrum of the non-interacting Hamiltonian \hat{H}_0 . In the presence of an interaction term⁷ \hat{U} , $\hat{H} = \hat{H}_0 + \hat{U}$, the Green's function can be formally obtained as a series expansion in powers of the interaction:

$$\begin{aligned} \mathcal{G}_\mathbf{p}(\tau - \tau') &= - \sum_{n=1}^{\infty} (-1)^n \int_0^\beta d\tau_1 \dots \int_0^\beta d\tau_n \\ &\times \text{Tr} \left[e^{-\beta(\hat{H}_0 - \mu\hat{N})} \hat{T}_\tau \hat{c}_\mathbf{p}(\tau) \hat{U}(\tau_1) \hat{U}(\tau_2) \dots \hat{U}(\tau_n) \hat{c}_\mathbf{p}^\dagger(\tau') \right]_{\text{unique connected}} \end{aligned} \quad (1.21)$$

Note that among the terms produced via application of the time ordering operator \hat{T}_τ , one should consider only those terms that are unique in terms of the dummy variables τ_1, \dots, τ_n equivalence and connected. We explain below the meaning of "connected".

The expansion (1.21) can be graphically represented as a sum of *Feynman diagrams* such that each expansion term is mapped into a corresponding diagram following certain

⁶The discrete frequencies are a result of the imaginary time being defined within a finite interval:

$$-\beta \leq \tau - \tau' \leq \beta.$$

⁷In the Hubbard model, $\hat{U}(\tau) = U \sum_i \hat{n}_{i\uparrow}(\tau) \hat{n}_{i\downarrow}(\tau)$.

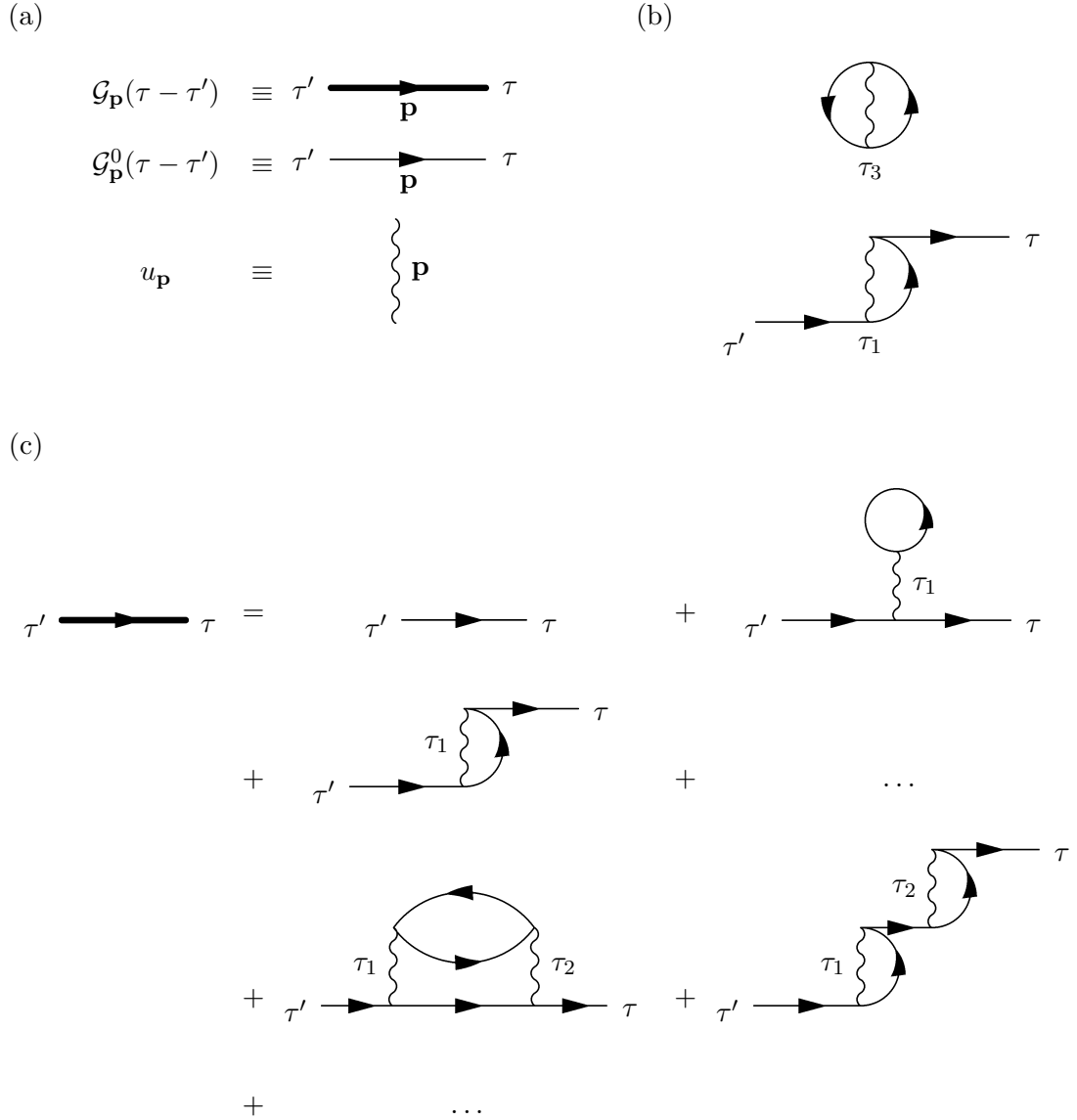


FIGURE 1.3: (a) $\mathcal{G}_{\mathbf{p}}(\tau - \tau')$, $\mathcal{G}_{\mathbf{p}}^0(\tau - \tau')$ and $u_{\mathbf{p}}$. (b) A disconnected diagram. (c) Expansion of $\mathcal{G}_{\mathbf{p}}(\tau - \tau')$.

prescriptions (see, *e. g.*, Ref. [Mahan81], page 111). Graphical representations of $\mathcal{G}_{\mathbf{p}}(\tau - \tau')$, $\mathcal{G}_{\mathbf{p}}^0(\tau - \tau')$ and $u_{\mathbf{p}} = \frac{4\pi e^2}{p^2}$ are shown in Fig. 1.3 (a), while Fig. 1.3 (c) displays Eq. (1.21) in a graphical form. The requirement for the expansion series terms to be connected can now be formulated as a requirement that the diagrams in the sum should all be without topologically isolated parts [an example of a *disconnected* diagram is shown in Fig. 1.3 (b)].

Now, the Hartree-Fock approximation consists in replacing the infinite series of Fig. 1.3 (c) by a bare propagator $\mathcal{G}_{\mathbf{p}}^0(\tau - \tau')$ plus two interaction terms that involve the interacting propagator $\mathcal{G}_{\mathbf{p}}(\tau - \tau')$ itself, as shown in Fig. 1.4. The first interaction term is called the

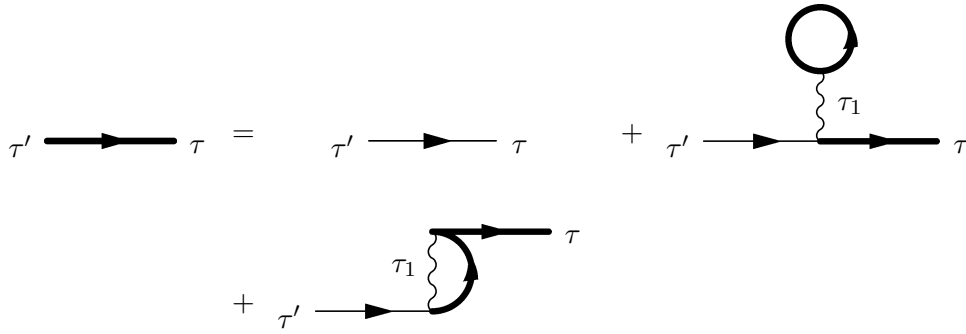


FIGURE 1.4: The Hartree-Fock approximation in terms of Feynman diagrams.

Hartree term and results from infinitely summing over a particular type of diagrams, such as the second expansion term in Fig. 1.3 (c), which represent an interaction of the propagating test electron with the mean field generated by the rest of electrons. Analogously, the second interaction term in Fig. 1.4 is a sum over all the *exchange* type diagrams, the first-order representative of which is shown as the third expansion term in Fig. 1.3 (c). The exchange term takes account of the electron scattering processes whereby the test electron is exchanged with one of the electrons from the medium. Such processes reflect the quantum-mechanical indistinguishability of electrons. Since $\mathcal{G}_{\mathbf{p}}(\tau - \tau')$ appears on both sides of the Hartree-Fock equation in Fig. 1.4, it has to be determined self-consistently, in accordance with our earlier formulation of the method.

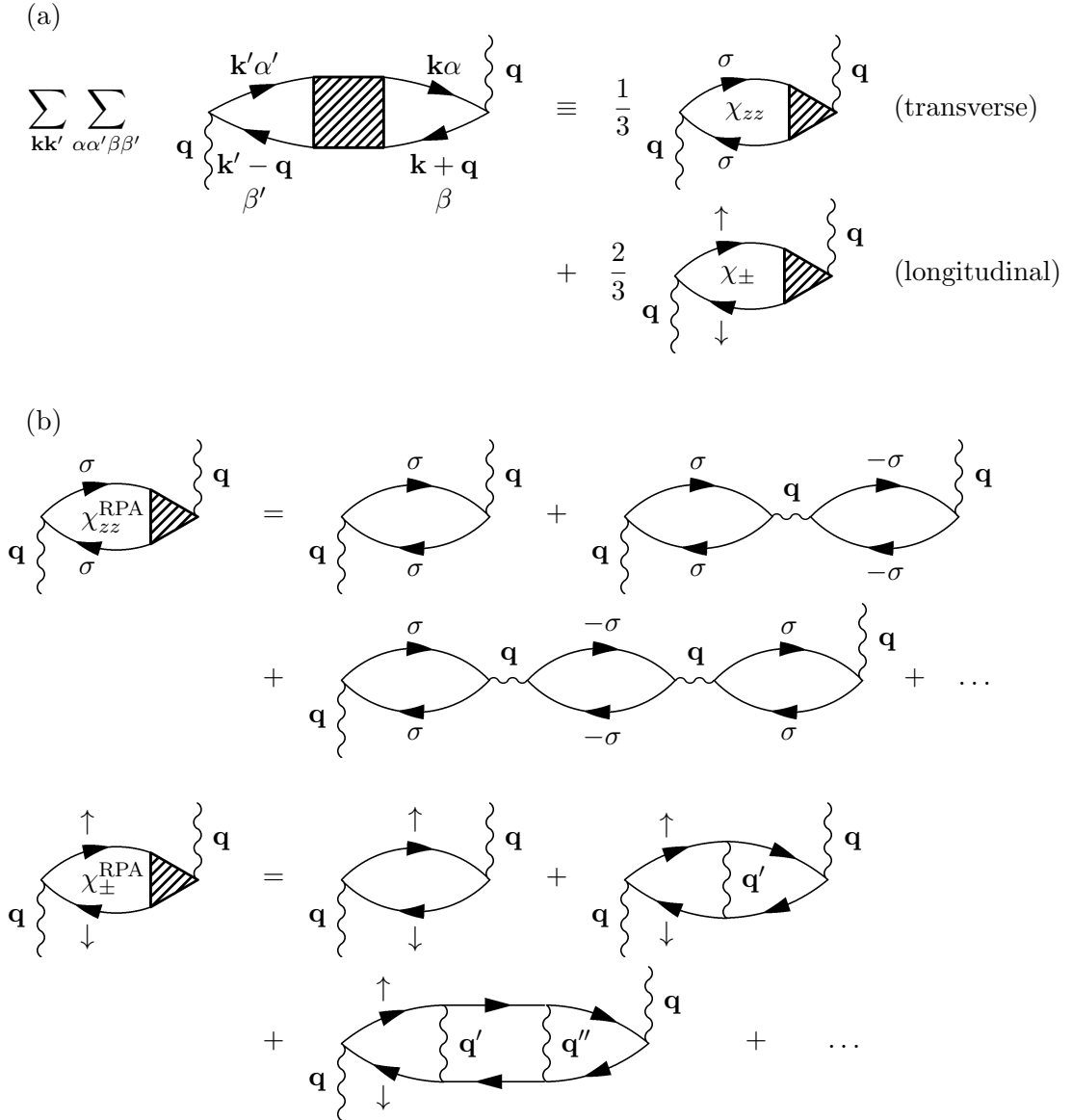
We consider next the *random phase approximation* (RPA) [Bohm53], which is a method commonly used to study the linear response of a many-body system to an external field. Within the RPA, the interaction between electrons is described in terms of electron-hole pairs excitations, which result in an effective *screening* of the Coulomb interaction⁸. The RPA gives accurate results for systems with high particle density.

Let us discuss the application of the RPA to the *dynamical spin susceptibility* $\chi(\mathbf{q}, i\omega)$. $\chi(\mathbf{q}, i\omega)$ is a measure of the system's response to an external magnetic field $H(\mathbf{r}, t)$ that varies in space and time. It can be calculated from a two-particle Matsubara Green's function:

$$\chi(\mathbf{q}, i\omega) = \int_0^\beta d\tau e^{i\omega(\tau - \tau')} \langle \hat{T}_\tau \hat{\mathbf{S}}_{\mathbf{q}}(\tau) \hat{\mathbf{S}}_{-\mathbf{q}}(\tau') \rangle, \quad \hat{\mathbf{S}}_{\mathbf{q}} = \frac{1}{2} \sum_{\mathbf{k}} \sum_{\alpha\beta} \hat{c}_{\mathbf{k}+\mathbf{q},\alpha}^\dagger \boldsymbol{\sigma}_{\alpha\beta} \hat{c}_{\mathbf{k},\beta}, \quad (1.22)$$

where α and β are spin indices and $\boldsymbol{\sigma}_{\alpha\beta}$ is the vector of Pauli matrices. Diagrammatically, $\chi(\mathbf{q}, i\omega)$ appears as a bubble in-between two interaction lines with wavevector \mathbf{q} ,

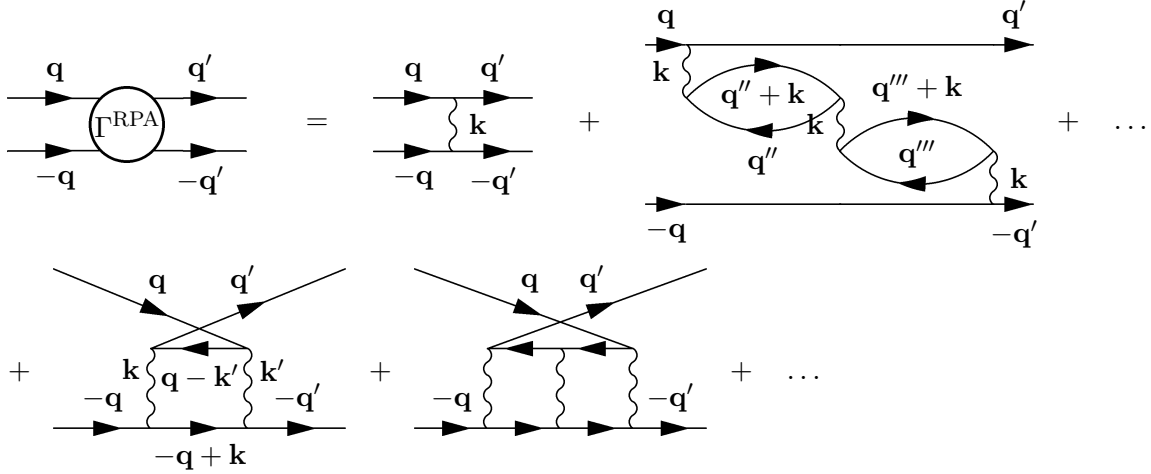
⁸In fact, approximations that are introduced to evaluate the infinite series expansion of a given response function within the RPA are equivalent to deriving that response function from the single-electron Green's function obtained within the *Hartree approximation*, which consists in keeping only the Hartree term in Fig. 1.4.

FIGURE 1.5: Magnetic susceptibility $\chi(\mathbf{q}, i\omega)$: (a) definition, (b) RPA expression.

as shown in Fig. 1.5 (a). The RPA for $\chi(\mathbf{q}, i\omega)$ consists in keeping only bubble- and ladder-like diagrams in the susceptibility expansion in terms of the interaction and the non-interacting magnetic susceptibility $\chi^0(\mathbf{q}, i\omega)$ [Fig. 1.5 (b)]. These diagrams represent scattering processes that excite electron-hole pairs on the way of the propagating electron.

Summing all the diagrams in Fig. 1.5 (b) up gives the following simple analytic expression for $\chi^{\text{RPA}}(\mathbf{q}, i\omega)$

$$\chi^{\text{RPA}}(\mathbf{q}, i\omega) = \frac{\chi^0(\mathbf{q}, i\omega)}{1 - U\chi^0(\mathbf{q}, i\omega)}, \quad (1.23)$$

FIGURE 1.6: RPA pairing vertex $\Gamma^{\text{RPA}}(\mathbf{q}, \mathbf{q}', i\omega)$.

where

$$\chi^0(\mathbf{q}, i\omega) = -\frac{1}{N\beta} \sum_{\mathbf{k}, i\omega_n} \mathcal{G}_{\mathbf{k}}(i\omega_n) \mathcal{G}_{\mathbf{k}+\mathbf{q}}(i\omega_n + i\omega). \quad (1.24)$$

On the other hand, the dynamical spin susceptibility is related to spin fluctuations via the *fluctuation-dissipation theorem*. Exchange of spin fluctuations between electrons results in their effective attraction or repulsion [Berk66]. In cuprates, the effective spin-fluctuation-exchange-mediated interaction between electrons is attractive, owing to the crystal and electronic structure peculiarities of these compounds, which has given rise to a development of a microscopic theory of magnetically driven high- T_c superconducting pairing (see Ref. [Scalapino95] and Section 5.2). In the RPA, the effective electron-electron interaction vertex $\Gamma^{\text{RPA}}(\mathbf{q}, \mathbf{q}', i\omega)$ arises from the RPA spin fluctuations, as shown in Fig. 1.6. After performing the summation, we get

$$\Gamma^{\text{RPA}}(\mathbf{q}, \mathbf{q}', i\omega) = U^2 \left(\frac{3}{2} \frac{\chi^0(\mathbf{q} - \mathbf{q}', i\omega)}{1 - U\chi^0(\mathbf{q} - \mathbf{q}', i\omega)} - \frac{1}{2} \frac{\chi^0(\mathbf{q} - \mathbf{q}', i\omega)}{1 + U\chi^0(\mathbf{q} - \mathbf{q}', i\omega)} \right) + U. \quad (1.25)$$

The pairing vertex $\Gamma^{\text{RPA}}(\mathbf{q}, \mathbf{q}', i\omega)$ can be straightforwardly used in the BCS gap equation [Bardeen57] as an effective attraction:

$$\Delta_{\mathbf{q}} = - \sum_{\mathbf{q}'} \frac{\Gamma^{\text{RPA}}(\mathbf{q}, \mathbf{q}', \omega = 0) \Delta_{\mathbf{q}'}}{2E_{\mathbf{q}'}} , \quad (1.26)$$

where $E_{\mathbf{q}} = \sqrt{\varepsilon(\mathbf{q}) + \Delta_{\mathbf{q}}}$. In Chapter 5, we use a multi-orbital version of the RPA expressions for the magnetic susceptibility and pairing vertex [Takimoto02].

Chapter 2

Electronic properties of solids within the density functional theory

Although the effective models for strongly correlated materials that we discussed in the previous chapter are very helpful in providing a *qualitative* description of the correlation effects, their common disadvantage is the fact that a major part of the system's degrees of freedom are neglected, except for those that are believed to be relevant for the effect of interest. With this kind of approximation, much of the material specific information is lost and the results of the model calculations cannot be easily compared to experimental results on a real material.

In this chapter, we would like to introduce a paradigm of methods that approach the many-body problem of solids (molecules, atomic clusters *etc.*) following quite a different route. In these methods, gathered under the name "*density functional theory*" (DFT), the central quantity is the electron density $\rho(\mathbf{r})$. The basic equations of the DFT are formulated in terms of the electron density, which in principle allows one to treat all electrons and all degrees of freedom in the system exactly and with as little effort as required to operate with only three spatial variables \mathbf{r} .

Also in the DFT, the complications due to the two-particle interaction terms in the Hamiltonian cannot be avoided and are eventually resolved using certain approximations. Nevertheless, the DFT provides an exact theoretical framework, which is open to continuous improvement on the approximations involved and can moreover be efficiently combined with many-body methods. The development of the combined DFT and many-body methods is a recently established research frontier in the solid state theory, which we have also tried to push forward in our work.

In the rest of this chapter, the reader will get familiar with the theoretical foundations of the DFT as well as with some of the practical aspects of its application to crystalline materials. The methods to derive effective model parameters for real systems by using the DFT will also be discussed.

2.1 Theoretical foundations

The microscopic world of atoms obeys quantum-mechanical laws. In a conventional quantum-mechanical language, the state of a many-particle microscopic system is described by the many-particle wave-function $\Psi(\mathbf{x}_1, \mathbf{x}_2, \dots, \mathbf{x}_N)$, where $\mathbf{x}_1, \mathbf{x}_2, \dots, \mathbf{x}_N$ are the spatial and spin coordinates of the system's N particles. The wave-function $\Psi(\mathbf{x}_1, \mathbf{x}_2, \dots, \mathbf{x}_N)$ is obtained by solving the time-independent¹ Schrödinger equation

$$\hat{H}\Psi = E\Psi, \quad (2.1)$$

where the Hamilton operator \hat{H} is given as

$$\hat{H} = \hat{H}_e + \hat{H}_{\text{Ion}} + \hat{H}_{e\text{-Ion}}, \quad (2.2)$$

with

$$\hat{H}_e = -\sum_i^{N_e} \frac{\hbar^2}{2m_e} \nabla_i^2 + \frac{1}{2} \frac{e^2}{4\pi\epsilon_0} \sum_i^{N_e} \sum_{j \neq i}^{N_e} \frac{1}{|\mathbf{r}_i - \mathbf{r}_j|}, \quad (2.3)$$

$$\hat{H}_{\text{Ion}} = -\sum_I^{N_{\text{Ion}}} \frac{\hbar^2}{2M_I} \nabla_I^2 + \frac{1}{2} \frac{e^2}{4\pi\epsilon_0} \sum_I^{N_{\text{Ion}}} \sum_{J \neq I}^{N_{\text{Ion}}} \frac{Z_I Z_J}{|\mathbf{R}_I - \mathbf{R}_J|}, \quad (2.4)$$

$$\hat{H}_{e\text{-Ion}} = -\frac{e^2}{4\pi\epsilon_0} \sum_i^{N_e} \sum_I^{N_{\text{Ion}}} \frac{Z_I}{|\mathbf{R}_I - \mathbf{r}_i|} \quad (2.5)$$

for an atomic system that consists of electronic (e) and ionic (Ion) subsystems. In Equations (2.3)–(2.5), N_e (N_{Ion}), m_e (M_I), $-e$ (eZ_I), \mathbf{r}_i (\mathbf{R}_I) are, respectively, the total number, mass, electric charge and spatial coordinates of electrons (ions). The double sum terms stand for the Coulomb interactions and the single sum terms represent the kinetic energy operators.

The Hamiltonian (2.2) can be considerably simplified if one recognizes that the ions are much less mobile than the electrons due to the much smaller electron mass (the proton mass is approximately equal $1836 m_e$). Then, the ions can be treated as being spatially fixed and the electrons as moving in an electrostatic potential of the motionless

¹It is assumed that there are no time-dependent potentials in the system's Hamiltonian \hat{H} .

ions $v_{\text{ext}}(\mathbf{r})$. This constitutes the *Born-Oppenheimer approximation* [Born27]. With the ionic degrees of freedom having been neglected, the Hamiltonian (2.2) reads

$$\hat{H} = \hat{H}_e + \hat{H}_{\text{e-Ion}} \equiv \hat{H}_e + \hat{V}_{\text{ext}}. \quad (2.6)$$

Unfortunately, even within the Born-Oppenheimer approximation solving the electron Schrödinger equation (2.1) still remains a complicated many-body problem.

With the Born-Oppenheimer approximation as a starting point, the fermionic density functional theory offers an alternative approach to this problem. The DFT considers the electron density $\rho(\mathbf{r})$,

$$\rho(\mathbf{r}) = \langle \Psi | \sum_i^{N_e} \delta(\mathbf{r} - \mathbf{r}_i) | \Psi \rangle, \quad (2.7)$$

as a quantity that incorporates all information about the system, which is justified by the *Hohenberg-Kohn theorem*. The electron density $\rho(\mathbf{r})$ is equivalent in this sense to the many-electron wave-function $\Psi(\mathbf{r}_1, \mathbf{r}_2, \dots, \mathbf{r}_{N_e})$ but is much easier to handle as $\rho(\mathbf{r})$ is a function of three variables whereas $\Psi(\mathbf{r}_1, \mathbf{r}_2, \dots, \mathbf{r}_{N_e})$ is a function of $3N_e$ variables. The DFT approach, though, has a disadvantage with respect to the conventional quantum-mechanical approach in that it only gives access to the *ground state* properties.

2.1.1 Hohenberg-Kohn theorem

The Hohenberg-Kohn theorem [Hohenberg64] is formulated in two statements.

Statement 1. The external potential $v_{\text{ext}}(\mathbf{r})$ is uniquely determined within an additive constant by the electron density $\rho(\mathbf{r})$.

$\rho(\mathbf{r})$ also determines the number of electrons N_{el} . It follows then that the ground state wave-function Ψ_0 and all the other properties of the system, which depend on $v_{\text{ext}}(\mathbf{r})$, are determined by the electron density. In particular, $\rho(\mathbf{r})$ determines the total energy E , *i. e.*, E is a *functional* of $\rho(\mathbf{r})$: $E[\rho]$. Just following the Hamiltonian decomposition (2.6), the total energy functional can be written as

$$\begin{aligned} E[\rho] &= H_e[\rho] + V_{\text{ext}}[\rho] \\ &= T[\rho] + V_{\text{e-e}}[\rho] + V_{\text{ext}}[\rho] \\ &= T[\rho] + V_{\text{e-e}}[\rho] + \int \rho(\mathbf{r}) v_{\text{ext}}(\mathbf{r}) d\mathbf{r} \\ &= F_{\text{HK}}[\rho] + \int \rho(\mathbf{r}) v_{\text{ext}}(\mathbf{r}) d\mathbf{r}, \end{aligned} \quad (2.8)$$

where T is the kinetic energy and $V_{\text{e-e}}$ is the electronic Coulomb repulsion.

Statement 2. With the energy functional $E[\rho]$ defined as (2.8), the ground state energy (E_0) variational principle reads:

$$E_0 \leq E[\tilde{\rho}], \quad (2.9)$$

where $\tilde{\rho}(\mathbf{r})$ is a trial density such that $\tilde{\rho}(\mathbf{r}) \geq 0$ and $\int \tilde{\rho}(\mathbf{r}) d\mathbf{r} = N_e$.

The ground state density should therefore satisfy the stationary principle

$$\delta \left\{ E[\rho] - \mu \left[\int \rho(\mathbf{r}) d\mathbf{r} - N_e \right] \right\} = 0, \quad (2.10)$$

where the second term expresses the total electron number constraint on $\rho(\mathbf{r})$ and μ is the associated Lagrange multiplier. Eq. (2.10) transforms into the Euler-Lagrange equation:

$$\begin{aligned} \mu &= \frac{\delta E[\rho]}{\delta \rho(\mathbf{r})} \\ &= v_{\text{ext}}(\mathbf{r}) + \frac{\delta F_{\text{HK}}[\rho]}{\delta \rho(\mathbf{r})}. \end{aligned} \quad (2.11)$$

The term $\frac{\delta F_{\text{HK}}[\rho]}{\delta \rho(\mathbf{r})}$ is decoupled from the external potential $v_{\text{ext}}(\mathbf{r})$ and therefore $F_{\text{HK}}[\rho]$ is a *universal* functional. The Euler-Lagrange equation is the central equation of the DFT and by solving it one could find the electron density and other quantities of interest. Unfortunately, this is never done in practice as the functional $F_{\text{HK}}[\rho]$ is not known. Instead, in order to proceed, one resorts to approximate schemes, which all consist in approximating certain terms in $F_{\text{HK}}[\rho]$.

$F_{\text{HK}}[\rho]$ can be written as [see Eq. (2.8)]

$$\begin{aligned} F_{\text{HK}}[\rho] &= T[\rho] + V_{e-e}[\rho] \\ &= T[\rho] + V_{\text{H}}[\rho] + V_{\text{xc}}[\rho], \end{aligned} \quad (2.12)$$

where $V_{\text{H}}[\rho]$ is the Hartree (classical) term,

$$V_{\text{H}}[\rho] = \frac{1}{2} \frac{e^2}{4\pi\epsilon_0} \int \frac{\rho(\mathbf{r})\rho(\mathbf{r}')}{|\mathbf{r} - \mathbf{r}'|} d\mathbf{r}d\mathbf{r}', \quad (2.13)$$

and $V_{\text{xc}}[\rho]$ is the exchange-correlation (non-classical) term, whose mathematical expression is unknown but assumed to exist. As a first approximation to $F_{\text{HK}}[\rho]$, the Thomas-Fermi model [Fermi27, Thomas27] only retains the Hartree term in $V_{e-e}[\rho]$ and approximates the kinetic term $T[\rho]$ by that of a non-interacting uniform electron gas. The Thomas-Fermi-Dirac model [Dirac30] is an improvement on top of the Thomas-Fermi model, where the exchange-correlation term $V_{\text{xc}}[\rho]$ is represented by the exchange energy

formula for a uniform electron gas². The most accurate and successful method to handle the functional $F_{\text{HK}}[\rho]$ was, however, proposed by Kohn and Sham in 1965.

2.1.2 Kohn-Sham equations

The *Kohn-Sham method* [Kohn65] treats in an indirect but exact way a larger part of the kinetic energy $T[\rho]$ by mapping the actual interacting electron system onto a *non-interacting reference system*.

The non-interacting reference system of Kohn and Sham is described by the Hamiltonian \hat{H}_s ,

$$\begin{aligned}\hat{H}_s &= \sum_i^{N_e} \hat{h}_s \\ &= \sum_i^{N_e} \left\{ -\frac{\hbar^2}{2m_e} \nabla_i^2 + v_s(\mathbf{r}_i) \right\} \\ &= \hat{T}_s + \sum_i^{N_e} v_s(\mathbf{r}_i),\end{aligned}\tag{2.14}$$

where the single-electron potential $v_s(\mathbf{r})$ is such that the ground state electron density of the system is exactly $\rho(\mathbf{r})$. For this system the ground state wave-function is a single Slater determinant

$$\Psi_0^s = \frac{1}{\sqrt{N!}} \det[\psi_1 \psi_2 \dots \psi_{N_e}],\tag{2.15}$$

with ψ_i being the N_e lowest eigenstates of \hat{h}_s :

$$\hat{h}_s \psi_i = \varepsilon_i \psi_i.\tag{2.16}$$

Kohn and Sham proposed to express the Euler-Lagrange equation (2.11) in terms of the functional $T_s[\rho]$ and the single-electron orbitals ψ_i by rearranging the $F_{\text{HK}}[\rho]$ terms as

$$F_{\text{HK}}[\rho] = T_s[\rho] + V_H[\rho] + E_{\text{xc}}[\rho],\tag{2.17}$$

with the *exchange-correlation functional* $E_{\text{xc}}[\rho]$ defined as

$$E_{\text{xc}}[\rho] \equiv T[\rho] - T_s[\rho] + V_{\text{e-e}}[\rho] - V_{\text{H}}[\rho].\tag{2.18}$$

So, the exchange-correlation functional $E_{\text{xc}}[\rho]$ incorporates the difference $T[\rho] - T_s[\rho]$, which is assumed to be small, and the non-classical part of the electronic interaction.

²Note that the Thomas-Fermi and Thomas-Fermi-Dirac models appeared before the Hohenberg-Kohn theorem and do not use the energy variational principle.

Now, the Euler-Lagrange equation becomes

$$\mu = v_{\text{eff}}(\mathbf{r}) + \frac{\delta T_s[\rho]}{\delta \rho(\mathbf{r})}, \quad (2.19)$$

where

$$v_{\text{eff}}(\mathbf{r}) = v_{\text{ext}}(\mathbf{r}) + \frac{\delta V_{\text{H}}[\rho]}{\delta \rho(\mathbf{r})} + \frac{\delta E_{\text{xc}}[\rho]}{\delta \rho(\mathbf{r})}, \quad (2.20)$$

$$\frac{\delta V_{\text{H}}[\rho]}{\delta \rho(\mathbf{r})} = \frac{e^2}{4\pi\epsilon_0} \int \frac{\rho(\mathbf{r}')}{|\mathbf{r} - \mathbf{r}'|} d\mathbf{r}', \quad (2.21)$$

$$\frac{\delta E_{\text{xc}}[\rho]}{\delta \rho(\mathbf{r})} = v_{\text{xc}}(\mathbf{r}). \quad (2.22)$$

From the analogy of Eq. (2.19) with the expression that one would obtain for the non-interacting system (2.14) under the condition $v_s(\mathbf{r}) = v_{\text{eff}}(\mathbf{r})$, it follows that the ground state $\rho(\mathbf{r})$ can be obtained by solving the N_e one-electron equations

$$\left\{ -\frac{\hbar^2}{2m_e} \nabla^2 + v_{\text{eff}}(\mathbf{r}) \right\} \psi_i = \varepsilon_i \psi_i \quad (2.23)$$

and setting (σ is the spin coordinate)

$$\rho(\mathbf{r}) = \sum_i^{N_e} \sum_{\sigma} |\psi_i(\mathbf{r}, \sigma)|^2. \quad (2.24)$$

Equations (2.20)–(2.24) are the *Kohn-Sham equations*. The Kohn-Sham eigenvalues ε_i are, in fact, mere Lagrange multipliers associated with the constraint that the single-electron orbitals be orthonormal and *not* the single-particle energies.

2.1.3 Exchange-correlation functional

The Kohn-Sham method allows to accumulate all the exchange and correlation effects in the functional $E_{\text{xc}}[\rho]$. If this functional were available, the solution of the Kohn-Sham equations would provide the exact ground state electron density, total energy *etc.* The functional $E_{\text{xc}}[\rho]$ is not known, however, but the power of the Kohn-Sham method is to provide an exact theoretical framework, within which the description of $E_{\text{xc}}[\rho]$ can be continuously improved.

The concept of a uniform electron gas from the Thomas-Fermi-Dirac model proved very useful in a search for a good approximation to $E_{\text{xc}}[\rho]$. Thus, in the *local-density*

approximation (LDA), the exchange-correlation functional is of the form

$$E_{\text{xc}}^{\text{LDA}}[\rho] = \int \rho(\mathbf{r})\varepsilon_{\text{xc}}(\rho)d\mathbf{r}, \quad (2.25)$$

where $\varepsilon_{\text{xc}}(\rho)$ is the exchange and correlation energy per particle of a uniform electron gas. $\varepsilon_{\text{xc}}(\rho)$ can be divided into the exchange and correlation contributions:

$$\varepsilon_{\text{xc}}(\rho) = \varepsilon_{\text{x}}(\rho) + \varepsilon_{\text{c}}(\rho). \quad (2.26)$$

The exchange contribution is available in an analytical form,

$$\varepsilon_{\text{x}}(\rho) = -C_x\rho(\mathbf{r})^{1/3}, \quad C_x = \frac{3}{4} \left(\frac{3}{\pi} \right)^{1/3}, \quad (2.27)$$

while the correlation contribution can be numerically calculated. Commonly used are the quantum Monte Carlo results for $\varepsilon_{\text{x}}(\rho)$ obtained by Ceperley and Alder [Ceperley80] and subsequently parameterized by Perdew and Zunger [Perdew81] and by Perdew and Wang [Perdew92].

By construction, the LDA method is expected to perform well for systems with slowly varying electron densities. Atoms and molecules are apparently not such systems, but the LDA has nevertheless been generally quite successful in describing them. Yet, the LDA fails for transition metal compounds, where the electron inhomogeneity due to the open $3d$ shell is particularly pronounced. The LDA, for example, does not reproduce the Mott insulating state in oxides MnO, NiO, NiS, YBa₂Cu₃O₆ and La₂CuO₄ [Terakura84, Pickett89, Singh91] as well as in the materials studied in this thesis Cs₂CuCl₄, Cs₂CuBr₄, Bi₂Sr₂CaCu₂O₈ and TiOCl.

Since a Mott insulating state is often associated with magnetic ordering, a natural improvement to the LDA would be a functional that allows magnetically-polarized solutions for the electron density. This idea is realized in the *local spin-density approximation* (LSDA) method. In order to derive the LSDA exchange-correlation functional $E_{\text{xc}}^{\text{LSDA}}[\rho]$, one needs to generalize the DFT for cases with a finite vector potential of magnetic field $\mathbf{B}(\mathbf{r})$. The generalized Hamiltonian reads [compare to Eq. (2.6)]

$$\hat{H} = \hat{H}_{\text{e}} + \hat{V}_{\text{ext}} + 2\mu_{\text{B}} \sum_i^{N_{\text{e}}} \mathbf{B}(\mathbf{r}) \cdot \mathbf{s}_i, \quad (2.28)$$

where μ_{B} is the Bohr magneton and \mathbf{s}_i is the spin angular momentum vector of electron i . It turns out that the properties of a system described by this Hamiltonian are uniquely determined by two quantities, the spin-up electron density $\rho^{\uparrow}(\mathbf{r})$ and the spin-down electron density $\rho^{\downarrow}(\mathbf{r})$, which is analogous to the role of $\rho(\mathbf{r}) = \rho^{\uparrow}(\mathbf{r}) + \rho^{\downarrow}(\mathbf{r})$ in the

spin-independent DFT. The Hohenberg-Kohn functional becomes now a functional of two variables [compare to Eq. (2.17)],

$$F_{\text{HK}}[\rho^\uparrow, \rho^\downarrow] = T_s[\rho^\uparrow, \rho^\downarrow] + V_{\text{H}}[\rho^\uparrow + \rho^\downarrow] + E_{\text{xc}}[\rho^\uparrow, \rho^\downarrow]. \quad (2.29)$$

In analogy to the LDA, $E_{\text{xc}}^{\text{LSDA}}[\rho^\uparrow, \rho^\downarrow]$ depends only on the local spin-up and -down electron densities,

$$E_{\text{xc}}^{\text{LSDA}}[\rho^\uparrow, \rho^\downarrow] = \int \left\{ \rho^\uparrow(\mathbf{r}) + \rho^\downarrow(\mathbf{r}) \right\} \varepsilon_{\text{xc}}(\rho^\uparrow, \rho^\downarrow) d\mathbf{r}, \quad (2.30)$$

where $\varepsilon_{\text{xc}}(\rho^\uparrow, \rho^\downarrow)$ corresponds to the exchange and correlation energy per particle of a uniform spin-polarized electron gas.

Even though the spin-density functional theory is defined such as to account for the presence of a magnetic field, it is also highly relevant for magnetically isolated systems with uncompensated spin (odd number of electrons), among which are many transition metal compounds. The mentioned MnO appears insulating and antiferromagnetically ordered within the LSDA [Terakura84], which is a big qualitative improvement with respect to the LDA. As the present work reveals, the same result is obtained for Cs_2CuCl_4 and Cs_2CuBr_4 . However, there are many Mott insulators, where the LSDA does not completely remove electronic states at the Fermi level as in, for example, the ZnV_2O_4 spinel [Maitra07].

Another improvement of the LDA is to also take into account the non-local dependence of the exchange-correlation potential $v_{\text{xc}}(\mathbf{r})$ on $\rho(\mathbf{r}')$, where $\mathbf{r}' \neq \mathbf{r}$. This is a reasonable step to consider for systems with strongly varying electron density. In the *generalized gradient approximation* (GGA), the non-locality of $v_{\text{xc}}(\mathbf{r})$ is introduced into the exchange-correlation functional through the local electron density gradient $\nabla\rho(\mathbf{r})$:

$$E_{\text{xc}}^{\text{GGA}}[\rho] = \int \rho(\mathbf{r}) F(\rho, \nabla\rho) d\mathbf{r}. \quad (2.31)$$

The function $F(\rho, \nabla\rho)$, which comprises a polynomial expression of $\nabla\rho(\mathbf{r})$, can be constructed and parameterized in various ways. Accordingly, there exist a number of GGA functionals $E_{\text{xc}}^{\text{GGA}}[\rho]$ [Langreth83, Perdew86, Wu06, Perdew96, Perdew08], some of them being based on fitting to experimental data. The GGA method has been shown to give slightly quantitatively better results for a number of transition metal compounds in terms of the binding energy and band gap.

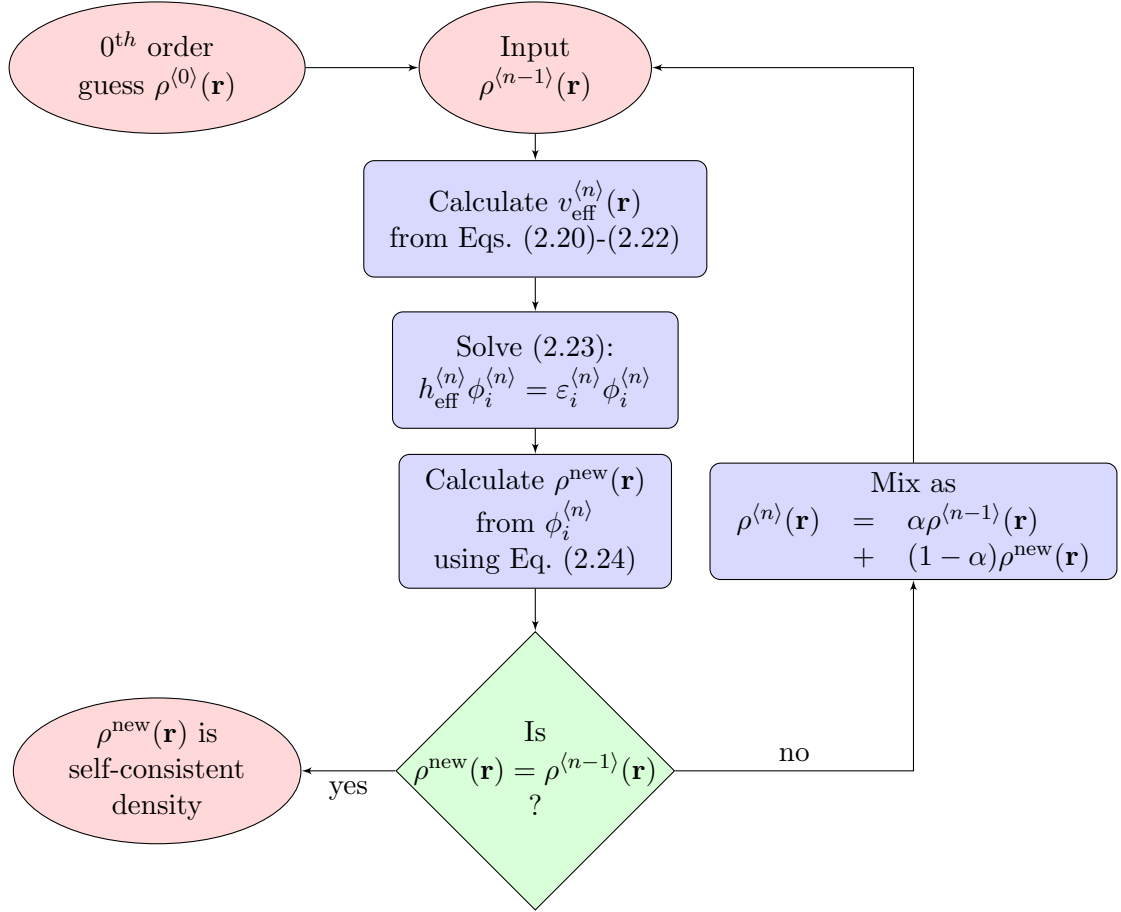


FIGURE 2.1: DFT cycle.

2.1.4 DFT cycle

The Kohn-Sham equations (2.20)–(2.24) present a non-linear problem to find the electron density $\rho(\mathbf{r})$ as the effective potential $v_{\text{eff}}(\mathbf{r})$ depends on $\rho(\mathbf{r})$ via Eq. (2.24). Therefore, the Kohn-Sham equations have to be solved *self-consistently* in an iterative way. In the first iteration, $v_{\text{eff}}(\mathbf{r})$ is calculated from a guessed electron density $\rho^{(0)}(\mathbf{r})$ and the Kohn-Sham equations are then numerically solved. The obtained new electron density $\rho^{(1)}(\mathbf{r})$ is used to generate a new potential for the second iteration. This cyclic procedure is repeated until convergence is reached, which means that the input electron density is equal, to specified accuracy, to the output electron density from the solution of the Kohn-Sham equations. The DFT cycle is schematically illustrated in Fig. 2.1.

It should be noted that although the Kohn-Sham eigenenergies ε_i do not have direct physical meaning they are usually regarded as a reasonable approximation to the true single-electron eigenenergies. As a function of the momentum \mathbf{k} vector, $\varepsilon_i(\mathbf{k})$ are used to reproduce the *bandstructure* of a periodical crystalline solid. The *density of states*

(DOS) as a function of energy E , $g(E)$, is also defined in terms of $\varepsilon_i(\mathbf{k})$:

$$g(E) = \frac{2}{V_{\text{BZ}}} \sum_i^{N_e} \int \delta \{E - \varepsilon_i(\mathbf{k})\} d\mathbf{k}, \quad (2.32)$$

where the integration is performed over the first Brillouin zone and V_{BZ} is the volume of the Brillouin zone.

2.2 Application to crystalline materials: variability of basis sets

In a crystalline solid, the ionic potential $v_{\text{ext}}(\mathbf{r})$ possesses translational symmetry,

$$v_{\text{ext}}(\mathbf{r} + \mathbf{R}^T) = v_{\text{ext}}(\mathbf{r}), \quad (2.33)$$

with \mathbf{R}^T being a lattice vector. According to the Bloch's theorem [Bloch29], the single-electron wave-functions [Eq. (2.23)] that correspond to this periodic potential are the Bloch wave-functions $\psi_{i\mathbf{k}}(\mathbf{r})$,

$$\psi_{i\mathbf{k}}(\mathbf{r}) = e^{i\mathbf{k}\cdot\mathbf{r}} u_{i\mathbf{k}}(\mathbf{r}), \quad (2.34)$$

where $u_{i\mathbf{k}}(\mathbf{r})$ is a periodic function with the same periodicity as $v_{\text{ext}}(\mathbf{r})$. Note that the momentum vector \mathbf{k} is a good quantum number in a periodic environment.

In order to solve the single-electron Kohn-Sham equations,

$$\left\{ -\frac{\hbar^2}{2m_e} \nabla^2 + v_{\text{eff}}(\mathbf{r}) \right\} \psi_{i\mathbf{k}}(\mathbf{r}) = \varepsilon_i(\mathbf{k}) \psi_{i\mathbf{k}}(\mathbf{r}), \quad (2.35)$$

$\psi_{i\mathbf{k}}(\mathbf{r})$ are expanded in terms of some given *basis functions* $\phi_{n\mathbf{k}}(\mathbf{r})$,

$$\psi_{i\mathbf{k}}(\mathbf{r}) = \sum_n^P c_i^n \phi_{n\mathbf{k}}(\mathbf{r}), \quad (2.36)$$

c_i^n being expansion coefficients³. The number of basis functions P can be, in general, infinite, but for practical applications one of course retains only a finite number of basis functions with, presumably, the highest contribution. In terms of the basis functions,

³This is a general prescription, applied also to systems without translational symmetry, like atomic clusters and molecules.

the Kohn-Sham equations now become

$$\begin{aligned}
& \begin{pmatrix} \langle \phi_{1\mathbf{k}} | \hat{h}_{\text{eff}} | \phi_{1\mathbf{k}} \rangle & \langle \phi_{1\mathbf{k}} | \hat{h}_{\text{eff}} | \phi_{2\mathbf{k}} \rangle & \cdots \\ \langle \phi_{2\mathbf{k}} | \hat{h}_{\text{eff}} | \phi_{1\mathbf{k}} \rangle & \langle \phi_{2\mathbf{k}} | \hat{h}_{\text{eff}} | \phi_{2\mathbf{k}} \rangle & \cdots \\ \vdots & \vdots & \ddots \\ & & & \langle \phi_{P\mathbf{k}} | \hat{h}_{\text{eff}} | \phi_{P\mathbf{k}} \rangle \end{pmatrix} \begin{pmatrix} c_i^1 \\ c_i^2 \\ \vdots \\ c_i^P \end{pmatrix} \\
= \varepsilon_i(\mathbf{k}) & \begin{pmatrix} \langle \phi_{1\mathbf{k}} | \phi_{1\mathbf{k}} \rangle & \langle \phi_{1\mathbf{k}} | \phi_{2\mathbf{k}} \rangle & \cdots \\ \langle \phi_{2\mathbf{k}} | \phi_{1\mathbf{k}} \rangle & \langle \phi_{2\mathbf{k}} | \phi_{2\mathbf{k}} \rangle & \cdots \\ \vdots & \vdots & \ddots \\ & & & \langle \phi_{P\mathbf{k}} | \phi_{P\mathbf{k}} \rangle \end{pmatrix} \begin{pmatrix} c_i^1 \\ c_i^2 \\ \vdots \\ c_i^P \end{pmatrix}. \quad (2.37)
\end{aligned}$$

This is a secular equation, which is solved for every \mathbf{k} -vector by diagonalizing the Hamiltonian matrix with $\langle \phi_{n\mathbf{k}} | \hat{h}_{\text{eff}} | \phi_{m\mathbf{k}} \rangle$ elements. Eq. (2.37) can be written in a shorter matrix form as

$$HC = SCE, \quad (2.38)$$

where H is the Hamiltonian matrix, S is the overlap matrix, $E = \text{diag}[\varepsilon_i(\mathbf{k})]$ and C is a matrix of expansion coefficients c_i^n .

There are quite a number of basis sets proposed and developed over the recent years. Here, we will consider in detail three of them, namely the linearized muffin-tin orbitals (LMTO), the full-potential local-orbital minimum-basis set (FPLO) and the linearized augmented plane waves (LAPW), as these are intensively used in our calculations. In general, calculations with basis sets constructed out of local orbitals (like LMTO and FPLO) are fast since a relatively small number of basis functions suffice in the $\psi_{i\mathbf{k}}(\mathbf{r})$ expansion, Eq. (2.36). In this sense, such basis sets are *efficient*. On the other hand, the resulting wave-functions $\psi_{i\mathbf{k}}(\mathbf{r})$ can inherit too much of the basis functions' features and thus be quite off the true wave-functions of the system. One says in this case that the basis set is *biased*. Basis sets constructed out of plane waves (like LAPW) are unbiased and thus better, in terms of accuracy, compared to local-orbital basis sets. However, one usually requires many plane-wave basis functions in the expansion (2.36), which means longer computational times.

In fact, the accuracy problems of local-orbital basis sets are much less severe in the case of the FPLO basis, thanks to an ingenious scheme of reconstructing the secular problem and to an exact representation of the lattice potential. The accuracy of the FPLO scheme is comparable to that of the LAPW scheme.

2.2.1 LMTO and NMTO

The basis functions of the LMTO method [Andersen75] are local orbitals centered at atomic positions \mathbf{R}_I . They are solutions to the Schrödinger equation with the potential

$$v_{\text{MTO}}(\mathbf{r} - \mathbf{R}_I) = \begin{cases} v_{\text{eff}}(|\mathbf{r} - \mathbf{R}_I|), & |\mathbf{r} - \mathbf{R}_I| < R_{\text{MT}}^I \\ v_{\text{MTO}}^0, & |\mathbf{r} - \mathbf{R}_I| \geq R_{\text{MT}}^I \end{cases}, \quad (2.39)$$

which is defined as a constant v_{MTO}^0 outside the *muffin-tin sphere* of atom I with radius R_{MT}^I and as the spherical average of the crystal potential $v_{\text{eff}}(r)$ inside the muffin tin sphere. The Schrödinger equation is solved separately for the region inside the muffin-tin sphere and for the outside region, called the *interstitial* region. The two solutions are matched by making use of the requirement that the *muffin-tin orbital* (MTO) has to be continuous and differentiable on the boundary between the two regions. This leads to the following MTO expression:

$$\phi_{lm}^{\text{MTO}}(\mathbf{r} - \mathbf{R}_I, E) = \begin{cases} N_l^I(E)\varphi_{lm}(\mathbf{r} - \mathbf{R}_I, E) + P_l^I(E)J_{lm}(\mathbf{r} - \mathbf{R}_I), & |\mathbf{r} - \mathbf{R}_I| \leq R_{\text{MT}}^I \\ K_{lm}(\mathbf{r} - \mathbf{R}_I), & |\mathbf{r} - \mathbf{R}_I| \geq R_{\text{MT}}^I \end{cases}. \quad (2.40)$$

Here, $J_{lm}(\mathbf{r} - \mathbf{R}_I)$ and $K_{lm}(\mathbf{r} - \mathbf{R}_I)$ are, respectively, the regular and irregular solutions of the Laplace equation in the interstitial region, $\varphi_{lm}(\mathbf{r} - \mathbf{R}_I, E)$ is the energy dependent solution of the Schrödinger equation inside the muffin-tin sphere (partial wave) and the functions $N_l^I(E)$ and $P_l^I(E)$, given in terms of $J_{lm}(\mathbf{r} - \mathbf{R}_I)$, $K_{lm}(\mathbf{r} - \mathbf{R}_I)$ and $\varphi_{lm}(\mathbf{r} - \mathbf{R}_I, E)$, take care of the boundary matching.

The energy dependence of $\phi_{lm}^{\text{MTO}}(\mathbf{r} - \mathbf{R}_I, E)$ considerably complicates the Kohn-Sham problem as the system's energy E is not available before the Kohn-Sham equations are solved. In order to get rid of the energy dependence of the basis, the MTO's are *linearized*, *i. e.*, the functions $\varphi_{lm}(\mathbf{r} - \mathbf{R}_I, E)$ are replaced by their Taylor expansions with respect to E up to a linear term:

$$\varphi_{lm}(\mathbf{r} - \mathbf{R}_I, E) \rightarrow \varphi_{lm}(\mathbf{r} - \mathbf{R}_I, E_l^I) + (E - E_l^I) \left. \frac{\partial \varphi_{lm}(\mathbf{r} - \mathbf{R}_I, E)}{\partial E} \right|_{E=E_l^I}. \quad (2.41)$$

The linear E dependence is removed by matching the linearized $\varphi_{lm}(\mathbf{r} - \mathbf{R}_I, E)$ at the muffin-tin sphere boundary with the interstitial solution.

In the *polynomial MTO method* (NMTO) [Andersen00], the muffin-tin sphere part of the basis function is given as a linear combination of partial waves evaluated at N fixed

energies E_n :

$$\chi_{lm}^{(N)}(\mathbf{r} - \mathbf{R}_I) = \sum_{n=0}^N \sum_{\mathbf{R}_{I'} m'} \varphi_{lm'}(\mathbf{r} - \mathbf{R}_{I'}, E_n) L_{\mathbf{R}_{I'} lm', \mathbf{R}_I lm; n}^{(N)}, \quad (2.42)$$

with

$$\sum_{n=0}^N L_{\mathbf{R}_{I'} lm', \mathbf{R}_I lm; n}^{(N)} = \delta_{\mathbf{R}_{I'} \mathbf{R}_I} \delta_{m' m}. \quad (2.43)$$

The advantage of the NMTO method compared to the (L)MTO method is its ability to produce the correct bandstructure in a wide energy window without increasing the basis set size, which makes it most suitable for downfolding.

The preparation of the LMTO/NMTO basis functions is finalized by constructing the Bloch sums:

$$\phi_{lm\mathbf{k}}^{\text{LMTO/NMTO}}(\mathbf{r} - \mathbf{R}_I) = \sum_{\mathbf{R}^T} \phi_{lm}^{\text{LMTO/NMTO}}(\mathbf{r} - \mathbf{R}_I) e^{i\mathbf{k} \cdot \mathbf{R}^T}, \quad (2.44)$$

which are the appropriate functions to be used for a periodic crystal.

The MTO methods are often applied jointly with the *atomic sphere approximation* (ASA), which consists in choosing overlapping muffin-tin spheres and introducing so-called empty spheres to fill the remaining interstitial space.

One feature of the LMTO and NMTO methods used in the present work that strongly affects their accuracy is that these methods are not *full-potential* as one uses the approximated potential (2.39) also to solve the Kohn-Sham equations.

2.2.2 FPLO

There exist several versions of the FPLO method, all having been developed by Eschrig, Koepnik and co-authors. The original ideas of the method were introduced in Ref. [Koepnik99]. The FPLO calculations of this thesis are performed with the latest versions FPLO8.50-33 and FPLO9.00-34, which differ in a few aspects from the original formulation and which we briefly review here.

The FPLO method uses non-orthogonal local orbitals obtained as solutions to the Schrödinger equation with the spherically symmetric potential that consists of three terms⁴:

$$v_{\text{FPLO}}(\mathbf{r} - \mathbf{R}_I) = v_{\text{eff}}^0(|\mathbf{r} - \mathbf{R}_I|) + v_{\text{conf}}(|\mathbf{r} - \mathbf{R}_I|) + v^Q(|\mathbf{r} - \mathbf{R}_I|). \quad (2.45)$$

⁴In the original version of the FPLO method by Koepnik and Eschrig [Koepnik99], $v_{\text{FPLO}}(\mathbf{r} - \mathbf{R}_I)$ only contained the first two terms of Eq. (2.45).

Here, $v_{\text{eff}}^0(|\mathbf{r} - \mathbf{R}_I|)$ is the free atom potential, $v_{\text{conf}}(|\mathbf{r} - \mathbf{R}_I|) \sim |\mathbf{r} - \mathbf{R}_I|^4$ is the confining potential and $v^Q(|\mathbf{r} - \mathbf{R}_I|)$ is the binding potential for higher states. The role of the confining potential is to compress the local valence basis orbitals.

The FPLO basis is adjusted in the beginning of calculations by choosing optimal parameters for v_{conf} and v^Q and is kept fixed in the self-consistent cycle. In the older FPLO versions, the basis set is updated for every new iteration as there one uses the spherically averaged actual crystal potential instead of the free atom potential for defining $v_{\text{FPLO}}(\mathbf{r} - \mathbf{R}_I)$, which is similar to the LMTO/NMTO basis construction.

The FPLO method is a *full-potential* method, with the crystal potential $v_{\text{eff}}(\mathbf{r})$ being decomposed for the sake of computational convenience as

$$v_{\text{eff}}(\mathbf{r}) = \sum_{\mathbf{R}^T + \mathbf{R}_I, lm} v_{\text{eff}}^{\mathbf{R}_I, lm}(|\mathbf{r} - \mathbf{R}^T - \mathbf{R}_I|) Y_{lm}(\mathbf{r} - \mathbf{R}^T - \mathbf{R}_I), \quad (2.46)$$

where $Y_{lm}(\mathbf{r} - \mathbf{R}^T - \mathbf{R}_I)$ are spherical harmonics. The sum over lm is convergent and can be approximated by a finite sum with a cut-off l_{max} .

The very efficient approach of the FPLO method to the Kohn-Sham problem is to divide the basis functions into *core* and *valence* states according to the criterion that the strongly localized core states are orthogonal among each other and use the orthogonality of core states to reduce the rank of the secular matrix. With the valence states labeled as v and the core states as c , the overlap matrix S can be written as

$$S = \begin{pmatrix} S_{cc} & S_{cv} \\ S_{vc} & S_{vv} \end{pmatrix}, \quad (2.47)$$

with

$$S_{cc} = \langle \phi_{c'}^{\text{FPLO}}(\mathbf{r} - \mathbf{R}_{I'}) | \phi_c^{\text{FPLO}}(\mathbf{r} - \mathbf{R}_I) \rangle = \delta_{c'c} \delta_{\mathbf{R}_{I'} \mathbf{R}_I} \quad (2.48)$$

and

$$S_{vc} = S_{cv}^\dagger. \quad (2.49)$$

The Hamiltonian matrix H simplifies to

$$H = \begin{pmatrix} H_{cc} & H_{cc} S_{cv} \\ S_{vc} H_{cc} & H_{vv} \end{pmatrix}, \quad (2.50)$$

with

$$H_{cc} = \langle \phi_{c'}^{\text{FPLO}}(\mathbf{r} - \mathbf{R}_{I'}) | \hat{H} | \phi_c^{\text{FPLO}}(\mathbf{r} - \mathbf{R}_I) \rangle = \varepsilon_{c, \mathbf{R}_I} \delta_{c'c} \delta_{\mathbf{R}_{I'} \mathbf{R}_I}. \quad (2.51)$$

The orthogonality of core states makes it possible to perform a simplified Cholesky decomposition of S :

$$S = S^l S^r = \begin{pmatrix} 1 & 0 \\ S_{vc}^l & S_{vv}^l \end{pmatrix} \begin{pmatrix} 1 & S_{cv}^r \\ 0 & S_{vv}^r \end{pmatrix}. \quad (2.52)$$

Rewriting the secular equation (2.38) as

$$(S^l)^{-1} H (S^r)^{-1} D = D E, \quad C = (S^r)^{-1} D, \quad (2.53)$$

where D is the unitary matrix that diagonalizes $(S^l)^{-1} H (S^r)^{-1}$, and making use of the fact that $D_{cc} = 1$ and $D_{cv} = 0$, we arrive at the reduced eigenvalue problem

$$(S_{vv}^l)^{-1} (H - S_{vc} H_{cc} S_{cv}) (S_{vv}^r)^{-1} D_{vv} = D_{vv} E_v, \quad (2.54)$$

which is now of rank N_v , with N_v the number of valence local orbitals.

2.2.3 APW+lo and LAPW

In the (L)APW method [Andersen75, Wimmer81, Blaha90], basis functions, being essentially plane waves, are *augmented* by a combination of atomic-like radial functions inside the non-overlapping muffin-tin spheres centered at atomic positions. In this way, the generally unbiased plane-wave basis is also made more efficient as it is assumed that radial functions are more adequate to describe atomic surroundings where the crystal potential is strongly varying.

The LAPW basis is given as

$$\phi_{\mathbf{G},\mathbf{k}}^{\text{LAPW}}(\mathbf{r}) = \begin{cases} \frac{1}{\sqrt{V}} e^{i(\mathbf{k}+\mathbf{G})\mathbf{r}}, & \mathbf{r} \notin R_{\text{MT}}^I \\ \sum_{lm} \left[A_{lm}^{I,\mathbf{k}+\mathbf{G}} u_l^I(r, E_{1l}^I) + B_{lm}^{I,\mathbf{k}+\mathbf{G}} \dot{u}_l^I(r, E_{1l}^I) \right] Y_{lm}(\mathbf{r} - \mathbf{R}_I), & \mathbf{r} \in R_{\text{MT}}^I \end{cases}, \quad (2.55)$$

where \mathbf{G} is a reciprocal lattice vector, V is the unit cell volume, $u_l^I(r, E_{1l}^I)$ and $\dot{u}_l^I(r, E_{1l}^I)$ are, respectively, the solutions to the radial Schrödinger equation of an isolated atom I and their energy derivatives, evaluated at linearization energies E_{1l}^I . The coefficients $A_{lm}^{I,\mathbf{k}+\mathbf{G}}$ and $B_{lm}^{I,\mathbf{k}+\mathbf{G}}$ are determined from the requirement that $\phi_{\mathbf{G},\mathbf{k}}^{\text{LAPW}}(\mathbf{r})$ has to be continuous and differentiable at the muffin-tin sphere boundary.

In order to improve description of semicore states, the LAPW basis is complemented by local orbitals (LO), which are defined only inside muffin-tin spheres:

$$\phi_{I,lm}^{\text{LO}}(\mathbf{r}) = \begin{cases} 0, & \mathbf{r} \notin R_{\text{MT}}^I \\ \left[A_{lm}^{I,\text{LO}} u_l^I(r, E_{1l}^I) + B_{lm}^{I,\text{LO}} \dot{u}_l^I(r, E_{1l}^I) + C_{lm}^{I,\text{LO}} u_l^I(r, E_{2l}^I) \right] Y_{lm}(\mathbf{r} - \mathbf{R}_I), & \mathbf{r} \in R_{\text{MT}}^I \end{cases}, \quad (2.56)$$

The third term $C_{lm}^{I,\text{LO}} u_l^I(r, E_{2l}^I)$, with the linearization energy $E_{2l}^I \neq E_{1l}^I$, takes account of the semicore state for a given atom I with a given l . The coefficients $A_{lm}^{I,\text{LO}}$, $B_{lm}^{I,\text{LO}}$ and $C_{lm}^{I,\text{LO}}$ are obtained by normalizing the local orbital and setting its value and slope at the muffin-tin sphere boundary equal to zero.

An alternative extension of the energy-dependent APW basis is a basis consisting of APW's, evaluated at fixed energies, and local orbitals [which are different from the LO's, Eq. (2.56), and which conventionally are abbreviated as "lo"]:

$$\phi_{\mathbf{G},\mathbf{k}}^{\text{APW}}(\mathbf{r}) = \begin{cases} \frac{1}{\sqrt{V}} e^{i(\mathbf{k}+\mathbf{G})\mathbf{r}}, & \mathbf{r} \notin R_{\text{MT}}^I \\ \sum_{lm} A_{lm}^{I,\mathbf{k}+\mathbf{G}} u_l^I(r, E_{1l}^I) Y_{lm}(\mathbf{r} - \mathbf{R}_I), & \mathbf{r} \in R_{\text{MT}}^I \end{cases}, \quad (2.57)$$

$$\phi_{I,lm}^{\text{lo}}(\mathbf{r}) = \begin{cases} 0, & \mathbf{r} \notin R_{\text{MT}}^I \\ \left[A_{lm}^{I,\text{lo}} u_l^I(r, E_{1l}^I) + B_{lm}^{I,\text{lo}} \dot{u}_l^I(r, E_{1l}^I) \right] Y_{lm}(\mathbf{r} - \mathbf{R}_I), & \mathbf{r} \in R_{\text{MT}}^I \end{cases} \quad (2.58)$$

$A_{lm}^{I,\mathbf{k}+\mathbf{G}}$ are obtained by requiring that $\phi_{\mathbf{G},\mathbf{k}}^{\text{APW}}(\mathbf{r})$ is continuous at the muffin-tin sphere boundary, and $A_{lm}^{I,\text{lo}}$ and $B_{lm}^{I,\text{lo}}$ are obtained from normalizing the local orbital and by requiring that its value at the muffin-tin sphere boundary is zero. The APW+lo basis set can also be extended by adding LO's for semicore states. These LO's differ from the LO's of the LAPW basis, Eq. (2.56), in that they do not contain the $B\dot{u}_l^I(r, E_{1l}^I)$ term.

The LAPW and APW+lo basis functions can be efficiently combined in order to achieve optimal accuracy at low computational costs, as is done in the full-potential LAPW/APW+lo code Wien2k [Blaha01], which we use in the present work.

2.3 Forces and lattice dynamics

The knowledge of nuclear forces, *i. e.*, forces imposed on a nucleus through the electrostatic field of other nuclei and through interaction with the electronic subsystem, enables one to optimize the crystal structure by finding optimal atomic positions that

correspond to zero nuclear forces and minimal total energy. This kind of structural optimization is employed in the present thesis in studies on the frustrated antiferromagnets Cs_2CuCl_4 and Cs_2CuBr_4 (Chapter 4) and the Mott insulator TiOCl (Chapter 6). In the case of Cs_2CuCl_4 and Cs_2CuBr_4 , structural optimization is required in order to refine the experimentally determined crystal structures of the compounds, while in the case of TiOCl relaxation of Na-doped TiOCl unit cells with the Car-Parinello molecular dynamics method (see below) was used for the modeling of Na doping of TiOCl at various Na concentrations. In fact, crystal structure relaxation has become a widely and frequently used procedure performed in the context of electronic structure calculations.

As stated in the *force (Hellmann-Feynman) theorem* [Hellmann37, Feynman39], the force acting on a nucleus (ion) I ,

$$\mathbf{F}_I = -\frac{\partial E}{\partial \mathbf{R}_I}, \quad (2.59)$$

does not depend on the kinetic energy and internal interactions but is given exclusively in terms of the electron density $\rho(\mathbf{r})$, external potential $v_{\text{ext}}(\mathbf{r})$ and electrostatic interaction between positively charged ions E_{II} :

$$\begin{aligned} \mathbf{F}_I &= -\frac{\partial E}{\partial \mathbf{R}_I} \\ &= -\langle \Psi_0 | \frac{\partial \hat{H}}{\partial \mathbf{R}_I} | \Psi_0 \rangle - \frac{\partial E_{II}}{\partial \mathbf{R}_I} \\ &= -\int \rho(\mathbf{r}) \frac{\partial v_{\text{ext}}(\mathbf{r})}{\partial \mathbf{R}_I} d\mathbf{r} - \frac{\partial E_{II}}{\partial \mathbf{R}_I}. \end{aligned} \quad (2.60)$$

This follows from the fact that the ground state wave-function $|\Psi_0\rangle$ is at a variational minimum with respect to any parameter and that the only term of \hat{H} that explicitly depends on ionic positions is the external potential.

Although the force expression (2.60) is exact in principle, in many cases actual calculations require consideration of additional terms. Some of them, sometimes referred to as the *Pulay correction terms* [Pulay69], result from the explicit dependence of the basis upon atomic positions, which is the case for local-orbital type basis sets, like the bases used in our calculations [(L)MTO, FPLO, (L)APW]. Calculations with a plane-wave basis, on the other hand, do not require the Pulay correction, which is an advantage as its calculation is computationally demanding. Another “real life“ contribution to the nuclear force, which is absent in Eq. (2.60), is due to non-self-consistency errors.

Structural optimization, which minimizes the total energy as a function of atomic positions $E(\{\mathbf{R}_I\})$, is performed iteratively. In each iteration step, an ordinary self-consistent DFT calculation with fixed atoms is carried out and for the next iteration the atomic positions are modified according to the calculated forces. There are a number of

algorithms for updating atomic positions, the Newton method and its extensions being among the most frequently used ones.

In 1985, Car and Parinello [Car85] proposed an alternative approach to the structural optimization, which, unlike the more straightforward approach sketched above, treats simultaneously the electronic system and the motion of nuclei. The *Car-Parinello* method introduces a fictitious Lagrangian, which depends on both classical ionic degrees of freedom $\{\mathbf{R}_I\}$ and electronic degrees of freedom, represented by single-particle Kohn-Sham orbitals $\{\psi_{i\mathbf{k}}(\mathbf{r})\}$:

$$\begin{aligned} \mathcal{L} = & \sum_i \frac{1}{2}(2\mu) \int |\dot{\psi}_{i\mathbf{k}}(\mathbf{r})|^2 d\mathbf{r} + \sum_I \frac{1}{2} M_I \dot{\mathbf{R}}_I^2 - E(\{\psi_{i\mathbf{k}}(\mathbf{r})\}, \{\mathbf{R}_I\}) \\ & + \sum_{ij} \Lambda_{ij} \left[\int \psi_{i\mathbf{k}}^*(\mathbf{r}) \psi_{j\mathbf{k}}(\mathbf{r}) d\mathbf{r} - \delta_{ij} \right]. \end{aligned} \quad (2.61)$$

Here, 2μ is a fictitious electron mass and Λ_{ij} are Lagrange multipliers associated with the orthonormality condition for the Kohn-Sham orbitals. The Lagrangian (2.61) leads to the following equations of motion

$$\begin{aligned} \mu \ddot{\psi}_{i\mathbf{k}}(\mathbf{r}, t) &= -\frac{\delta E}{\delta \psi_{i\mathbf{k}}^*(\mathbf{r}, t)} + \sum_j \Lambda_{ij} \psi_{j\mathbf{k}}(\mathbf{r}, t) \\ &= -\hat{H} \psi_{i\mathbf{k}}(\mathbf{r}, t) + \sum_j \Lambda_{ij} \psi_{j\mathbf{k}}(\mathbf{r}, t), \end{aligned} \quad (2.62)$$

$$M_I \ddot{\mathbf{R}}_I = \mathbf{F}_I = -\frac{\partial E}{\partial \mathbf{R}_I}. \quad (2.63)$$

It can be easily shown that the stationary solution of Equations (2.62) and (2.63), corresponding to vanishing time derivatives, is equivalent to the conventional Kohn-Sham equations. The equations of motions are solved numerically with discrete time steps.

The Car-Parinello approach does not only offer an efficient scheme for optimizing crystal structures, but it can also deal with simulations of the coupled motion of nuclei and electrons, *i. e.*, the real dynamics of an atomic system. Among others, this includes modelling of thermal motion, liquids and thermal phase transitions.

Since in the Car-Parinello method the nuclear forces are calculated in each time step, one needs a basis that would allow for fast calculation of forces. As mentioned, the plane-wave basis meets this requirement, so the Car-Parinello method has been developed mainly on a basis of plane-wave type basis sets, like in the "ultrasoft" pseudopotentials method [Laasonen91] and in the *projector-augmented wave* (PAW) method [Blöchl90]. The latter method was used in the modeling of Na doping of TiOCl (Section 6).

2.4 Extensions of DFT for strongly correlated materials

Despite the numerous successful applications of the local approximations to the exchange-correlation functional (LDA, LSDA, GGA, *etc.*), they describe rather badly correlated materials with localized d (and f) electrons. For example, notoriously known is their disability to reproduce an insulating state in many Mott insulators. In the 1990s, addressing this problem, a number of approaches were proposed, among which the LDA+U methods [Anisimov91, Czyżyk94] and the LDA+DMFT (dynamical mean-field theory) method [Anisimov97, Lichtenstein98] stand out. The former method is used in our present work.

LDA+U

In fact, the term LDA+U refers to a class of functionals which are constructed in a similar way. In the LDA+U method, a local functional is extended by introducing additional terms for selected (correlated) orbitals that mimic the strong many-body interaction between the localized electrons residing on them. The general form of an LDA+U functional can be written as⁵

$$E^{\text{LDA+U}} = E^{\text{LDA}} + H_{\text{int}} - \langle H_{\text{int}} \rangle, \quad (2.64)$$

where H_{int} is the interaction part of the many-body Hamiltonian and the average $\langle H_{\text{int}} \rangle$ is supposed to comprise the part of electronic correlations that is already present in E^{LDA} and is subtracted in order to avoid double counting (hence the term "*double-counting correction*"). In the most general case, H_{int} is given in terms of the Coulomb interaction matrix $U_{mm'}$ and the Hund's rule coupling matrix $J_{mm'}^{\text{H}}$, which describe interactions between the $2l + 1$ correlated orbitals m ,

$$H_{\text{int}} = \frac{1}{2} \sum_{m,m',\sigma} U_{mm'} n_{m\sigma} n_{m'-\sigma} + \frac{1}{2} \sum_{m \neq m', \sigma} (U_{mm'} - J_{mm'}^{\text{H}}) n_{m\sigma} n_{m'\sigma}, \quad (2.65)$$

where σ and $n_{m\sigma}$ denote, respectively, spin projection and occupation number.

The two most popular versions of the LDA+U method, which we shortly discuss below, differ in the definition of the double-counting correction term. One of them is the *around mean-field* (AMF) LDA+U method proposed in the pioneering work of Anisimov *et al.* [Anisimov91]. Originally, the AMF LDA+U functional was derived in the "*fluctuation-around-the-mean*" form, which can be easily transformed into the form

⁵Here, we put "LDA" to label the local functional, which, however, can as well be the LSDA, GGA *etc.* functional.

given by Eq. (2.64). The AMF LDA+U functional, proposed subsequently by Czyżyk and Sawatzky [Czyżyk94] as an extension of the LSDA functional, allows for richer physics and more realistic spin-polarized solutions and is given as

$$\begin{aligned} E^{\text{AMF}} &= E^{\text{LSDA}} + \frac{1}{2} \sum_{m,m',\sigma} U_{mm'} (n_{m\sigma} - \bar{n}_\sigma)(n_{m'-\sigma} - \bar{n}_{-\sigma}) \\ &\quad + \frac{1}{2} \sum_{m \neq m', \sigma} (U_{mm'} - J_{mm'}^{\text{H}}) (n_{m\sigma} - \bar{n}_\sigma)(n_{m'\sigma} - \bar{n}_\sigma), \end{aligned} \quad (2.66)$$

where $\bar{n}_\sigma = \frac{1}{2l+1} \sum_m n_{m\sigma}$ is the spin-resolved average occupation number. In the same paper [Czyżyk94], the authors introduced the *atomic limit* (AL) version of the LDA+U method, where the double-counting correction is taken to be

$$\langle H_{\text{int}} \rangle^{\text{AL}} = \frac{1}{2} U N(N-1) - \frac{1}{2} J^{\text{H}} N_\uparrow(N_\uparrow-1) - \frac{1}{2} J^{\text{H}} N_\downarrow(N_\downarrow-1), \quad (2.67)$$

$$E^{\text{AL}} = E^{\text{LSDA}} + H_{\text{int}} - \langle H_{\text{int}} \rangle^{\text{AL}}, \quad (2.68)$$

with $N = \sum_{m\sigma} n_{m\sigma}$, $U = \frac{1}{(2l+1)^2} \sum_{mm'} U_{mm'}$ and $U - J^{\text{H}} = \frac{1}{2l(2l+1)} \sum_{mm'} (U_{mm'} - J_{mm'}^{\text{H}})$. The LDA+U calculations presented in this thesis are performed by using either the AMF version of the LDA+U method, Eq. (2.66), or the AL version, Equations (2.67) and (2.68).

Although in the LDA+U method the description of strongly correlated materials is significantly improved, usage of the method is associated with a number of problematic issues. The interaction parameters U and J^{H} are basis-dependent and the localized orbital for which the orbital-dependent terms are added in the functional should be manually chosen. Actually, the very fact of adding extra terms to the DFT functional makes such calculations somewhat less *ab initio*.

2.5 DFT-based derivation of effective models

2.5.1 Tight-binding and Hubbard models

The kinetic energy term of the Hubbard Hamiltonian (1.3),

$$\begin{aligned} \hat{H}^{\text{TB}} &= \sum_{i,m_i,m'_i} \mu_{m_i m'_i} \hat{c}_{im_i\sigma}^\dagger \hat{c}_{im'_i\sigma} \\ &\quad - \sum_{\substack{\langle ij \rangle \\ \sigma, m_i, m_j}} \left(t_{ij}^{m_i m_j} \hat{c}_{im_i\sigma}^\dagger \hat{c}_{jm_j\sigma} + \text{h.c.} \right), \end{aligned}$$

is referred to as the *tight-binding* (TB) model. The hopping integrals $t_{ij}^{m_i m_j}$ are obtained following the assumption that the TB model eigenvalues should match the DFT calculated Kohn-Sham energies $\varepsilon_\nu(\mathbf{k})$ in the reciprocal space. This assumption neglects the fact that effects of the Coulomb interaction are already partially taken into account within the DFT and therefore the DFT bandstructure is not purely that of a non-interacting electron system. In order to achieve the match, the TB Hamiltonian is Fourier-transformed into the reciprocal \mathbf{k} -vector space and the hopping integrals are optimized such as to fit the TB model spectrum to the DFT bandstructure. The effective Coulomb interaction $U - J^H$ can be calculated by the *constrained LDA* method [Madsen05] or the *constrained RPA* method [Aryasetiawan04].

An alternative derivation of the hopping integrals employs *Wannier functions*, which are defined as

$$\begin{aligned} w_{im_i}(\mathbf{r} - \mathbf{R}^T) &= \sum_{\mathbf{k}} e^{-i\mathbf{k}\cdot\mathbf{R}^T} \sum_{\nu \in W} P_{im_i\nu}(\mathbf{k}) \psi_{\nu\mathbf{k}}(\mathbf{r}) \\ &= \sum_{\mathbf{k}} e^{-i\mathbf{k}\cdot\mathbf{R}^T} w_{im_i\mathbf{k}}(\mathbf{r}). \end{aligned} \quad (2.69)$$

Here, i runs over all the transition atoms in the unit cell and m_i runs over correlated orbitals; W is an energy window covering the bands that can be associated with the correlated orbitals, and the expansion coefficients $P_{im_i\nu}(\mathbf{k})$ are called *projectors*. The construction of projectors in the (L)APW basis, which we use in our calculations, is discussed in detail by Aichhorn *et al.* [Aichhorn09]. In short, the (L)APW-based projectors are calculated as orthonormalized within the energy window W overlaps between the self-consistently obtained Bloch functions $\psi_{\nu\mathbf{k}}(\mathbf{r})$ and the radial solution to the Schrödinger equation $u_l^I(r, E_{lI}^I) Y_{lm}(\mathbf{r})$.

With the Wannier functions considered as localized electrons' eigenfunctions, the overlap integrals and the Coulomb interaction are given as

$$t_{ij}^{m_i m_j} = \int d\mathbf{r} w_{im_i}^*(\mathbf{r}) \left(-\frac{\hbar^2}{2m_e} \nabla^2 \right) w_{jm_j}(\mathbf{r}), \quad (2.70)$$

$$U_{m_i m_i'} = \int d\mathbf{r}_1 d\mathbf{r}_2 w_{im_i}^*(\mathbf{r}_1) w_{im_i}(\mathbf{r}_1) \frac{e^2}{4\pi\epsilon_0} \frac{1}{|\mathbf{r}_1 - \mathbf{r}_2|} w_{im_i'}^*(\mathbf{r}_2) w_{im_i'}(\mathbf{r}_2). \quad (2.71)$$

In practice, in order to obtain the hopping integrals, one does not need to explicitly calculate the Wannier functions and the integral (2.70). Since the TB Hamiltonian

matrix is known to be diagonal in the basis of Bloch states,

$$\begin{pmatrix} \psi_{\nu=1,\mathbf{k}}^*(\mathbf{r}) & \psi_{\nu=2,\mathbf{k}}^*(\mathbf{r}) & \cdots & \psi_{\nu=N_\nu,\mathbf{k}}^*(\mathbf{r}) \end{pmatrix} \hat{H}^{\text{TB}} \begin{pmatrix} \psi_{\nu=1,\mathbf{k}}(\mathbf{r}) \\ \psi_{\nu=2,\mathbf{k}}(\mathbf{r}) \\ \vdots \\ \psi_{\nu=N_\nu,\mathbf{k}}(\mathbf{r}) \end{pmatrix} = \begin{pmatrix} \epsilon_{\nu=1}(\mathbf{k}) & 0 & \cdots & 0 \\ 0 & \epsilon_{\nu=2}(\mathbf{k}) & \cdots & 0 \\ \vdots & \vdots & \ddots & \\ 0 & 0 & & \epsilon_{\nu=N_\nu}(\mathbf{k}) \end{pmatrix}, \quad (2.72)$$

where N_ν is the number of energy bands inside W , one can make use of the definition (2.69) to obtain the TB Hamiltonian matrix in the basis of Wannier functions as

$$\begin{pmatrix} w_{M=1,\mathbf{k}}^*(\mathbf{r}) & w_{M=2,\mathbf{k}}^*(\mathbf{r}) & \cdots & w_{M=N_M,\mathbf{k}}^*(\mathbf{r}) \end{pmatrix} \hat{H}^{\text{TB}} \begin{pmatrix} w_{M=1,\mathbf{k}}(\mathbf{r}) \\ w_{M=2,\mathbf{k}}(\mathbf{r}) \\ \vdots \\ w_{M=N_M,\mathbf{k}}(\mathbf{r}) \end{pmatrix} = P^\dagger(\mathbf{k}) \begin{pmatrix} \epsilon_{\nu=1}(\mathbf{k}) & 0 & \cdots & 0 \\ 0 & \epsilon_{\nu=2}(\mathbf{k}) & \cdots & 0 \\ \vdots & \vdots & \ddots & \\ 0 & 0 & & \epsilon_{\nu=N_\nu}(\mathbf{k}) \end{pmatrix} P(\mathbf{k}), \quad (2.73)$$

where $P(\mathbf{k})$ is

$$P(\mathbf{k}) = \begin{pmatrix} P_{M=1,\nu=1}(\mathbf{k}) & P_{M=1,\nu=2}(\mathbf{k}) & \cdots \\ P_{M=2,\nu=1}(\mathbf{k}) & P_{M=2,\nu=2}(\mathbf{k}) & \cdots \\ \vdots & \vdots & \ddots \\ & & & P_{M=N_M,\nu=N_\nu}(\mathbf{k}) \end{pmatrix}. \quad (2.74)$$

In the last two equations, M combines indices i and m_i . After this transformation, performed for every \mathbf{k} -vector, we have a numerically given overlap matrix

$$\begin{pmatrix} \langle w_{M=1,\mathbf{k}} | \hat{H}^{\text{TB}} | w_{M=1,\mathbf{k}} \rangle & \langle w_{M=1,\mathbf{k}} | \hat{H}^{\text{TB}} | w_{M=2,\mathbf{k}} \rangle & \cdots \\ \langle w_{M=2,\mathbf{k}} | \hat{H}^{\text{TB}} | w_{M=1,\mathbf{k}} \rangle & \langle w_{M=2,\mathbf{k}} | \hat{H}^{\text{TB}} | w_{M=2,\mathbf{k}} \rangle & \cdots \\ \vdots & \vdots & \ddots \\ & & & \langle w_{M=N_M,\mathbf{k}} | \hat{H}^{\text{TB}} | w_{M=N_M,\mathbf{k}} \rangle \end{pmatrix} \quad (2.75)$$

as a function of \mathbf{k} . By Fourier transforming $\langle w_{M,\mathbf{k}} | \hat{H}^{\text{TB}} | w_{M',\mathbf{k}} \rangle$, one obtains the overlap integrals $t_{MM'}$ and onsite energies $\mu_{m_i} = t_{ii}^{m_i m_i}$ as

$$t_{i-\mathbf{R}_i^T, j-\mathbf{R}_j^T}^{m_i m_j} = \frac{1}{N_{\mathbf{k}}} \sum_{\mathbf{k}} \langle w_{im_i, \mathbf{k}} | \hat{T} | w_{jm_j, \mathbf{k}} \rangle e^{-i\mathbf{k} \cdot (\mathbf{R}_j^T - \mathbf{R}_i^T)}, \quad (2.76)$$

$$\mu_{m_i} = \frac{1}{N_{\mathbf{k}}} \sum_{\mathbf{k}} \langle w_{im_i, \mathbf{k}} | \hat{T} | w_{im_i, \mathbf{k}} \rangle, \quad (2.77)$$

where $N_{\mathbf{k}}$ is the number of \mathbf{k} -vectors chosen for a numerical integration over the Brillouin zone.

It has to be noted that in order to achieve high reproducibility of the DFT bandstructure by the projection method presented above, the number N_{ν} of projected Bloch functions $\psi_{\nu, \mathbf{k}}(\mathbf{r})$ should be equal to the number of correlated orbitals in the cell N_M . If it is not possible to choose an energy window that would include only the bands of interest, a *selective projection* has to be performed, which consists in selecting the required number of bands using, *e. g.*, their high correlated orbital weight as a selection criterion.

Downfolding

The two presented methods for the TB model parameterization – the fitting and the projection onto Wannier basis – are both *postprocessing* methods, which implies that the Wannier functions are constructed after the Bloch functions have been generated. A *preprocessing* parameterization, where the Wannier functions are constructed before the Hamiltonian diagonalization, is also possible and has been implemented on a basis of NMTOs [Andersen00]. The idea of the method, termed *downfolding*, consists in a systematic reduction of the Hilbert space by "folding" down the state that are located far enough from the Fermi energy.

In order to provide some insight into the basics of the downfolding procedure, we consider the eigenvalue problem [Eq. (2.38)]

$$HC = EC, \quad (2.78)$$

defined on an orthonormal basis. Let C_1 comprise the eigenfunctions to be retained and C_2 the rest of the Hilbert space to be downfolded. Then, the secular equation (2.78) can be written as

$$\begin{aligned} H_{11}C_1 + H_{12}C_2 &= EC_1, \\ H_{21}C_1 + H_{22}C_2 &= EC_2. \end{aligned} \quad (2.79)$$

The downfolded solution is obtained from the following effective eigenvalue problem

$$H^{\text{eff}}C_1 = EC_1, \quad (2.80)$$

where

$$H^{\text{eff}} = H_{11} - H_{12}(H_{22} - E)^{-1}H_{21}. \quad (2.81)$$

The NMTO basis is a suitable choice for the downfolding because the NMTOs are constructed to be orthonormal and, most importantly, they are localized functions that can play the role of Wannier functions. The TB model parameters, defined as the matrix elements of the kinetic energy operator in the basis of Wannier functions [Eq. (2.70)], are obtained by Fourier transforming H^{eff} .

2.5.2 Heisenberg model

In this thesis, we parameterize the Heisenberg Hamiltonian (1.6),

$$\hat{H}^{\text{H}} = \sum_{\langle ij \rangle} J_{ij} \hat{\mathbf{S}}_i \hat{\mathbf{S}}_j, \quad (2.82)$$

for the antiferromagnetic insulators Cs_2CuCl_4 and Cs_2CuBr_4 (Chapter 4) using the *total energy difference* method. This method treats the localized spins of magnetic atoms as if they were classical vectors, whose direction can be fixed. To give an idea of how the total energy difference method works, it is convenient to consider a simple case of two classical spins S :

$$\hat{H}^{\text{H}} = J\hat{\mathbf{S}}_1\hat{\mathbf{S}}_2. \quad (2.83)$$

The energies of the collinear ferromagnetic and antiferromagnetic configurations of the system are, respectively,

$$E^{\text{FM}} = JS^2, \quad (2.84)$$

$$E^{\text{AFM}} = -JS^2. \quad (2.85)$$

Combining the two equations, one expresses the exchange coupling J in terms of the ferromagnetic and antiferromagnetic energy differences:

$$J = \frac{E^{\text{FM}} - E^{\text{AFM}}}{2S^2}. \quad (2.86)$$

In real systems, one is usually interested in several exchange couplings n , so $n + 1$ different spin configurations need to be considered for deriving a system of n coupled

equations. The total energies of different spin configurations are calculated with a DFT code, with the spins of magnetic atoms fixed in certain directions.

Chapter 3

Strongly correlated materials under study

This chapter provides an overview of the studied correlated materials: Cs_2CuCl_4 , Cs_2CuBr_4 , $\text{Bi}_2\text{Sr}_2\text{CaCu}_2\text{O}_8$ and TiOCl . We discuss their crystal structure and physical properties. In order to fully appreciate the non-trivial physics demonstrated by these materials, some general introduction to such phenomena as frustration in spin systems and cuprate superconductivity will be presented as well.

In addition to reviewing the experimental situations around the studied materials, we discuss the current status of their theoretical understanding, mainly, in terms of model description. We also outline possible applications of the DFT, which could provide new information on the microscopic properties of the materials and guide future theoretical as well as experimental investigations.

3.1 Low-dimensional frustrated antiferromagnets CsCu_2Cl_4 and Cs_2CuBr_4

3.1.1 Magnetic frustration

Antiferromagnets Cs_2CuCl_4 and Cs_2CuBr_4 are representatives of frustrated spin systems. The term “frustration“ is applied to systems with competing interactions, whose actions favour different ground states. Due to the interplay of competing interactions, a frustrated system can realize either a complex compromising ground state or, in case of complete frustration (none of the interactions can win), a degenerate ground state, with non-zero entropy.

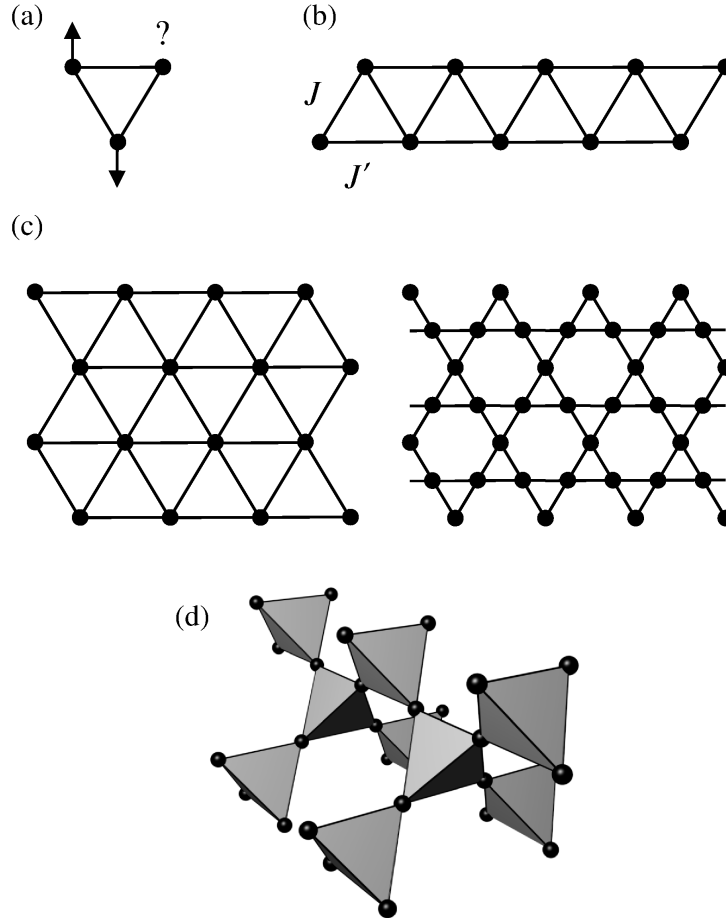


FIGURE 3.1: Examples of frustrated lattices: (a) zero-dimensional three-site lattice, (b) 1D J - J' model, (c) 2D triangular and Kagome lattices and (d) pyrochlore lattice.

Presence of triangular motifs in a magnetic sublattice consisting of localized spins together with antiferromagnetic interactions between them are prerequisites for magnetic frustration [Balents10]. A textbook example of a frustrated spin system is the system of three Ising spins displayed in Fig. 3.1 (a). In crystalline materials, one encounters frustration in periodic lattices, which can be of any dimensionality. Some examples are the J - J' model (1D) [Fig. 3.1 (b)], the periodic triangular and Kagome lattices (2D) [Fig. 3.1 (c)] and the pyrochlore lattice (3D) [Fig. 3.1 (d)].

Frustration hinders long-range magnetic ordering. In fact, the absence of magnetic ordering at the Curie-Weiss temperature θ_{CW} (Fig. 3.2) is an experimental indication of magnetic frustration in a given material. Since in most real frustrated systems magnetic ordering does occur due to small stabilizing interactions at the Néel temperature T_{N} , $T_{\text{N}} \ll \theta_{\text{CW}}$, the ratio

$$f = \frac{\theta_{\text{CW}}}{T_{\text{N}}} \quad (3.1)$$

is used as a measure of frustration.

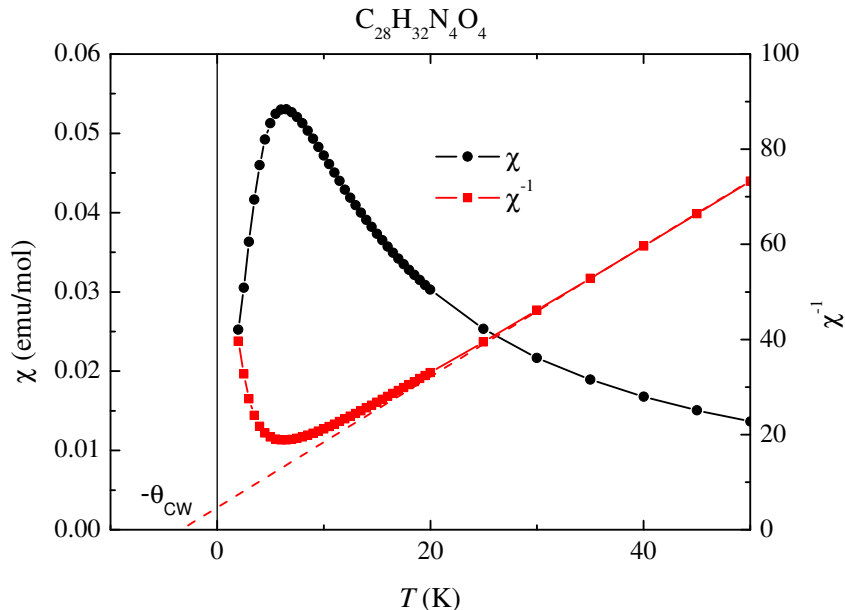


FIGURE 3.2: Magnetic susceptibility of the frustrated material $\text{C}_{28}\text{H}_{32}\text{N}_4\text{O}_4$ χ and its inverse χ^{-1} as a function of temperature T . The red dashed line is a linear fit to χ^{-1} above ~ 25 K. The experimental data are presented under permission of Pham Thanh Cong.

Instead of becoming ordered, a frustrated system at low enough temperature develops short-range magnetic correlations between spins. In the temperature dependent magnetic susceptibility, the onset of short-range correlations manifests itself as a broad maximum (Fig. 3.2). This state is called a *spin liquid*.

Most interesting behavior is expected from low-spin systems, the $S = \frac{1}{2}$ being the lowest-spin case. In the low-spin systems, quantum effects are particularly strong. When combined with frustrating geometry and low dimensionality, they can give rise to the most exotic quantum states. One of such states is the *resonating valence bond* (RVB) state conjured up by Anderson [Anderson73], where the neighbouring $S = \frac{1}{2}$ spins couple into dimers and the ground state is the superposition of differently coupled dimers (Fig. 3.3).

Another fascinating feature of a spin liquid is that its elementary excitations are unconventional in terms of "classical" expectations. Classical excitation quasiparticles in a spin system are magnons, one magnon corresponding to a single spin flip that spreads through the crystal with certain wavevector and energy. In a dimerized spin liquid, on the other hand, elementary excitations would be of different nature. These excitations, called spinons, result from dimer breaking and carry half of the classical excitation spin. While in 1D spin systems the physics of spinons is theoretically well understood and their existence has been experimentally detected, the possibility of spinon excitations in 2D systems is still under debate [Misguich05].

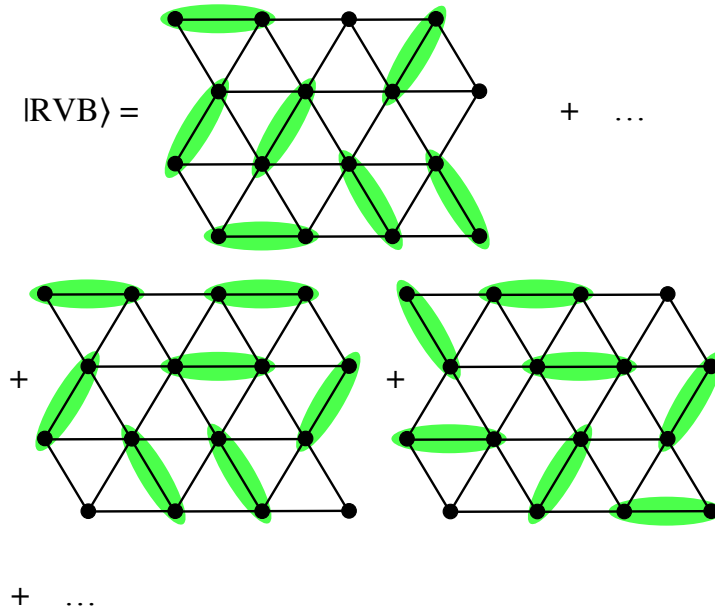
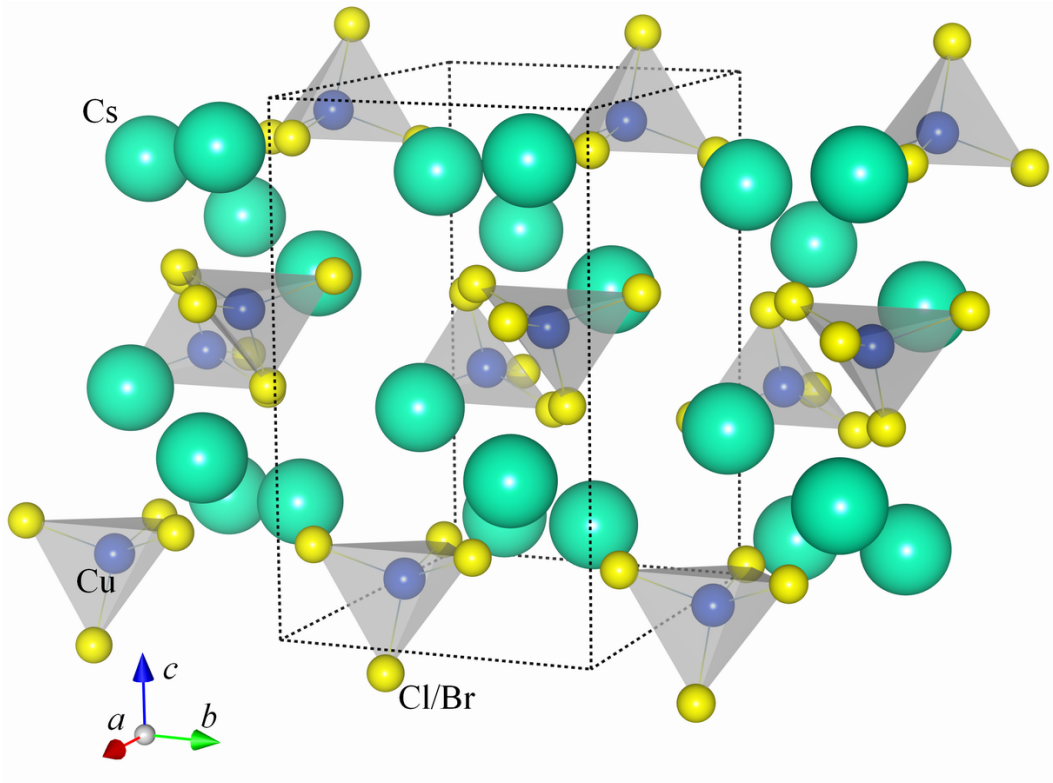


FIGURE 3.3: Resonating valence bond state $|\text{RVB}\rangle$. The dimerized spins on the triangular lattice are marked by green ellipses.

3.1.2 Cs_2CuCl_4 and Cs_2CuBr_4 : experimental background and theoretical description

In view of the presented highlights on the physics of frustrated magnets, let us now examine the crystal and magnetic structures of the studied Cs_2CuCl_4 and Cs_2CuBr_4 . The two materials are isostructural, with the space group $Pnma$ and an orthorhombic unit cell [Bailleul91, Morosin60], shown in Fig. 3.4. One recognizes that the Cu atoms, each being surrounded by a tetrahedron of ligand Cl or Br atoms, form layers parallel to the bc plane and are arranged within each layer in a periodic triangular pattern. The Cu atoms are in a Cu^{2+} ionization state, with the outer shell electrons being in a $3d^9$ configuration. This implies that there is an electron hole localized on each Cu ion with spin $S = \frac{1}{2}$. Effectively, the physics of the insulators Cs_2CuCl_4 and Cs_2CuBr_4 can thus be discussed in terms of the Heisenberg spin model (1.6). The well-pronounced layered arrangement of Cu ions in Cs_2CuCl_4 and Cs_2CuBr_4 suggests a possibility of a two-dimensional network of exchange interactions between the Cu spins, while the triangular lattice that the ions form in a layer allows for magnetic frustration, provided that the spin interactions are antiferromagnetic. The possible low dimensionality and magnetic frustration attracted attention of the condensed matter community and triggered a series of intensive theoretical and experimental investigations of the Cs_2CuCl_4 and Cs_2CuBr_4 magnetic properties.

Measurements of the temperature dependent magnetic susceptibility of Cs_2CuCl_4 [Carlin85,

FIGURE 3.4: Cs_2CuCl_4 and Cs_2CuBr_4 crystal structure.

Tokiwa06] and Cs_2CuBr_4 [Ono03] showed a characteristic broad-peak structure (see Fig. 3.2), signaling the onset of short-range spin correlations, and confirmed the anticipated antiferromagnetic and hence frustrating nature of the leading spin exchange interactions in the two systems. In the absence of external magnetic field, Cs_2CuCl_4 magnetically orders at the Néel temperature $T_N = 0.62$ K, determined using elastic neutron scattering [Coldea96], and Cs_2CuBr_4 orders at $T_N = 1.4$ K, determined from specific heat measurements [Ono03].

Detailed measurements of the thermodynamic properties of Cs_2CuCl_4 [Radu05, Tokiwa06] and Cs_2CuBr_4 [Ono03, Fortune09, Tsujii07] as a function of temperature T and magnetic field H , applied along different crystallographic directions, together with nuclear magnetic resonance (NMR) [Fujii07] and neutron scattering [Coldea01] experiments, revealed their rich T - H phase diagrams, featuring a number of ordered phases (see Fig. 3.5). Some of these phases and phase transitions are particularly interesting. Thus, the magnetic field controlled phase transition from the high-field fully polarized ferromagnetic phase to the low-field non-collinear antiferromagnetic phase in Cs_2CuCl_4 at vanishing temperature, observed when the magnetic field is applied perpendicular to the Cu planes, has been interpreted as the *Bose-Einstein condensation* of magnons [Matsubara56] [Fig. 3.6 (a)]. In Cs_2CuBr_4 , quantum fluctuations can stabilize, under

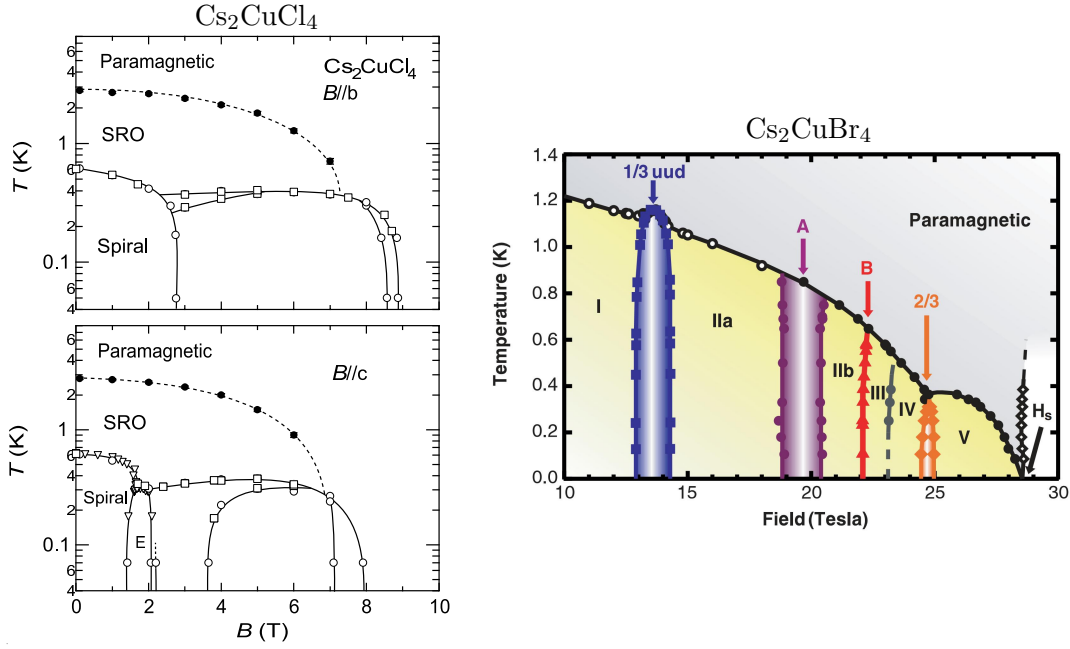


FIGURE 3.5: Left panel: the Cs_2CuCl_4 phase diagram in the plane of temperature T and magnetic field B (taken from Ref. [Tokiwa06]). In the top (bottom) diagram, the field is applied parallel to the b (c) direction. Data points of open circles (magnetization), squares (specific heat) and triangles (neutrons [Coldea01]) connected by solid lines indicate phase boundaries. Solid circles show positions of the maximum in the temperature dependence of the magnetization and indicate a cross-over from paramagnetic to short-range order (SRO). “E” in the bottom phase diagram denotes the elliptical phase, and “SRO” denotes the short-range ordered phase. Right panel: the Cs_2CuBr_4 phase diagram in the plane of temperature T and magnetic field $B \parallel c$ (taken from Ref. [Fortune09]) deduced from the magnetocaloric-effect data. Circles indicate second-order phase boundaries, whereas other symbols except the open diamonds indicate first-order boundaries. Lines are guides to the eye. The phases labeled as I, IIa, IIb and III are incommensurate, the phase V is presumably a canted-spiral phase. The uud, A, B and $2/3$ phases correspond to a commensurate collinear alignment of spins. The uud phase features a magnetization plateau at $1/3M_s$, where M_s is the saturation magnetization. The A phase does not have a plateau and is presumably gapless with magnetization of $1/2M_s$. The only 70 mT wide B phase might have a magnetization plateau at $5/9M_s$ and gapped low-lying excitations. The $2/3$ phase has a magnetization plateau at $2/3M_s$.

certain conditions, a collinear up-up-down spin order, which shows up as a *magnetization plateau* inside a finite field range [Ono03]. Two such plateaux were observed [Ono05] when the magnetic field was applied along the b and c axes [Fig. 3.6 (b)].

In the region of the Cs_2CuCl_4 T - H phase diagram above the long-range ordered phase [Fig. 3.6 (a)], magnetic properties are governed by short-range spin correlations. Probing this region with inelastic neutron scattering, Coldea *et al.* [Coldea01, Coldea03] discovered extended scattering continua in the magnetic excitation spectra of Cs_2CuCl_4 , which were interpreted as a signature of spinon-like quasiparticle excitations in the Cs_2CuCl_4 spin system, and Cs_2CuCl_4 was classified as a rare example of a 2D spin liquid. Later,

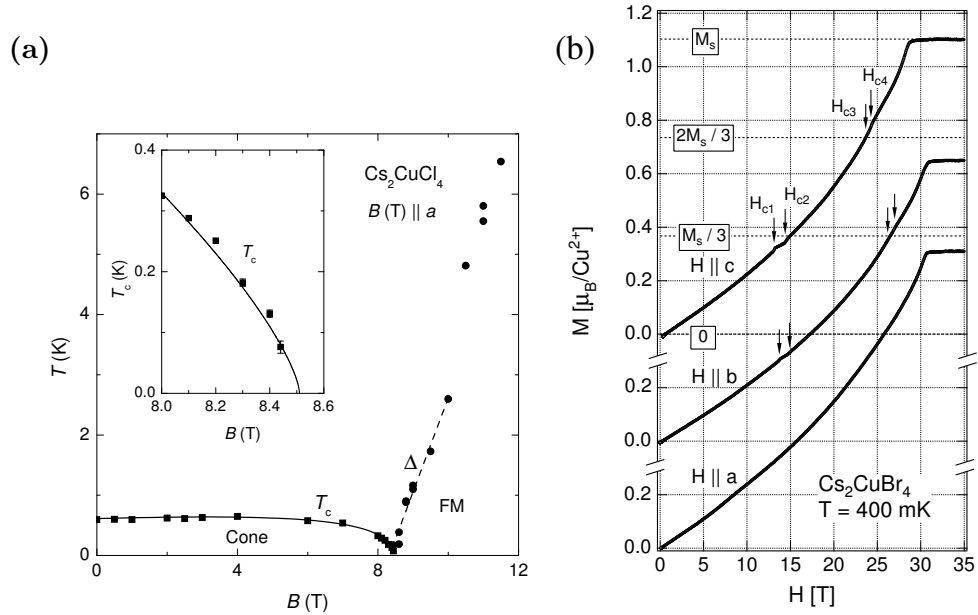


FIGURE 3.6: (a) The T - B phase diagram of Cs_2CuCl_4 demonstrating the Bose-Einstein condensation of magnons upon the transition from the ferromagnetic phase ("F") to the cone phase ("Cone") (taken from Ref. [Radu05]). (b) Magnetization plateaux in Cs_2CuBr_4 (taken from Ref. [Ono04]).

this conclusion was, however, abandoned when Kohno *et al.* [Kohno07] showed that spinons in Cs_2CuCl_4 , which do exist, are in fact confined to the Cu chains with the strongest exchange interaction (along b axis) as a result of the so-called *dimensional reduction* induced by frustration and quantum fluctuations (see below).

Inelastic neutron scattering measurements also provided information on the Cs_2CuCl_4 magnon dispersion spectrum in the fully polarized ferromagnetic phase, which was used to determine the Heisenberg Hamiltonian for this system, by fitting an exactly derivable in this case analytical expression to the experimental spectrum [Coldea02]. The result confirmed that Cs_2CuCl_4 is a 2D spin system with antiferromagnetic exchange couplings within the Cu planes as almost no magnon dispersion was detected in the perpendicular direction along the a axis. Exchange interaction between Cu spins along the b axis, J , was found to be 0.374 meV, while the zig-zag coupling J' appeared smaller by a factor of three: $J' = 0.123 \text{ meV} \approx J/3$ (Fig. 3.7). Additionally, it was concluded that there exists a small but detectable exchange coupling between Cu spins from adjacent Cu layers J'' , whose value was estimated as $J'' = 0.017 \text{ meV} \approx J/22$, and an anisotropic Dzyaloshinsky-Moriya interaction at zig-zag bonds, with the vector \mathbf{D} pointing in the a direction and $D_a = 0.02 \text{ meV}$. The Dzyaloshinsky-Moriya interaction plays an important role in stabilizing the long-range order in Cs_2CuCl_4 . Determination of the Cs_2CuBr_4 Heisenberg model with the same method is complicated by the need to apply an $H \gtrsim 32 \text{ T}$ magnetic field [Ono03] in order to fully polarize the spins, which is beyond the

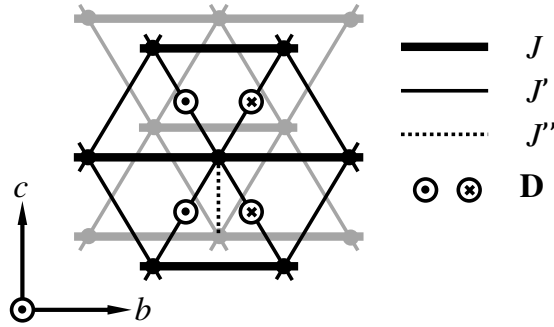


FIGURE 3.7: Interaction paths for the effective spin model of Cs_2CuCl_4 and Cs_2CuBr_4 .

maximum value of ~ 17 T compatible with inelastic neutron scattering measurements [Ono]. It was, though, possible to deduce the ratio $J'/J = 0.74$ from a comparison [Ono05] of the wave number of the incommensurate cycloidally ordered spin structure of Cs_2CuBr_4 at zero field [Ono04] with results of linked-cluster expansions [Weihong99]. Compared to Cs_2CuCl_4 , Cs_2CuBr_4 is thus closer to the maximal frustration limit of $J'/J = 1$. The absolute value of J in Cs_2CuBr_4 was estimated from its saturation field as 0.97 meV [Tsujii07]. Ref. [Tsujii07] also concludes that interlayer interactions in Cs_2CuBr_4 are weaker than those in Cs_2CuCl_4 .

The theoretical understanding of the experimentally observed behavior of Cs_2CuCl_4 and Cs_2CuBr_4 has made significant progress over the last years (see Ref. [Chung03, Zheng05, Veillette05, Veillette06, Kohno07, Starykh07, Starykh10] for theoretical studies of Cs_2CuCl_4 and Ref. [Zheng05, Alicea09] for those of Cs_2CuBr_4). The initial dispute over the origin of the continuous magnetic excitation spectra in Cs_2CuCl_4 has led Kohno *et al.* [Kohno07] to the idea that these continua are a reflection of 1D spinon excitations confined to the Cu chains with the strongest spin coupling J . This effect of dimensional reduction appears to be a universal property of anisotropic triangular antiferromagnets. The quite plausible suggestion by Kohno *et al.* weakened considerably the widely supported belief in Cs_2CuCl_4 as an experimental realization of a 2D spin liquid with truly 2D spinon excitations. They explained the observed substantial dispersion of the peak energy in the direction transverse to the chains by pairs of spinons getting bound into spin-1 triplons that are able to hop between chains. In Refs. [Starykh07] and [Starykh10], the concept of dimensional reduction, which allows to develop a solution to a 2D anisotropic triangular spin system from a 1D limit, was employed to explore the complex T - H phase diagram of Cs_2CuCl_4 . In these studies, the role of some of the weak exchange couplings, such as J'' and the next-nearest-chain coupling J_{14} (see Fig. 4.8), and the Dzyaloshinsky-Moriya interaction in stabilizing various Cs_2CuCl_4 phases was analyzed in detail. Theoretical studies of Cs_2CuBr_4 have been somewhat less intensive, probably due to its effective model becoming available more recently and also

due to its larger frustration, which would require more involved theoretical methods. The Cs_2CuBr_4 magnetization plateaux and the up-up-down collinear phase have been attracting particular attention [Alicea09].

The differences in the Cs_2CuCl_4 and Cs_2CuBr_4 magnetic properties, *e. g.*, the more pronounced tendency to sustain spinon excitations in Cs_2CuCl_4 and additional, quantum fluctuation driven phases with magnetization plateaux in Cs_2CuBr_4 , are often considered as being caused by the differences in their spin effective models. The Heisenberg model is definitely a good approximation to describe Cs_2CuCl_4 and Cs_2CuBr_4 , but taking also into account electronic degrees of freedom on a model level would provide a more complete picture. Electronic structure calculations with DFT methods can be used as a first step towards a deeper understanding of the Cs_2CuCl_4 and Cs_2CuBr_4 electronic properties. They allow the determination of the Hubbard model parameters for Cs_2CuCl_4 and Cs_2CuBr_4 , which have been not available so far. Also, using the total energy difference method (Section 2.5.2) one can theoretically calculate the spin exchange couplings in Cs_2CuCl_4 and Cs_2CuBr_4 , in addition to the experimentally established values. Such calculations are especially desirable in the case of Cs_2CuBr_4 , where experimental determination of exchange couplings was indirect and the results are therefore somewhat uncertain.

Recently, several experimental groups have been exploring properties of the mixed systems $\text{Cs}_2\text{CuCl}_{4-x}\text{Br}_4$ [Krüger10, Cong11]. It is expected that by varying the Cl to Br ratio one will be able to tune the effective model parameters and observe the corresponding variation of macroscopic properties of $\text{Cs}_2\text{CuCl}_{4-x}\text{Br}_4$ in experiment, which would be a valuable reference to guide theory. The density functional theory would then be of a great assistance in characterizing the $\text{Cs}_2\text{CuCl}_{4-x}\text{Br}_4$ crystal structures as well as in determining their effective models.

3.2 Oxygen-doped high- T_c superconductor $\text{Bi}_2\text{Sr}_2\text{CaCu}_2\text{O}_8$

3.2.1 Cuprates – unconventional superconductors

Superconductivity is a fascinating example of collective electronic behavior which macroscopically manifests itself through (i) vanishing electrical resistivity below certain critical temperature T_c and (ii) the Meissner effect, which consists in an expulsion of magnetic field from the interior of a superconductor upon the transition.

The superconducting state was first observed by Kamerlingh Onnes in 1911 [Kamerlingh Onnes11]. After about half a century, Bardeen, Cooper and

Schrieffer (BCS) [Bardeen57] proposed a microscopic theory to explain the phenomenon. According to the *BCS theory*, superconductivity arises as a result of pairing between electrons with wavevectors \mathbf{k} and $-\mathbf{k}$ near the Fermi surface into bound states, called *Cooper pairs*, which becomes energetically favorable at low enough temperature. The Cooper pairs can propagate through the crystal without scattering, which explains the absence of electrical resistance. The pairing is possible if there is an *effective attractive interaction* between electrons. In *conventional* superconductors, which were the only type of superconductors known at the time BCS were developing their theory, this effective attraction is a consequence of the *electron-phonon interaction*. The BCS ground state, where a certain number of electrons are bound into Cooper pairs, is separated from the first excited state by an *energy gap* $\Delta_{\mathbf{k}}$, which in general is \mathbf{k} -vector dependent. In *conventional* superconductors, the gap is nearly isotropic and the Cooper pair wave-function $g(\mathbf{k})$ has the symmetry of the crystal lattice.

The BCS theory is one of the most successful theories in condensed matter physics, capable of describing many experimental findings on conventional superconductors even on a quantitative level [Claeson74]. However, with the discovery of superconducting heavy fermion compounds [Steglich79] and copper oxides [Bednorz86], whose properties greatly deviated from the BCS predictions, it became clear that the BCS theory is at best just a special case of a more general theory of superconductivity, which is yet to be developed. A class of superconductors that demonstrate non-BCS properties are traditionally referred to as *unconventional*.

Copper oxides – or cuprates – are probably the most intensively studied unconventional superconductors. The unprecedentedly high interest in the cuprates is partly due to their transition temperatures being the highest among all superconductor families (*e. g.*, $T_c = 94$ K in $\text{Bi}_2\text{Sr}_2\text{CaCu}_2\text{O}_{8+\delta}$ [Ando99], $T_c = 135$ K in $\text{HgBa}_2\text{Ca}_2\text{Cu}_3\text{O}_{8+\delta}$ [Kim95]), which positions them as very valuable materials from the practical point of view. The high transition temperatures is one of the cuprates' properties that point to their unconventionality since in the BCS theory the transition temperature of a superconductor would not exceed ~ 30 K. This is dictated by the maximally possible electron-phonon coupling. On the other hand, the cuprates are strongly correlated materials, as is manifested, *e. g.*, by an antiferromagnetically ordered insulating ground state observed in the undoped compounds, whose non-interacting bandstructure with a half-filled Cu $3d_{x^2-y^2}$ band would rather suggest a metallic state. It has been proposed therefore that electron pairing in the cuprates might be realized through the strong electronic correlations. As can be seen from a typical temperature T – charge carrier concentration n diagram in Fig. 3.8 (a), the spin-ordered insulating state at low n is destroyed at larger

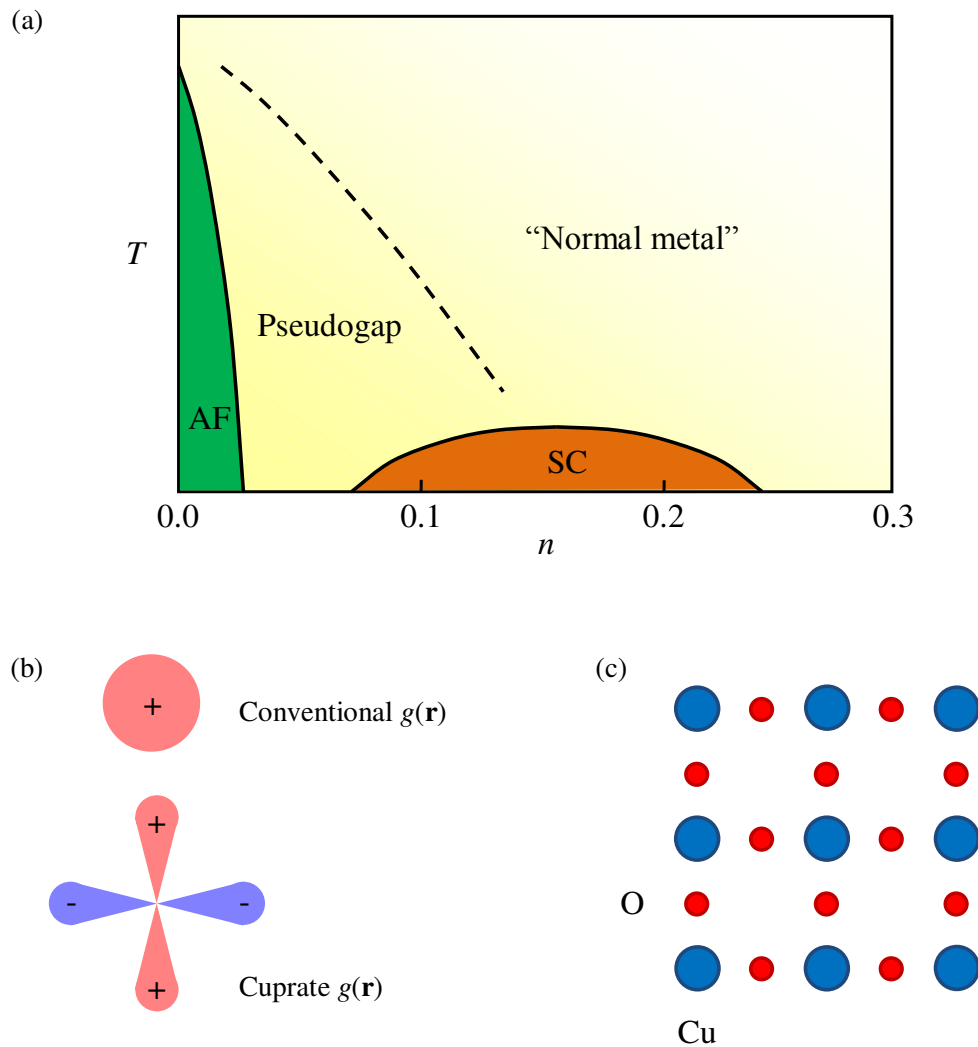


FIGURE 3.8: (a) Typical T - n phase diagram of a cuprate superconductor, (b) the symmetry of the Cooper pair function $g(\mathbf{k})$ in the cuprates, compared with that in conventional superconductors, and (c) a schematic drawing of the CuO_2 plane where Cu (O) atoms are represented by blue (red) circles.

doping concentrations giving place to a metallic phase with non-Fermi-liquid properties¹ [Pruschke95], in accordance with the Mott transition scenario. Upon increasing the doping concentration, superconductivity sets in, with the T_c reaching its maximum at some *optimal doping concentration*, followed by another phase transition to a conventional Fermi-liquid metallic state. The low n region of the cuprates' phase diagram strongly resembles that of the Hubbard model, and it is widely believed that one should

¹ Most prominent anomalous properties of the normal state in cuprates are:

- (i) the linear T -dependence of the resistivity;
- (ii) the linear T -dependence of the NMR-relaxation rate of the Cu spins;
- (iii) the T^2 increase of a Hall angle over a wide temperature range.

also be able to describe the superconducting phase in the framework of the doped Hubbard model (see, *e. g.*, Refs. [Anderson87, Lee06, Imada98, Dagotto94]).

Another unconventional feature of the cuprate superconductivity is related to the spatial symmetry of the Cooper pair wave-function $g(\mathbf{k})$. While in conventional superconductors $g(\mathbf{k})$ assumes the symmetry of the crystal and would, *e. g.*, stay invariant under the \hat{C}_4 symmetry transformation (a 90° rotation) in a tetragonal system (*s-wave pairing*), the Cooper pair wave-function in the cuprates has a lower symmetry such that $\hat{C}_4 g(\mathbf{k}) = -g(\mathbf{k})$ (*d-wave pairing*), with the nodes [$g(\mathbf{k}) = 0$] lying on the $|k_x| = |k_y|$ lines. The spatial symmetry of the conventional and cuprate Cooper pair wave-function is schematically shown in Fig. 3.8 (b). At the same time, in spin space both conventional and cuprate $g(\mathbf{k})$ are singlet functions. The *d-wave* pairing symmetry of the Cooper pair wave-function has an important consequence for the \mathbf{k} -vector dependence of the energy gap $\Delta_{\mathbf{k}}$, making it disappear in the $|k_x| = |k_y|$ directions. The *d-wave* pairing in the cuprates has been evidenced by numerous experiments probing the \mathbf{k} dependence of $g(\mathbf{k})$ as well as the nodal structure of $\Delta_{\mathbf{k}}$ [Tsuei00].

All superconducting copper oxides share a common structural feature, namely, layers of Cu and O atoms in a square lattice arrangement [Fig. 3.8 (c)], their number typically varying from one to three in different compounds. Superconductivity is believed to occur in the CuO_2 layers as a result of strongly correlated motion of the electrons within the layers. One therefore considers a 2D Hubbard model defined for the CuO_2 layer. Three orbitals – Cu $3d_{x^2-y^2}$ and O $2p_x/\text{O } 2p_y$ – are primarily involved in electron hopping, which leads to a *three-band* Hamiltonian [Emery87]. Alternatively, by downfolding the oxygen states, one can derive an effective *single-band* Hamiltonian, with renormalized hopping parameters [Zhang88]. The single-band model has been shown to describe many of the low-energy cuprate properties equally well (see, *e. g.*, Ref. [Medici09b]). It has also been suggested that other orbitals, such as the apical O $2p_z$ or the Cu $3d_{z^2}$ orbital, should be included in the model Hamiltonian [Andersen94].

Although the high relevance of the Hubbard model and the importance of the proximity to the Mott insulating transition in the cuprates has been recognized by most researchers in the field, there exist many different proposals for the high- T_c pairing mechanism that exploit strong electronic correlations encoded in the Hubbard model. Their number is continuously growing, but we will mention here only two such mechanisms, which have withstood critique and have been gaining experimental support through the years. One of them relies on Anderson's idea of the RVB state as the ground state in parent cuprate compounds, where upon doping the singlet pairs are retained and carry charge to support supercurrents [Anderson87, Anderson04, Ruckenstein87, Baskaran87, Kotliar88]. The other theory considers strong antiferromagnetic spin fluctuations near the Mott

insulating state as the pairing glue, by drawing the analogy with the ferromagnetic-spin-fluctuations-mediated superconductivity in ^3He [Scalapino86, Miyake86, Bickers89, Berk66, Scalapino95, Moriya00]. An appreciated merit of the *spin-fluctuation-exchange model* is that the $d_{x^2-y^2}$ -wave pairing symmetry is obtained in its framework as a natural result. In Chapter 5, the model is applied to calculate the superconducting properties of a cuprate $\text{Bi}_2\text{Sr}_2\text{CaCu}_2\text{O}_8$; there, as well as in Section 1.3.1, the reader can find the technical formulation of the model and of the computational method associated with it.

Though successful in describing the superconducting state, many of the present-day models for the high- T_c superconductivity, including the spin-fluctuation-exchange model, still face difficulties when making an attempt to understand the properties of the anomalous metallic state. One has to mention here the *pseudogap* signatures observed in many experiments [Timusk99] in the hole-underdoped regime [see Fig. 3.8 (a)], often accompanied by charge- and spin-ordering phenomena, such as *stripes* (see, *e. g.*, Ref. [Tranquada95]), and the *linear temperature dependence of the resistance* in the metallic phase near optimal doping [Gurvitch87, Martin88].

3.2.2 Doping-induced inhomogeneity of the superconducting gap in $\text{Bi}_2\text{Sr}_2\text{CaCu}_2\text{O}_{8+\delta}$

In our work, we focus on a $\text{Bi}_2\text{Sr}_2\text{CaCu}_2\text{O}_8$ compound. By means of DFT calculations of the electronic structure of the parent (pure, undoped) $\text{Bi}_2\text{Sr}_2\text{CaCu}_2\text{O}_8$ system and that of the oxygen-doped $\text{Bi}_2\text{Sr}_2\text{CaCu}_2\text{O}_{8+\delta}$ system, we are aiming to model and explore the experimentally observed spatial inhomogeneity of the superconducting gap in oxygen-doped $\text{Bi}_2\text{Sr}_2\text{CaCu}_2\text{O}_{8+\delta}$ samples, as measured in scanning tunneling microscopy (STM) and scanning tunneling spectroscopy (STS) experiments [Cren00, Howald01, Pan01, Lang02, Kinoda03, McElroy05].

$\text{Bi}_2\text{Sr}_2\text{CaCu}_2\text{O}_8$ has two superconducting CuO_2 layers [see Fig. 3.9 (a)], separated by Ca atoms. The symmetry of the parent compound $\text{Bi}_2\text{Sr}_2\text{CaCu}_2\text{O}_8$ conventional unit cell is base-centered tetragonal, with the space group $I4/mmm$. This (nominal) unit cell is in fact an approximation to the real crystal structure of $\text{Bi}_2\text{Sr}_2\text{CaCu}_2\text{O}_8$, where the periodic lattice of nominal unit cells is additionally modulated with an incommensurate density wave, whose wavelength equals approximately 4.8 nominal unit cells [Fig. 3.9 (b)]. The result of such modulation are corrugated CuO_2 planes [He08]. The parameters of the approximated $\text{Bi}_2\text{Sr}_2\text{CaCu}_2\text{O}_8$ unit cell which we adopt for our DFT calculations are taken from Ref. [Liang88].

The peculiar crystal structure of $\text{Bi}_2\text{Sr}_2\text{CaCu}_2\text{O}_8$, with its adjacent BiO_2 layers being bound together by weak van der Waals forces, makes a $\text{Bi}_2\text{Sr}_2\text{CaCu}_2\text{O}_8$ crystal an ideal

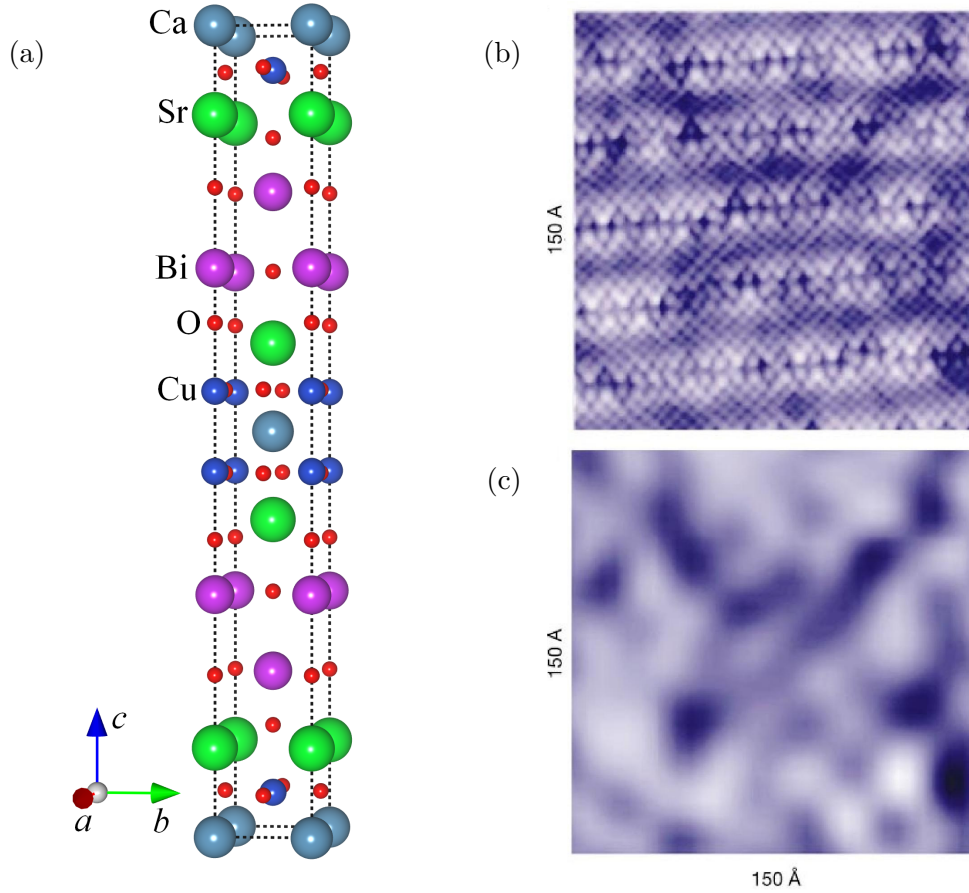


FIGURE 3.9: (a) Crystallographic unit cell of $\text{Bi}_2\text{Sr}_2\text{CaCu}_2\text{O}_8$. (b) The structural supermodulation in $\text{Bi}_2\text{Sr}_2\text{CaCu}_2\text{O}_8$ as observed in the integrated LDOS which has been measured by an STS scan [Pan01]. (c) The nano-scale electronic inhomogeneity in the integrated LDOS. This image has been obtained (Ref. [Pan01]) by Fourier filtering the well-ordered topological structure visible in (b).

object for STM studies (see, for instance, Ref. [Fischer07] for an overview on STM of high- T_c superconductors). Indeed, the $\text{Bi}_2\text{Sr}_2\text{CaCu}_2\text{O}_8$ crystal can be easily cleaved along the weakly bound BiO_2 layers to produce a high-quality surface required for an STM scan.

Atomic-scale resolution STM and STS experiments conducted recently on a $\text{Bi}_2\text{Sr}_2\text{CaCu}_2\text{O}_{8+\delta}$ surface [Cren00, Howald01, Pan01, Lang02, Kinoda03] gave surprising results. The measured tunneling spectra are found to be highly inhomogeneous in space on a scale of several nanometers [Fig. 3.9 (c)]. The observed variation of the tunneling spectra has several peculiar features. First, the superconducting gap, measured as a distance between coherence peaks, may vary by as much as a factor of three (Fig. 3.10). Second, the superconducting gap variation is found to be correlated with the positions of dopant atoms. Thus, Pan *et al.* [Pan01] observed correlations between the size of

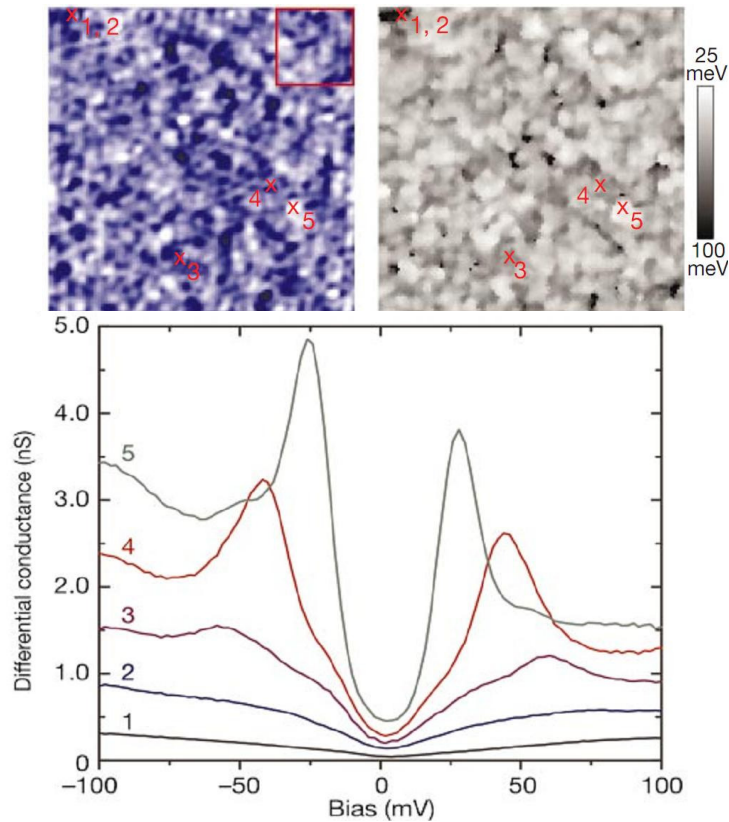


FIGURE 3.10: The integrated LDOS (left top panel) and the superconducting gap (right top panel) measured by STS and STM scans on the surface of cleaved $\text{Bi}_2\text{Sr}_2\text{CaCu}_2\text{O}_{8+\delta}$ (taken from Ref. [Pan01]). The red square indicates the region shown in Fig. 3.9 (c) with higher resolution. The bottom panel displays tunneling spectra measured at different positions on the surface, with are marked by crosses in the two upper panels.

the gap and the integrated local density of states (LDOS)² (Fig. 3.10). These findings put under question the previously dominating point of view that doping a cuprate with, *e. g.*, oxygen atoms would only produce additional charge carriers in the superconducting CuO_2 layer, resulting in a uniform shift of the chemical potential. Pan *et al.* [Pan01] also noted the analogy between the superconducting gap *versus* LDOS dependence in their measured $\text{Bi}_2\text{Sr}_2\text{CaCu}_2\text{O}_{8+\delta}$ sample and the spatially averaged³ superconducting gap *versus* oxygen concentration dependence in a series of differently doped samples.

The gap and LDOS inhomogeneities have been interpreted by some authors [Howald01, Pan01, Lang02] as a signature of electronic phase separation, which plays a key role in one of the models proposed to explain the high- T_c superconductivity [Phillips03]. In an

²The local density of states is assumed to be proportional to the directly measured differential conductance [Pan01, Fischer07]. The states that are integrated over are all states below and above the Fermi level.

³Such an averaged gap is measured by angle-resolved photoelectron spectroscopy.

alternative hypothesis, the inhomogeneous tunneling spectra are caused by *extrinsic*⁴ influences, such as inhomogeneous distribution of non-stoichiometric doping atoms. In Ref. [McElroy05], McElroy *et al.* provided strong evidences for extrinsic mechanisms being at work by showing that the size of superconducting gap as well as other spectral features are positively correlated with the oxygen dopant position. There are also theories relating inhomogeneous electronic structure to a competing order parameter [Kivelson03, Atkinson05, Alvarez05].

Several attempts to explain the nanoscale inhomogeneities in $\text{Bi}_2\text{Sr}_2\text{CaCu}_2\text{O}_{8+\delta}$ in the framework of traditional inhomogeneous BCS theory did not succeed in describing its STS spectra [Hettler99, Shnirman99]. More recently, however, a significant progress has been made by Nunner *et al.* [Nunner05], who showed that all spectral features can be reconciled within a single theoretical model if one assumes that the Cooper pair attraction is locally enhanced by dopant atoms. Interestingly, in order to arrive at this conclusion, Nunner *et al.* did not need to specify the Cooper pairing mechanism in their model. As the microscopic origin of superconducting pairing in cuprates is still a matter of debate, we thus get one more criterion to identify the right microscopic theory for high- T_c superconductivity, among a few of those that have been proposed, through its ability to also account for such local enhancement of superconducting pairing.

When a magnetically mediated mechanism of Cooper pairing is assumed, the local pairing enhancement can be a result of the local increase of spin-fluctuation exchange, which in turn might be caused by local structural modifications induced by a dopant atom. In order to explore possible effects of local structure modifications on the superexchange interaction, one way would be to derive the effective exchange interaction from an inhomogeneous Hubbard model by means of perturbation expansion. In this procedure, it is assumed that structural modifications affect locally electronic structure and are thus directly reflected in the Hubbard model parameters, such as on-site energies and transfer integrals. Application of this procedure to an inhomogeneous single-band Hubbard model [Maška07] gives as a result that superexchange interaction would always increase in the vicinity of a source of crystal and electronic structure inhomogeneity, *i. e.*, in the vicinity of a dopant atom. In their calculations, Maška *et al.* assumed that the dopant shifts on-site energies of neighboring Cu $3d_{x^2-y^2}$ orbitals, but has no effect on transfer integrals. However, analogous calculations performed on a three-band Hubbard model [Foyevtsova09], which are presented in Section 5.3 of this thesis, as well as cluster-model calculations [Johnston09], which also consider local variation of hopping integrals, lead to an opposite behavior of the local exchange interaction. These

⁴Extrinsic influences should be understood as such that are in opposition to intrinsic mechanisms related with electron self-organization.

contradictory results indicate that the calculated dopant-induced effect on local superexchange is sensitive to the quality of approximations used. This motivated us to derive an accurate single-band Hubbard model for oxygen-doped $\text{Bi}_2\text{Sr}_2\text{CaCu}_2\text{O}_{8+\delta}$ using *ab initio* methods (Section 5.1), which provide considerably improved accuracy of evaluating doping-induced variations of model parameters compared to the electrostatic calculations of Johnston *et al.* [Johnston09]. The derived inhomogeneous Hubbard model is used to explore superconducting properties of the doped $\text{Bi}_2\text{Sr}_2\text{CaCu}_2\text{O}_{8+\delta}$ crystal by performing RPA calculations of its magnetic and charge susceptibilities and Cooper pairing strength [Foyevtsova10].

3.3 Quasi-1D quantum magnet TiOCl

The Mott insulator TiOCl, with a quasi-1D network of spin- $\frac{1}{2}$ interactions, has initially attracted intense interest as one of the few inorganic systems [Hase93, Isobe96] manifesting a spin-Peierls transition [Buzdin80]. The high-temperature ($> T_{c_2} = 91$ K) crystal structure of TiOCl is orthorhombic $Pmmn$. The TiOCl crystal is formed by bilayers of Ti and O atoms, stacked along the crystallographic c direction, which weakly interact through van der Waals forces. The van der Waals interaction is mediated by the Cl atoms, which, together with the O atoms, make up distorted ligand octahedra around the Ti atoms [see Fig. 3.11 (a)]. The triply ionized Ti ion hosts one electron in the $3d$ shell, which induces a localized spin- $\frac{1}{2}$ magnetic moment. The interactions between the Ti spins are of pronounced 1D character [Seidel03, Saha-Dasgupta04, Zhang08a], with chains of antiferromagnetically coupled Ti spins ($J_b = 660$ K) running along the crystallographic b direction. The two additional spin interactions $J_c = -16.7$ K and $J_a = -10.5$ K couple the antiferromagnetic chains from adjacent layers and along the a direction, respectively, as shown in Fig. 3.11 (b) [Zhang08a].

The high-temperature phase of TiOCl is unstable towards the spin-Peierls transition, whereby the antiferromagnetic Ti chains distort to form a double-period structure with short and long Ti-Ti distances and the Ti spins dimerize at the short Ti-Ti bonds in a chain. The spin-Peierls transition in TiOCl has a bunch of atypical features [Kataev03, Lemmens04, Caimi04, Hemberger05] indicating an important role of, presumably, orbital degrees of freedom and magnetic frustration, which act simultaneously with the conventional spin-Peierls mechanisms. These are likely to be responsible, in particular, for the fact that there are two phase transitions upon temperature lowering, one at $T_{c_2} = 91$ K to an incommensurate structure phase and the other at $T_{c_1} = 67$ K to a dimerized phase. The second transition at T_{c_1} is of the first order, which also deviates from the conventional spin-Peierls scenario.

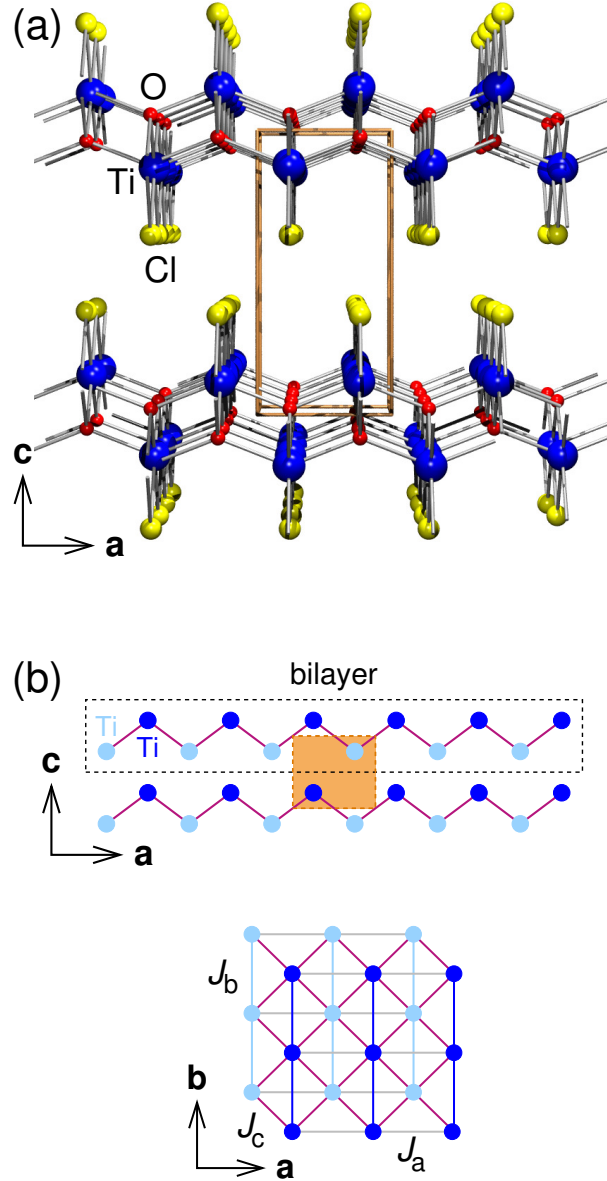


FIGURE 3.11: (a) TiOCl crystal structure and (b) exchange coupling pathways between Ti spins. In (b), the Ti atoms are schematically shown as blue and light blue circles. The orange rectangle represents the TiOCl unit cell. The figures are taken from Ref. [Zhang08a]

Though being promoted in some early works on TiOCl [Kataev03], the relevance of orbital fluctuations for the stabilization of the incommensurate phase between T_{c_2} and T_{c_1} seems now to be less convincing. The DFT calculations of Ref. [Saha-Dasgupta04] have shown that the ground state of TiOCl, obtained with the LDA+U⁵ exchange-correlation functional, consists of a well separated Ti $3d_{xy}$ band⁶ (Fig. 3.12). The direct overlap

⁵Qualitatively, the TiOCl DOS calculated within the LDA+U does not depend on the choice of U and J^H over the ranges $0.3 \text{ eV} \leq J^H \leq 1 \text{ eV}$ and $2 \text{ eV} \leq U \leq 7 \text{ eV}$. The susceptibility data are best described by a spin model with the exchange coupling constants obtained from the LDA+U calculations with $U = 3.3 \text{ eV}$ and $J^H = 1 \text{ eV}$.

⁶This is with respect to the coordinate system, in which $\hat{z} = a$ and \hat{x} and \hat{y} are rotated by 45° .

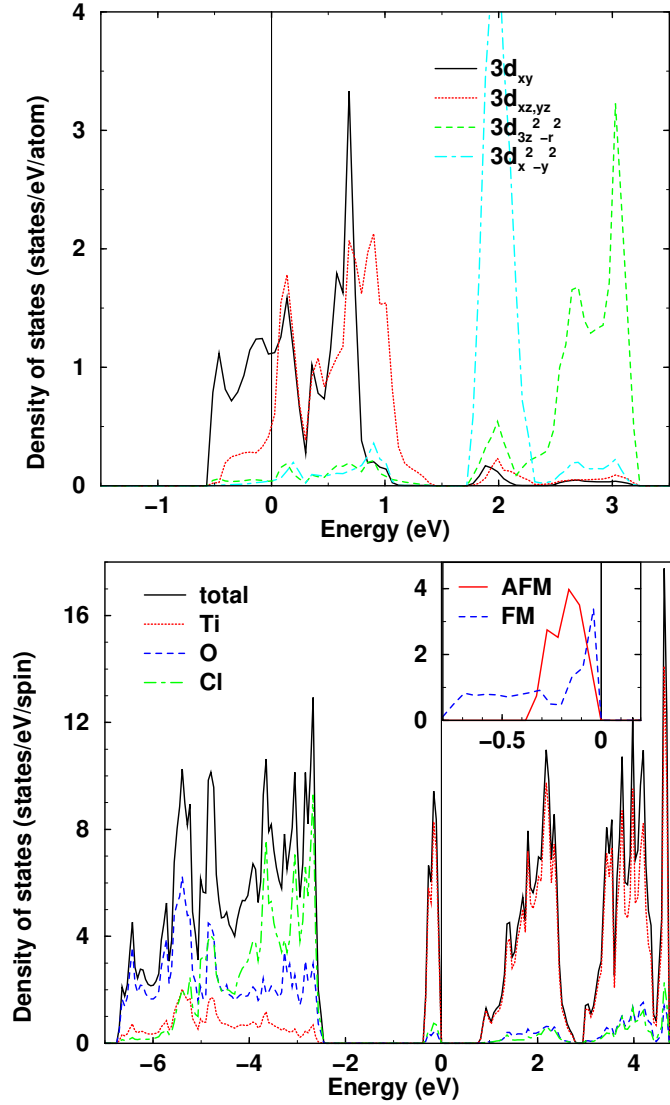


FIGURE 3.12: The DOS of TiOCl obtained with the FPLO code [Koepernik99] in Ref. [Saha-Dasgupta04]. Top panel: orbital resolved Ti $3d$ states from non-spin-polarized LDA calculations. Bottom panel: atomic resolved DOS from antiferromagnetically polarized LDA+ U calculations ($U = 3.3$ eV, $J^{\text{H}} = 1$ eV). In the LDA+ U ground state, the Ti $3d_{xy}$ band appears well-separated from the rest of the Ti $3d$ bands and fully occupied.

between the Ti $3d_{xy}$ electron clouds is responsible for the strong antiferromagnetic coupling J_b , with the transfer integral being estimated as ~ -0.25 eV. As opposed to the orbital fluctuations, a number of theoretical [Saha-Dasgupta04, Zhang08a] as well as experimental [Rückamp05, Hoinkis05] studies provide evidences in favor of frustration induced spin fluctuations being the key driving force behind the transition to the incommensurate phase at T_{c1} .

Much effort has also been invested into finding a route to metallize TiOCl by either

- (i) applying pressure [Kuntscher06, Forthaus08, Zhang08b] or
- (ii) doping [Zhang10, Sing11].

As a low-dimensional Mott insulator, TiOCl is anticipated to exhibit properties similar to, *e. g.*, 2D cuprate superconductors. In particular, it is speculated whether a doped – or metallized in some other way – TiOCl might become superconducting.

While Car-Parinello molecular dynamics (Section 2.3) simulations do find a pressure-induced insulator-to-metal transition in TiOCl [Zhang08b], which is accompanied by a structural transition and Ti-Ti dimerization, the electric transport measurements on pressurized TiOCl samples up to 24 GPa [Forthaus08] point to a persisting band gap. The electrical resistance anomaly at 13 GPa and the strong suppression of the light transmittance in the infrared and visible frequency range [Kuntscher06] at 13.9 GPa indicate, however, a change in the electronic structure, which is probably overestimated in the DFT calculations.

Recently, Sing *et al.* [Sing11] have succeeded in producing Na doped TiOCl samples in order to explore the second possibility to drive TiOCl into a metallic state. The photoemission spectroscopy of the doped samples finds, however, that a band gap at the Fermi level remains for all concentrations of Na. The microscopic origin of this persistent insulating state should apparently be related with the local crystal and electronic structural changes that the intercalated Na ions induce. In our work [Zhang10], presented in Chapter 6, we employ the DFT methods to study these effects.

Chapter 4

Cs_2CuCl_4 and Cs_2CuBr_4 microscopic models

This chapter presents a detailed DFT study of the frustrated antiferromagnets Cs_2CuCl_4 and Cs_2CuBr_4 , which was initiated in order to gain a better understanding of the experimentally observed properties of the compounds on a microscopic level. Among others, we were searching for the answers to the following questions: Can the different magnetic behavior of Cs_2CuCl_4 and Cs_2CuBr_4 be traced back to the differences in their electronic structure? Will the experimentally established Heisenberg models for Cs_2CuCl_4 and Cs_2CuBr_4 be confirmed also by DFT calculations? Which are the main features of their electronic TB models? How important is the role of electronic correlations in these materials?

On our way to establishing the DFT-based microscopic models of Cs_2CuCl_4 and Cs_2CuBr_4 , we discovered that electronic correlations play an important role in these systems and should be treated on (at least) the LDA+U level. Moreover, an interplay between electronic correlations, which tune localization of the Cu 3d electrons and the value of the Cu magnetic moment, and lattice dynamics via the Jahn-Teller effect results in the Cs_2CuCl_4 and Cs_2CuBr_4 equilibrium crystal structures being dependent on the DFT optimization functional. The decisive role of electronic correlations and magnetism in the two compounds becomes evident with the observation that the values of spin exchange couplings couple to the variation of the Cs_2CuCl_4 and Cs_2CuBr_4 structural parameters obtained with different optimization functionals. This knowledge enables us to make correct predictions for the $\text{Cs}_2\text{CuCl}_{4-x}\text{Br}_x$ crystal structures and study these mixed systems with DFT methods in the future.

4.1 Electronic properties

In our discussion of the Cs_2CuCl_4 and Cs_2CuBr_4 electronic properties, we will be analyzing and comparing several sets of calculated data for each compound. For a given compound, the different data sets are obtained by using slightly different structural parameters during DFT calculations, which in one case are determined by x-ray measurements and in the rest of cases obtained by performing structural optimization within the DFT. Our motivation to perform crystal structure optimization for Cs_2CuCl_4 and Cs_2CuBr_4 was the surprisingly large disagreement between the Heisenberg model determined for Cs_2CuCl_4 from DFT calculations when using the experimental crystal structure and the experimentally determined model. The nuclear forces calculated by the DFT turned out to be large in the experimental crystal structure of Cs_2CuCl_4 (as well as in that of Cs_2CuBr_4), which gave us a reason to expect that structural relaxation would improve the DFT description of spin exchange in the two systems. Since it was not known *a priori* which exchange-correlation functional is most suitable in the case of Cs_2CuCl_4 and Cs_2CuBr_4 , we performed a number of structural relaxations using different exchange-correlation functionals. We will now proceed by introducing the functionals we chose for this purpose and presenting computational details of the optimization.

4.1.1 Structure optimization schemes

The crystal structure relaxations of the compounds are performed using as a starting point the room temperature experimental structural data, as reported in Ref. [Bailleul91] for Cs_2CuCl_4 and in Ref. [Morosin60] for Cs_2CuBr_4 . Each relaxation consisted in optimizing atomic positions under constraints imposed by the space group symmetry of the Cs_2CuCl_4 and Cs_2CuBr_4 unit cell and with fixed lattice constants. We chose to fix the experimental lattice constants as these are usually determined with high accuracy, while, on the other hand, the LDA and GGA are known to, respectively, underestimate or overestimate the unit cell volume.

We consider the following optimization schemes with different approximations to the exchange-correlation functional within the DFT and different magnetic configurations:

- (1) the local density approximation (LDA[nm]) [Perdew92];
- (2) the generalized gradient approximation (GGA[nm]) [Perdew96];
- (3) the spin-dependent GGA with a ferromagnetic Cu spin configuration (GGA[fm]);

- (4) the spin-dependent GGA+U (AMF functional [Czyżyk94]) with a ferromagnetic Cu spin configuration (GGA+U[fm]). The on-site Coulomb interaction $U = 6$ eV and the Hund’s rule coupling $J^H = 1$ eV are introduced for Cu ions.

For Cs_2CuCl_4 , we also considered two optimization schemes with an antiferromagnetic Cu spin configuration:

- (5) GGA[afm] and
 (6) GGA+U[afm] ($U = 6$ eV, $J^H = 1$ eV).

Additionally, for both compounds we completed the LDA series of structural optimizations with LDA[fm] and LDA+U[fm] optimizations. However, due to the analogous behavior of the structural properties of Cs_2CuCl_4 and Cs_2CuBr_4 observed within this series with those observed within the GGA series, we will not discuss the full LDA series in detail.

Calculations with an antiferromagnetic spin configuration were performed for a Cs_2CuCl_4 supercell with a reduced symmetry $P21/c$. A detailed description of this antiferromagnetic configuration as well as other computational details of structural optimization can be found in Appendix A.1.

In order to better understand the effects responsible for the differences in crystal structures optimized using different exchange-correlation functionals, let us compare the densities of states of the unrelaxed Cs_2CuCl_4 and Cs_2CuBr_4 crystal structures calculated with GGA[nm], GGA[fm] and GGA+U[fm] functionals, presented in Fig. 4.1. The spin-independent GGA[nm] functional renders the two compounds metallic, with a finite DOS at the Fermi level [Fig. 4.1 (a) and (d)]. However, when the spin-dependent GGA[fm] functional is applied instead, Cs_2CuCl_4 and Cs_2CuBr_4 are found in a spin-polarized state, with a band gap opened at the Fermi level¹ [Fig. 4.1 (b) and (e)]. Upon introducing the on-site Coulomb repulsion for Cu $3d$ electrons in the GGA+U[fm] scheme, the gaps in both compounds increase considerably [Fig. 4.1 (c) and (f)].

Apparently, the spin-dependent functionals GGA[fm] and GGA+U[fm] perform much better than the spin-independent GGA[nm], correctly reproducing the insulating ground state of Cs_2CuCl_4 and Cs_2CuBr_4 . Therefore, we should expect to obtain more accurately relaxed Cs_2CuCl_4 and Cs_2CuBr_4 crystal structures when using the spin-dependent functionals.

Along with the band gap opening, the spin-dependent functional calculations find a finite Cu magnetic moment, which grows as the Coulomb interaction is switched on.

¹In Cs_2CuBr_4 , the GGA[fm] gap is rather small (~ 0.03 eV).

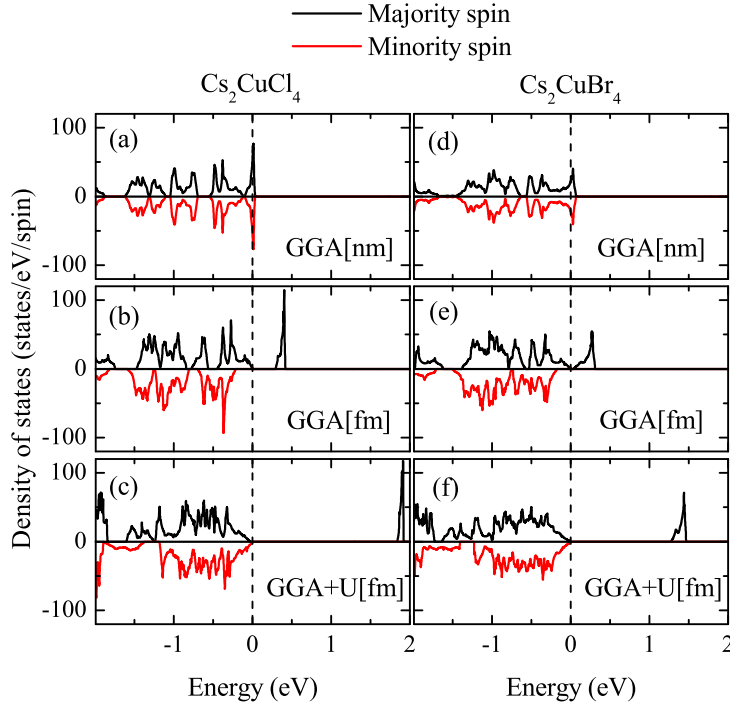


FIGURE 4.1: Total DOS's for majority and minority electron spin for (a) Cs_2CuCl_4 , calculated with GGA[nm], (b) Cs_2CuCl_4 , calculated with GGA[fm], (c) Cs_2CuCl_4 , calculated with GGA+U[fm], (d) Cs_2CuBr_4 , calculated with GGA[nm], (e) Cs_2CuBr_4 , calculated with GGA[fm], and (f) Cs_2CuBr_4 , calculated with GGA+U[fm]. For an easier comparison, the two DOS's are plotted with opposite signs. In the case of GGA+U[fm], the AMF scheme is employed, with $U = 6$ eV and $J^{\text{H}} = 1$ eV. The Fermi level is set to zero.

Tables 4.1 and 4.2 display the Cu magnetic moments μ_{Cu} in, respectively, Cs_2CuCl_4 and Cs_2CuBr_4 calculated with the GGA[fm] and GGA+U[fm] functionals.

4.1.2 Structural analysis

The relaxed as well as experimental Cs_2CuCl_4 and Cs_2CuBr_4 structural parameters are listed in Appendix A.2.

In our discussion of the various Cs_2CuCl_4 and Cs_2CuBr_4 crystal structures we focus on geometry variations of the CuX_4 ($X = \text{Cl}, \text{Br}$) tetrahedron, which, as will become evident later, determine the strength of important exchange couplings. Let us introduce below the CuX_4 tetrahedron parameters that we find to be of special interest.

In Cs_2CuCl_4 and Cs_2CuBr_4 , the CuX_4 tetrahedron is distorted due to the Jahn-Teller effect and also due to the steric pressure originating from Cs^+ ions [Morosin60]. The Jahn-Teller effect results in a squeezing of the tetrahedron such that the $X\text{-Cu-X}$ bond angles γ_{12} and γ_{33} increase and the $X\text{-Cu-X}$ bond angles γ_{13} and γ_{23} decrease (Fig. 4.2).

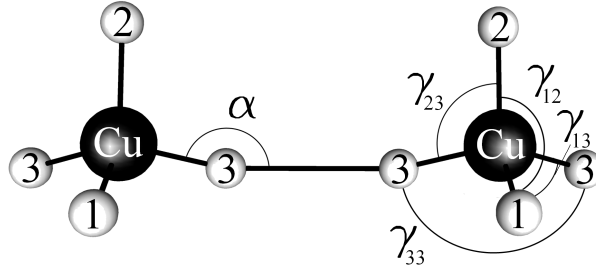


FIGURE 4.2: Neighboring CuX_4 tetrahedra. Labels 1, 2 and 3 of the X atoms denote the three inequivalent X atoms: $X(1)$, $X(2)$ and $X(3)$. As indicated, angles γ_{12} , γ_{13} , γ_{23} and γ_{33} correspond to the angles $X(1)\text{-Cu-}X(2)$, $X(1)\text{-Cu-}X(3)$, $X(2)\text{-Cu-}X(3)$ and $X(3)\text{-Cu-}X(3)$, respectively.

The steric pressure by $\text{Cs}(2)$ on $X(3)$ causes additional symmetry lowering by increasing γ_{13} and decreasing γ_{33} . In order to compare the strengths of the two types of distortions in different structures, we define the Jahn-Teller deviation Δ^{JT} as the difference between averages $\frac{1}{2}(\gamma_{12} + \gamma_{33})$ and $\frac{1}{2}(\gamma_{13} + \gamma_{23})$,

$$\Delta^{\text{JT}} = \left| \frac{1}{2}(\gamma_{12} + \gamma_{33}) - \frac{1}{2}(\gamma_{13} + \gamma_{23}) \right|, \quad (4.1)$$

and the steric pressure deviations δ_1^{steric} and δ_2^{steric} as

$$\delta_1^{\text{steric}} = \frac{\frac{1}{2}|\gamma_{12} - \gamma_{33}|}{\frac{1}{2}(\gamma_{12} + \gamma_{33})} \quad \text{and} \quad \delta_2^{\text{steric}} = \frac{\frac{1}{2}|\gamma_{13} - \gamma_{23}|}{\frac{1}{2}(\gamma_{13} + \gamma_{23})}. \quad (4.2)$$

We first compare results of spin-dependent functional relaxations of Cs_2CuCl_4 with ferromagnetic and antiferromagnetic spin configurations in order to find out how big is the effect of relaxing with different spin configurations. As it turns out, it is rather small as the Cs_2CuCl_4 structures relaxed with GGA[fm] and GGA[afm] are very close as well as the structures relaxed with GGA+U[fm] and GGA+U[afm] (see Appendix A.2). The tetrahedron parameters in these structures are also similarly close. This demonstrates that, within the spin-dependent GGA and GGA+U, interatomic forces in Cs_2CuCl_4 are very weakly dependent on the actual Cu spin configuration. Therefore, we find it sufficient to consider in the following only ferromagnetic spin-dependent relaxation schemes for Cs_2CuCl_4 and Cs_2CuBr_4 . The observed insensitivity of the structural relaxation results to magnetic order is a consequence of the rather small energy scale of magnetic interactions between Cu spins, which is much smaller than the difference between total energies usually involved in structural relaxations².

²It should also be noted that the energy difference between various spin-polarized DFT ground states with localized Cu magnetic moments is much smaller than the energy difference between any of the

TABLE 4.1: Tetrahedron parameters for the Cs_2CuCl_4 structures and corresponding values of the Cu magnetic moment μ_{Cu} during structural relaxation. The angles are given in degrees, the deviations δ_1^{steric} and δ_2^{steric} in percent and the averaged Cu-Cl distance \bar{d}_{Cu-Cl} in Ångström.

	exp	GGA+U[fm]	GGA[fm]	GGA[nm]	LDA[nm]
γ_{12}	131.33	130.97	133.05	133.66	135.56
γ_{13}	101.67	101.60	100.67	99.69	98.26
γ_{23}	99.58	99.43	98.55	97.86	97.11
γ_{33}	126.79	127.78	130.41	134.34	138.56
Δ^{JT}	28.44	28.86	32.12	35.22	39.38
α	153.99	153.89	155.21	157.17	159.28
δ_1^{steric}	1.76	1.23	1.00	0.25	1.10
δ_2^{steric}	1.04	1.08	1.06	0.93	0.59
\bar{d}_{Cu-Cl}	2.232	2.263	2.263	2.267	2.227
μ_{Cu}	-	$0.78\mu_B$	$0.50\mu_B$	0	0

TABLE 4.2: Tetrahedron parameters for the Cs_2CuBr_4 structures and corresponding values of the Cu magnetic moment μ_{Cu} during structural relaxation. The angles are given in degrees, the deviations δ_1^{steric} and δ_2^{steric} in percent and the averaged Cu-Br distance \bar{d}_{Cu-Br} in Ångström.

	exp	GGA+U[fm]	GGA[fm]	GGA[nm]	LDA[nm]
γ_{12}	130.40	130.06	131.77	132.53	133.72
γ_{13}	102.16	102.16	101.70	100.48	99.03
γ_{23}	99.93	99.75	98.89	97.94	97.34
γ_{33}	126.42	126.42	128.05	133.07	137.48
Δ^{JT}	27.52	27.28	29.62	33.59	37.41
α	153.21	153.22	154.03	156.53	158.74
δ_1^{steric}	1.55	1.42	1.43	0.20	1.38
δ_2^{steric}	0.96	1.19	1.40	1.28	0.86
\bar{d}_{Cu-Br}	2.376	2.407	2.407	2.411	2.368
μ_{Cu}	-	$0.73\mu_B$	$0.42\mu_B$	0	0

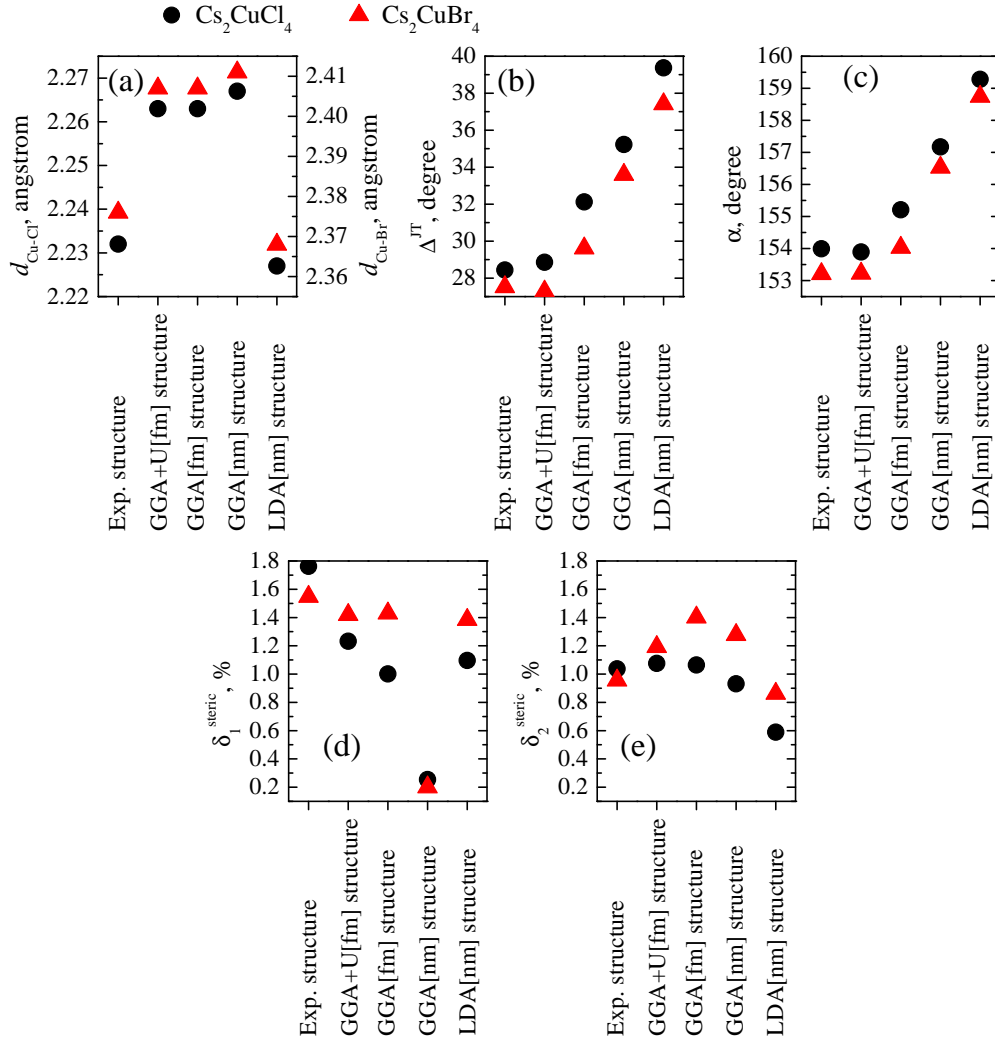


FIGURE 4.3: Parameters of the CuX₄ tetrahedron in the experimental as well as relaxed crystal structures of Cs₂CuCl₄ and Cs₂CuBr₄: (a) the average Cu-X (X = Cl, Br) bond distance $\bar{d}_{\text{Cu-X}}$, (b) Jahn-Teller deviation Δ^{JT} , (c) Cu-X-X angle α in the J superexchange bridge, (d) steric pressure deviation δ_1^{steric} and (e) steric pressure deviation δ_2^{steric} .

In Tables 4.1 and 4.2, we present the tetrahedron parameters defined above for the experimental and relaxed crystal structures of Cs₂CuCl₄ and Cs₂CuBr₄, respectively. Some of them are additionally shown in Fig. 4.3 in order to facilitate comparison of different crystal structures. In both compounds, the crystal structures of the GGA relaxation series (GGA+U[fm], GGA[fm] and GGA[nm]) are featured by a continuous variation of the X-Cu-X angles. In terms of these angles, the relaxed crystal structures of Cs₂CuCl₄ and Cs₂CuBr₄ closest to the corresponding experimental structures are the GGA+U[fm] structures. However, in terms of the Cu-X bond distances, represented here

spin-polarized states and the spin-unpolarized state obtained with a spin-independent functional. The latter energy difference is comparable with the energy differences involved in structural relaxations.

by the averaged distance $\bar{d}_{\text{Cu}-X}$, the GGA crystal structures are further away from the experimental structures than the LDA structures [see Fig. 4.3 (a)]. In the LDA structures of Cs_2CuCl_4 and Cs_2CuBr_4 ³, parameter $\bar{d}_{\text{Cu}-X}$ is smaller than in the corresponding experimental structures, but the difference is less compared to the GGA series. The GGA relaxation tends to increase the bond distances in the CuX_4 tetrahedron while the LDA relaxation decreases them.

In the GGA series, the Jahn-Teller distortion [Δ^{JT} , Fig. 4.3 (b)] is most pronounced in the Cs_2CuCl_4 and Cs_2CuBr_4 crystal structures relaxed with the spin-independent functionals LDA[nm] and GGA[nm]. With application of the spin-dependent functionals GGA[fm] and GGA+U[fm], when the systems become insulating and there appears a finite Cu magnetic moment, the Jahn-Teller distortions in Cs_2CuCl_4 and Cs_2CuBr_4 reduce. They reach minimal values, which are also very close to the corresponding experimentally found Jahn-Teller distortions, in the GGA+U[fm] relaxed structures. An explanation to such behavior will be given in Section 4.3.

The X -Cu- X bond angle γ_{33} and the structurally coupled angle α of the Cu- X - X -Cu bridge (Fig. 4.2) behave analogously to the Jahn-Teller distortion Δ^{JT} [compare Figures 4.3 (b) and (c)]. The angle α is one of the geometrical parameters of the superexchange path J , so the observed variation of α in differently relaxed crystal structures points to a possible variation of the exchange coupling J . We indeed find such a variation in the total energy difference calculations, which, moreover, turns out to be unexpectedly strong (see Section 4.2.2).

4.1.3 Bandstructure and density of states

Let us discuss now electronic properties of Cs_2CuCl_4 and Cs_2CuBr_4 calculated with the experimental and relaxed crystal structures introduced above. We show here results obtained with the spin-independent GGA exchange-correlation functional. Calculations are performed with both the FPLO (Section 2.2.2) and Wien2k codes (Ref. [Blaha01], Section 2.2.3). We present here the Wien2k calculated data, which are in good agreement with the FPLO results.

We first concentrate on generic features of the electronic structures of Cs_2CuCl_4 and Cs_2CuBr_4 , equally found in calculations with any of the Cs_2CuCl_4 and Cs_2CuBr_4 crystal structures. Fig. 4.4 displays projected densities of states (DOS) for Cs_2CuCl_4 and Cs_2CuBr_4 obtained using their experimental structures. In both compounds, the hybridized Cu $3d$ and Cl $3p$ /Br $4p$ bands occupy the energy range between about -4 eV and 0 eV [see, for instance, the atomic DOS in Figs. 4.4 (a) and (c)]. There is almost no

³This includes also the LDA[fm] and LDA+U[fm] structures, which are not listed in the tables.

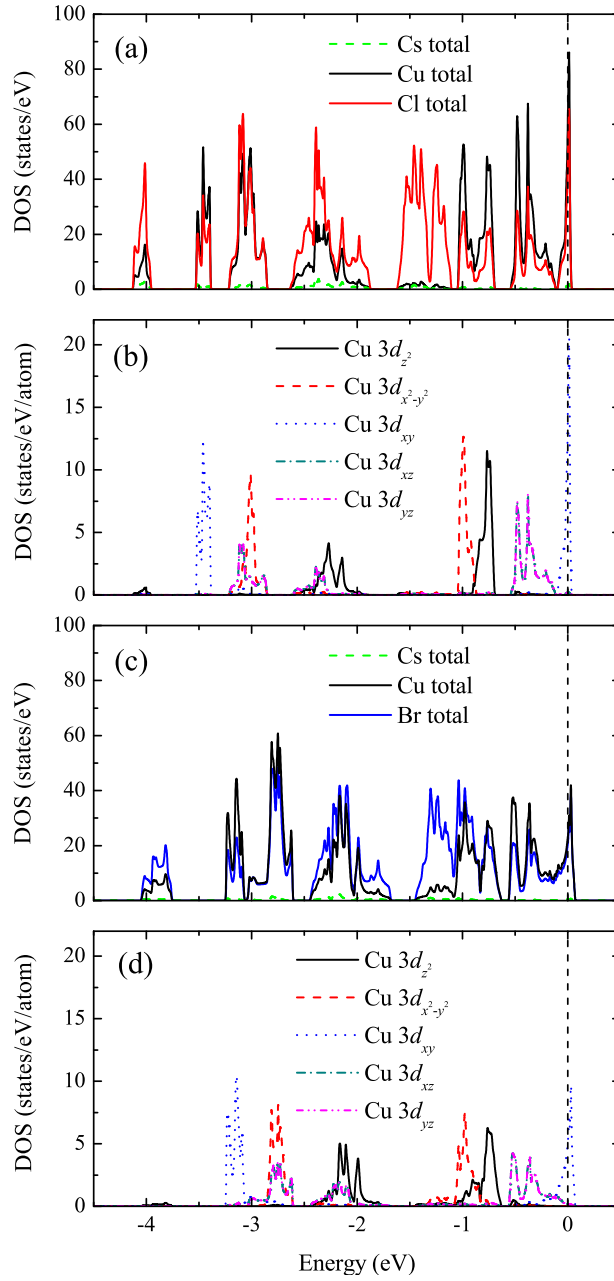


FIGURE 4.4: Atomic species resolved DOS calculated from the experimental crystal structures for (a) Cs_2CuCl_4 and (c) Cs_2CuBr_4 and the orbital projected DOS of Cu $3d$ for (b) Cs_2CuCl_4 and (d) Cs_2CuBr_4 . Energy is measured relative to the Fermi level E_F .

contribution from Cs atoms to the DOS near the Fermi level, which indicates a negligible hybridization of Cu with Cs. This allows us to conclude, in particular, that the exchange coupling J along the Cu chains in the b direction arises mainly from the Cu- X -Cu hybridization. A gap of approximately 4 eV separates the Cu and X ($X = \text{Cl}, \text{Br}$) bands from the next unoccupied states [not shown in Figs. 4.4 (a) and (c)], which have significant Cs contribution.

The Cu and X band manifold is an assembly of bonding states in the interval between

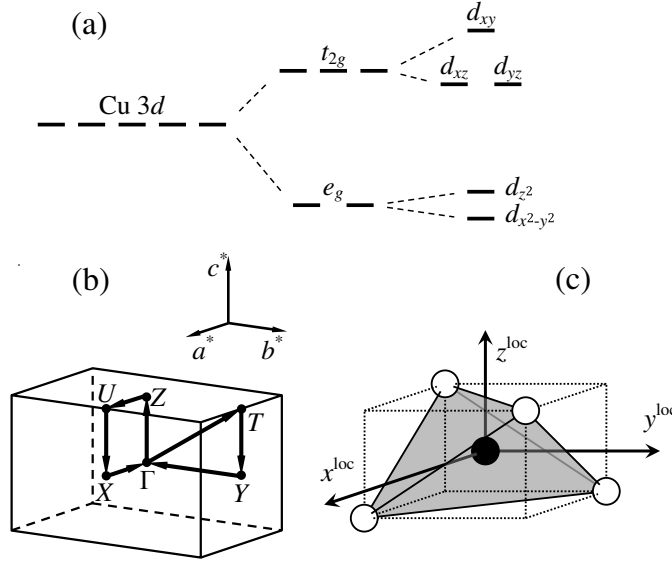


FIGURE 4.5: (a) Schematic splitting of the Cu 3d orbitals in the crystal field with tetrahedral symmetry. (b) The path in the $\text{Cs}_2\text{CuCl}_4/\text{Cs}_2\text{CuBr}_4$ Brillouin zone for bandstructure calculations (Figs. 4.6 and 4.7). (c) The local reference frame of a Cu atom, in which its orbital projected density of states is defined.

-4 eV and -2 eV and anti-bonding states in the interval between -2 eV and the Fermi level. The Cu anti-bonding states are split by the crystal field generated by X^- ions surrounding a Cu^{2+} ion into the energetically lower e_g doublet ($d_{x^2-y^2}$ and d_{z^2}) and the energetically higher t_{2g} triplet (d_{xy} , d_{xz} and d_{yz}). Due to the Jahn-Teller uniaxial distortion of the tetrahedron, the t_{2g} triplet is further split into the degenerate d_{xz}/d_{yz} states and the half-filled d_{xy} states. This splitting is schematically illustrated in Fig. 4.5 (a), and the orbital projected densities of Cu 3d states for the experimental Cs_2CuCl_4 and Cs_2CuBr_4 structures are presented in Figs. 4.4 (b) and (d), respectively. Note that the orbital designation is given according to the local reference frame of the CuX_4 tetrahedron as shown in Fig. 4.5 (c).

In Figs. 4.6 and 4.7, we present the total DOS and bandstructures for the experimental as well as relaxed crystal structures (GGA+U[fm], GGA[fm], GGA[nm], LDA[nm]) of Cs_2CuCl_4 and Cs_2CuBr_4 , respectively. In contrast to Cs_2CuCl_4 , the t_{2g} states in Cs_2CuBr_4 are strongly hybridizing, which is indicated by the non-separable character of the overlap of the Cs_2CuBr_4 d_{xy} and d_{xz}/d_{yz} bands in the bandstructure.

We now inspect how the differences in the experimental and variously relaxed crystal structures of Cs_2CuCl_4 and Cs_2CuBr_4 manifest themselves in their electronic structures. For this purpose, we focus at energies close to the Fermi level⁴. In both Cs_2CuCl_4 and Cs_2CuBr_4 , the splitting between the Cu $3d_{xy}$ bands and the degenerate Cu $3d_{xz}$

⁴This region defines the low-energy physics in Cs_2CuCl_4 and Cs_2CuBr_4 and thus is of special interest.

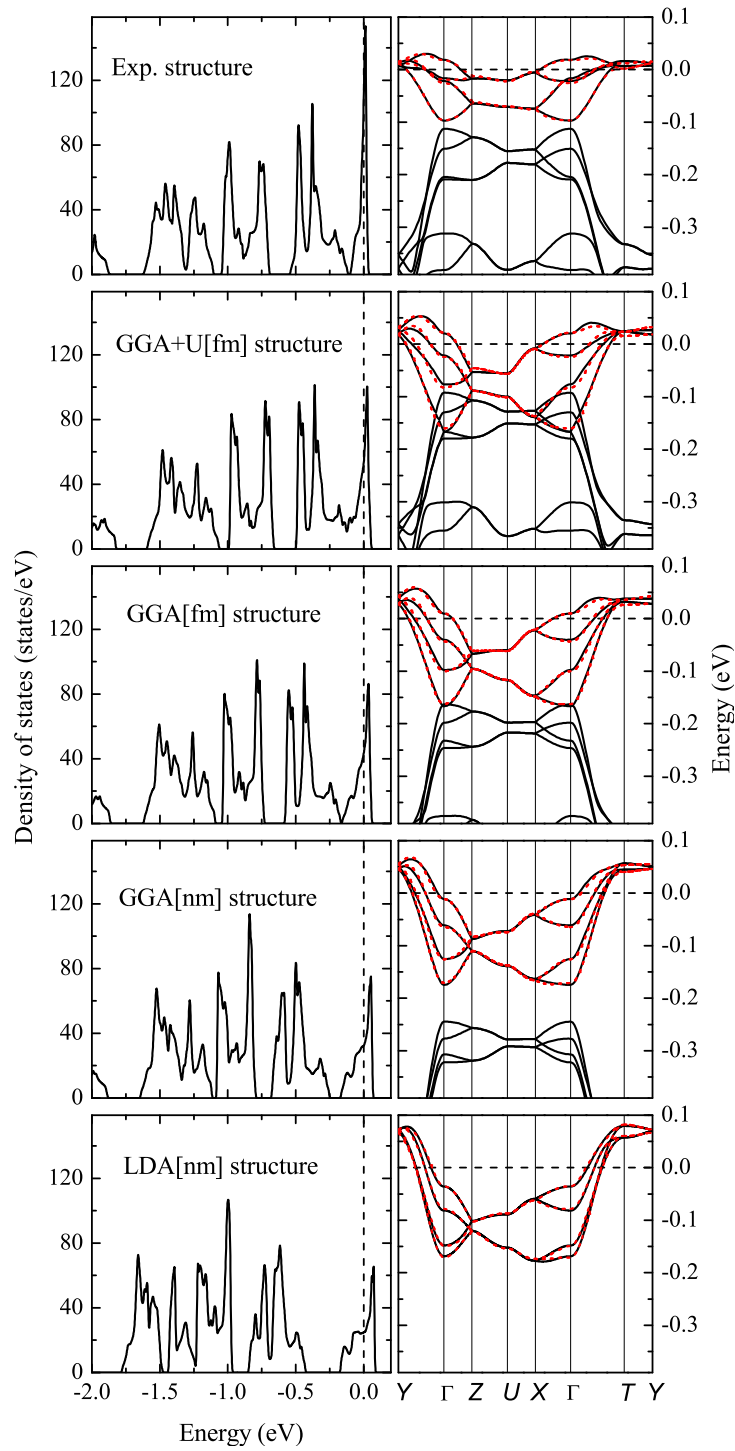


FIGURE 4.6: DOS and bandstructures for various Cs_2CuCl_4 structures (specified by the panel captions). In the bandstructure plots, the DFT calculated bands are in black (solid) lines and the tight-binding fits are in red (dashed) lines. The bandstructure path in the Brillouin zone is shown in Fig. 4.5 (b). Energy is again measured relative to the Fermi level E_F .

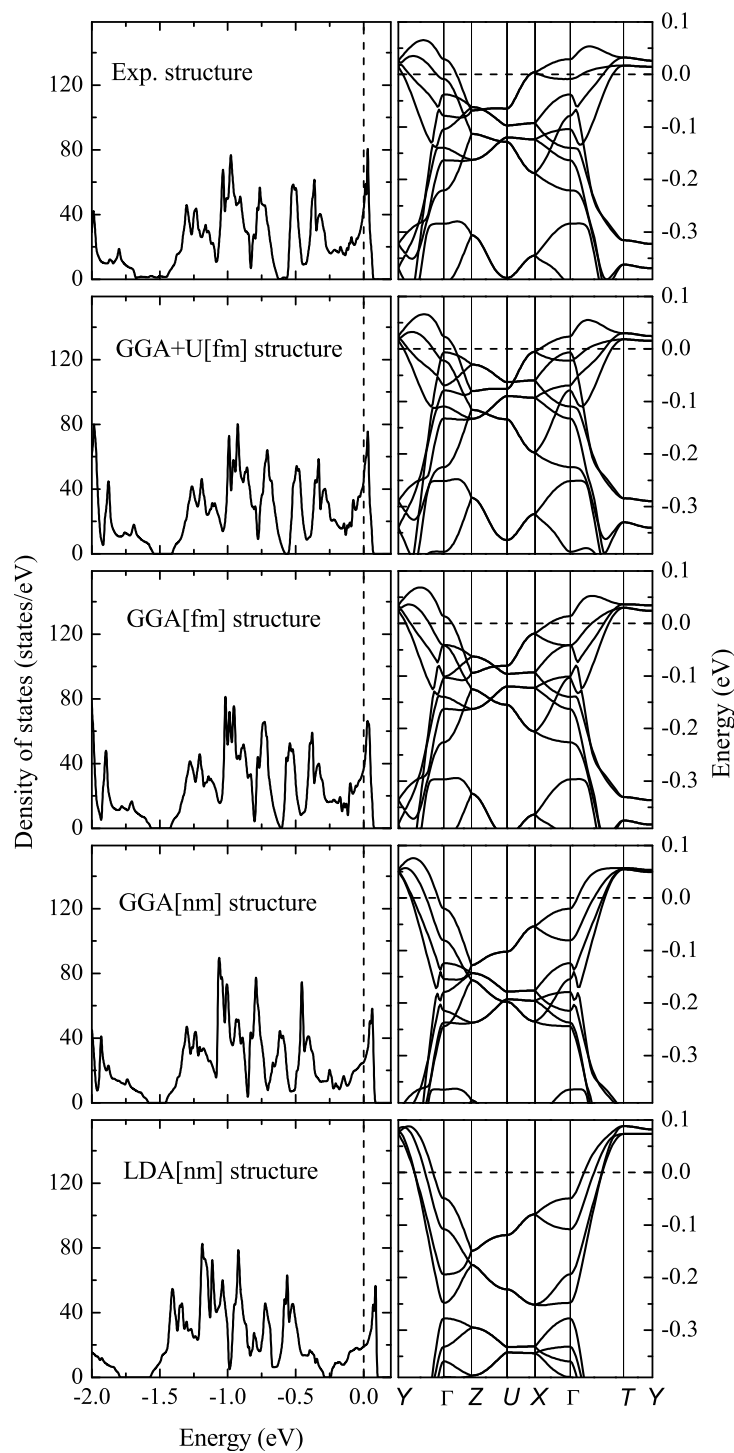


FIGURE 4.7: DOS and bandstructures of various Cs_2CuBr_4 structures (specified by the panel captions). The bandstructure path in the Brillouin zone is shown in Fig. 4.5 (b).

and Cu $3d_{yz}$ bands decreases for structures which have been relaxed with a higher Cu magnetic moment, *i. e.*, from the GGA[nm] relaxed structure to the GGA+U[fm] relaxed one. We relate this behavior to the variation of the Jahn-Teller distortion of the CuX_4 tetrahedron, which has direct influence on the band splitting. The trend is better seen in Cs_2CuCl_4 where the d_{xy} band is separated by a gap (except for the GGA+U[fm] structure).

The Cu $3d_{xy}$ bandwidth appears to be weakly dependent on the relaxation functional in both Cs_2CuCl_4 as well as Cs_2CuBr_4 relaxed structures. However, when calculated with the experimental crystal structure, the Cu $3d_{xy}$ bandwidth of Cs_2CuCl_4 is found to be by a factor of two smaller than the roughly uniform Cu $3d_{xy}$ bandwidth of the relaxed Cs_2CuCl_4 structures. In Cs_2CuBr_4 , on the contrary, there is no big difference in the Cu $3d_{xy}$ bandwidths of the relaxed and experimental structures. The narrowing of the Cu $3d_{xy}$ band in the experimental structure of Cs_2CuCl_4 results in a sharply peaked DOS at the Fermi level. This is a signature of strong structural instability, which is apparently much stronger than in the case of the Cs_2CuBr_4 experimental structure.

4.2 Derivation of effective models

4.2.1 Tight-binding model

We have just discussed the Cs_2CuCl_4 and Cs_2CuBr_4 bandstructures and their variations as a function of the exchange-correlation functional used for relaxation on a qualitative level. It is also possible to quantify the observed variations by mapping the bandstructure onto a tight-binding (TB) model H^{TB} ,

$$\hat{H}^{\text{TB}} = - \sum_{\substack{\langle ij \rangle \\ \sigma, m_i, m_j}} \left(t_{ij}^{m_i m_j} \hat{c}_{i m_i \sigma}^\dagger \hat{c}_{j m_j \sigma} + \text{h.c.} \right), \quad (4.3)$$

where every feature of the bandstructure will be described by a certain hopping integral $t_{ij}^{m_i m_j}$.

For Cs_2CuCl_4 , the Hamiltonian (4.3) simplifies to a *single-band* TB model:

$$\hat{H}^{\text{TB}} = - \sum_{\langle ij \rangle \sigma} \left(t_{ij} \hat{c}_{i \sigma}^\dagger \hat{c}_{j \sigma} + \text{h.c.} \right), \quad (4.4)$$

since in this case only one orbital Cu $3d_{xy}$, being well separated from other bands, is involved in electron hopping. A single-band TB model can be in most cases parameterized

TABLE 4.3: The TB model parameters in meV for the Cs_2CuCl_4 Cu $3d_{xy}$ band, calculated from the various Cs_2CuCl_4 crystal structures. The hopping integral index corresponds to the order of the neighbor.

	LDA[nm]	GGA[nm]	GGA[fm]	GGA+U[fm]	exp.
t	-44.9	-35.9	-27.4	-21.7	-11.0
t'	12.5	-13.6	14.0	14.4	6.7
t''	-1.4	-4.5	-6.0	-6.8	-6.3
t_1	6.3	-7.4	-6.3	-3.6	-3.9
t_3	-9.5	8.4	7.5	7.5	8.2
t_7	2.4	2.3	2.6	2.9	2.3
t_8	-2.2	-2.5	-2.7	-3.0	3.6
t_6	-2.4	-2.8	-3.0	-2.7	1.7
t_{14}	0.6	0.9	1.1	1.4	1.6
t_{18}	0.0	0.2	0.3	0.6	-0.1
t_{22}	-4.8	-5.1	-4.5	-4.4	-2.4
μ	-15.3	-17.3	-17.6	-17.8	-11.7

by means of fitting as well as downfolding or projecting onto Wannier functions (Section 2.5.1). Table 4.3 contains the Cs_2CuCl_4 TB model parameters for various crystal structures obtained through fitting; the corresponding TB models' spectra are plotted in red dashed lines on top of the DFT bandstructure in Fig. 4.6. These values have also been confirmed by applying the projecting technique.

In the case of Cs_2CuBr_4 , on the other hand, one needs to consider the full *multi-band* TB model (4.3) because of the hybridization between the Cu $3d_{xy}$ and Cu $3d_{xz}/\text{Cu } 3d_{yz}$ orbitals. Due to additional orbital degrees of freedom, such a model is featured by a considerably larger number of parameters compared to the single-band model. With increasing number of model parameters, parameterization through fitting becomes less reliable and therefore is rarely applied to multi-band models. The Cs_2CuBr_4 TB models calculated via projection onto Wannier functions are presented in Appendix A.3.

In the following discussion of the TB model parameterization results, the reader should be guided by the schematic diagram of interaction pathways for Cs_2CuCl_4 and Cs_2CuBr_4 shown in Fig. 4.8, which displays the 11 most important interactions that we consider in our modeling. We denote the hopping integrals associated with interaction paths J , J' , J'' and J_i by, respectively, t , t' , t'' and t_i ($i = 1, 3, 6, 7, 8, 14, 18, 22$).

The parameterization reveals an unexpected fact: there are more non-negligible inter-layer interactions in Cs_2CuCl_4 and Cs_2CuBr_4 that are associated with electronic degrees of freedom than expected when being guided by their experimentally determined Heisenberg models. In particular, we observe that the interlayer hopping integrals t_1 and t_3 are

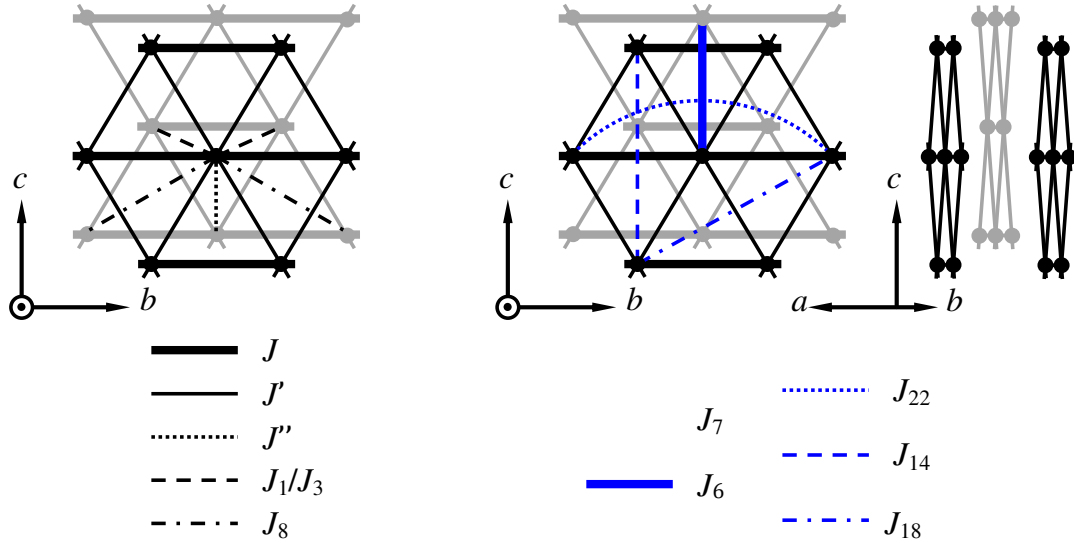


FIGURE 4.8: Cs_2CuCl_4 interaction pathways considered for the TB model parameterization.

in most cases larger than the interlayer hopping t'' and in some cases even comparable with the zig-zag in-plane bond interaction t' .

In either Cs_2CuCl_4 or Cs_2CuBr_4 , the dominant intrachain hopping integral t shows a systematic variation as a function of crystal structure. As can be more easily seen in Table 4.3 for Cs_2CuCl_4 , where each interaction path is described by a single hopping integral between the Cu $3d_{xy}$ orbitals, t strongly decreases for structures relaxed with a higher Cu magnetic moment, *i. e.*, from the GGA[nm] or LDA[nm] relaxed structures to the GGA+U[fm] relaxed structure, and reaches a minimal value in the experimental structure. The zig-zag bond hopping integral t' and the interlayer hopping integral t_3 are rather insensitive to the relaxation functional, but in the experimental crystal structure t' is reduced with respect to the relaxed structures by a factor of roughly two.

We associate the above discussed variation of the hopping integral t with the variation of the CuX_4 tetrahedron geometry and, in particular, with the variation of the angle α in the Cu-X(3)-X(3)-Cu interaction path: increasing α results in the increase of t . Such a relation can be understood when one notices that α is the defining angle for the Cu $3d_{xy}$ -Cl $3p$ /Br $4p$ -Cl $3p$ /Br $4p$ -Cu $3d_{xy}$ hybridization. By considering perturbation theory on the on-site Coulomb repulsion U up to the second order, the effective Cu-Cu superexchange coupling can be obtained from t as⁵ $J = \frac{4t^2}{U}$ (Section 1.2.2). Then, the relation between t and α fulfills the Kanamori-Goodenough rule [Goodenough58,

⁵In the multi-band case of Cs_2CuBr_4 , the exchange coupling J is evaluated as a sum of contributions from hoppings from the fully filled Cu $3d_{xz}$ and Cu $3d_{yz}$ orbitals and the half-filled Cu $3d_{xy}$ orbital to the half-filled Cu $3d_{xy}$ orbital. All three contributions are antiferromagnetic and therefore should depend on $\sin(\alpha/2)$, as the exchange through the Cu $3d_{xy} \rightarrow \text{Cu } 3d_{xy}$ hopping in the single-band case

Kanamori59], stating that J reaches a maximum when the cation-anion-cation angle equals 180° . In the present case of the cation-anion-anion-cation (Cu-X-X-Cu) bridge, the four atoms get aligned along a straight line when α increases.

4.2.2 Heisenberg model

We calculate exchange couplings of the Cs_2CuCl_4 and Cs_2CuBr_4 Heisenberg models employing the total energy difference method, which was introduced in Section 2.5.2. As before, we will compare the results obtained with various crystal structures of Cs_2CuCl_4 and Cs_2CuBr_4 . All calculations presented in this section were performed with the FPLO code, using the AMF GGA+U or, in one case, the AL GGA+U exchange-correlation functional, with the Coulomb interaction $U = 4, 6$ or 8 eV and the Hund's rule coupling $J^{\text{H}} = 1$ eV introduced for the Cu $3d$ shell. Other computational details can be found in Appendix A.4. We consider three values of the Coulomb interaction U because the exact value of U , which also depends on a basis set, is not known but is expected to lie between 4 and 8 eV for Cu $3d$ electrons and is probably close to 6 eV⁶.

The calculated exchange couplings are plotted in Figures 4.9 (a)-(i), as a function of $1/U$. For an easy comparison, we also mark by horizontal dashed lines of corresponding colors the experimentally determined values of J , J' and J'' for Cs_2CuCl_4 [Coldea02] and of J and J' for Cs_2CuBr_4 [Tsuji07]. A common feature of all the Cs_2CuCl_4 and Cs_2CuBr_4 structures is the 2D character of their spin interactions, with J being the leading interaction followed by J' . This result is in agreement with the picture derived from experimental data and thus justifies the 2D Hamiltonian Ansatz used for the data analysis by Coldea *et al.* [Coldea02] and Tsujii *et al.* [Tsuji07].

Let us now examine in more detail the Heisenberg models obtained with the experimental crystal structures of Cs_2CuCl_4 and Cs_2CuBr_4 . Unlike Cs_2CuBr_4 , Cs_2CuCl_4 demonstrates in this case strong disagreement between its DFT model and experimentally determined model, namely, in Cs_2CuCl_4 the DFT derived exchange couplings J and J' are by a factor of more than two smaller than the experimental values, if we take as reference DFT couplings the values in the vicinity of $U = 6$ eV [Fig. 4.9 (b)]. As mentioned in the beginning of this chapter, this disagreement motivated us to study in depth effects of crystal structure relaxation with different exchange-correlation functionals. In Cs_2CuBr_4 , the DFT exchange couplings calculated using the experimental

does. This theoretical expectation for Cs_2CuBr_4 is in accordance with the relations between the hopping integrals from Table A.1 and the angle α from Table 4.2.

⁶This assumption is supported, for instance, by Wien2k calculations [Haas07] of electric field gradients at Cu^{2+} ions in a number of Cu^{2+} oxides and halides performed using the LDA+U functional, with $U^{\text{eff}} = U - J^{\text{H}} = 5$ eV, which successfully reproduce experiment.

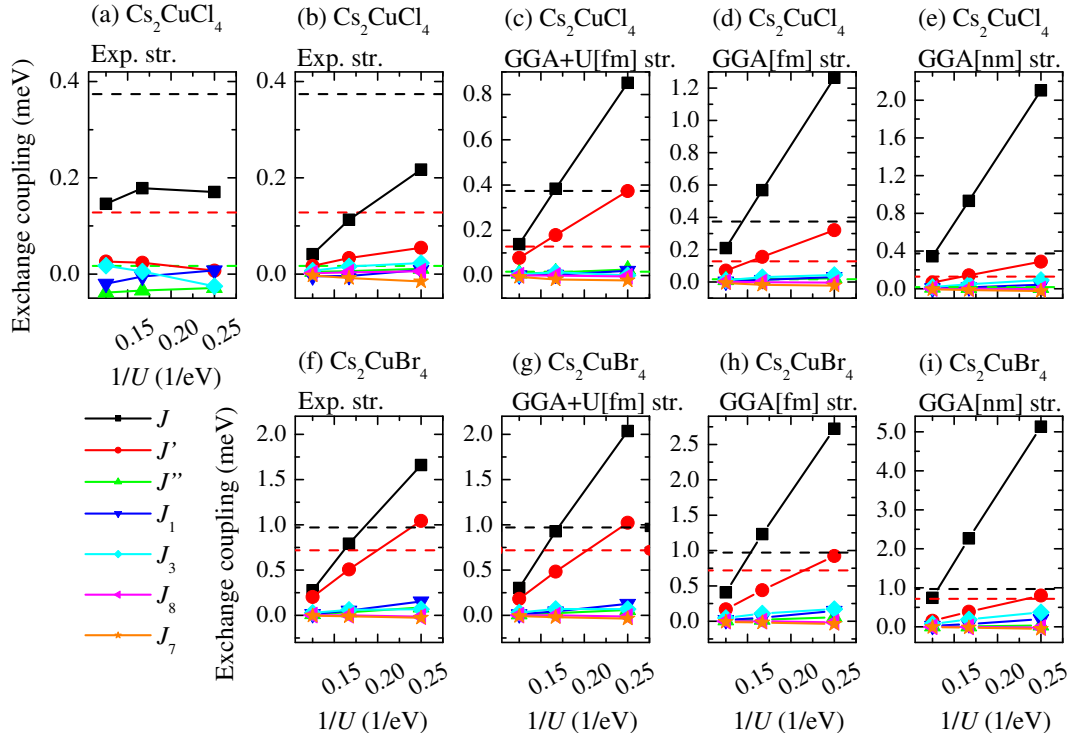


FIGURE 4.9: The spin exchange coupling constants as a function of $1/U$ for (a) the Cs_2CuCl_4 experimental structure calculated with the atomic limit version of the GGA+U, (b) the Cs_2CuCl_4 experimental structure (c) the Cs_2CuCl_4 GGA+U[fm] relaxed structure, (d) the Cs_2CuCl_4 GGA[fm] relaxed structure, (e) the Cs_2CuCl_4 GGA[nm] relaxed structure, (f) the Cs_2CuBr_4 experimental structure, (g) the Cs_2CuBr_4 GGA+U[fm] relaxed structure, (h) the Cs_2CuBr_4 GGA[fm] relaxed structure, (i) the Cs_2CuBr_4 GGA[nm] relaxed structure. When not specified otherwise, the exchange couplings are obtained with the around mean field version of the GGA+U. The three sets of exchange couplings correspond to $U = 8, 6$ and 4 eV. Dashed lines mark the experimentally determined values of J, J' and J'' .

crystal structure are quite close to the experimentally established values in the range of $U \sim 6$ eV [Fig. 4.9 (f)].

Exchange couplings calculated using the relaxed crystal structures of Cs_2CuCl_4 [Fig. 4.9 (c)-(e)] and Cs_2CuBr_4 [Fig. 4.9 (g)-(i)] depend, as expected, on the relaxation potential. In both compounds, the intrachain exchange coupling J grows fast in structures relaxed with a lower Cu magnetic moment (from the GGA+U[fm] structure to the GGA[nm] structure), whereas the zig-zag bond exchange coupling J' is much less sensitive to the variation of structural parameters. Consequently, the ratio J'/J is also strongly dependent on the relaxation functional and decreases from the GGA+U[fm] structure to the GGA[nm] structure. In both Cs_2CuCl_4 and Cs_2CuBr_4 , the exchange couplings calculated with the GGA+U[fm] relaxed structures are in the best agreement with the experimentally determined models. Implications of these results are discussed in the next section.

The strong interplane electronic interactions that are found in the Cs_2CuCl_4 and Cs_2CuBr_4 TB models, like t_3 , (see, for instance, Table 4.3) do not result in equally strong interplane exchange couplings of their spin models. This quite surprising effect of “dimensional reduction” upon reducing electronic model degrees of freedom to just spin degrees of freedom can be caused by the presence of compensating ferromagnetic direct exchange along the interaction pathway J_3 . Calculation of spin exchange couplings with the DFT revealed, however, that, in addition to the interlayer coupling J'' , there are a few other interlayer couplings that are of the same order of magnitude, such as J_3 and J_7 .

To conclude this section, we briefly comment on the performance of the atomic limit version of the GGA+U exchange-correlation functional. The exchange couplings of the experimental Cs_2CuCl_4 structure calculated with the AL double-counting correction differ considerably from those obtained with the AMF double-counting correction [compare panels (b) and (c) of Fig. 4.9]. The AL calculated exchange couplings J and J' do not behave linearly with $1/U$, as expected from the $J = 4t^2/U$ relation, valid for these antiferromagnetic couplings. Therefore, we restricted our discussion to the calculations with the AMF double-counting correction.

4.3 Discussion

4.3.1 Analysis of the results

Let us summarize the main results on the Cs_2CuCl_4 and Cs_2CuBr_4 electronic properties obtained by means of DFT calculations.

- Structural parameters of both Cs_2CuCl_4 and Cs_2CuBr_4 depend on the exchange-correlation functional employed during structural relaxation. The performed structural relaxations consisted in optimizing atomic coordinates within a given space group and with fixed lattice constants.
- Depending on the exchange-correlation functional, DFT calculations can render the Cs_2CuCl_4 and Cs_2CuBr_4 ground state either metallic or insulating, with varying localization of the Cu magnetic moment. Thus, the GGA[nm] and LDA[nm] functionals give a metallic ground state, whereas the GGA(+U)[fm/afm] and LDA(+U)[fm/afm] give an insulating ground state. The Cu magnetic moment is zero within the GGA[nm] and LDA[nm] and non-zero within the GGA(+U)[fm/afm] and LDA(+U)[fm/afm], increasing as the U value increases.

- The strength of the Jahn-Teller distortion of the CuX_4 tetrahedron and the angle α in the superexchange path J which is coupled to it depend on the relaxation functional. This dependence is systematic and can be characterized as “the smaller the Cu magnetic moment during relaxation the stronger the Jahn-Teller distortion”.
- The hopping integral t and the corresponding superexchange coupling J depend systematically on the relaxation potential such that the bigger the Cu magnetic moment during relaxation the smaller the t and J values.
- The Heisenberg models of Cs_2CuCl_4 and Cs_2CuBr_4 calculated with the GGA+U[fm] relaxed structures are in the best agreement with the experimentally established models, while the models calculated with the GGA[nm] relaxed structures are most far away from the experimental models, both in terms of the exchange couplings’ absolute values as well as in terms of their relative strength.
- In Cs_2CuBr_4 , the Heisenberg model calculated with the experimental crystal structure is in quite good agreement with the experimentally established model (and with the model of the GGA+U[fm] structure), while in Cs_2CuCl_4 the model calculated with the experimental crystal structure is featured by unrealistically small exchange couplings.

The stated dependence of the interaction parameters t and J on the relaxation functional is realized through the direct dependence of these parameters on the angle α , which is the Cu- X - X angle in the superexchange path Cu- X - X -Cu, so that the observed behavior is in accordance with the Kanamori-Goodenough rule. The rather unusually strong variation of the exchange interaction J among different crystal structures of Cs_2CuCl_4 and Cs_2CuBr_4 is probably due to its smallness.

More interesting is the mechanism behind the variation of α in the relaxed structures. Here, one should first recognize that this variation is just a consequence of the variation of the Jahn-Teller distortion of the CuX_4 tetrahedron. To explain the latter effect, we argue that by means of electron-lattice interaction the electron system induces strengthening of the Jahn-Teller distortion in order to alleviate the strong instability due to large DOS at the Fermi level. Since the Jahn-Teller distortion is responsible for the electronic levels’ splitting, the instability is removed by redistributing electronic states. We note that this mechanism need not involve variation of bond distances, which is in fact also observed in our results [Fig. 4.3 (a)].

In this scenario, the relaxation functional and the Jahn-Teller distortion are related through the amount of electron system instability (DOS at the Fermi level) obtained within different functionals. The GGA[nm] and LDA[nm] functionals render Cs_2CuCl_4

and Cs_2CuBr_4 metallic [Fig. 5.7], which is in a sharp contrast with the true ground state. This results in the strongest instability and, correspondingly, in the strongest Jahn-Teller distortion needed to remove it. The same kind of reasoning explains the minimal distortion for the GGA+U[fm] and LDA+U[fm] relaxed structures.

The correct insulating state obtained with the GGA(+U)[fm] and LDA(+U)[fm] functionals is already an indication that the realistic crystal structures of Cs_2CuCl_4 and Cs_2CuBr_4 should be searched by employing these approximations. This conclusion is also supported by the results for the Heisenberg model. We saw that only the GGA(+U)[fm] and LDA(+U)[fm] relaxation schemes produce crystal structures whose calculated Heisenberg models are in reasonable agreement with experimentally determined models.

Based on these observations, we can identify the key ingredients that have to be taken into consideration in order to correctly describe the Cs_2CuCl_4 and Cs_2CuBr_4 crystal and electronic structures. The first ingredient is magnetism, which, more specifically, acts through allowing for spin-polarization of the electron system in calculations with spin-dependent functionals. The other ingredient is electronic correlations, which tune the Cu magnetic moment and which are modeled though introducing the on-site Coulomb repulsion between correlated Cu 3d electrons in the LDA+U and GGA+U exchange-correlation functionals.

Finally, the strong deviation of the Cs_2CuCl_4 Heisenberg model calculated with the experimental crystal structure from the experimentally determined model is likely to be a result of the insufficiently accurate determination of the Cs_2CuCl_4 crystal structure by x-ray measurements [Bailleul91]. We dare to propose that the x-ray analysis of the Cs_2CuCl_4 crystal structure might have been affected by the presence of non-stoichiometric hydrogen containing compounds (HCl, H_2O , *etc.*), which was indeed experimentally detected [Bailleul91, Krüger].

4.3.2 Placing the DFT study in the context of our general knowledge about Cs_2CuCl_4 and Cs_2CuBr_4

One of the tasks set in the beginning of our investigations was to derive *ab initio* Heisenberg models for Cs_2CuCl_4 and Cs_2CuBr_4 in order to check the validity of the previously proposed models that were established from experimental data. Due to complications caused, on one hand, by the lack of exact x-ray structural data for Cs_2CuCl_4 and, on the other hand, by approximations involved in any DFT calculation, we came up in the end with several models and used their agreement (or disagreement) with the experimentally

determined Heisenberg models as a correctness criterion to pick up the most accurate DFT model.

Some features of the calculated DFT models, however, turn out to be approximation-independent and can thus be regarded as “truly *ab initio* derived”. These features are the two-dimensionality of spin interactions in both Cs_2CuCl_4 and Cs_2CuBr_4 , the fact that the interactions are stronger in Cs_2CuBr_4 and that Cs_2CuBr_4 is more frustrated, *i. e.*, has a larger J'/J ratio. These findings justify, in particular, the 2D model Ansätze used for analysing experimentally measured Cs_2CuCl_4 and Cs_2CuBr_4 magnetic excitation spectra.

Our DFT calculations also revealed the principal difference in electronic structures of Cs_2CuCl_4 and Cs_2CuBr_4 , namely, that the Cs_2CuBr_4 electronic structure at the Fermi level maps onto a three-band Hubbard model, whereas the Cs_2CuCl_4 electronic structure maps onto a single-band model. The significance of this fact for understanding the different macroscopic properties of the compounds still needs to be explored.

Recently, some more insight has been gained into the rich phase diagrams of Cs_2CuCl_4 and Cs_2CuBr_4 by recognizing the importance of small (perturbative) exchange couplings and the Dzyaloshinsky-Moriya interaction [Starykh10]. In the context of this study, the DFT derived models can serve as a guide to identify the “second-order“ interactions, which are nonetheless strong enough to play a role. Possible candidates could be J_1 , J_3 and J_7 .

Finally, it is important to mention that the thorough investigation of the Cs_2CuCl_4 and Cs_2CuBr_4 electronic properties, which, in particular, allowed us to recognize the important role of magnetism and electronic correlations, prepared a solid ground for future DFT studies of the mixed systems $\text{Cs}_2\text{CuCl}_{4-x}\text{Br}_x$.

Chapter 5

Modulation of pairing interaction in $\text{Bi}_2\text{Sr}_2\text{CaCu}_2\text{O}_{8+\delta}$ by an oxygen dopant

Section 3.2.2 introduces the *state-of-the-art* research problem of nanoscale electronic structure inhomogeneities in the oxygen-doped cuprate superconductor $\text{Bi}_2\text{Sr}_2\text{CaCu}_2\text{O}_{8+\delta}$. Understanding the mechanism through which oxygen dopants enhance in their vicinity superconducting pairing would be an important step in unveiling the still unclear nature of the high- T_c superconductivity. DFT and many-body calculations that model oxygen doping of $\text{Bi}_2\text{Sr}_2\text{CaCu}_2\text{O}_{8+\delta}$ in order to explore microscopic processes associated with doping, such as local crystal and electronic structure modifications, are a subject of the present chapter.

In particular, Section 5.1 presents a comparative DFT study of electronic structures of pure and doped $\text{Bi}_2\text{Sr}_2\text{CaCu}_2\text{O}_8$ crystals by means of mapping the valence Cu $3d_{x^2-y^2}$ band of $\text{Bi}_2\text{Sr}_2\text{CaCu}_2\text{O}_8$ onto a single-band tight-binding model. Such mapping allows us to quantify the dopant-induced local variations of the $\text{Bi}_2\text{Sr}_2\text{CaCu}_2\text{O}_8$ electronic structure in a more accurate way than by electrostatic considerations used in Ref. [Johnston09].

Then, based on the derived single-band tight-binding models of the pure and oxygen-doped $\text{Bi}_2\text{Sr}_2\text{CaCu}_2\text{O}_8$, the spin and charge susceptibilities and the pairing strength are calculated with corresponding Hubbard models in the framework of the random phase approximation (RPA) (Section 5.2). It is shown that the dopant-induced local variations of electronic structure in $\text{Bi}_2\text{Sr}_2\text{CaCu}_2\text{O}_{8+\delta}$ result in an enhancement of superconducting pairing.

We also perform perturbation theory calculations of the local superexchange in the vicinity of a dopant with a three-band Hubbard model. In these calculations, presented in Section 5.3, dopant-induced effects are described on a new accuracy level, when the effective model itself is being improved, which is in contrast to our single-band DFT based calculations of Sections 5.1 and 5.2, where emphasis is put on precise determination of the single-band model parameters.

In future studies, achievements of the three-band model calculations (Section 5.3) and of the DFT assisted determination of the single-band Hubbard model parameters (Sections 5.1 and 5.2) can be combined. The proposed DFT-based approach of evaluating dopant-induced effects on the single-band TB model parameters, which has proven to give accurate results, can be applied to the three-band TB model, which would be the next step in improving model description of oxygen doping in cuprates.

5.1 DFT-assisted TB model parameterization of the oxygen-doped $\text{Bi}_2\text{Sr}_2\text{CaCu}_2\text{O}_8$

5.1.1 Crystal structure of $\text{Bi}_2\text{Sr}_2\text{CaCu}_2\text{O}_{8+\delta}$

Before we proceed, it might be helpful to clarify some notation. Throughout this chapter, we will be using the name $\text{Bi}_2\text{Sr}_2\text{CaCu}_2\text{O}_8$ or “parent compound“ when referring to a pure structure, which we approximate in our calculations by a $I4/mmm$ tetragonal unit cell (Section 3.2.2), and the name $\text{Bi}_2\text{Sr}_2\text{CaCu}_2\text{O}_{8+\delta}$ or ”doped compound” when referring to an oxygen-doped structure.

Oxygen doping of $\text{Bi}_2\text{Sr}_2\text{CaCu}_2\text{O}_{8+\delta}$ is modeled by constructing a supercell that consists of eight $\text{Bi}_2\text{Sr}_2\text{CaCu}_2\text{O}_8$ unit cells with a single interstitial oxygen. The extension to eight unit cells is done in the xy plane such that in terms of a , which is the $\text{Bi}_2\text{Sr}_2\text{CaCu}_2\text{O}_8$ unit cell lattice vector in the xy plane, the xy face of the supercell is given as $(2\sqrt{2}a \times 2\sqrt{2}a)R45^\circ$, where $R45^\circ$ means rotation of the lattice basis by 45° around the z axis [see Fig. 5.1 (a)]. In the supercell, constructed via such an extension, one slab – an atomic layer confined in-between BiO_2 planes – is replaced by 15 \AA of vacuum, whereas the remaining slab is doped by an oxygen atom.

The exact atomic positions in the slab were obtained by He *et al.* [He06], who relaxed the supercell with the Vienna *ab initio* simulation program VASP [Kresse96] within the local density approximation. In particular, He *et al.* established that the dopant enters the interstitial region between the BiO_2 and SrO_2 planes, *i. e.*, close to the surface of the

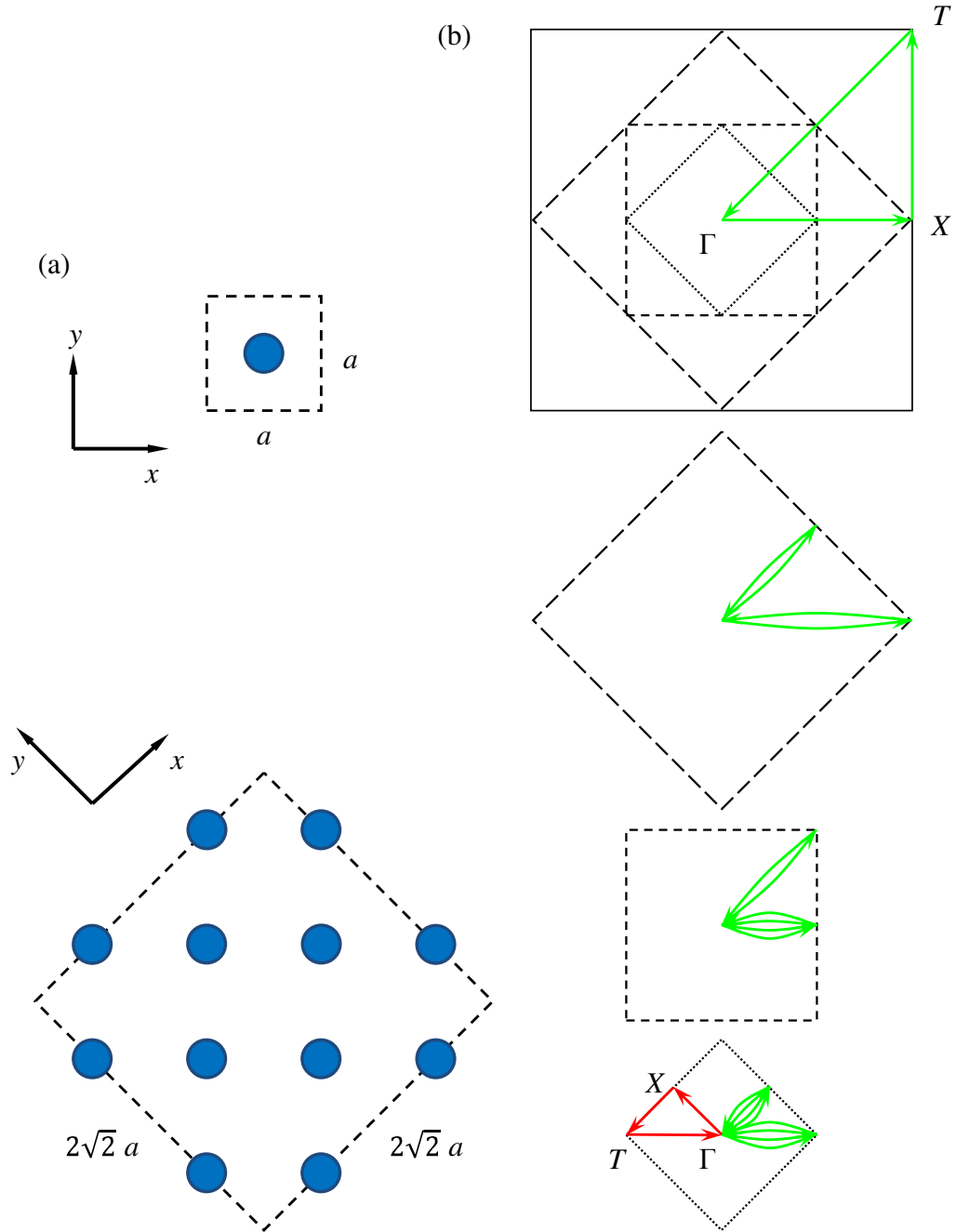


FIGURE 5.1: (a) Schematic xy projection of the $\text{Bi}_2\text{Sr}_2\text{CaCu}_2\text{O}_8$ unit cell (top) and of the $\text{Bi}_2\text{Sr}_2\text{CaCu}_2\text{O}_{8+\delta}$ supercell (bottom) where only Cu atoms (blue circles) are shown. (b) The primitive Brillouin zones of $\text{Bi}_2\text{Sr}_2\text{CaCu}_2\text{O}_8$ (top) and $\text{Bi}_2\text{Sr}_2\text{CaCu}_2\text{O}_{8+\delta}$ (bottom) in the a^*b^* plane. The two intermediate drawings illustrate the transformation from the $\text{Bi}_2\text{Sr}_2\text{CaCu}_2\text{O}_8$ Brillouin zone to the $\text{Bi}_2\text{Sr}_2\text{CaCu}_2\text{O}_{8+\delta}$ Brillouin zone.

slab. The supercell space group is centered monoclinic Cm , with symmetry operations being the identity transformation and a mirror plane reflection m , shown in Fig. 5.5.

The considered doped supercell of $\text{Bi}_2\text{Sr}_2\text{CaCu}_2\text{O}_{8+\delta}$ corresponds to $\delta = 1/8$ of hole concentration per formula unit, which is a bit less than the hole concentration in an

optimally doped $\text{Bi}_2\text{Sr}_2\text{CaCu}_2\text{O}_{8+\delta}$ sample δ_{opt} [Maeda88]:

$$\delta = 0.125 < \delta_{\text{opt}} = 0.16,$$

so that our $\text{Bi}_2\text{Sr}_2\text{CaCu}_2\text{O}_{8+\delta}$ crystal is in the underdoped regime.

In the reciprocal space, the primitive Brillouin zone of the $\text{Bi}_2\text{Sr}_2\text{CaCu}_2\text{O}_{8+\delta}$ supercell is obtained from the primitive $\text{Bi}_2\text{Sr}_2\text{CaCu}_2\text{O}_8$ Brillouin zone by consecutively folding the rectangular corners of the latter towards the center of the Brillouin zone three times [Fig. 5.1 (b)]. The paths between the high-symmetry points $\Gamma = (0, 0, 0)$, $X = (\pi, 0, 0)$ and $T = (\pi, \pi, 0)$ in the $k_z = 0$ plane¹ of the parent and doped compounds are not equivalent. The original $\Gamma \rightarrow X \rightarrow T \rightarrow \Gamma$ path in the pure compound Brillouin zone undergoes transformations upon being folded down to the supercell Brillouin zone as shown in Fig. 5.1 (b) by a green line with arrows. It is obviously not the $\Gamma \rightarrow X \rightarrow T \rightarrow \Gamma$ path in the doped supercell Brillouin zone, shown as a red line with arrows in the bottom panel of Fig. 5.1 (b).

5.1.2 Electronic structures of the parent and oxygen-doped compounds

The electronic bandstructures of $\text{Bi}_2\text{Sr}_2\text{CaCu}_2\text{O}_8$ and $\text{Bi}_2\text{Sr}_2\text{CaCu}_2\text{O}_{8+\delta}$ are calculated in the LAPW basis (Section 2.2.3) and with the GGA exchange-correlation functional. Calculations for the parent compound are carried out with an energy cut-off for the basis set size given by $R_{\text{MT}}K_{\text{max}} = 5.50^2$. The muffin tin radii for the different atoms in the unit cell are chosen as $R_{\text{MT}}(\text{Bi}) = 1.88$ bohr, $R_{\text{MT}}(\text{Sr}) = 2.22$ bohr, $R_{\text{MT}}(\text{Ca}) = 2.17$ bohr, $R_{\text{MT}}(\text{Cu}) = 1.82$ bohr, and $R_{\text{MT}}(\text{O}) = 1.61$ bohr. We consider a mesh of 240 \mathbf{k} -points in the irreducible Brillouin zone that corresponds to the space group $I4/mmm$ of the parent compound unit cell. Both $R_{\text{MT}}K_{\text{max}}$ and the number of \mathbf{k} -points have been tested to be sufficient for rendering an accurate electronic bandstructure. For the supercell calculations, we used the same $R_{\text{MT}}K_{\text{max}}$ and R_{MT} values as for the parent compound and 64 \mathbf{k} -points in the irreducible Brillouin zone of the supercell.

The electronic bandstructures of $\text{Bi}_2\text{Sr}_2\text{CaCu}_2\text{O}_8$ and $\text{Bi}_2\text{Sr}_2\text{CaCu}_2\text{O}_{8+\delta}$ are presented in, respectively, Figures 5.2 (a) and (b) for the $\Gamma \rightarrow X \rightarrow T \rightarrow \Gamma$ \mathbf{k} -paths shown in Fig. 5.1 (b) (the green line for $\text{Bi}_2\text{Sr}_2\text{CaCu}_2\text{O}_8$ and the red line for $\text{Bi}_2\text{Sr}_2\text{CaCu}_2\text{O}_{8+\delta}$). As explained, these paths are not equivalent in the pure and doped compound Brillouin zones, which is the reason why the two bandstructures are seemingly incomparable.

¹The k_z direction is not considered as there is no interaction between CuO_2 planes from adjacent slabs and hence no band dispersion in this direction.

² R_{MT} is the smallest muffin tin radius and K_{max} is the maximal reciprocal lattice vector considered.

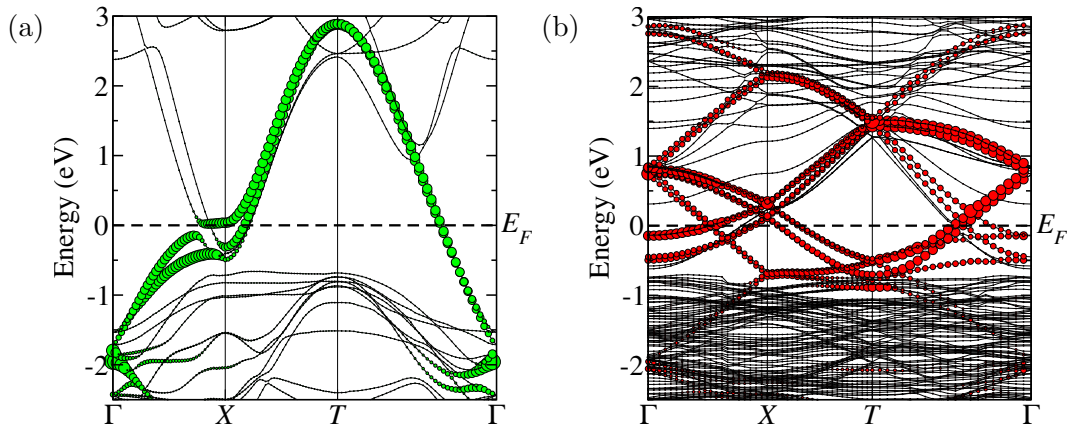


FIGURE 5.2: DFT electronic bandstructure of (a) $\text{Bi}_2\text{Sr}_2\text{CaCu}_2\text{O}_8$ and (b) $\text{Bi}_2\text{Sr}_2\text{CaCu}_2\text{O}_{8+\delta}$. The weight of the Cu $3d_{x^2-y^2}$ character in the eigenvalues is proportional to the circles' size.

We first discuss main features of the simpler bandstructure of $\text{Bi}_2\text{Sr}_2\text{CaCu}_2\text{O}_8$. In Fig. 5.2 (a), the two Cu $3d_{x^2-y^2}$ bands of the parent compound are marked by circles with sizes proportional to the Cu $3d_{x^2-y^2}$ weight. They are rather dispersive, which is a typical feature of the cuprate family (see, for instance, Refs. [Mattheiss87] and [Markiewicz05]). The two bands crossing the Fermi level are the anti-bonding bands in the chemical bonding between the Cu and O atoms in the superconducting layer. The bonding bands lie in the region between -8 eV and -5 eV. At the X point the Cu $3d_{x^2-y^2}$ bands show a strong overlap with the Bi-O bands near the Fermi level, and at the Γ point there is strong hybridization between the Cu $3d_{x^2-y^2}$ and some of the lower-lying O $2p$ and Cu $3d$ bands.

The bandstructure of $\text{Bi}_2\text{Sr}_2\text{CaCu}_2\text{O}_8$ in Fig. 5.2 (a) is plotted in the primitive Brillouin zone, which explains why there are only two Cu $3d_{x^2-y^2}$ bands instead of four, the number of Cu atoms in the conventional $I4/mmm$ unit cell of $\text{Bi}_2\text{Sr}_2\text{CaCu}_2\text{O}_8$. The $\text{Bi}_2\text{Sr}_2\text{CaCu}_2\text{O}_{8+\delta}$ supercell also has a centered lattice, therefore one sees 16 Cu $3d_{x^2-y^2}$ bands in Fig. 5.2 (b), depicting the $\text{Bi}_2\text{Sr}_2\text{CaCu}_2\text{O}_{8+\delta}$ bandstructure in the primitive Brillouin zone, instead of 32, which corresponds to the number of Cu atoms in the conventional unit cell.

Since the $\Gamma \rightarrow X \rightarrow T \rightarrow \Gamma$ paths of the parent and doped compounds are not equivalent, their bandstructures cannot be straightforwardly compared. In order to make such a comparison, one needs to recalculate the electronic structure of the parent compound in the folded Brillouin zone. Once this is done, small but traceable changes in the shape of the Cu $3d_{x^2-y^2}$ bands as a function of oxygen doping become apparent. In the next section, we will carry out quantitative evaluation of these changes in terms of on-site energies and hopping integrals of a single-band tight-binding Hamiltonian.

5.1.3 Parameterization of a single-band tight-binding model

We will parameterize the single-band TB model for Cu $3d_{x^2-y^2}$ orbitals in the parent and oxygen-doped compounds employing the fitting procedure.

As the symmetry of the $\text{Bi}_2\text{Sr}_2\text{CaCu}_2\text{O}_8$ unit cell is high, the number of distinct adjustable model parameters to fit the Cu $3d_{x^2-y^2}$ DFT bands of $\text{Bi}_2\text{Sr}_2\text{CaCu}_2\text{O}_8$ is small. In this case, TB parametrization via fitting is rather straightforward and has been already performed in previous studies [Markiewicz05, Andersen94]. The complexity of the problem is dramatically increased when trying to obtain the TB parameters for the doped supercell bands shown in Fig. 5.2 (b): first, because the number of bands to be mapped increases by a factor of eight, which means that, in order to optimize the TB parameters, a global minimum of a complex mathematical function expressed by a 16×16 matrix needs to be found; second, because the number of distinct hopping integrals is expected to rise considerably as we increase the size of the unit cell and lower its symmetry. Our strategy to overcome these complications is to use the hopping integrals and on-site energies obtained for the parent compound Cu $3d_{x^2-y^2}$ bands as starting values for parameterizing the doped supercell bands.

The desired TB models for $\text{Bi}_2\text{Sr}_2\text{CaCu}_2\text{O}_8$ and $\text{Bi}_2\text{Sr}_2\text{CaCu}_2\text{O}_{8+\delta}$ should reproduce their DFT bandstructures with high accuracy and within the entire energy range of the Cu $3d_{x^2-y^2}$ band dispersion. The need to pursue highly accurate fits is due to the fact that we want to compare bandstructures that are only slightly different. Indeed, the differences between the Cu $3d_{x^2-y^2}$ bands of the parent and doped compounds are small, which is reasonable since we do not expect the interstitial oxygen to have a drastic effect on the orbital overlap of its neighboring Cu atoms.

Parent compound

Another complication that arises already when parameterizing the TB model for the parent compound is the strong hybridization of its Cu $3d_{x^2-y^2}$ orbital with oxygen orbitals, which affects the shape of the Cu $3d_{x^2-y^2}$ bands. For example, as a result of such hybridization, the Cu $3d_{x^2-y^2}$ bands near the Γ point are anomalously flat and show $\varepsilon_k \propto k^4$ behavior [Andersen94].

Our single-band model should, however, also reproduce these hybridization-caused features of the bandstructure. In terms of model equations, this can be achieved through inclusion of high-order harmonics. In terms of physics, the high-order harmonics correspond to hopping integrals between nearest neighbors of higher orders, which play

TABLE 5.1: $\text{TB1}_{\text{undoped}}$ results: Optimized values of the on-site energy μ and hopping integrals $t_{\mathbf{l}}$ between 12 Cu nearest neighbors in eV. The vector $\mathbf{l} = (n, m, z)$ is given by integers n, m ; z can take values of 0 or $z = 0.099$ as $0.099c$ is the distance between two CuO_2 layers.

μ	t_{00z}	t_{100}	t_{10z}	t_{110}	t_{11z}
0.4212	0.0543	-0.5196	0.0056	0.1115	-0.0221
t_{200}	t_{20z}	t_{210}	t_{21z}	t_{220}	t_{22z}
-0.0859	0.0117	-0.0078	-0.0064	0.0025	-0.0103
					t_{300}
					-0.0238

roles of effective parameters without reflecting real interactions, which of course are moderately short-ranged.

When considering the *nearest Cu neighbors*, we find that, in order to *accurately* reproduce the DFT Cu $3d_{x^2-y^2}$ bands of the parent compound [Fig. 5.2 (a)], 12 Cu-Cu neighbors have to be included in the model TB Hamiltonian. They are listed in Table 5.1. One observes that hoppings between high-order neighbors, such as t_{20z} , t_{210} *etc.*, are considerably smaller than the second, t_{100} , and the fourth, t_{110} , nearest-neighbor hoppings. As these high-order hoppings are, as argued, effective parameters, *alternative* single-band models for $\text{Bi}_2\text{Sr}_2\text{CaCu}_2\text{O}_8$ can exist, corresponding to a different choice of effective parameters, which need not necessarily be the nearest neighbors and which can reproduce the DFT bandstructure equally well.

We therefore discuss two possible sets of single-band TB Hamiltonian parameters for the parent compound to give a sense of how robust the TB models can be.

- $\text{TB1}_{\text{undoped}}$

The first parameter set is obtained for a TB model considering 12 nearest neighbors, which has already been introduced (Table 5.1). This model, denoted as $\text{TB1}_{\text{undoped}}$, contains six effective interlayer hoppings.

- $\text{TB2}_{\text{undoped}}$

The other TB model, denoted as $\text{TB2}_{\text{undoped}}$, considers 13 interaction pathways between Cu atoms, among which there are four effective interlayer hoppings. The 13 hopping integrals as well as the on-site energy of the $\text{TB2}_{\text{undoped}}$ model are listed in Table 5.2.

In physical terms, the $\text{TB2}_{\text{undoped}}$ model has some advantages over the $\text{TB1}_{\text{undoped}}$ model. Thus, it includes only four hopping integrals between the two CuO_2 layers – t_{00z} , t_{11z} , t_{21z} and t_{33z} – whose relevance can be justified either by the close proximity of the two Cu atoms (t_{00z}) or by the presence of a Ca atom along the Cu-Cu connection mediating electron hopping (t_{11z} , t_{21z} and t_{33z}). In the $\text{TB1}_{\text{undoped}}$

TABLE 5.2: TB2_{undoped} results: Optimized values of the on-site energy μ and hopping integrals t_1 in eV for the parent compound as well as for the homogeneous Hamiltonian TB2_{hom. doped} of the doped compound. The meaning of the three subindices is the same as in Table 5.1.

	μ	t_{100}	t_{110}	t_{200}	t_{00z}
TB2 _{undoped}	0.4464	-0.5174	0.1085	-0.0805	0.0818
TB2 _{hom. doped}	0.4900	-0.5150	0.1158	-0.0800	0.0700

	t_{11z}	t_{210}	t_{300}	t_{400}	t_{21z}
TB2 _{undoped}	-0.0264	-0.0073	-0.0182	-0.0122	-0.0044
TB2 _{hom. doped}	-0.0229	-0.0075	-0.0177	-0.0046	-0.0062

	t_{220}	t_{330}	t_{500}	t_{33z}
TB2 _{undoped}	0.0068	-0.0052	-0.0049	-0.0047
TB2 _{hom. doped}	0.0045	-0.0015	-0.0012	-0.0003

model, on the other hand, the mechanism of some of its six interlayer interactions is not as clear. Furthermore, one would rather expect the contribution of interacting far Cu neighbors within a CuO_2 layer to be more important as considered in the TB2_{undoped} model.

Parameters t_{100} and t_{110} of both models have quite close values, which are also in agreement with the results of previous DFT calculations [Markiewicz05] and with the analysis of photoemission measurements of the $\text{Bi}_2\text{Sr}_2\text{CaCu}_2\text{O}_8$ electronic structure [Radtk94].

Figures 5.3 and 5.4 compare energy spectra (lines) of, respectively, the TB1_{undoped} and TB2_{undoped} Hamiltonians against the DFT calculated Cu $d_{x^2-y^2}$ bands (dots). Panels (a) of both figures display the model spectra and the DFT calculated Cu $d_{x^2-y^2}$ bands of the parent compound in the full Brillouin zone, *i. e.*, in the primitive Brillouin zone of $\text{Bi}_2\text{Sr}_2\text{CaCu}_2\text{O}_8$ [upper panel of Fig. 5.1 (b)]. Apparently, the quality of both TB1_{undoped} and TB2_{undoped} fits is very good, the TB2_{undoped} fit matching the DFT bandstructure slightly better in the vicinity of the Γ point. In panels (b) of Figures 5.3 and 5.4, the model spectra are replotted in the folded Brillouin zone in order to be compared with the DFT Cu $3d_{x^2-y^2}$ bands of the doped supercell. The small differences between the doped supercell DFT bands and the TB spectra of the parent compound are due to the presence of the interstitial oxygen, which displaces neighboring Cu atoms and thus modifies their on-site energies as well as overlap integrals between their Cu $d_{x^2-y^2}$ orbitals.

In the next section, we will discuss the derivation of the TB Hamiltonian for the doped $\text{Bi}_2\text{Sr}_2\text{CaCu}_2\text{O}_{8+\delta}$ supercell, obtained when either the parameter set of the TB1_{undoped} model (Table 5.1) or that of the TB2_{undoped} model (Table 5.2) is used as initial values for mapping the supercell DFT bands.

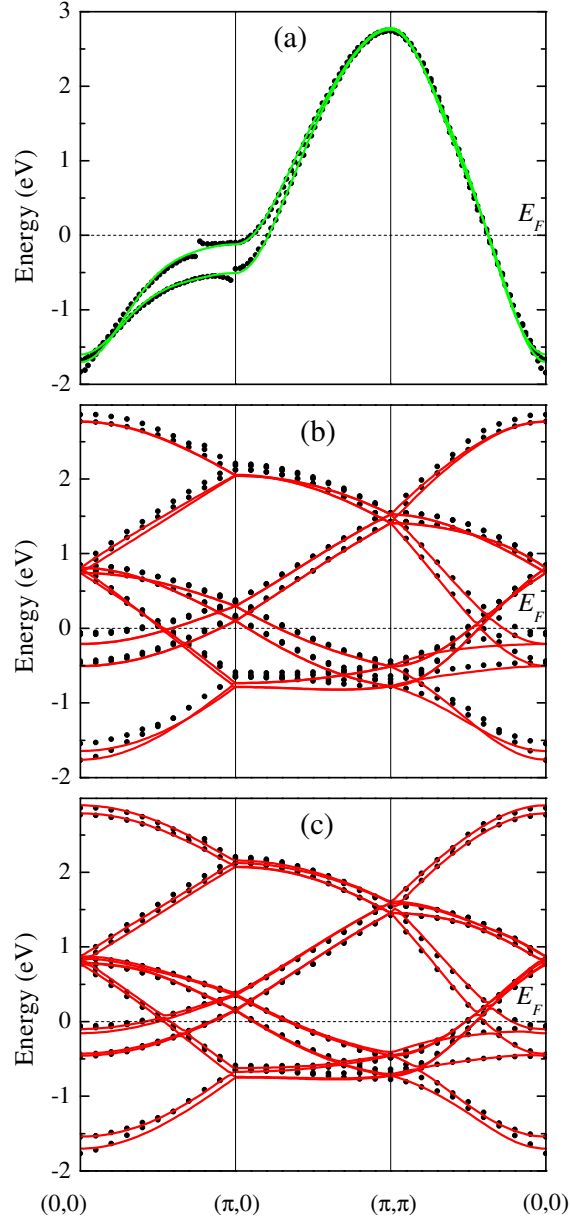


FIGURE 5.3: Plot of the DFT calculated Cu $3d_{x^2-y^2}$ bands (dots) and the TB1 Hamiltonian spectrum (lines) for $\text{Bi}_2\text{Sr}_2\text{CaCu}_2\text{O}_8$ and $\text{Bi}_2\text{Sr}_2\text{CaCu}_2\text{O}_{8+\delta}$: (a) comparison of the $\text{Bi}_2\text{Sr}_2\text{CaCu}_2\text{O}_8$ electronic structure to the $\text{TB1}_{\text{undoped}}$ model; (b) comparison of the $\text{Bi}_2\text{Sr}_2\text{CaCu}_2\text{O}_{8+\delta}$ electronic structure to the $\text{TB1}_{\text{undoped}}$ model plotted in the folded Brillouin zone; (c) comparison of the $\text{Bi}_2\text{Sr}_2\text{CaCu}_2\text{O}_{8+\delta}$ electronic structure to the $\text{TB1}_{\text{loc. doped}}$ model (see Fig. 5.5). High symmetry points are given by (k_x, k_y) only, $k_z = 0$; thus $(0, 0) = \Gamma$, $(\pi, 0) = X$, $(\pi, \pi) = T$.

Oxygen-doped supercell

In order to parameterize interactions between Cu $d_{x^2-y^2}$ orbitals for the doped compound, one has to construct a 16×16 Hamiltonian matrix. Since the interstitial oxygen introduces inhomogeneity that breaks the symmetry, the number of distinct model parameters for the supercell is not defined as simply the number of parameters of the parent

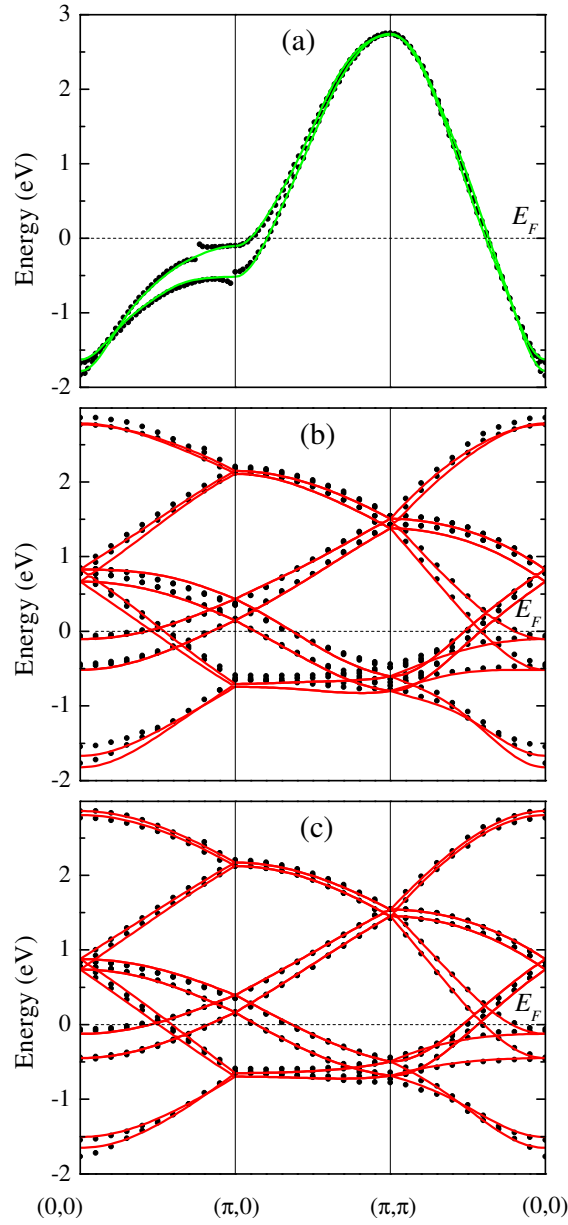


FIGURE 5.4: Plot of DFT calculated Cu $3d_{x^2-y^2}$ bands (dots) and the TB2 Hamiltonian spectrum (line) for $\text{Bi}_2\text{Sr}_2\text{CaCu}_2\text{O}_8$ and $\text{Bi}_2\text{Sr}_2\text{CaCu}_2\text{O}_{8+\delta}$: (a) comparison of the $\text{Bi}_2\text{Sr}_2\text{CaCu}_2\text{O}_8$ electronic structure to the $\text{TB2}_{\text{undoped}}$ model; (b) comparison of the $\text{Bi}_2\text{Sr}_2\text{CaCu}_2\text{O}_{8+\delta}$ electronic structure to the $\text{TB2}_{\text{undoped}}$ model plotted in the folded Brillouin zone; (c) comparison of the $\text{Bi}_2\text{Sr}_2\text{CaCu}_2\text{O}_{8+\delta}$ electronic structure to the homogeneous $\text{TB2}_{\text{hom. doped}}$ model (Table 5.2, second row).

compound unit cell – which is 12 and 13 for the $\text{TB1}_{\text{undoped}}$ and $\text{TB2}_{\text{undoped}}$ models, respectively, plus the on-site energy – but increases considerably. The total number of independent hopping integrals in the supercell TB Hamiltonian would be as big as 238 if one chooses to perform the derivation starting from the $\text{TB1}_{\text{undoped}}$ Ansatz. Technically, it is impossible to find a unique and unambiguous parameter set by performing optimization of such a huge number of parameters, especially since our aim is to capture

the slight differences between the bandstructures of the parent and doped compounds.

One way to proceed would be to approximate hopping integrals that become distinct in the supercell by their average values. In this “averaged” *homogeneous* TB model for the supercell, there would be as many parameters as in the corresponding model for the parent compound, and their optimization would be simple; an example is given in Table 5.2 (TB2_{hom. doped} row). With such an approach, however, the most interesting physics concerning *local* effects due to the dopant is left out.

As discussed in detail in Section 3.2.2, the exact knowledge of how the Cu on-site energies and most relevant Cu-Cu hopping integrals t_{100} and t_{110} are modified near the dopant is very important for understanding the dopant-induced effects on the local spin superexchange coupling, which is related to the size of the local superconducting gap in cuprates. Therefore, in order to be able to study local variations in the model parameters, we propose the following approximate treatment of the problem. We assume that the on-site energies and hopping integrals most affected by the dopant are those that are nearest to the dopant and concentrate on the largest TB model parameters, such as μ , t_{100} and t_{110} . Then, the supercell TB Hamiltonian is optimized by adjusting the selected parameters, while preserving initial values for the rest of parameters.

This approach is applied to derive a supercell TB model using the TB1_{undoped} model as an Ansatz. As adjustable parameters, we select eight hopping integrals: three hopping integrals of the t_{100} type (solid lines in Fig. 5.5), two of the t_{110} type (dashed lines) and three of the t_{200} type (dash-dotted lines). The selected interactions are between the Cu atom that experiences the largest displacement due to the interstitial oxygen and its neighbors. We also allow for different on-site energies μ for $3d_{x^2-y^2}$ orbitals of the eight Cu atoms in the CuO_2 layer closest to the dopant. Making use of the crystal symmetry, the number of μ parameters is reduced to six. We then assign a unique μ value to the on-site energies of the other eight Cu atoms since we expect that they are less affected by the dopant. The seven on-site energies together with the selected eight hopping integrals are varied during Hamiltonian optimization. The optimized values of the hopping integrals are given in Fig. 5.5 in eV and the on-site energies are listed in the Figure caption. We denote this model TB1_{loc. doped}. From Fig. 5.3 (c), which compares the DFT Cu $d_{x^2-y^2}$ bands of $\text{Bi}_2\text{Sr}_2\text{CaCu}_2\text{O}_{8+\delta}$ and the spectrum of the TB1_{loc. doped} model, one can appreciate the good quality of the fit.

The resulting variation of the selected TB model parameters in the TB1_{loc. doped} model is in agreement with the expected dopant-induced effects, according to electrostatic calculations of Ref. [Johnston09] as well as general physical considerations. Thus, one finds that the on-site energy μ of the most displaced Cu atom (marked with an arrow in Fig. 5.5), whose value is 0.5757 eV, deviates the most from the μ value of the TB1_{undoped}

model 0.4212 eV. On the other hand, the Cu atoms of the second – with respect to the dopant – CuO_2 layer are hardly affected, with their common μ being equal 0.4445 eV. Variation of the selected hopping integrals in the $\text{TB1}_{\text{loc. doped}}$ model also follows a physically reasonable trend. For example, t_{100} increases when the two Cu atoms get closer and slightly decreases when they are pushed apart by the interstitial oxygen. The decrease is even stronger when the Cu atoms shift with respect to each other parallel to the mirror plane, which appreciably reduces the orbital overlap.

We also considered the same 15 parameters (seven μ 's and eight t 's) to map the DFT Cu $3d_{x^2-y^2}$ bands with a supercell TB Hamiltonian based on the $\text{TB2}_{\text{undoped}}$ for the parent compound, Table 5.2. While in this case a mapping to the DFT bands is almost as good as the one given by the previous model, the resulting model parameters assume seemingly chaotic values not consistent with their expected behavior. One faces similar inconsistencies also when other trial sets of adjustable parameters are used. The failure of the $\text{TB2}_{\text{undoped}}$ model (Table 5.2) in describing the dopant-induced changes in the bandstructure of $\text{Bi}_2\text{Sr}_2\text{CaCu}_2\text{O}_{8+\delta}$ indicates that the results provided by the approach based on optimizing certain selected model parameters depend very strongly on the choice of effective far neighbor interactions that are not optimized.

To conclude this section, we give some comments on the homogeneous TB model for the doped compound $\text{TB2}_{\text{hom. doped}}$, which is derived using the $\text{TB2}_{\text{undoped}}$ $\text{Bi}_2\text{Sr}_2\text{CaCu}_2\text{O}_8$ model. The $\text{TB2}_{\text{hom. doped}}$ model parameters are listed in Table 5.2, while Fig. 5.4 (c) demonstrates that this model can describe the $\text{Bi}_2\text{Sr}_2\text{CaCu}_2\text{O}_{8+\delta}$ bandstructure as good as the above discussed $\text{TB1}_{\text{loc. doped}}$ model. Even though the homogeneous model does not reflect the local dopant-induced effects, it can still be useful as it provides information on how the model parameters change on average. For instance, it is interesting to observe that the average ratio t_{110}/t_{100} increases in the doped supercell compared to that in the parent compound (from 0.2097 to 0.2249); this might suggest a possible increase of the superconducting transition temperature upon doping, in analogy with the observation within the cuprate family, that the materials characterized by a larger t_{110}/t_{100} ratio have higher transition temperatures [Pavarini01]. Unlike the situation with the mapping approach discussed previously, which aimed at capturing local physics, the parameters of the homogeneous Hamiltonian demonstrate the same behavior upon doping regardless of the parent compound TB model ($\text{TB1}_{\text{undoped}}$ or $\text{TB2}_{\text{undoped}}$) chosen as a starting point for mapping the doped supercell electronic structure.

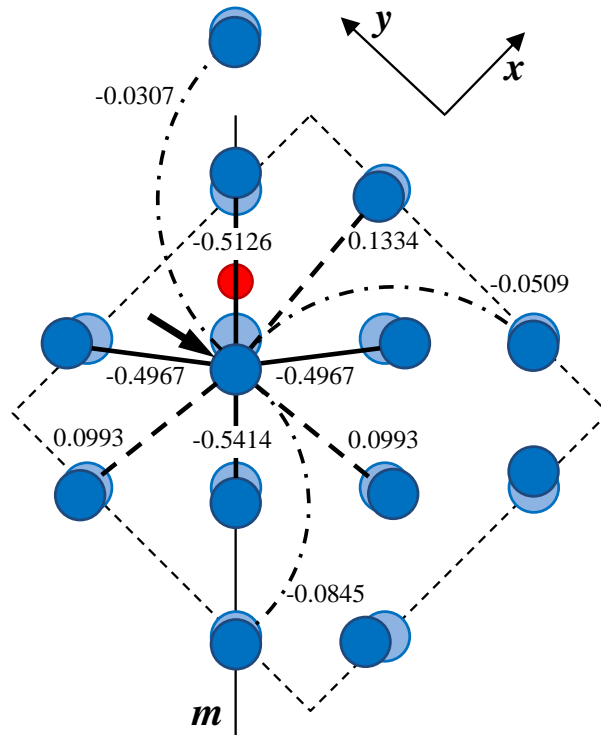


FIGURE 5.5: The schematic lattice of dopant-displaced Cu atoms in the oxygen-doped supercell of $\text{Bi}_2\text{Sr}_2\text{CaCu}_2\text{O}_{8+\delta}$. The smallest circle represents the interstitial oxygen atom, and the larger circles stand for Cu atoms. Darker color is used for Cu atoms in the CuO_2 layer closest to the interstitial oxygen. The Cu-Cu bonds that correspond to the hopping integrals of the t_{100} type are represented by solid lines, the hopping integrals of the t_{110} type by dashed lines, and the hopping integrals of the t_{200} type by dash-dotted lines. The numbers over the bonds stand for the optimized values of corresponding hopping integrals of the doped supercell TB model based upon the $\text{TB1}_{\text{undoped}}$ model of the parent compound (see text). The optimized value of the on-site energy of this model for the Cu in the next-nearest CuO_2 layer (the light Cu atom symbols) is $\mu = 0.4445$ eV. The six optimized on-site energy values for Cu in the nearest CuO_2 layer (the dark Cu atom symbols) are $\mu = 0.5757$ eV, 0.5057 eV, 0.5341 eV, 0.5151 eV, 0.4930 eV, and 0.5186 eV. $\mu = 0.5757$ eV corresponds to the Cu atom which is displaced most by the dopant and is marked with an arrow. m labels the mirror plane. The size and direction of displacements are qualitatively reflected in the figure.

5.2 RPA susceptibility and spin fluctuation pairing

5.2.1 Spin susceptibility

In this section, we calculate the magnetic spin susceptibility for the pure and doped compounds with the TB models obtained previously, namely,

- (i) the $\text{TB1}_{\text{undoped}}$ model for $\text{Bi}_2\text{Sr}_2\text{CaCu}_2\text{O}_8$ (Table 5.1);
- (ii) the $\text{TB2}_{\text{undoped}}$ model for $\text{Bi}_2\text{Sr}_2\text{CaCu}_2\text{O}_8$ (Table 5.2, first row);

- (iii) the inhomogeneous $\text{TB1}_{\text{loc. doped}}$ model for $\text{Bi}_2\text{Sr}_2\text{CaCu}_2\text{O}_{8+\delta}$ (Fig. 5.5);
- (iv) the homogeneous $\text{TB2}_{\text{hom. doped}}$ model for $\text{Bi}_2\text{Sr}_2\text{CaCu}_2\text{O}_{8+\delta}$ (Table 5.2, second row).

We remind that the TB models describe non-interacting electron systems; Coulomb interaction between electrons will be considered on an RPA level in the next subsection.

Calculations of the spin susceptibility are carried out within the Matsubara Green's functions formalism (Ref. [Mahan81], Section 1.3.1), making use of non-interacting Green's functions. The spin susceptibility corresponds to a retarded two-particle Green's function which is obtained from the Matsubara Green's function (1.22) by performing analytical continuation to the real frequency axis. In a general formulation, the spin susceptibility is a function of four orbital indices, $(\chi_s)_{st}^{pq}$, which, in the considered case of a single orbital but multiple atoms in a unit cell, refer to the orbitals on different atoms. For the non-interacting case, the spin susceptibility $(\chi_s)_{st}^{pq}$ is equivalent to the charge susceptibility $(\chi_c)_{st}^{pq}$, $(\chi_s)_{st}^{pq} = (\chi_c)_{st}^{pq} \equiv \chi_{st}^{pq}$, and is given by [Graser09]:

$$\chi_{st}^{pq}(\mathbf{q}, \omega) = -\frac{1}{NN_{\mathbf{k}}} \sum_{\mathbf{k}, \mu\nu} [f(\varepsilon_\nu(\mathbf{k} + \mathbf{q})) - f(\varepsilon_\mu(\mathbf{k}))] \frac{a_\mu^s(\mathbf{k})a_\mu^{p*}(\mathbf{k})a_\nu^q(\mathbf{k} + \mathbf{q})a_\nu^{t*}(\mathbf{k} + \mathbf{q})}{\omega + \varepsilon_\nu(\mathbf{k} + \mathbf{q}) - \varepsilon_\mu(\mathbf{k}) + i0^+}. \quad (5.1)$$

In this expression, indices s, p, q and t refer to the N Cu atoms in the unit cell and run from 1 to N while indices μ and ν distinguish the N eigenvalues $\varepsilon_\nu(\mathbf{k})$ of the diagonalized TB Hamiltonian. The matrix elements $a_\mu^s(\mathbf{k})$ are the components of the eigenvectors of the TB Hamiltonian³. The integration over the Brillouin zone has been replaced by a sum over a sufficiently large number $N_{\mathbf{k}}$ of \mathbf{k} -points. $f(\varepsilon)$ is the Fermi-Dirac distribution function. In the following, we will focus on the static non-interacting spin susceptibility $\chi_S(\mathbf{q})$,

$$\chi_S(\mathbf{q}) = \frac{1}{2} \sum_{sp} \chi_{ss}^{pp}(\mathbf{q}, \omega = 0), \quad (5.2)$$

and examine its behavior in the four cases of interest along the main symmetry directions in the Brillouin zone.

The static spin susceptibilities $\chi_S(\mathbf{q})$ of the parent compound calculated for temperature $k_B T = 0.01$ eV with the $\text{TB1}_{\text{undoped}}$ model of Table 5.1 (bold black line) and with the $\text{TB2}_{\text{undoped}}$ model of Table 5.2 (bold dashed line) are plotted in Fig. 5.6 (a). The two susceptibilities show similar features with double peaks along the $(0, 0, 0) - (\pi, 0, 0)$ and $(\pi, \pi, 0) - (0, 0, 0)$ directions and a broad plateau at $(\pi, \pi, 0)$. These similarities can be understood in terms of the fact that most important parameters in the two TB models

³The matrix elements $a_\mu^s(\mathbf{k})$ are also equivalent to projector components, which follows from their definition in Section 2.5.1.

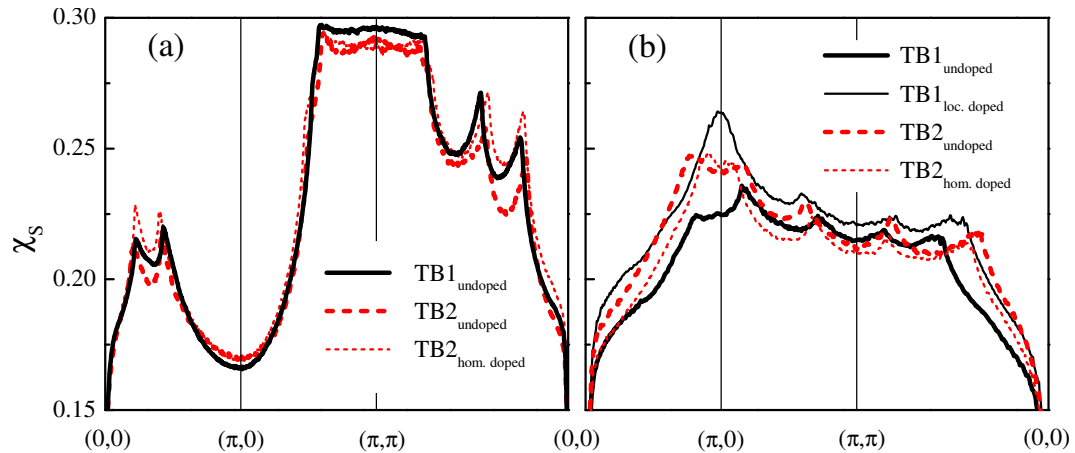


FIGURE 5.6: The static spin susceptibility of (a) the two parent compound TB models $TB1_{\text{undoped}}$ and $TB2_{\text{undoped}}$ and the homogeneous doped supercell model $TB2_{\text{hom. doped}}$, plotted in the full Brillouin zone, and (b) the two parent compound TB models $TB1_{\text{undoped}}$ and $TB2_{\text{undoped}}$ and the inhomogeneous $TB1_{\text{loc. doped}}$ and homogeneous $TB2_{\text{hom. doped}}$ doped supercell models, plotted in the folded Brillouin zone.

(t_{100} , t_{110} etc.) have close values. In this respect, it is not surprising that the spin susceptibility calculated with the averaged TB parameters of the homogeneous Hamiltonian $TB2_{\text{hom. doped}}$ for $\text{Bi}_2\text{Sr}_2\text{CaCu}_2\text{O}_{8+\delta}$ [thin dashed line in Fig. 5.6 (a)] qualitatively reproduces the same behavior as the TB models for the parent compound.

We next calculate the spin susceptibility with the *inhomogeneous* TB Hamiltonian $TB1_{\text{loc. doped}}$ for the doped $\text{Bi}_2\text{Sr}_2\text{CaCu}_2\text{O}_{8+\delta}$ supercell. Of course, in this case the spin susceptibility must be calculated with the full supercell (16×16) Hamiltonian matrix and is accordingly defined in the folded Brillouin zone. Fig. 5.6 (b) shows the spin susceptibility calculated with the inhomogeneous $TB1_{\text{loc. doped}}$ model (thin black line) and, for comparison, the two parent compound susceptibilities replotted in the folded Brillouin zone [as in Fig. 5.6 (a), bold solid and bold dashed lines]. Within the inhomogeneous model, a pronounced peak in the spin susceptibility evolves at $(\pi, 0, 0)$ upon doping whereas in both parent compound susceptibilities this region is featured by a shallow minimum in between two asymmetrical peaks located at some distance from $(\pi, 0, 0)$. A peak in the spin susceptibility of a non-interacting system can transform into a divergence indicating magnetic instabilities and possible ordering, when the interparticle interactions are switched on. $(\pi, 0, 0)$ corresponds to a commensurate antiferromagnetic striped order with period $2\sqrt{2}a$, with stripes along the (110) direction of the parent compound unit cell.

5.2.2 Superconducting gap function

We consider now the models $\text{TB1}_{\text{undoped}}$ and $\text{TB1}_{\text{loc. doped}}$ in order to analyze the superconducting properties of $\text{Bi}_2\text{Sr}_2\text{CaCu}_2\text{O}_8$ and $\text{Bi}_2\text{Sr}_2\text{CaCu}_2\text{O}_{8+\delta}$, respectively. We calculate the pairing vertex by assuming that superconductivity in the high- T_c cuprates is driven by the exchange of spin and charge fluctuations [Bickers89]. The many-body effects of the Coulomb interaction are treated within the RPA (Section 1.3.1).

In order to calculate the pairing vertex, the RPA charge and spin susceptibilities, $\chi_c^{\text{RPA}}(\mathbf{q}, \omega)$ and $\chi_s^{\text{RPA}}(\mathbf{q}, \omega)$, are required. They can be obtained from the non-interacting susceptibility $\chi(\mathbf{q}, \omega)$ in the form of Dyson-type equations as

$$(\chi_c^{\text{RPA}})_{st}^{pq} = \chi_{st}^{pq} - \sum_{uvwz} (\chi_c^{\text{RPA}})_{uv}^{pq} (U^c)_{wz} \chi_{st}^{wz} \quad (5.3)$$

and

$$(\chi_s^{\text{RPA}})_{st}^{pq} = \chi_{st}^{pq} + \sum_{uvwz} (\chi_s^{\text{RPA}})_{uv}^{pq} (U^c)_{wz} \chi_{st}^{wz}. \quad (5.4)$$

For a single-band model, only the diagonal U^c and U^s matrices' components are non-zero:

$$(U^c)_{ii}^{ii} = U, \quad (U^s)_{ii}^{ii} = U, \quad (5.5)$$

where U is the strength of the on-site intraband Coulomb repulsion between electrons. The singlet pairing vertex is then given by

$$\begin{aligned} \Gamma_{st}^{pq}(\mathbf{k}, \mathbf{k}', \omega) = & \left[\frac{3}{2} U^s \chi_s^{\text{RPA}}(\mathbf{k} - \mathbf{k}', \omega) U^s + \frac{1}{2} U^s \right. \\ & \left. - \frac{1}{2} U^c \chi_c^{\text{RPA}}(\mathbf{k} - \mathbf{k}', \omega) U^c + \frac{1}{2} U^c \right]_{ps}^{tq}. \end{aligned} \quad (5.6)$$

The scattering of a Cooper pair from the state $(\mathbf{k}, -\mathbf{k})$ to the state $(\mathbf{k}', -\mathbf{k}')$ on the Fermi surface is determined by the projected interaction vertex

$$\begin{aligned} \Gamma(\mathbf{k}, \mathbf{k}', \omega) = & \sum_{stpq} a_\nu^t(-\mathbf{k}) a_\nu^s(\mathbf{k}) \Gamma_{st}^{pq}(\mathbf{k}, \mathbf{k}', \omega) \\ & \times a_{\nu'}^{p,*}(\mathbf{k}') a_{\nu'}^{q,*}(-\mathbf{k}'), \end{aligned} \quad (5.7)$$

where indices ν and ν' refer to the eigenvectors of the TB Hamiltonian with the corresponding energy eigenvalues close to the Fermi level. As the strength of the pairing interaction is defined by a frequency integral of the imaginary part of $\Gamma(\mathbf{k}, \mathbf{k}', \omega)$ weighted by ω^{-1} , it is sufficient to consider the real part of $\Gamma(\mathbf{k}, \mathbf{k}', \omega = 0)$ according to

the Kramers-Kronig relation:

$$\int_0^\infty d\omega \frac{\text{Im}[\Gamma(\mathbf{k}, \mathbf{k}', \omega)]}{\pi\omega} = \text{Re}[\Gamma(\mathbf{k}, \mathbf{k}', \omega = 0)]. \quad (5.8)$$

If the superconducting gap is decomposed into an amplitude Δ and a normalized gap function $g(\mathbf{k})$, the latter can be evaluated from the following eigenvalue equation

$$-\oint \frac{d\mathbf{k}'_{\parallel}}{2\pi} \frac{1}{2\pi v_F(\mathbf{k}')} \Gamma^{\text{symm}}(\mathbf{k}, \mathbf{k}') g(\mathbf{k}') = \lambda g(\mathbf{k}). \quad (5.9)$$

Here,

$$\Gamma^{\text{symm}}(\mathbf{k}, \mathbf{k}') = \frac{1}{2} \text{Re} [\Gamma(\mathbf{k}, \mathbf{k}', 0) + \Gamma(\mathbf{k}, -\mathbf{k}', 0)] \quad (5.10)$$

is the symmetric part of the full interaction and

$$v_F(\mathbf{k}) = |\nabla_{\mathbf{k}} E_{\nu}(\mathbf{k})| \quad (5.11)$$

is the Fermi velocity at point \mathbf{k} on the Fermi surface. The largest eigenvalue λ of Eq. (5.9) determines the superconducting transition temperature and its corresponding eigenfunction $g(\mathbf{k})$ has the symmetry of the gap.

We have solved the eigenvalue problem (5.9) for the pure compound model TB1_{undoped} and doped compound model TB1_{loc. doped} in the folded Brillouin zone of the supercell. The folded Brillouin zone has been considered in both cases in order to ensure that the eigenvalue equations are constructed under the same conditions, which is important when the resulting pairing strengths are compared. The calculations have been performed for the temperature $k_B T = 0.01$ eV and we considered Coulomb repulsion U values that range from 1.00 eV to 1.66 eV. Note that these values represent renormalized values of the Hubbard U appropriate for RPA treatments and are smaller than bare U 's [Bulut93].

We find that the doped Bi₂Sr₂CaCu₂O_{8+ δ} model TB1_{loc. doped} is characterized by a larger value of the pairing strength λ compared to that of the Bi₂Sr₂CaCu₂O₈ model TB1_{undoped}. The pairing strengths for the two models are presented in Fig. 5.7 (a) as a function of U . Below $U \sim 1.5$ eV the two λ values are almost equal, but at larger U values the pairing strength for the doped compound model grows faster and diverges at $U = 1.65$ eV.

Fig. 5.7 (b) displays the gap functions $g(\mathbf{k})$ of the pure and doped compound models, corresponding to the leading eigenproblem solutions λ of Fig. 5.7 (a) at $U = 1.64$ eV. The gap function $g(\mathbf{k})$, as it is obtained from Eq. (5.9), is defined on the mesh of \mathbf{k} -points at the Fermi surface of the folded Brillouin zone. In Fig. 5.7 (b), the \mathbf{k} -point

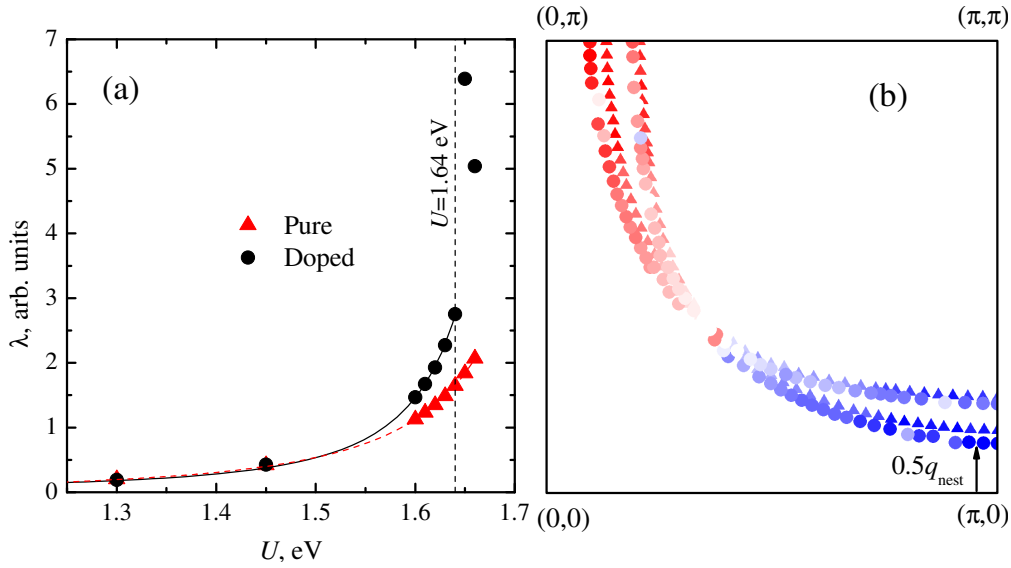


FIGURE 5.7: (a) The pairing strength λ for the undoped (triangles) and doped (circles) $\text{Bi}_2\text{Sr}_2\text{CaCu}_2\text{O}_{8+\delta}$ TB models as a function of Coulomb repulsion U . (b) The superconducting gap function $g(\mathbf{k})$ on the \mathbf{k} -point mesh at the Fermi surface of the undoped $\text{Bi}_2\text{Sr}_2\text{CaCu}_2\text{O}_8$ unit cell for the undoped (triangles) and doped (circles) models. The red (blue) color represents positive (negative) $g(\mathbf{k})$ values, and the intensity of the color is proportional to the absolute value of $g(\mathbf{k})$. Half the nesting vector q_{nest} is shown by an arrow.

mesh was unfolded to the Brillouin zone of the pure compound unit cell in order to allow a comparison of the Fermi surface behavior for the two systems with experiment. One should note that in the case of the doped supercell such an unfolding is, strictly speaking, not allowed and results in a tearing of the Fermi surface. Yet, since the symmetry lowering effects caused by a dopant are small, the unfolding in this case is a reasonable approximation. In particular, the unfolded way of presenting $g(\mathbf{k})$ allows us to observe that the symmetry of the pure compound model $g(\mathbf{k})$ is $d_{x^2-y^2}$ and that upon doping it is roughly preserved, though slightly distorted⁴. We also note the characteristic reduction of the norm of the nesting wavevector q_{nest} .

To summarize, the gap equation calculations show that the TB model derived for the oxygen-doped $\text{Bi}_2\text{Sr}_2\text{CaCu}_2\text{O}_{8+\delta}$, $\text{TB1}_{\text{loc. doped}}$, shows an enhanced superconducting pairing compared to the parent compound model $\text{TB1}_{\text{undoped}}$. This model also demonstrates the appearance of the $(\pi, 0, 0)$ peak in the non-interacting static spin susceptibility. These two features of the doped model prove the suggested important role of local crystal and electronic structure inhomogeneities due to doping for the local superconducting properties of $\text{Bi}_2\text{Sr}_2\text{CaCu}_2\text{O}_{8+\delta}$.

⁴Under the distorted d -wave form of the order parameter, it is meant that $g(\mathbf{k})$ has the $d_{x^2-y^2}$ symmetry, *e. g.*, $g(k_x, k_y) = -g(k_y, k_x)$, only within some error bars.

It is important to note that the calculated pairing strength λ [Fig. 5.7 (a)] is an averaged value of the corresponding spatially resolved quantity $\lambda(\mathbf{r})$, whose spatial inhomogeneity is the key assumption of the theory by Nunner *et al.* [Nunner05]. Therefore, our results cannot be used directly to justify the *local* enhancement of superconducting pairing, yet the local enhancement seems to be quite plausible when the average value is increased.

5.3 One-band versus three-band Hubbard Hamiltonians

Up to now, we have been concerned with developing and testing a method that allows accurate characterization of electronic structure variations in the oxygen-doped $\text{Bi}_2\text{Sr}_2\text{CaCu}_2\text{O}_{8+\delta}$. The proposed method is based on DFT calculations of the $\text{Bi}_2\text{Sr}_2\text{CaCu}_2\text{O}_{8+\delta}$ bandstructure, which is then mapped to a *single-band* TB model. Calculations of superconducting properties of $\text{Bi}_2\text{Sr}_2\text{CaCu}_2\text{O}_8$ and $\text{Bi}_2\text{Sr}_2\text{CaCu}_2\text{O}_{8+\delta}$ using their derived TB Hamiltonians show that the superconducting pairing strength is enhanced in $\text{Bi}_2\text{Sr}_2\text{CaCu}_2\text{O}_{8+\delta}$ with respect to the parent compound.

Our results for the single-band Hubbard model are in agreement with the model calculations of Maška *et al.* [Maška07], which show that local dopant-induced variations of the Cu $3d_{x^2-y^2}$ orbital on-site energies lead to enhancement of the local superexchange interaction between Cu spins. We have shown, in particular, that this behavior is robust and remains upon improving the single-band model by taking into account local modifications of hopping integrals.

On the other hand, model calculations performed on a *three-band* Hubbard model [Foyevtsova09] in a manner analogous to the single-band model calculations of Ref. [Maška07] do not find the local spin superexchange coupling to be universally enhanced in the vicinity of a dopant. Instead, it is observed in Ref. [Foyevtsova09] that depending on the dopant-induced relative shifts of the Cu $3d_{x^2-y^2}$ and O $2p_x/2p_y$ on-site energies the superexchange coupling can be both enhanced as well as suppressed. The possibility of the superexchange coupling suppression is confirmed by cluster-model calculations [Johnston09], where the dopant-induced local variations of on-site energies *and* hopping integrals of the three-band model were determined based on electrostatic considerations.

This section presents a detailed discussion of the three-band model results. It also introduces the underlying three-band Hubbard Hamiltonian together with the perturbation expansion method used to derive the local effective spin interaction.

5.3.1 Three-band Hubbard Hamiltonian in the presence of an oxygen dopant

We consider the three-band Hubbard Hamiltonian \hat{H}^{3b} , which incorporates the Cu $3d_{x^2-y^2}$ orbital and the two degenerate O $2p$ orbitals, O $2p_x$ and O $2p_y$. The relevance of this model for the high- T_c superconductivity was first discussed by Emery in Ref. [Emery87]. In the hole representation, which is a convenient choice as in $\text{Bi}_2\text{Sr}_2\text{CaCu}_2\text{O}_8$ the Cu $3d$ shell hosts nine electrons or, equivalently, one hole, \hat{H}^{3b} can be written as

$$\begin{aligned}
\hat{H}^{3b} &= \sum_{i,\sigma} (\varepsilon_d + V_i) \hat{d}_{i\sigma}^\dagger \hat{d}_{i\sigma} + \sum_{l,\sigma} (\varepsilon_d + \Delta + \delta_l) \hat{p}_{l\sigma}^\dagger \hat{p}_{l\sigma} \\
&+ \sum_{\langle i,l \rangle \sigma} t_{pd}^{il} \left(\hat{d}_{i\sigma}^\dagger \hat{p}_{l\sigma} + \text{h.c.} \right) \\
&+ \sum_{\langle l,n \rangle \sigma} t_{pp}^{ln} \left(\hat{p}_{l\sigma}^\dagger \hat{p}_{n\sigma} + \text{h.c.} \right) \\
&+ U_d \sum_i \hat{d}_{i\uparrow}^\dagger \hat{d}_{i\uparrow} \hat{d}_{i\downarrow}^\dagger \hat{d}_{i\downarrow} + U_p \sum_l \hat{p}_{l\uparrow}^\dagger \hat{p}_{l\uparrow} \hat{p}_{l\downarrow}^\dagger \hat{p}_{l\downarrow}.
\end{aligned} \tag{5.12}$$

In Eq. (5.12), $\hat{d}_{i\sigma}^\dagger$ ($\hat{d}_{i\sigma}$) creates (annihilates) a hole with spin σ in the $3d_{x^2-y^2}$ orbital of a Cu atom at site i . Correspondingly, $\hat{p}_{l\sigma}^\dagger$ ($\hat{p}_{l\sigma}$) creates (annihilates) a hole with spin σ in one of the two O $2p$ orbitals at site l . ε_d is the on-site energy of the Cu $3d_{x^2-y^2}$ orbital, while Δ is the difference between the Cu $3d_{x^2-y^2}$ and the O $2p$ energies in the pure system. t_{pd}^{il} and t_{pp}^{ln} describe the nearest-neighbor Cu-O and O-O hoppings, respectively. Only hoppings within the CuO_2 plane are considered. The sign of t_{pd}^{il} and t_{pp}^{ln} depends on the relative phase of the overlapping $3d_{x^2-y^2}$ and $2p$ orbitals. U_d (U_p) is the on-site Coulomb repulsion for a pair of holes on a Cu (O) atom. The presence of a dopant shifts the atomic Cu and O energy levels in its neighborhood. We denote the energy shift for a Cu atom at position i as V_i and for an O atom at position l between Cu ions at positions i and j as $\delta_l = \delta_{ij}$ (see Fig. 5.8). In our model calculations on the three-band model, we neglect local modifications of the hopping integrals t_{pd}^{il} and t_{pp}^{ln} . It is also assumed that the dopant-induced atomic level shifts V_i and δ_l are much smaller compared to the characteristic energies of the homogeneous system:

$$V_i, \delta_l \ll \Delta, U_d U_p. \tag{5.13}$$

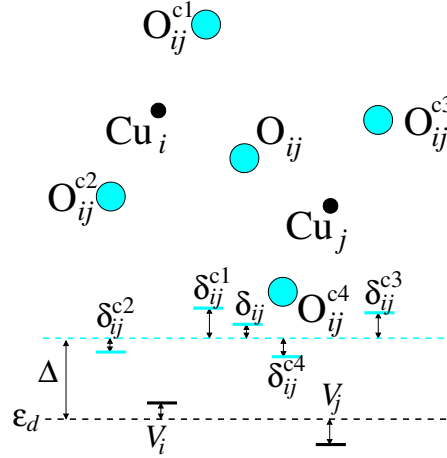


FIGURE 5.8: Energy level diagram for a Cu_2O_5 cluster illustrating the notation used for the dopant-induced shifts of Cu and O atomic energy levels. Each schematic energy level is located beneath its corresponding atom and is accordingly colored [black for Cu and cyan for O levels].

5.3.2 Application of the perturbation expansion

We calculate the local spin superexchange coupling J_{ij} between spins of Cu $3d_{x^2-y^2}$ holes at sites i and j from Hamiltonian \hat{H}^{3b} [Eq. (5.12)] by applying the Rayleigh-Schrödinger perturbation theory. Within the Rayleigh-Schrödinger perturbation theory, we treat the hopping terms of \hat{H}^{3b} as a perturbation \hat{H}_1 ,

$$\hat{H}_1 = \sum_{\langle i,l \rangle \sigma} t_{pd}^{il} \left(\hat{d}_{i\sigma}^\dagger \hat{p}_{l\sigma} + \text{h.c.} \right) + \sum_{\langle l,n \rangle \sigma} t_{pp}^{ln} \left(\hat{p}_{l\sigma}^\dagger \hat{p}_{n\sigma} + \text{h.c.} \right), \quad (5.14)$$

in order to determine interaction parameters of the effective spin Hamiltonian \hat{H}_{eff} , which is valid in the limit of strong electron (hole) localization, $t \ll U$.

With the perturbation defined as (5.14), the ground state of the unperturbed Hamiltonian \hat{H}_0 ($\hat{H}^{3b} = \hat{H}_0 + \hat{H}_1$) corresponds to all Cu atoms being occupied by one hole each. This ground state is $2^{N_{\text{Cu}}}$ -fold degenerate due to the various possible electron spin distributions

$$|\sigma_1 \cdots \sigma_{N_{\text{Cu}}}\rangle = \prod_{i=1}^{N_{\text{Cu}}} \hat{d}_{i\sigma_i}^\dagger |\text{vac}\rangle, \quad (5.15)$$

where $\sigma_1, \dots, \sigma_{N_{\text{Cu}}} = \uparrow$ or \downarrow and i runs over Cu sites.

The effective Hamiltonian \hat{H}_{eff} is calculated as a perturbation expansion of \hat{H}^{3b} in powers of \hat{H}_1 [Lindgren86, Takahashi77, Müller-Hartmann02]. For the set of states (5.15), we can ignore many terms of the perturbation series by making use of the fact that the terms containing $\hat{P}\hat{H}_1\hat{P}$, where the operator \hat{P} projects on the ground state manifold Eq. (5.15), will all vanish since it is not possible to connect any two states out of the

ground state manifold Eq. (5.15) by a single hopping process. This observation leads to the following expression for \hat{H}_{eff} , where expansion has been performed up to the fifth order,

$$\begin{aligned}
\hat{H}_{\text{eff}} &= E_0\hat{P} + \hat{P}\hat{H}_1\hat{R}\hat{H}_1\hat{P} + \hat{P}\hat{H}_1\hat{R}\hat{H}_1\hat{R}\hat{H}_1\hat{P} \\
&+ \hat{P}\hat{H}_1\hat{R}\hat{H}_1\hat{R}\hat{H}_1\hat{R}\hat{H}_1\hat{P} - \frac{1}{2}\hat{P}\hat{H}_1\hat{R}^2\hat{H}_1\hat{P}\hat{H}_1\hat{R}\hat{H}_1\hat{P} - \frac{1}{2}\hat{P}\hat{H}_1\hat{R}\hat{H}_1\hat{P}\hat{H}_1\hat{R}^2\hat{H}_1\hat{P} \\
&+ \hat{P}\hat{H}_1\hat{R}\hat{H}_1\hat{R}\hat{H}_1\hat{R}\hat{H}_1\hat{P} \\
&- \frac{1}{2}\hat{P}\hat{H}_1\hat{R}\hat{H}_1\hat{R}^2\hat{H}_1\hat{P}\hat{H}_1\hat{R}\hat{H}_1\hat{P} - \frac{1}{2}\hat{P}\hat{H}_1\hat{R}\hat{H}_1\hat{P}\hat{H}_1\hat{R}^2\hat{H}_1\hat{R}\hat{H}_1\hat{P} \\
&- \frac{1}{2}\hat{P}\hat{H}_1\hat{R}^2\hat{H}_1\hat{R}\hat{H}_1\hat{P}\hat{H}_1\hat{R}\hat{H}_1\hat{P} - \frac{1}{2}\hat{P}\hat{H}_1\hat{R}\hat{H}_1\hat{P}\hat{H}_1\hat{R}\hat{H}_1\hat{R}^2\hat{H}_1\hat{P} \\
&- \frac{1}{2}\hat{P}\hat{H}_1\hat{R}^2\hat{H}_1\hat{P}\hat{H}_1\hat{R}\hat{H}_1\hat{R}\hat{H}_1\hat{P} - \frac{1}{2}\hat{P}\hat{H}_1\hat{R}\hat{H}_1\hat{R}\hat{H}_1\hat{P}\hat{H}_1\hat{R}^2\hat{H}_1\hat{P}, \tag{5.16}
\end{aligned}$$

In Eq. (5.16), $\hat{R} = (1 - \hat{P})/(E_0 - \hat{H}_0)$ so that, for a state $|\phi\rangle \notin \{|\sigma_1 \cdots \sigma_{N_{\text{Cu}}}\rangle\}$,

$$\hat{R}|\phi\rangle = \frac{1}{E_0 - E_\phi} |\phi\rangle, \tag{5.17}$$

where E_0 is the ground state energy of \hat{H}_0 and $E_\phi = \langle\phi|\hat{H}_0|\phi\rangle$.

Among the terms in \hat{H}_{eff} , Eq. (5.16), we only need to consider those terms that are of the form

$$\sum_{\langle i,j \rangle, \sigma} \hat{d}_{i\sigma}^\dagger \hat{d}_{j\bar{\sigma}}^\dagger \hat{d}_{j\sigma} \hat{d}_{i\bar{\sigma}}, \tag{5.18}$$

with $\bar{\sigma} = -\sigma$, since the corresponding prefactor determines J_{ij} . The terms of interest result from calculating the fourth-order term $\hat{P}\hat{H}_1\hat{R}\hat{H}_1\hat{R}\hat{H}_1\hat{P}$ and the fifth-order term $\hat{P}\hat{H}_1\hat{R}\hat{H}_1\hat{R}\hat{H}_1\hat{R}\hat{H}_1\hat{P}$ in Eq. (5.16). All other terms will only add a constant energy term to the effective Hamiltonian. We denote the contributions of the fourth-order and fifth-order terms to the exchange coupling J_{ij} as, respectively, $J_{ij}^{(4)}$ and $J_{ij}^{(5)}$. It is convenient to derive expressions for $J_{ij}^{(4)}$ and $J_{ij}^{(5)}$ by making use of the graphical representation of hopping processes (see examples in Fig. 5.9). All possible graphs representing the fourth- and fifth-order hopping processes that result in the exchange of spins between two Cu atoms are considered to be summed up for the corresponding $\hat{P}\hat{H}_1\hat{R}\hat{H}_1\hat{R}\hat{H}_1\hat{P}$ and $\hat{P}\hat{H}_1\hat{R}\hat{H}_1\hat{R}\hat{H}_1\hat{R}\hat{H}_1\hat{P}$ expressions.

5.3.3 Results: Effect of doping on local superexchange

We will now consider in turn dopant-induced variations of the local superexchange, which is determined up to the fifth order in perturbation theory

$$J_{ij} \approx J_{ij}^{(4)} + J_{ij}^{(5)}, \tag{5.19}$$

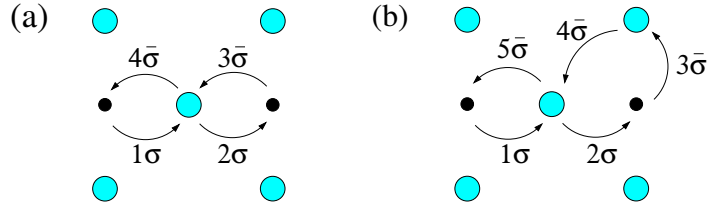


FIGURE 5.9: Graphs describing (a) the fourth- and (b) the fifth-order hole hopping processes that result in the exchange of spins between two Cu atoms. Black (cyan) circles represent Cu (O) atoms. Arrows denote hopping processes, with the accompanying number indicating the order, in which the hoppings occur. Symbols σ or $\bar{\sigma}$ stand for the spin of the hole.

contributed by the fourth- and fifth-order expansion terms. The fifth-order perturbation expansion is apparently the highest that is still technically possible to perform as the number of graphs grows fast and reaches 120 in the case of $J_{ij}^{(5)}$. On the other hand, it is known from the homogeneous problem solution [Eskes93] that the fifth-order contribution is of the same order of magnitude as the fourth-order contribution and that the higher-order terms are required in order to obtain a quantitatively accurate result. Due to this unfortunate property of the expansion series (5.16), the results of our fifth-order perturbation expansion cannot be used for drawing firm conclusions as to the quantitative variation of J_{ij} but rather should provide an estimation of general trends in the behavior of J_{ij} .

The fourth-order term $J_{ij}^{(4)}$ can be written as the homogeneous model result $J^{(4)}$ [Eskes93] plus the dopant-induced correction $\Delta J_{ij}^{(4)}$:

$$J_{ij}^{(4)} = J^{(4)} + \Delta J_{ij}^{(4)}, \quad (5.20)$$

with

$$J^{(4)} = \frac{4t_{pd}^4}{\Delta^2} \left\{ \frac{1}{U_d} + \frac{2}{2\Delta + U_p} \right\}. \quad (5.21)$$

In Eq. (5.21) as well as in the following, we adopt the simplified notation $t_{pd} = |t_{pd}^{il}|$, $t_{pp} = |t_{pp}^{ln}|$.

There are 12 graphs contributing to the fourth-order term $J_{ij}^{(4)}$, one of which is shown in Fig. 5.9 (a). In a homogeneous model, these 12 graphs reduce to only two terms in $J^{(4)}$ [Eq. (5.21)]. In our inhomogeneous model with random atomic level shifts [Eq. (5.12)], the terms in the sum for $J_{ij}^{(4)}$ corresponding to hoppings that start from a Cu ion at site i will differ from those corresponding to hoppings that start from a Cu ion at site j due to different V_i and V_j . It is convenient to write the analytical expression for $\Delta J_{ij}^{(4)}$ as a

sum of two terms $-\Delta J_{ij}^{(4)} = \eta'_{ij} + \eta''_{ij}$ – which are given as

$$\begin{aligned} \eta'_{ij} &= \frac{4t_{pd}^4}{\Delta^2} \\ &\times \frac{1}{U_d} \frac{a_0 + a_1 U_d + a_2 U_d^2}{(\Delta - v_i)^2 (\Delta - v_j)^2 [U_d^2 - (v_j - v_i)^2]}, \end{aligned} \quad (5.22)$$

$$\begin{aligned} a_0 &= (v_j - v_i)^2 (\Delta - v_j)^2 (\Delta - v_i)^2, \\ a_1 &= \frac{1}{2} (v_j - v_i)^2 (2\Delta - (v_i + v_j)) \Delta^2, \\ a_2 &= \frac{1}{2} (\Delta - v_j)^2 (2\Delta - v_i) v_i + \frac{1}{2} (\Delta - v_i)^2 (2\Delta - v_j) v_j, \end{aligned}$$

and

$$\begin{aligned} \eta''_{ij} &= \frac{4t_{pd}^4}{\Delta^2} \frac{2}{2\Delta + U_p} \\ &\times \frac{b_0 + b_1 U_p}{[(2\Delta - v_i - v_j) + U_p] (\Delta - v_j)^2 (\Delta - v_i)^2}, \end{aligned} \quad (5.23)$$

$$\begin{aligned} b_0 &= (\Delta - v_j)^2 (\Delta^2 + \Delta(\Delta - v_i) + (\Delta - v_i)^2) v_i \\ &+ (\Delta - v_i)^2 (\Delta^2 + \Delta(\Delta - v_j) + (\Delta - v_j)^2) v_j \\ &- \frac{1}{2} \Delta^3 (v_j - v_i)^2, \end{aligned}$$

$$\begin{aligned} b_1 &= \frac{1}{2} [(\Delta - v_j) v_i + (\Delta - v_i) v_j] \\ &\times \left[\Delta \left(\Delta - \frac{v_i + v_j}{2} \right) + (\Delta - v_i) (\Delta - v_j) \right]. \end{aligned}$$

The terms n'_{ij} and n''_{ij} can be viewed as corrections to the first and second summands in the $J^{(4)}$ expression (5.21), respectively. In Equations (5.22) and (5.23), we have defined $v_i = V_i - \delta_{ij}$ and $v_j = V_j - \delta_{ij}$. It is easy to check that the correction terms η'_{ij} and η''_{ij} vanish when the impurity-induced potentials v_i vanish.

The sign of $\Delta J_{ij}^{(4)}$ depends on the signs and magnitudes of v_i and v_j , *i. e.*, the actual energy separation between the dopant-shifted Cu and O levels. In particular, for $v_i, v_j \ll \Delta$, $\Delta J_{ij}^{(4)}$ is proportional to $v_i + v_j$. In general, the behavior of $\Delta J_{ij}^{(4)}$ as a function of v_i and v_j is shown diagrammatically in Fig. 5.10 for a typical set of model parameters in Bi superconductors ($U_d = 8.8$ eV, $U_p = 4.1$ eV and $\Delta = 2.92$ eV [Johnston09]). In the space of v_i and v_j , negative and positive $\Delta J_{ij}^{(4)}$ contributions to $J_{ij}^{(4)}$ are shown as white and cyan areas, respectively. For the parameters considered in the cluster calculation of Ref. [Johnston09], the correction $\Delta J_{ij}^{(4)}$ is negative (black dot d in Fig. 5.10) and therefore $J_{ij}^{(4)}$ is suppressed in that case.

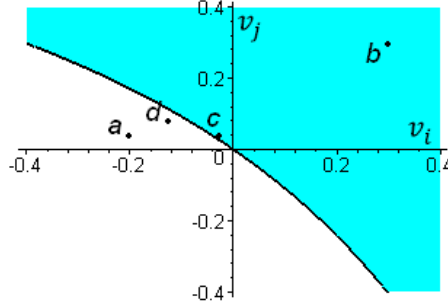


FIGURE 5.10: $\text{Sign}(\Delta J_{ij}^{(4)})$ diagram for a typical set of the model parameters ($U_d = 8.8$ eV, $U_p = 4.1$ eV and $\Delta = 2.92$ eV [Johnston09]) in the space of abscissa $v_i = V_i - \delta_{ij}$ and ordinate $v_j = V_j - \delta_{ij}$. White and cyan regions indicate negative and positive $\Delta J_{ij}^{(4)}$, respectively. Points *a-d* denote the values of v_i and v_j used for generating diagrams (a)-(d) in Fig. 5.11.

Now, let us discuss the fifth-order perturbation expansion term $J_{ij}^{(5)}$. Just as the fourth-order term $J_{ij}^{(4)}$, it can be written as a sum of the homogeneous part $J^{(5)}$ [Esques93],

$$J^{(5)} = \frac{4t_{pd}^4}{\Delta^2} \left\{ \frac{1}{U_d} \frac{8t_{pp}}{\Delta} + \frac{2}{2\Delta + U_p} \frac{8t_{pp}}{\Delta} + \frac{4t_{pp}}{\Delta^2} \right\}, \quad (5.24)$$

and the dopant-induced correction $\Delta J_{ij}^{(5)}$:

$$J_{ij}^{(5)} = J^{(5)} + \Delta J_{ij}^{(5)}. \quad (5.25)$$

There are 120 graphs that contribute to the fifth-order spin exchange, all involving hoppings to one of the four corner O ions. A typical fifth-order spin exchange hopping process is illustrated in Fig. 5.9 (b). Since the corner oxygen ions participate in the fifth-order spin exchange, $\Delta J_{ij}^{(5)}$ depends on the atomic level shifts δ_{ij}^{c1} , δ_{ij}^{c2} , δ_{ij}^{c3} and δ_{ij}^{c4} of the corner oxygens (Fig. 5.8). As the analytical expression for $\Delta J_{ij}^{(5)}$ turns out to be rather lengthy and does not give an immediate feeling of the $\Delta J_{ij}^{(5)}$ behavior, we only write the (relatively short) correction to the first term of $J^{(5)}$ [Eq. (5.24)], μ'_{ij} , in order

to exemplify how the corner oxygen level shifts enter the $\Delta J_{ij}^{(5)}$ expression:

$$\begin{aligned}
 \mu'_{ij} &= 4t_{pd}^4 t_{pp} \\
 &\times \left(\frac{1}{(\Delta + \delta_{ij} - V_i)^2} \frac{1}{U_d + \{V_j - V_i\}} \left\{ \frac{1}{\Delta + \delta_{ij}^{c1} - V_i} \right. \right. \\
 &+ \left. \frac{1}{\Delta + \delta_{ij}^{c2} - V_i} + \frac{1}{\Delta + \delta_{ij}^{c3} - V_i} + \frac{1}{\Delta + \delta_{ij}^{c4} - V_i} \right\} \\
 &+ \frac{1}{(\Delta + \delta_{ij} - V_j)^2} \frac{1}{U_d - \{V_j - V_i\}} \left\{ \frac{1}{\Delta + \delta_{ij}^{c1} - V_j} \right. \\
 &+ \left. \left. \frac{1}{\Delta + \delta_{ij}^{c2} - V_j} + \frac{1}{\Delta + \delta_{ij}^{c3} - V_j} + \frac{1}{\Delta + \delta_{ij}^{c4} - V_j} \right\} \right). \tag{5.26}
 \end{aligned}$$

As one can observe, the sign of μ'_{ij} depends on v_i , v_j , $v_i^{c1} = V_i - \delta_{ij}^{c1}$, $v_i^{c2} = V_i - \delta_{ij}^{c2}$, $v_j^{c3} = V_j - \delta_{ij}^{c3}$ and $v_j^{c4} = V_j - \delta_{ij}^{c4}$. These six parameters define the sign of the *total* fifth-order correction $\Delta J_{ij}^{(5)}$ as well.

With the increased number of v parameters, it more difficult to visualize the behavior of $\Delta J_{ij}^{(5)}$ than in the $\Delta J_{ij}^{(4)}$ case. In order to nevertheless perform some qualitative analysis of the fifth-order correction to the spin exchange, we consider the case where $v_i^{c1} = v_i^{c2} = v_i^c$ and $v_j^{c3} = v_j^{c4} = v_j^c$. For given v_i and v_j , one can in this case draw a phase diagram of the sign of $\Delta J_{ij} \approx \Delta J_{ij}^{(4)} + \Delta J_{ij}^{(5)}$ in the space of v_i^c and v_j^c . In Fig. 5.11, we present, as an example, four such diagrams corresponding to different sets of v_i and v_j (the four dots *a*, *b*, *c* and *d* in Fig. 5.10). For calculating these diagrams, we chose $t_{pd}=1.2$ eV and $t_{pp}=0.5$ eV, as also considered in the cluster calculations of Ref. [Johnston09]. The local Cu and O onsite energies calculated by Johnston *et al.* correspond to the choice of $v_i=-0.13$ eV and $v_j=0.08$ eV in Fig. 5.11 (d). In Fig. 5.11 (d), we also indicate by a black dot the values of v_i^c and v_j^c that have been obtained in Ref. [Johnston09] from electrostatic calculations. In agreement with the result of Ref. [Johnston09], we obtain with this choice of parameters that the dopant-induced local correction to J is negative, *i. e.*, the spin exchange is suppressed in the vicinity of a dopant.

5.4 Discussion

We summarize the most important results on the microscopic modeling of oxygen doping of the cuprate superconductor $\text{Bi}_2\text{Sr}_2\text{CaCu}_2\text{O}_8$ [Maška07, Johnston09, Foyevtsova09,

⁵Alternatively, $v_j^{c2} = V_j - \delta_{ij}^{c2}$ *etc.* could be considered.

⁶Such a symmetry is realized when the dopant atom is located on the line connecting the two Cu atoms [Johnston09].

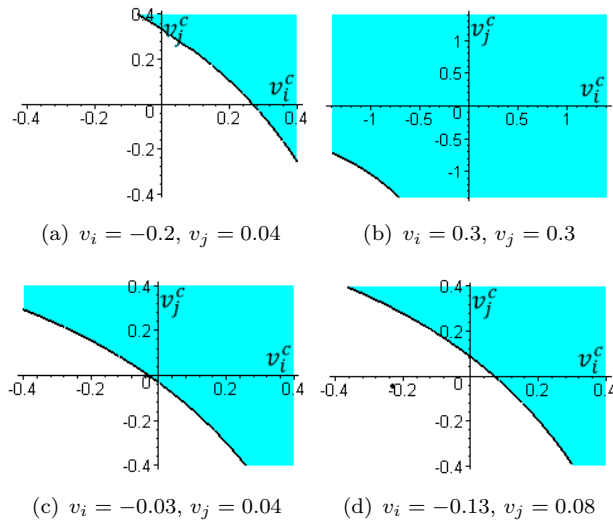


FIGURE 5.11: $\text{Sign}(\Delta J_{ij})$ diagrams in the space of abscissa v_i^c and ordinate v_j^c . White and cyan correspond to negative and positive values of ΔJ_{ij} , respectively. The point $v_i^c = -0.23$ eV, $v_j^c = -0.05$ eV in diagram (d) corresponds to the energy levels distribution shown in Fig. 2 of Ref. [Johnston09].

Foyevtsova10].

- In a single-band Hubbard model for the CuO_2 planes, the dopant-induced random variation of the Cu $3d_{x^2-y^2}$ on-site energies *always* leads to an enhancement of local superexchange interaction between Cu spins. This is shown in perturbation theory calculations by Maška *et al.* [Maška07].
- When local modifications of transfer integrals are also considered in the inhomogeneous single-band Hubbard model in addition to the on-site energy variation, the *non-local* RPA calculations find an enhancement of superconducting pairing strength in the oxygen-doped $\text{Bi}_2\text{Sr}_2\text{CaCu}_2\text{O}_{8+\delta}$ [Foyevtsova10].
- The single-band model results of References [Maška07] and [Foyevtsova10] provide strong evidences that the presence of dopant-induced inhomogeneities in the single-band Hamiltonian enhances superconductivity locally as well as on a macro-scale.
- The inhomogeneous three-band model, which includes the Cu $3d_{x^2-y^2}$ and O $2p_x/2p_y$ orbitals, was considered within the cluster-model calculations [Johnston09] and the fifth-order perturbation theory [Foyevtsova09]. In both studies, the local spin exchange interaction is found to be *suppressed* in the vicinity of an oxygen dopant in the case when electrostatically estimated values of the local Hubbard model parameters are used.

- It follows from the perturbation expansion calculations [Foyevtsova09] that in the three-band model the local superexchange can be both enhanced as well as suppressed depending on the magnitudes and signs of the energy level shifts on Cu and O ions.

Apparently, the *universality* of the dopant-induced enhancement of local superexchange, which emerges in the single-band model calculations [Maška07], is lost in the three-band model. From the analysis of our results on the three-band model (Section 5.3), we conclude that the key effect responsible for such a difference between the single- and three-band models' behavior is *local modulation of the charge-transfer gap* Δ between the Cu $3d_{x^2-y^2}$ and O $2p_x/2p_y$ atomic levels, which can take place only in the three-band model. Such modulation of Δ is just another side of the simultaneous variation of the Cu $3d_{x^2-y^2}$ and O $2p_x/2p_y$ atomic levels by V_i and δ_{ij} .

The importance of the local modulation of Δ becomes clear when one considers the following simple argument. One writes the local gap Δ_{ij} as

$$\Delta_{ij} = \Delta - (V_i - \delta_{ij}). \quad (5.27)$$

Then, in the limit $|V_i - V_j| \ll (V_i - \delta_{ij})$, the inhomogeneous solutions for $J_{ij}^{(4)}$ and $J_{ij}^{(5)}$ can be obtained by simply replacing Δ by Δ_{ij} in Equations (5.21) and (5.24) so that Δ_{ij} becomes the only parameter that determines the J variation⁷.

An adequate microscopic theory designed to explain the nano-scale inhomogeneities in the $\text{Bi}_2\text{Sr}_2\text{CaCu}_2\text{O}_{8+\delta}$ STS spectra should not only model the superconducting gap enhancement in the vicinity of a dopant but also give a correct *quantitative account of the intensity* of the superconducting gap modulation. In this respect, the 5% suppression of the local superexchange obtained within the three-band Hubbard model with the electrostatically evaluated model parameters (Section 5.3) is too small to produce a variation of the pairing strength required for the realization of the Nunner *et al.* scenario [Nunner05]. On the other hand, the single-band model calculations of the non-local RPA pairing strength λ give a 30% enhancement of λ in the doped compound (Section 5.2), which agrees well with the STS measurements.

These observations bring us to a conclusion that there is still a possibility to obtain the required enhancement of local superexchange in the inhomogeneous three-band Hubbard model by improving the accuracy of the model parameters evaluation. Indeed,

⁷In Fig. 5.10, the condition $|V_i - V_j| \ll (V_i - \delta_{ij})$ is fulfilled in the vicinity of the $v_i = v_j$ line (on the line, $V_j - V_i = 0$), and indeed $J_{ij}^{(4)}$ increases in the first quarter and reduces in the third quarter of the diagram. In the second and fourth quarters, the relative variation of the Cu ion levels, $V_i - V_j$, becomes equally important.

from the perturbation expansion we saw that there exist vast regions of the superexchange enhancement in the v -diagrams of Figures 5.10 and 5.11. The parameter regime appropriate for our problem can be determined more accurately when the inhomogeneous three-band model parameters are calculated within the DFT in the spirit of the DFT-assisted single-band model parameterization presented in Section 5.1.

The ambiguity of the fitting method, which has become evident during parameterization of the single-band TB model (Section 5.1), can pose an insurmountable obstacle when the method is applied to the three-band model. Fortunately, the parameterization method based on projecting onto Wannier functions does not suffer from this problem and is expected to perform well in the three-band model case.

With the realistic parameters of the inhomogeneous three-band model at hand, one could perform an RPA calculation for $\text{Bi}_2\text{Sr}_2\text{CaCu}_2\text{O}_8$ and $\text{Bi}_2\text{Sr}_2\text{CaCu}_2\text{O}_{8+\delta}$ in order to study their non-local superconducting properties. Alternatively, it might be worthwhile to refine the perturbation theory calculations of Section 5.3 by considering also the hopping integrals variation in addition to the variation of the Cu and O on-site energies.

Chapter 6

Doped Mott insulator TiOCl

As discussed in Section 3.3, the experimentally observed insulating state in TiOCl that survives electron doping [Sing11] is quite puzzling in view of our general understanding of Mott insulators, which are expected to become metallic when doped (Chapter 1). In this chapter, we wish to understand this unusual behavior by identifying doping induced microscopic processes that are specific to TiOCl. By using the DFT methods, we carefully analyze the electronic structural changes in Na-doped TiOCl cells at various Na concentrations and compare our DFT results with the photoemission results of Ref. [Sing11]. In addition, we carry out a similar analysis for TiOCl cells doped with V (or Sc), F and S, so that our generalized molecular formula under doping is defined as $\text{Na}_x\text{Ti}_{1-y}\text{V}_y(\text{Sc}_y)\text{O}_{1-z}\text{F}_z\text{Cl}_{1-w}\text{S}_w$, where x , y , z and w are the doping concentrations [see Fig. 6.1 (a)].

As a result, we find within the DFT that TiOCl would remain insulating for all Na concentrations studied and that the change of spectral weight at elevated Na concentration is in good agreement with the photoemission results [Sing11]. The persistent insulating state is shown to be a consequence of two Na^+ induced effects:

- (i) strong modification of the crystal field splitting of Ti $3d$ states and
- (ii) induction of coexisting Ti^{3+} and Ti^{2+} ions, which are further stabilized by long-range Coulomb interaction as usually observed in mixed-valence compounds [Zhang05].

In the following, our analysis shall consist of a number of important computational steps. First, we perform structural optimizations for all the considered doping cases:

- Na_xTiOCl for six different values $x=0, 1/8, 1/4, 1/2, 3/4, 1$;

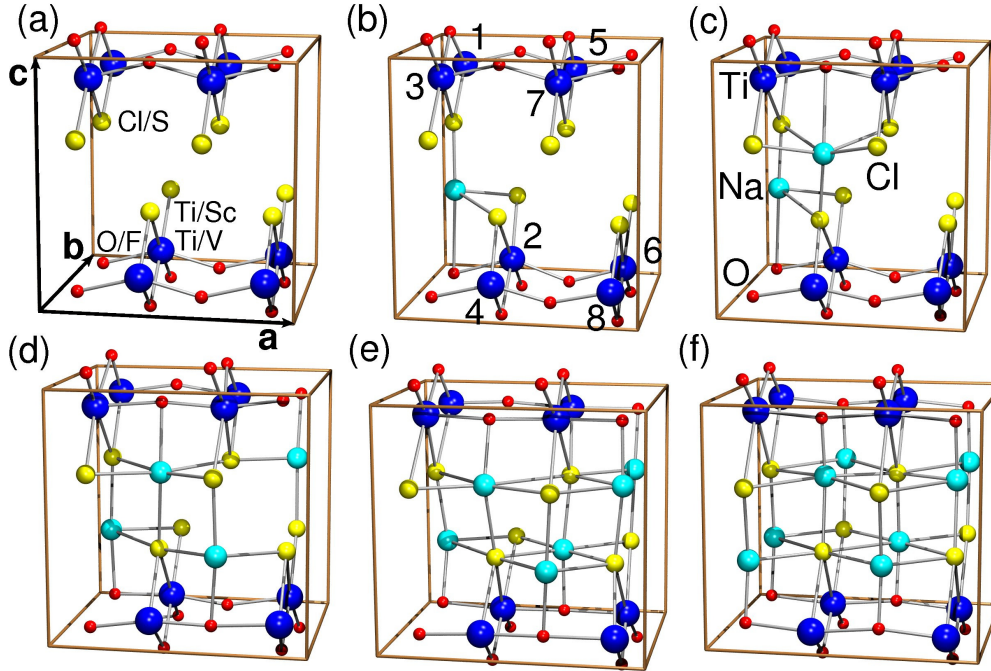


FIGURE 6.1: Superlattices at six different concentrations of Na doping. (a) Undoped case. The atoms where substitutions of Cl by S, O by F and Ti by V(Sc) are performed are also specified. (b) 12.5 % Na doping: $\text{Na}_{1/8}\text{TiOCl}$. The 8 Ti ions in the cell are labeled by numbers 1 to 8. (c) 25 % doping: $\text{Na}_{1/4}\text{TiOCl}$, (d) 50 % doping: $\text{Na}_{1/2}\text{TiOCl}$, (e) 75 % doping: $\text{Na}_{3/4}\text{TiOCl}$, and (f) 100 % doping: NaTiOCl .

- $\text{TiO}_{7/8}\text{F}_{1/8}\text{Cl}$;
- $\text{TiOCl}_{7/8}\text{S}_{1/8}$;
- $\text{Ti}_{7/8}\text{V}_{1/8}\text{OCl}$ and $\text{Ti}_{7/8}\text{Sc}_{1/8}\text{OCl}$.

For that purpose, we employ the Car-Parinello molecular dynamics method (Ref. [Car85], Section 2.3) as implemented in the projector-augmented wave (PAW) code of Blöchl [Blöchl94]. To approximately treat exchange and correlation effects within the DFT, we use the GGA+U functional, with $U = 4.5$ eV and $J^{\text{H}} = 1.0$ eV for the Ti 3d states. This choice allows us to reproduce the correct insulating gap of 2 eV for undoped TiOCl . In each doping case, structural relaxation is carefully converged with respect to lattice parameters and atomic positions, with high energy cutoffs of 45 Ry and 180 Ry for the wave functions and charge density expansion, respectively.

While the TiOCl cells doped with F, S and V (Sc) are constructed by simply replacing, respectively, the O, Cl or Ti atom by the dopant, in the case of Na doping structural optimization is more involved. Since no experimental data for the Na positions are available, numerous possibilities have to be tested by *ab initio* molecular dynamics. However, according to Pauling's rule that the coordination number is determined by the

radius ratio [Pauling29], the most probable Na positions are in the cages of five Cl and one O, as shown in Figs. 6.1 (b)-(f). In fact, by performing *ab initio* molecular dynamics starting from several different initial Na positions, we find that the Na atoms always fall into this cage to reach the coordination number of six. The remaining uncertainty is given by the various combinations of locating Na atoms into the eight cages of the supercell¹. We performed *ab initio* molecular dynamics for all the different combinations at various doping concentrations and compared the total energies. Fig. 6.1 presents the final stable lattice structures with lowest total energies for the six Na concentration values x studied.

In the rest of this chapter, we will present the electronic structures of the variously doped TiOCl cells (Section 6.1), which provide sufficiently clear information on the microscopic origin of the persistent under doping insulating state, and propose an appropriate model to effectively describe the behavior of doped TiOCl (Section 6.2). A major part of the calculations have been carried out by Dr. Yu-Zhong Zhang, especially, the *ab initio* molecular dynamics simulations and PAW electronic structure calculations. My contribution consisted in parameterizing the effective TB model for Na-doped TiOCl supercells using the downfolding technique (page 41) and the NMTO basis (Section 2.2.1).

6.1 Electronic structure of $\text{Na}_x\text{Ti}_{1-y}\text{V}_y(\text{Sc}_z)\text{O}_{1-z}\text{F}_z\text{Cl}_{1-w}\text{S}_w$

For the discussion of orbital-resolved electronic states, we choose the local coordinate frame as $x \parallel b$, $y \parallel c$ and $z \parallel a$ with $d_{x^2-y^2}$, d_{xz} , d_{yz} forming the t_{2g} bands and d_{xy} , d_{z^2} the e_g bands.

6.1.1 Na doping

In Fig. 6.2, we present the total DOS for the six Na-doped TiOCl cases considered. The DOS of the undoped case [Fig. 6.2 (a)] is correctly reproduced, with an energy gap around 2 eV and the peak close to the Fermi level predominantly of the $d_{x^2-y^2}$ character. With Na doping [Figs. 6.2 (b)-(f)], the whole spectral weight is suddenly shifted towards lower energies, and an additional peak with weight $2x$ appears close to the Fermi level as compared to the undoped case. The separation of the two Ti peaks is about 1 eV for $x = 1/8$ and a gap always persists at the Fermi level in all Na-doped cases. All the findings are consistent with the experimental observations [Sing11].

¹We use a $2 \times 2 \times 1$ supercell that is obtained by doubling the primitive unit cell in both a and b directions.

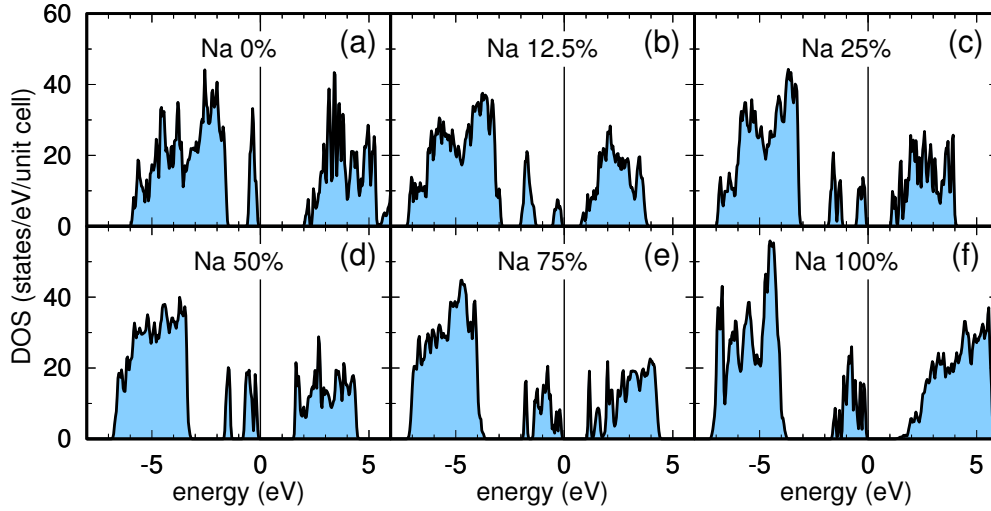


FIGURE 6.2: Total density of states at the six different concentrations of Na doping shown in Fig. 6.1. (a) Undoped case: TiOCl, (b) $\text{Na}_{1/8}\text{TiOCl}$, (c) $\text{Na}_{1/4}\text{TiOCl}$, (d) $\text{Na}_{1/2}\text{TiOCl}$, (e) $\text{Na}_{3/4}\text{TiOCl}$, and (f) NaTiOCl .

The insulating state in the Na-doped TiOCl results from the interplay of two effects associated with Na intercalation. First, owing to the Hund's rule coupling, the additional electrons donated by the Na ions occupy the Ti $3d_{xz}$ orbitals and not the Ti $3d_{x^2-y^2}$ orbitals that are already occupied by one electron. Second, the doped electrons would end up trapped on the Ti atoms that are closest to the Na atoms because the latter are strongly distorting their crystalline environment, which leads to a strong modification of the crystal field splitting of the Ti $3d$ states.

The above asserted scenario can be deduced from examining the orbital-resolved DOS for, *e. g.*, a Na doping of $x = \frac{1}{8}$, shown in Fig. 6.3 (d). Indeed, close to the Fermi level, both $d_{x^2-y^2}$ and d_{xz} orbitals contribute to the DOS. Some qualitative understanding of this result can be gained from a rough energy estimation in the atomic limit when one additional electron is added to the Ti t_{2g} bands. While the change of total energy is $U + 2J^{\text{H}}$ if the additional electron occupies the $d_{x^2-y^2}$ orbital, it is $U - J^{\text{H}} + \Delta$ if the electron occupies the d_{xz} orbital, where Δ is the orbital excitation from $d_{x^2-y^2}$ to d_{xz} . Since $\Delta \sim 0.1$ eV and $J^{\text{H}} \sim 1$ eV, adding the additional electron to the d_{xz} orbital is always preferable. This analysis indicates the importance of the Hund's rule coupling in the doping case.

The trapping of the additional electron on one of the Ti atoms becomes evident after also inspecting the atom-resolved DOS in Fig. 6.3 (a) as well as comparing the crystal field splitting of the undoped case with that of the $\frac{1}{8}$ Na-doped case in Figs. 6.4 (a) and (b) [in these figures, the Ti ions are labeled from Ti1 to Ti8 as shown in Fig. 6.1 (b)]. In the undoped case, all eight Ti ions in the supercell are equivalent and the orbital

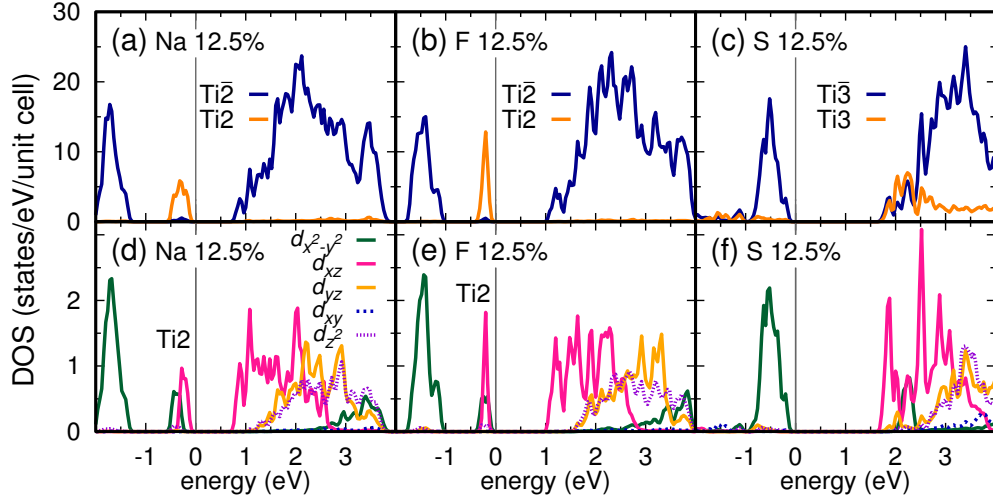


FIGURE 6.3: Partial DOS for (a), (d) 12.5% Na doping: $\text{Na}_{1/8}\text{TiOCl}$, (b), (e) 12.5% F substitution: $\text{TiO}_{7/8}\text{F}_{1/8}\text{Cl}$, and (c), (f) 12.5% S substitution: $\text{TiOCl}_{7/8}\text{S}_{1/8}$. In (a), (b) and (c) the total Ti-resolved DOS are shown. The orange curve denotes the DOS for the Ti ion nearest to the doping ion (Ti2 for the Na- and F-doped cases, Ti3 for the S-doped case). The blue curve denotes the DOS for the rest of Ti ions. In (d), (e), and (f) the corresponding orbital-resolved DOS are shown. Below E_F the contributions of Ti2 for the electron-doped cases are explicitly marked.

excitations are the same. In the $\frac{1}{8}$ Na-doped case, all Ti ions become inequivalent and the crystal field splittings are different from site to site. Most importantly, the splittings of t_{2g} orbitals on the Ti2 (closest Ti to Na) become strikingly small, which makes it possible to trap the additional electron into the d_{xz} orbital on this Ti site. This is consistent with the partial DOS in Figs. 6.3 (a) and (d) where the peaks near the Fermi level are mainly contributions from the $d_{x^2-y^2}$ and d_{xz} orbitals of Ti2. The peak at lower energies is from the rest of Ti ions (all denoted by Ti $\bar{2}$) and is of purely $d_{x^2-y^2}$ character. Further investigations of the crystal field splittings and partial DOS for the other Na doping concentrations reveal that the same mechanism can be applied to the observed insulating states, *i. e.*, each Na ion strongly modifies the lattice structure locally, reduces the crystal field splitting of the t_{2g} orbitals on the closest Ti ion and leads to localization of the doped electron, which reduces the Ti^{3+} ($3d^1$) to Ti^{2+} ($3d^2$) and prevents conduction. Furthermore, long-range Coulomb repulsion becomes effective due to the appearance of a mixed-valence state of Ti^{3+} and Ti^{2+} and further stabilizes the symmetry-breaking insulator. Within the point-charge approximation [Sing11], the combination of crystal field splitting and the long-range Coulomb interaction can account for the gap of 1 eV.

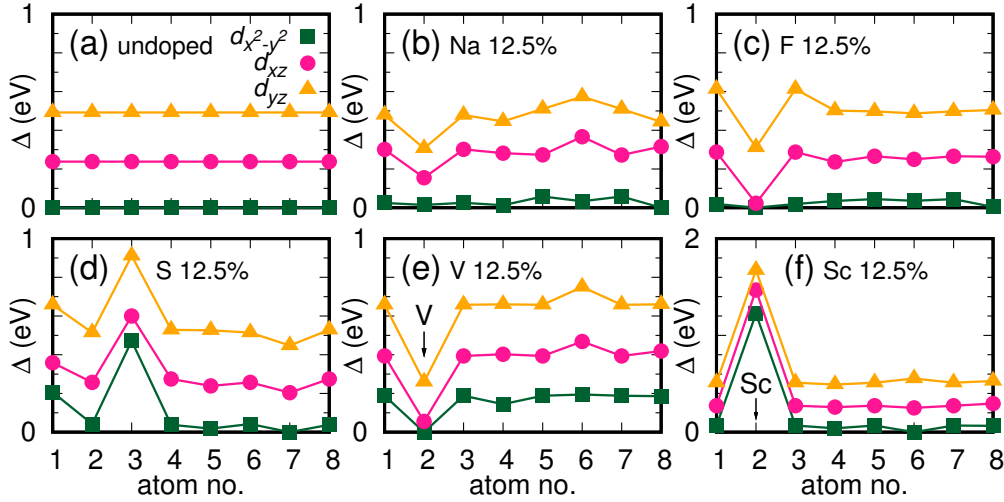


FIGURE 6.4: t_{2g} crystal field splitting energies obtained from GGA calculations. The horizontal axis denotes 8 Ti ions in the supercell labeled by numbers from 1 to 8 as shown in Fig. 6.1 (b). (a) TiOCl , (b) $\text{Na}_{1/8}\text{TiOCl}$, (c) $\text{TiO}_{7/8}\text{F}_{1/8}\text{Cl}$, (d) $\text{TiOCl}_{7/8}\text{S}_{1/8}$, (e) $\text{Ti}_{7/8}\text{V}_{1/8}\text{OCl}$, and (f) $\text{Ti}_{7/8}\text{Sc}_{1/8}\text{OCl}$.

6.1.2 V (Sc), F and S doping

In all the doped cases where O is substituted by F [Fig. 6.3 (b), (e)], Cl by S [Fig. 6.3 (c), (f)], and Ti by V or Sc (not shown) gaps still open at the Fermi level.

The DOS of the F-doped case [Fig. 6.3 (b), (e)] is similar to that of the Na-doped case with a double peak structure below the Fermi level, since both are electron doping processes. The similarities can be also observed in the crystal field splittings [Fig. 6.4 (c)]. However, in the F-doped case the Ti2 $d_{x^2-y^2}$ and d_{xz} orbitals are almost degenerate.

Substituting Cl by S implies taking out an electron from the $d_{x^2-y^2}$ orbital (hole doping), and one would expect the system to be metallic. However, from Fig. 6.4 (d), we find that the on-site orbital energies of Ti3, which is closest to the substituted S ion, are significantly raised due to the large distortion of the lattice structure, again leading to a localized state for the doped hole. In this case, no spectral weight from the Ti3 3d orbitals is detected close to the Fermi level [Fig. 6.3 (c)]. Interestingly, the Ti1 $d_{x^2-y^2}$ orbital energy is almost degenerate with the Ti7 d_{xz} orbital energy, indicating the importance of on-site Coulomb interaction which avoids double occupation on each Ti ion. This leads to a DOS below the Fermi level of only $d_{x^2-y^2}$ character [Fig. 6.3 (f)]. On the other hand, doping with S might result in the formation of S_2^{2-} ions, which are isoelectronic to two Cl^- ions and do not contribute to doping. The system will then remain insulating.

Finally, substituting Ti by V (electron doping) and Sc (hole doping) we observe a similar effect as seen in the previous electron- and hole-doped cases. The on-site orbital energies

are much lower (higher) on the V (Sc) ion than on the Ti ion [Figs. 6.4 (e) and (f)], which can again account for the localization of the doped electron (hole) and the absence of a metallic state. However, the oxidations are all +3 (Ti^{3+} , V^{3+} , Sc^{3+}), indicating that the role of long-range Coulomb interaction is negligible.

6.2 Effective microscopic model

From the above analysis, we conclude that the appropriate microscopic model that accounts for the persistence of the insulating state upon doping is given by a multi-band ionic Hubbard model:

$$\begin{aligned}
\hat{H} = & \sum_{i,j,\sigma,m_i,m_j} t_{ij}^{m_i m_j} \hat{c}_{im_i\sigma}^\dagger \hat{c}_{jm_j\sigma} + (U + 2J^{\text{H}}) \sum_{i,m_i} \hat{n}_{im_i\uparrow} \hat{n}_{im_i\downarrow} \\
& + U \sum_{i,m_i>m'_i,\sigma} \hat{n}_{im_i\sigma} \hat{n}_{im'_i\bar{\sigma}} + (U - J^{\text{H}}) \sum_{i,m_i>m'_i,\sigma} \hat{n}_{im_i\sigma} \hat{n}_{im'_i\sigma} \\
& + \sum_{i,\sigma,m_i} \Delta_{i,m_i} \hat{n}_{im_i\sigma} + \sum_{i,j} V_{ij} \hat{n}_i \hat{n}_j.
\end{aligned} \tag{6.1}$$

The first term describes the hopping between Ti sites i, j within the three t_{2g} orbitals (m_i, m_i), the second to fourth terms are the intra- and interorbital Coulomb interactions and the Hund's rule coupling, respectively, the fifth term the crucial on-site orbital energies Δ_{i,m_i} , and the last term the effective long-range inter-site Coulomb interaction V_{ij} . Upon Na doping, Δ_{i,m_i} differs from site to site which forms a local trapping potential and leads to a coexistence of Ti^{3+} and Ti^{2+} stabilized by V_{ij} . Then, a doping-induced phase transition from undoped Mott insulator to doped insulator with charge disproportionation occurs. While a similar transition has been extensively investigated in the one-band case [Fabrizio99, Garg06, Kancharla07], inclusion of orbital degrees of freedom may result in an even richer phase diagram [Medici09a, Lee10].

As has been shown before, upon Na doping the Ti $3d_{xz}$ orbitals become occupied by the additional electrons and, together with the Ti $3d_{x^2-y^2}$ orbitals, get involved into electron transfer, which necessitates the usage of the effective multi-band Hamiltonian (6.1). Moreover, it turns out that the inclusion of the d_{xz} orbitals results in switching the system from the 1D interactions regime to the 2D regime. We arrive at this conclusion by parameterizing the TB Hamiltonian [the first term in Eq. (6.1)] for several Na doped TiOCl systems using the NMTO downfolding. The NMTO calculations have been performed with the GGA functional for $x = \frac{1}{8}, \frac{1}{2}$ and 1 concentrations of Na. After folding down all the electronic states except for the three t_{2g} orbitals, we find in each considered case that the hopping integrals within d_{xz} orbitals along a and within one TiO bilayer are comparable to the hopping integrals within $d_{x^2-y^2}$ orbitals along b .

6.3 Discussion

Although our DFT calculations are only performed for several commensurate Na doping cases, we argue that the scenario for this insulating state under doping can be applied to all doping concentrations: the Na ion enters an individual cage consisting of five Cl and one O ions and creates a trapping potential reducing the crystal field splitting of the t_{2g} orbitals on the closest Ti ion and resulting in a localized state for the doped electron with the help of long-range Coulomb interaction.

With the understanding of the mechanism for the insulating state, we propose two ways to metallize TiOCl by doping which would favor a possible superconducting state in a doped Mott insulator by suppressing other symmetry-breaking states. The first idea is to avoid the strong modification of crystal field splitting and the formation of a trapping potential due to the lattice deformation induced by the cation or anion. Therefore, a possible direction is to intercalate Na together with organic ligands to prevent the doped Na from entering the cage, in the spirit of intercalating organosolvated Li into β -HfNCl [Yamanaka98]. A second practicable way is to apply external pressure after carrying out electron doping. Due to the appearance of the additional peak and the reduction of the gap under doping, the doped system becomes much easier to metallize under pressure than the undoped one.

Summary and outlook

In this work, we performed density functional theory (DFT) calculations for several Mott insulators – Cs_2CuCl_4 , Cs_2CuBr_4 , $\text{Bi}_2\text{Sr}_2\text{CaCu}_2\text{O}_{8+\delta}$ and TiOCl – in order to derive their microscopic models. From the analysis of the derived models (which in the case of $\text{Bi}_2\text{Sr}_2\text{CaCu}_2\text{O}_{8+\delta}$ was performed quantitatively using many-body methods) we were able to draw important conclusions as to the compounds’ microscopic behavior and the connection between their electronic properties and experimentally observed macroscopic properties.

In the case of Cs_2CuCl_4 and Cs_2CuBr_4 , we found that the equilibrium crystal structures obtained by structural relaxation of internal parameters within the DFT strongly depend on the approximation to the exchange-correlation functional employed during the relaxation. Moreover, the evaluated parameters of the tight-binding (TB) and Heisenberg models for Cs_2CuCl_4 and Cs_2CuBr_4 turn out to be extremely sensitive to fine structural variations. The two dependencies result in the variation of the model parameters as a function of the exchange-correlation functional used for the relaxation. As the various exchange-correlation functionals that we used differed mainly in the accuracy of treating electronic correlations and describing spin-polarized states, we conclude that electronic correlations and magnetism play an essential role in defining the structural properties of Cs_2CuCl_4 and Cs_2CuBr_4 ². Also, an important result on Cs_2CuCl_4 and Cs_2CuBr_4 is the identification of a number of weak interlayer interactions in the microscopic model that might play a stabilizing role for some of the compounds’ exotic magnetic phases. Finally, we find a qualitative difference between the electronic structures of Cs_2CuCl_4 and Cs_2CuBr_4 , namely, that in Cs_2CuCl_4 only one of the Cu t_{2g} bands participates in electron hopping whereas in Cs_2CuBr_4 all three t_{2g} bands are involved.

Another topic that we address in this thesis is the electronic inhomogeneities in the oxygen-doped $\text{Bi}_2\text{Sr}_2\text{CaCu}_2\text{O}_{8+\delta}$ superconductor. We were interested, in particular, in

²This situation is in fact not unique to Cs_2CuCl_4 and Cs_2CuBr_4 . For instance, in many of the recently discovered iron pnictide superconductors, structural relaxation with standard DFT approximations does not give accurate enough results so that it is often a better choice to calculate electronic properties of the pnictides with unrelaxed experimental structures.

the superconducting properties of the compound, such as the Cooper pairing strength, as a function of doping. In order to perform RPA calculations of the magnetic susceptibility and superconducting pairing strength, we derived *single-band* TB models for both the pure and oxygen-doped superconductors by means of the DFT bandstructure parameterization of the Cu $3d_{x^2-y^2}$ band. The high-quality correspondence between the TB spectra and DFT bandstructures was achieved through the inclusion of effective long-distance interactions as variable parameters in the model Hamiltonians. The bandstructure parameterization of the doped $\text{Bi}_2\text{Sr}_2\text{CaCu}_2\text{O}_{8+\delta}$ supercell, which otherwise would be technically too involved, was carried out by introducing certain approximations and thus reducing the number of variable parameters. As a result, the Cooper pairing strength calculated in the framework of the RPA was found to increase by $\sim 30\%$ in the doped $\text{Bi}_2\text{Sr}_2\text{CaCu}_2\text{O}_{8+\delta}$, compared to the pure compound. We also carried out model calculations of the doping-induced effects on local superexchange for a *three-band* Hubbard model, with the O $3p_x$ and $3p_y$ bands included. We found that this model shows a qualitatively different behavior. Depending on the parameter regime of the three-band model, the dopant atom can induce both the enhancement as well as suppression of the local superexchange coupling and – within the spin-fluctuation-exchange model – of the local superconducting gap.

In the case of the layered Mott insulator TiOCl, our primary goal was to understand on a microscopic level the nature of the insulating state of TiOCl that persists upon doping. For this purpose, we compared the electronic structure of the undoped TiOCl with the electronic structures of the Na-, F-, S-, V- and Sc-doped TiOCl. The comparison of electronic structures was preceded by careful determination of the doped TiOCl structural parameters by means of Car-Parrinello molecular dynamics simulations. In agreement with photoemission experiments, the DFT finds TiOCl insulating in each doping case. It also reveals that the insulating state is a result of the interplay between the Hund's rule coupling, which makes a doped electron occupy a new Ti $3d$ orbital, and the dopant induced modification of the crystal field splitting of Ti states, which leads to the trapping of the doped electron on a Ti ion. Using the downfolding technique, we established that the doped TiOCl should be described in terms of a 2D multi-band ionic Hubbard model.

As a general conclusion, the considered cases all point to the importance of an accurate treatment of strong electronic correlations when the application of the DFT to strongly correlated materials, *e. g.*, transition metal compounds, is concerned. Due to the lack of an exact expression for the exchange-correlation functional within the DFT, there is always a certain amount of uncertainty in any DFT calculation regarding which should be the most appropriate approximation to be used in each particular case. Sometimes, in order to obtain reliable results, elaborate multi-step computational schemes have to

be considered, as, *e. g.*, in the case of Cs_2CuCl_4 and Cs_2CuBr_4 . We find ourselves in a position to reasonably state, however, that the LDA+DMFT method, which is the next step beyond the LDA+U, should improve the situation considerably. Once we have the method implemented and well tested, it would be interesting, for example, to perform structural relaxations for Cs_2CuCl_4 and Cs_2CuBr_4 (as well as for the mixed compounds $\text{Cs}_2\text{CuCl}_{4-x}\text{Br}_x$) and compare the obtained structures to our earlier results. In fact, the calculations for Cs_2CuCl_4 and Cs_2CuBr_4 that have been carried out so far are only a small portion of what can be done within the DFT. Another DFT application could be, for instance, the calculation of phonon spectra. Also in this case, the LDA+DMFT approach is expected to provide more accurate results compared to the standard approximations. The second attractive direction of the future research is related to the application of the projection technique for the TB model parameterization, which gives us access to effective multi-band models of a broad variety of systems and enables to solve many relevant open questions. As was already mentioned in the end of Chapter 5, with the projection technique it is in principle possible to accurately and unambiguously calculate TB parameters for supercells, such as the $\text{Bi}_2\text{Sr}_2\text{CaCu}_2\text{O}_{8+\delta}$ supercell, even in the case of multiple bands. This technique is a powerful computational tool for studies of inhomogeneity effects in strongly correlated systems.

Appendix A

Additional information for Cs_2CuCl_4 and Cs_2CuBr_4

A.1 Computational details of the Cs_2CuCl_4 and Cs_2CuBr_4 crystal structure optimization

The DFT crystal structure optimizations for Cs_2CuCl_4 and Cs_2CuBr_4 are performed with the FPLO code (Ref. [Koepernik99], Section 2.2.2), in the scalar relativistic approximation with up to 512 \mathbf{k} -points in the full Brillouin zone.

The antiferromagnetic spin arrangement of the GGA[afm] and GGA+U[afm] optimization schemes is shown in Fig. A.1, where the Cs_2CuCl_4 unit cell is doubled in the b direction, along the Cu chains. In order to produce such an arrangement, the symmetry of the supercell is lowered to the space group $P21/c$, with two inequivalent Cu atoms. Our choice of this particular antiferromagnetic configuration is due to its resemblance to the experimentally observed 120° ground state configuration [Coldea01]. The considered antiferromagnetic configuration is collinear, which is beneficial in terms of computational effort, and also fulfills the requirement that the strongest couplings J are satisfied and the second strongest couplings J' are partially satisfied.

A.2 Experimental and relaxed crystal structures of Cs_2CuCl_4 and Cs_2CuBr_4

Below, we provide the Cs_2CuCl_4 and Cs_2CuBr_4 relative atomic positions obtained after structural optimization within different schemes. For a quick reference, we also cite

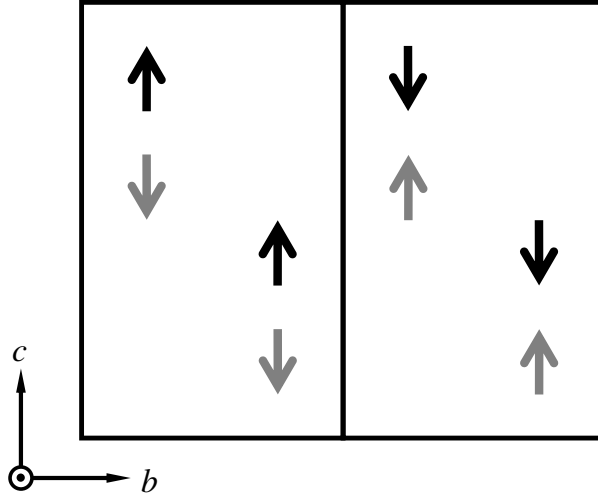


FIGURE A.1: Cu spin configuration of a $1 \times 2 \times 1$ supercell of Cs_2CuCl_4 adopted for the structural optimization within the GGA+U[afm] scheme.

Ref. [Bailleul91] for the experimentally found structure of Cs_2CuCl_4 and Ref. [Morosin60] for that of Cs_2CuBr_4 .

In the case of Cs_2CuCl_4 , for the experimental structure and structures relaxed with non-spin-resolved and ferromagnetic calculations, the lattice constants are $a = 9.769 \text{ \AA}$, $b = 7.607 \text{ \AA}$, $c = 12.381 \text{ \AA}$ and the space group is $Pnma$. The structures relaxed with antiferromagnetic calculations (GGA[afm] and GGA+U[afm]), for which the relaxation was constrained by the symmetry of the $P21/c$ space group in a supercell, were found to eventually belong to the same space group $P21/c$ but in a reduced cell, with the same unit cell parameters as those of the original full-symmetry unit cell of the compound.

LDA[nm] relaxed structure of Cs_2CuCl_4

	x	y	z
Cs(1)	0.1322	0.25	0.1005
Cs(2)	0.9837	0.75	0.3287
Cu	0.2322	0.25	0.4149
Cl(1)	0.0115	0.25	0.3692
Cl(2)	0.3494	0.25	0.5697
Cl(3)	0.2824	0.9772	0.3654

GGA[nm] relaxed structure of Cs_2CuCl_4

	x	y	z
Cs(1)	0.1329	0.25	0.1050
Cs(2)	0.9864	0.75	0.3321
Cu	0.2320	0.25	0.4165
Cl(1)	0.0045	0.25	0.3751
Cl(2)	0.3507	0.25	0.5743
Cl(3)	0.2878	0.9779	0.3615

GGA[fm] relaxed structure of Cs_2CuCl_4

	x	y	z
Cs(1)	0.1318	0.25	0.1042
Cs(2)	0.9903	0.75	0.3308
Cu	0.2311	0.25	0.4178
Cl(1)	0.0039	0.25	0.3768
Cl(2)	0.3479	0.25	0.5764
Cl(3)	0.2918	0.9823	0.3588

GGA+U[fm] relaxed structure of Cs_2CuCl_4

	x	y	z
Cs(1)	0.1321	0.25	0.1026
Cs(2)	0.9948	0.75	0.3302
Cu	0.2320	0.25	0.4175
Cl(1)	0.0043	0.25	0.3791
Cl(2)	0.3442	0.25	0.5779
Cl(3)	0.2961	0.9848	0.3556

GGA[afm] relaxed structure of Cs_2CuCl_4

	x	y	z
Cs(1)	0.1317	0.2503	0.1044
Cs(2)	0.9899	0.7504	0.3309
Cu	0.2312	0.2502	0.4177
Cl(1)	0.0037	0.2497	0.3765
Cl(2)	0.3483	0.2507	0.5762
Cl(3a)	0.2912	0.5181	0.3591
Cl(3b)	0.2916	0.9823	0.3595

GGA+U[afm] relaxed structure of Cs_2CuCl_4

	x	y	z
Cs(1)	0.1321	0.2501	0.1029
Cs(2)	0.9946	0.7501	0.3302
Cu	0.2319	0.2501	0.4175
Cl(1)	0.0037	0.2499	0.3790
Cl(2)	0.3446	0.2501	0.5777
Cl(3a)	0.2959	0.5151	0.3558
Cl(3b)	0.2959	0.9851	0.3557

Experimentally determined structure of Cs_2CuCl_4

	x	y	z
Cs(1)	0.1340	0.25	0.1031
Cs(2)	0.9433	0.75	0.3252
Cu	0.2302	0.25	0.4182
Cl(1)	0.0050	0.25	0.3820
Cl(2)	0.3433	0.25	0.5739
Cl(3)	0.2936	0.9881	0.3550

In the case of Cs_2CuBr_4 , the lattice constants are $a = 10.195 \text{ \AA}$, $b = 7.965 \text{ \AA}$, $c = 12.936 \text{ \AA}$ and the space group is $Pnma$.

LDA[nm] relaxed structure of Cs_2CuBr_4

	x	y	z
Cs(1)	0.1244	0.25	0.1030
Cs(2)	0.0142	0.25	0.6638
Cu	0.2345	0.25	0.4159
Br(1)	0.0090	0.25	0.3715
Br(2)	0.3497	0.25	0.5751
Br(3)	0.2882	0.5267	0.3649

GGA[nm] relaxed structure of Cs_2CuBr_4

	x	y	z
Cs(1)	0.1272	0.25	0.1072
Cs(2)	0.0117	0.25	0.6619
Cu	0.2322	0.25	0.4168
Br(1)	0.0001	0.25	0.3756
Br(2)	0.3499	0.25	0.5787
Br(3)	0.2921	0.5257	0.3603

GGA[fm] relaxed structure of Cs_2CuBr_4

	x	y	z
Cs(1)	0.1260	0.25	0.1059
Cs(2)	0.0060	0.25	0.6628
Cu	0.2312	0.25	0.4187
Br(1)	-0.0002	0.25	0.3773
Br(2)	0.3456	0.25	0.5818
Br(3)	0.2977	0.5197	0.3570

GGA+U[fm] relaxed structure of Cs_2CuBr_4

	x	y	z
Cs(1)	0.1268	0.25	0.1044
Cs(2)	0.0030	0.25	0.6637
Cu	0.2326	0.25	0.4180
Br(1)	0.0004	0.25	0.3789
Br(2)	0.3435	0.25	0.5825
Br(3)	0.3004	0.5177	0.3542

Experimentally determined structure of Cs_2CuBr_4

	x	y	z
Cs(1)	0.1290	0.25	0.1058
Cs(2)	0.0049	0.25	0.6694
Cu	0.2311	0.25	0.4187
Br(1)	0.0010	0.25	0.3819
Br(2)	0.3440	0.25	0.5797
Br(3)	0.2960	0.5138	0.3546

A.3 Tight-binding model for Cs_2CuBr_4

The bandstructures of Cs_2CuBr_4 that have been calculated using the experimental and relaxed structural parameters (Fig. 4.7) are parametrized in terms of three-band TB models by means of the Wannier function projection method (Section 2.5.1). The three-band TB model includes the Cu $3d_{x^2-y^2}$, $3d_{xz}$ and $3d_{yz}$ orbitals making up the t_{2g} states in the local coordinate frame, which we choose to be rotated by 45° around the z axis with respect to the coordinate frame shown in Fig. 4.5 (c). With this choice, the number of independent model parameters has been found to be minimal. The five sets of the TB model parameters corresponding to the LDA[nm], GGA[nm], GGA[fm] and GGA+U[fm] relaxed structures as well as to the experimental structure of Cs_2CuBr_4 are presented in Table A.1. In the case of the LDA[nm] relaxed structure, where the Cu $3d_{x^2-y^2}$ band at the Fermi level is well separated, the parameterization is performed for the single-band model, similarly to the Cs_2CuCl_4 case. To illustrate the excellent agreement between the model and DFT bandstructures that can be achieved with the projection method, we show in Fig. A.2 the model (red dashed lines) and DFT (black solid lines) bandstructures of Cs_2CuBr_4 , calculated using the experimental structural data. The model bandstructure has been obtained from a model that includes 22 nearest

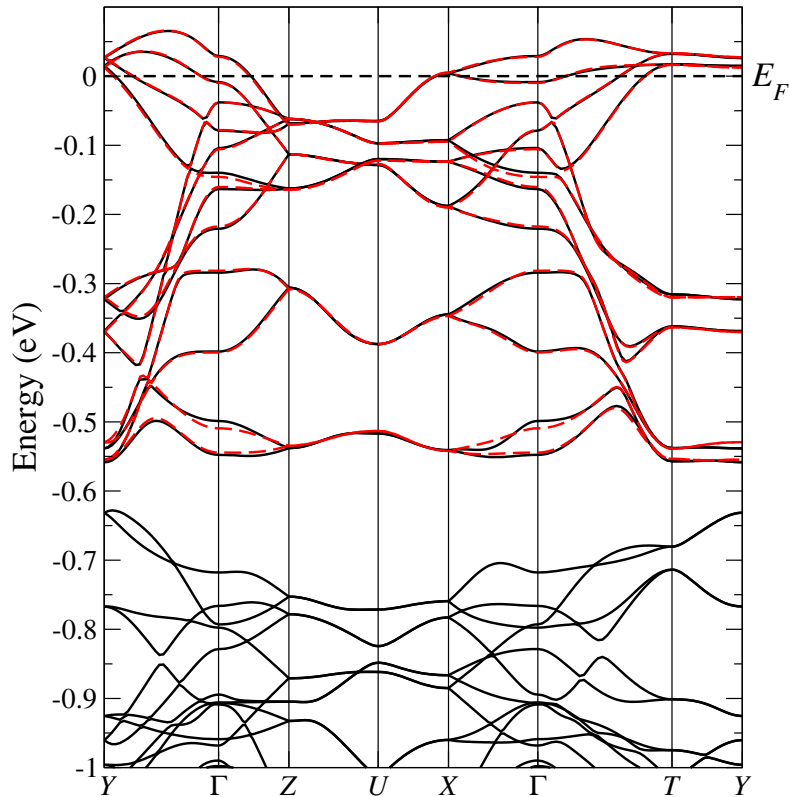


FIGURE A.2: The DFT (black solid lines) and TB model (red dashed lines) bandstructures of Cs_2CuBr_4 , calculated with the experimental structural data.

neighbors and has 151 independent model parameters that describe various intra- and interorbital electron hopping integrals.

A.4 Calculation of exchange couplings for Cs_2CuCl_4 and Cs_2CuBr_4 : Computational details

For Cs_2CuCl_4 and Cs_2CuBr_4 , we take into account seven important exchange couplings corresponding to the first seven hopping integrals in Table 4.3, which are J , J' , $J''_{\text{eff}} = J'' + J_6$, J_1 , J_3 , J_7 and J_8 [see Fig. 4.8]. This choice defines the number of antiferromagnetic configurations to be calculated. The combined coupling J''_{eff} is introduced because the considered unit cell (which is a $2 \times 2 \times 1$ supercell) does not allow a separate calculation of the couplings J'' and J_6 but only their calculation as a sum. Since J'' is presumably larger than J_6 , J''_{eff} gives an approximate value of J'' .

The choice of the supercell is dictated by the peculiarities of the Cs_2CuCl_4 and Cs_2CuBr_4 magnetic sublattices. First, since the candidate for the largest coupling J connects Cu

TABLE A.1: The TB model parameters in meV for the Cs_2CuBr_4 Cu $3d_{x^2-y^2}$, $3d_{xz}$ and $3d_{yz}$ bands, calculated from the various Cs_2CuBr_4 crystal structures by means of the projection technique.

		LDA[nm]	GGA[nm]	GGA[fm]	GGA+U[fm]	exp.
μ	$d_{x^2-y^2} \leftrightarrow d_{x^2-y^2}$	-19.1	-52.3	-45.4	-45.9	-41.0
	$d_{xz} \leftrightarrow d_{xz}$		-425.1	-329.2	-289.3	-310.0
	$d_{yz} \leftrightarrow d_{yz}$		-476.9	-410.4	-364.0	-393.9
	$d_{x^2-y^2} \leftrightarrow d_{yz}$		16.5	16.7	13.6	13.3
t	$d_{x^2-y^2} \leftrightarrow d_{x^2-y^2}$	57.3	46.0	38.3	33.5	30.6
	$d_{x^2-y^2} \leftrightarrow d_{xz}$		59.4	48.7	44.1	41.0
	$d_{x^2-y^2} \leftrightarrow d_{yz}$		0.4	0.6	0.8	0.8
	$d_{xz} \leftrightarrow d_{xz}$		119.1	110.1	105.8	100.2
	$d_{xz} \leftrightarrow d_{yz}$		1.4	0.6	0.5	0.7
	$d_{yz} \leftrightarrow d_{yz}$		17.1	15.0	14.1	13.0
t'	$d_{x^2-y^2} \leftrightarrow d_{x^2-y^2}$	17.0	20.4	22.7	23.7	23.7
	$d_{x^2-y^2} \leftrightarrow d_{xz}$		10.2	10.8	10.8	11.0
	$d_{x^2-y^2} \leftrightarrow d_{yz}$		11.9	15.7	17.4	17.0
	$d_{x^2-y^2} \leftrightarrow d_{yz}$		5.5	5.7	6.1	6.0
	$d_{x^2-y^2} \leftrightarrow d_{yz}$		15.2	16.9	17.6	17.1
	$d_{xz} \leftrightarrow d_{xz}$		0.1	0.2	0.3	0.6
	$d_{xz} \leftrightarrow d_{yz}$		2.9	4.2	4.9	5.0
	$d_{xz} \leftrightarrow d_{yz}$		13.7	14.3	14.7	14.2
	$d_{yz} \leftrightarrow d_{yz}$		3.5	4.8	5.5	5.4
t''	$d_{x^2-y^2} \leftrightarrow d_{x^2-y^2}$	3.9	0.6	5.8	6.4	7.2
	$d_{x^2-y^2} \leftrightarrow d_{yz}$		11.2	18.8	21.7	23.4
	$d_{x^2-y^2} \leftrightarrow d_{yz}$		6.4	7.7	8.2	8.4
	$d_{xz} \leftrightarrow d_{xz}$		15.0	14.2	14.0	12.5
	$d_{yz} \leftrightarrow d_{yz}$		2.2	1.5	1.6	1.0
t_1	$d_{x^2-y^2} \leftrightarrow d_{x^2-y^2}$	10.6	9.6	8.0	7.6	8.8
	$d_{x^2-y^2} \leftrightarrow d_{xz}$		5.3	4.1	3.8	5.1
	$d_{x^2-y^2} \leftrightarrow d_{yz}$		1.3	1.8	2.2	1.8
	$d_{xz} \leftrightarrow d_{xz}$		3.0	2.3	2.2	2.8
	$d_{xz} \leftrightarrow d_{yz}$		3.7	3.3	2.8	2.8
	$d_{yz} \leftrightarrow d_{yz}$		11.6	10.6	10.1	9.9
t_3	$d_{x^2-y^2} \leftrightarrow d_{x^2-y^2}$	15.1	15.8	13.8	11.4	10.2
	$d_{x^2-y^2} \leftrightarrow d_{xz}$		4.1	4.8	5.5	5.4
	$d_{x^2-y^2} \leftrightarrow d_{yz}$		12.7	13.0	13.2	11.5
	$d_{xz} \leftrightarrow d_{xz}$		5.6	7.8	8.5	8.4
	$d_{xz} \leftrightarrow d_{yz}$		26.3	27.7	27.7	27.0
	$d_{yz} \leftrightarrow d_{yz}$		50.5	49.2	48.0	46.9

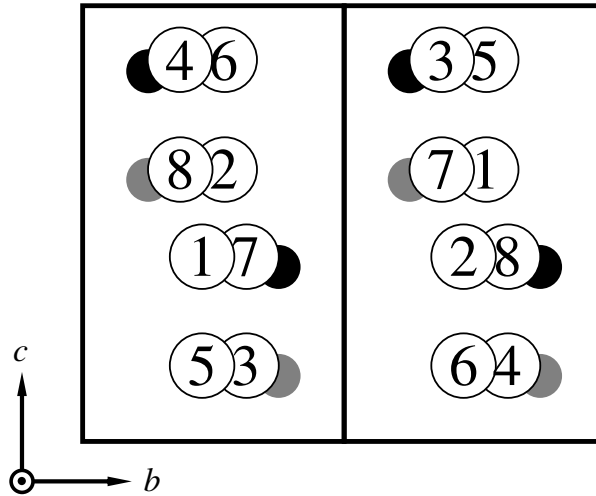


FIGURE A.3: Labeling of the Cu atoms in the $2 \times 2 \times 1$ supercell of Cs_2CuCl_4 or Cs_2CuBr_4 . The black and gray circles denote Cu atoms that belong to adjacent Cu layers, parallel to the bc plane. Since the supercell contains two unit cells along the a axis, the black and gray Cu lattices are doubled, which is not visible in the bc projection. The two encircled figures, one on top of the other, label the Cu atoms that have common y and z coordinates, but whose x coordinates differ by the lattice constant a such that the top figure refers to the Cu atom with larger x coordinate.

atoms that belong to adjacent primitive unit cells in Cs_2CuCl_4 and Cs_2CuBr_4 , the primitive unit cell has to be doubled in the b direction. Otherwise, J would be always canceled in any $E^{\text{FM}} - E_i^{\text{AFM}}$ difference. Also, in order to be able to discern the inequivalent couplings J_1 and J_3 , we double the unit cell once more in the a direction and thus end up with a $2 \times 2 \times 1$ supercell. In the supercell, we set eight out of 16 Cu atoms inequivalent in order to be able to arrange the required seven antiferromagnetic configurations within the same unit cell space group, which is $P-1$. It is important to stay within the same space group during total energy calculations for Cs_2CuCl_4 and Cs_2CuBr_4 as in these compounds the exchange couplings are small and integration over differently sampled Brillouin zones can affect the accuracy of the results.

Given that the Cu atoms in the $2 \times 2 \times 1$ supercell of Cs_2CuCl_4 or Cs_2CuBr_4 are labeled as shown in Fig. A.3, the seven antiferromagnetic (or ferrimagnetic) spin configurations, considered in order to calculate exchange couplings J , J' , J''_{eff} , J_1 , J_3 , J_7 and J_8 by the total energy difference method, are the following:

	Cu1	Cu2	Cu3	Cu4	Cu5	Cu6	Cu7	Cu8
conf. 1:	↑	↓	↑	↓	↑	↓	↑	↓
conf. 2:	↓	↓	↑	↑	↑	↑	↓	↓
conf. 3:	↑	↑	↑	↑	↑	↑	↓	↓
conf. 4:	↑	↑	↑	↑	↓	↓	↓	↓
conf. 5:	↑	↓	↓	↑	↑	↓	↓	↑
conf. 6:	↓	↓	↑	↑	↓	↓	↑	↑
conf. 7:	↑	↓	↓	↓	↓	↑	↑	↑

Each of these spin configurations leads to a corresponding equation:

$$\begin{aligned}
2J + 2J' + J_1 + J_3 + 4J_8 &= E_1/4, \\
2J' + J''_{\text{eff}} + 2J_8 &= E_2/8, \\
2J' + J''_{\text{eff}} + J_1 + 2J_8 + J_7 &= E_3/4, \\
J''_{\text{eff}} + J_1 + J_3 + 2J_8 + 2J_7 &= E_4/4, \\
2J + 2J' + J''_{\text{eff}} + J_1 + J_3 + 2J_8 + 2J_7 &= E_5/4, \\
4J' + J''_{\text{eff}} + J_1 + J_3 + 2J_8 + 2J_7 &= E_6/4, \\
4J + 8J' + 6J''_{\text{eff}} + 3J_1 + 3J_3 + 8J_8 + 4J_7 &= E_7,
\end{aligned}$$

where $E_i = E^{\text{FM}} - E_i^{\text{AFM}}$, $i = 1, \dots, 7$, with E^{FM} being the energy of the supercell in the ferromagnetic configuration of Cu spins and E_i^{AFM} being the energy of the supercell in the antiferromagnetic configuration i .

The total energy calculations were performed with the FPLO code. Test calculations with Wien2k confirm the results. In the FPLO code, we chose a $5 \times 4 \times 3$ mesh of \mathbf{k} -points for the supercell Brillouin zone integration and kept other settings at default. The scheme to compute magnetic exchange for a given structure consisted of a series of total energy calculations within the AMF version of the GGA+U, with $U = 4, 6$ and 8 eV and $J = 1$ eV in all cases. This scheme was applied to the experimental structures of Cs_2CuCl_4 and Cs_2CuBr_4 as well as to their GGA[nm], GGA[fm] and GGA+U[fm] relaxed structures.

Bibliography

- [Ahn03] C. H. Ahn, J. M. Triscone and J. Mannhart. *Electric field effect in correlated oxide systems*. Nature **424**, 1015–1018 (2003).
- [Aichhorn09] Markus Aichhorn, Leonid Pourovskii, Veronica Vildosola, Michel Ferrero, Olivier Parcollet, Takashi Miyake, Antoine Georges and Silke Biermann. *Dynamical mean-field theory within an augmented plane-wave framework: Assessing electronic correlations in the iron pnictide LaFeAsO*. Phys. Rev. B **80**, 085101 (2009).
- [Alicea09] Jason Alicea, Andrey V. Chubukov and Oleg A. Starykh. *Quantum Stabilization of the 1/3-Magnetization Plateau in Cs₂CuBr₄*. Phys. Rev. Lett. **102**, 137201 (2009).
- [Alvarez05] Gonzalo Alvarez, Matthias Mayr, Adriana Moreo and Elbio Dagotto. *Areas of superconductivity and giant proximity effects in underdoped cuprates*. Phys. Rev. B **71**, 014514 (2005).
- [Andersen75] O. Krogh Andersen. *Linear methods in band theory*. Phys. Rev. B **12**, 3060–3083 (1975).
- [Andersen94] O. K. Andersen, O. Jepsen, A. I. Liechtenstein and I. I. Mazin. *Plane dimpling and saddle-point bifurcation in the band structures of optimally doped high-temperature superconductors: A tight-binding model*. Phys. Rev. B **49**, 4145–4157 (1994).
- [Andersen00] O. K. Andersen and T. Saha-Dasgupta. *Muffin-tin orbitals of arbitrary order*. Phys. Rev. B **62**, R16219–R16222 (2000).
- [Anderson59] P. W. Anderson. *New Approach to the Theory of Superexchange Interactions*. Phys. Rev. **115**, 2 (1959).
- [Anderson73] P.W. Anderson. *Resonating valence bonds: A new kind of insulator?* Materials Research Bulletin **8**, 153–160 (1973).

- [Anderson87] P. W. Anderson. *The resonating valence bond state in La_2CuO_4 and superconductivity*. Science **235**, 1196–1198 (1987).
- [Anderson04] P. W. Anderson, P. A. Lee, M. Randeria, T. M. Rice, N. Trivedi and F. C. Zhang. *The physics behind high-temperature superconducting cuprates: the 'plain vanilla' version of RVB*. Journal of Physics: Condensed Matter **16**, R755 (2004).
- [Ando99] Yoichi Ando, G. S. Boebinger, A. Passner, L. F. Schneemeyer, T. Kimura, M. Okuya, S. Watauchi, J. Shimoyama, K. Kishio, K. Tamasaku, N. Ichikawa and S. Uchida. *Resistive upper critical fields and irreversibility lines of optimally doped high- T_c cuprates*. Phys. Rev. B **60**, 12475–12479 (1999).
- [Anisimov91] Vladimir I. Anisimov, Jan Zaanen and Ole K. Andersen. *Band theory and Mott insulators: Hubbard U instead of Stoner I* . Phys. Rev. B **44**, 943–954 (1991).
- [Anisimov97] V. I. Anisimov, A. I. Poteryaev, M. A. Korotin, A. O. Anokhin and G. Kotliar. *First-principles calculations of the electronic structure and spectra of strongly correlated systems: dynamical mean-field theory*. Journal of Physics: Condensed Matter **9**, 7359 (1997).
- [Aryasetiawan04] F. Aryasetiawan, M. Imada, A. Georges, G. Kotliar, S. Biermann and A. I. Lichtenstein. *Frequency-dependent local interactions and low-energy effective models from electronic structure calculations*. Phys. Rev. B **70**, 195104 (2004).
- [Atkinson05] W. A. Atkinson. *Local density of states of a d -wave superconductor with inhomogeneous antiferromagnetic correlations*. Phys. Rev. B **71**, 024516 (2005).
- [Bailleul91] S. Bailleul, D. Svoronos, P. Porcher and A. Tomas. *Précisions sur la structure de Cs_2CuCl_4* . C. R. Acad. Sci. (Paris), Sér. II **313**, 1149–1153 (1991).
- [Balents10] Leon Balents. *Spin liquids in frustrated magnets*. Nature **464**, 199–208 (2010).
- [Bardeen57] J. Bardeen, L. N. Cooper and J. R. Schrieffer. *Theory of Superconductivity*. Phys. Rev. **108**, 1175–1204 (1957).
- [Baskaran87] G. Baskaran, Z. Zou and P. W. Anderson. *The resonating valence bond state and high- T_c superconductivity – A mean field theory*. Solid State Communications **63**, 973 – 976 (1987).

-
- [Bednorz86] J. G. Bednorz and K. A. Müller. *Possible high- T_c superconductivity in the BaLaCuO system*. Zeitschrift für Physik B Condensed Matter **64**, 189–193 (1986).
- [Berk66] N. F. Berk and J. R. Schrieffer. *Effect of Ferromagnetic Spin Correlations on Superconductivity*. Phys. Rev. Lett. **17**, 433–435 (1966).
- [Bickers89] N. E. Bickers, D. J. Scalapino and S. R. White. *Conserving Approximations for Strongly Correlated Electron Systems: Bethe-Salpeter Equation and Dynamics for the Two-Dimensional Hubbard Model*. Phys. Rev. Lett. **62**, 961–964 (1989).
- [Blaha90] P. Blaha, K. Schwarz, P. Sorantin and S.B. Trickey. *Full-potential, linearized augmented plane wave programs for crystalline systems*. Computer Physics Communications **59**, 399 – 415 (1990).
- [Blaha01] P. Blaha, K. Schwarz, G. K. H. Madsen, D. Kvasnicka and J Luitz. *WIEN2k, An Augmented Plane Wave + Local Orbitals Program for Calculating Crystal Properties*. (Karlheinz Schwarz, Techn. Universität Wien, Austria) (2001). ISBN 3-9501031-1-2.
- [Bloch29] Felix Bloch. *Über die Quantenmechanik der Elektronen in Kristallgittern*. Zeitschrift für Physik A Hadrons and Nuclei **52**, 555–600 (1929).
- [Blöchl90] Peter E. Blöchl. *Generalized separable potentials for electronic-structure calculations*. Phys. Rev. B **41**, 5414–5416 (1990).
- [Blöchl94] P. E. Blöchl. *Projector augmented-wave method*. Phys. Rev. B **50**, 17953–17979 (1994).
- [Bohm53] David Bohm and David Pines. *A Collective Description of Electron Interactions: III. Coulomb Interactions in a Degenerate Electron Gas*. Phys. Rev. **92**, 609–625 (1953).
- [Born27] M. Born and R. Oppenheimer. *Zur Quantentheorie der Moleküle*. Annalen der Physik **84**, 457–484 (1927).
- [Bulut93] N. Bulut and D.J. Scalapino. *The effective electron-electron interaction in the 2D Hubbard model*. Journal of Physics and Chemistry of Solids **54**, 1109 – 1113 (1993). Special Issue Spectroscopies in Novel Superconductors.

- [Buzdin80] Aleksandr I. Buzdin and L. N. Bulaevskii. *Spin-Peierls transition in quasi-one-dimensional crystals*. Soviet Physics Uspekhi **23**, 409 (1980).
- [Caimi04] G. Caimi, L. Degiorgi, N. N. Kovaleva, P. Lemmens and F. C. Chou. *Infrared optical properties of the spin- $\frac{1}{2}$ quantum magnet $TiOCl$* . Phys. Rev. B **69**, 125108 (2004).
- [Car85] R. Car and M. Parrinello. *Unified Approach for Molecular Dynamics and Density-Functional Theory*. Phys. Rev. Lett. **55**, 2471–2474 (1985).
- [Carlin85] Richard L. Carlin, Ramon Burriel, Fernando Palacio, Rachel A. Carlin, S. F. Keij and David W. Carnegie. *Linear chain antiferromagnetic interactions in Cs_2CuCl_4* . J. Appl. Phys. **57**, 3351–3352 (1985).
- [Ceperley80] D. M. Ceperley and B. J. Alder. *Ground State of the Electron Gas by a Stochastic Method*. Phys. Rev. Lett. **45**, 566–569 (1980).
- [Chao77] K. A. Chao, J. Spalek and A. M. Oles. *Kinetic exchange interaction in a narrow S -band*. Journal of Physics C: Solid State Physics **10**, L271 (1977).
- [Chung03] Chung-Hou Chung, Klaus Voelker and Yong Baek Kim. *Statistics of spinons in the spin-liquid phase of Cs_2CuCl_4* . Phys. Rev. B **68**, 094412 (2003).
- [Claeson74] Tord Claeson and Stig Lundqvist. *The Microscopic Theory of Superconductivity – Verifications and Extensions*. Physica Scripta **10**, 5 (1974).
- [Coldea96] R. Coldea, D. A. Tennant, R. A. Cowley, D. F. McMorrow, B. Dorner and Z. Tylczynski. *Neutron scattering study of the magnetic structure of Cs_2CuCl_4* . Journal of Physics: Condensed Matter **8**, 7473–7491 (1996).
- [Coldea01] R. Coldea, D. A. Tennant, A. M. Tsvelik and Z. Tylczynski. *Experimental Realization of a 2D Fractional Quantum Spin Liquid*. Phys. Rev. Lett. **86**, 1335–1338 (2001).
- [Coldea02] R. Coldea, D. A. Tennant, K. Habicht, P. Smeibidl, C. Wolters and Z. Tylczynski. *Direct Measurement of the Spin Hamiltonian*

-
- and Observation of Condensation of Magnons in the 2D Frustrated Quantum Magnet Cs_2CuCl_4* . Phys. Rev. Lett. **88**, 137203 (2002).
- [Coldea03] R. Coldea, D. A. Tennant and Z. Tylczynski. *Extended scattering continua characteristic of spin fractionalization in the two-dimensional frustrated quantum magnet Cs_2CuCl_4 observed by neutron scattering*. Phys. Rev. B **68**, 134424 (2003).
- [Cong11] P. T. Cong, B. Wolf, M. de Souza, N. Krüger, A. A. Haghighirad, S. Gottlieb-Schoenmeyer, F. Ritter, W. Assmus, I. Opahle, K. Foyevtsova, H. O. Jeschke, R. Valentí, L. Wiehl and M. Lang. *Distinct magnetic regimes through site-selective atom substitution in the frustrated quantum antiferromagnet $Cs_2CuCl_{4-x}Br_x$* . Phys. Rev. B **83**, 064425 (2011).
- [Cren00] T. Cren, D. Roditchev, W. Sacks, J. Klein, J.-B. Moussy, C. Deville-Cavellin and M. Laguës. *Influence of Disorder on the Local Density of States in High- T_c Superconducting Thin Films*. Phys. Rev. Lett. **84**, 147–150 (2000).
- [Czyżyk94] M. T. Czyżyk and G. A. Sawatzky. *Local-density functional and on-site correlations: The electronic structure of La_2CuO_4 and $LaCuO_3$* . Phys. Rev. B **49**, 14211–14228 (1994).
- [Dagotto94] Elbio Dagotto. *Correlated electrons in high-temperature superconductors*. Rev. Mod. Phys. **66**, 763–840 (1994).
- [Dagotto05] Elbio Dagotto. *Complexity in Strongly Correlated Electronic Systems*. Science **309**, 257–262 (2005).
- [Dirac30] P. A. M. Dirac. *Note on Exchange Phenomena in the Thomas Atom*. Proc. Cambridge Phil. Soc. **26**, 376–385 (1930).
- [Emery87] V. J. Emery. *Theory of high- T_c superconductivity in oxides*. Phys. Rev. Lett. **58**, 2794–2797 (1987).
- [Eskes93] Henk Eskes and John H. Jefferson. *Superexchange in the cuprates*. Phys. Rev. B **48**, 9788–9798 (1993).
- [Fabrizio99] Michele Fabrizio, Alexander O. Gogolin and Alexander A. Nersisyan. *From Band Insulator to Mott Insulator in One Dimension*. Phys. Rev. Lett. **83**, 2014–2017 (1999).

- [Fermi27] E. Fermi. *Un Metodo Statistico per la Determinazione di alcune Propriet dell'Atomo*. Rend. Accad. Naz. Lincei **6**, 602–607 (1927).
- [Feynman39] R. P. Feynman. *Forces in Molecules*. Phys. Rev. **56**, 340–343 (1939).
- [Fischer07] Øystein Fischer, Martin Kugler, Ivan Maggio-Aprile, Christophe Berthod and Christoph Renner. *Scanning tunneling spectroscopy of high-temperature superconductors*. Rev. Mod. Phys. **79**, 353–419 (2007).
- [Forthaus08] Martin K. Forthaus, Timo Taetz, Angela Möller and Mohsen M. Abd-Elmeguid. *Effect of pressure on the electrical transport and structure of $TiOCl$* . Phys. Rev. B **77**, 165121 (2008).
- [Fortune09] N. A. Fortune, S. T. Hannahs, Y. Yoshida, T. E. Sherline, T. Ono, H. Tanaka and Y. Takano. *Cascade of Magnetic-Field-Induced Quantum Phase Transitions in a Spin- $\frac{1}{2}$ Triangular-Lattice Antiferromagnet*. Phys. Rev. Lett. **102**, 257201 (2009).
- [Foyevtsova09] Kateryna Foyevtsova, Roser Valentí and P. J. Hirschfeld. *Effect of dopant atoms on local superexchange in cuprate superconductors: A perturbative treatment*. Phys. Rev. B **79**, 144424 (2009).
- [Foyevtsova10] Kateryna Foyevtsova, H. C. Kandpal, Harald O. Jeschke, S. Graser, H.-P. Cheng, Roser Valentí and P. J. Hirschfeld. *Modulation of pairing interaction in $Bi_2Sr_2CaCu_2O_{8+\delta}$ by an O dopant: A density functional theory study*. Phys. Rev. B **82**, 054514 (2010).
- [Fujii07] Y Fujii, H Hashimoto, Y Yasuda, H Kikuchi, M Chiba, S Matsubara and M Takigawa. *Commensurate and incommensurate phases of the distorted triangular antiferromagnet Cs_2CuBr_4 studied using ^{133}Cs NMR*. Journal of Physics: Condensed Matter **19**, 145237 (2007).
- [Garg06] Arti Garg, H. R. Krishnamurthy and Mohit Randeria. *Can Correlations Drive a Band Insulator Metallic?* Phys. Rev. Lett. **97**, 046403 (2006).
- [Georges96] Antoine Georges, Gabriel Kotliar, Werner Krauth and Marcelo J. Rozenberg. *Dynamical mean-field theory of strongly correlated fermion systems and the limit of infinite dimensions*. Rev. Mod. Phys. **68**, 13 (1996).

-
- [Goodenough58] J. B. Goodenough. *An interpretation of the magnetic properties of the perovskite-type mixed crystals*. J. Phys. Chem. Solids **6**, 287 (1958).
- [Graser09] S. Graser, T. A. Maier, P. J. Hirschfeld and D. J. Scalapino. *Near-degeneracy of several pairing channels in multiorbital models for the Fe pnictides*. New Journal of Physics **11**, 025016 (2009).
- [Gros87] C. Gros, R. Joynt and T. M. Rice. *Antiferromagnetic correlations in almost-localized Fermi liquids*. Phys. Rev. B **36**, 381–393 (1987).
- [Gurvitch87] M. Gurvitch and A. T. Fiory. *Resistivity of $La_{1.825}Sr_{0.175}CuO_4$ and $YBa_2Cu_3O_7$ to 1100 K: Absence of saturation and its implications*. Phys. Rev. Lett. **59**, 1337–1340 (1987).
- [Haas07] H. Haas and J. G. Correia. *EFG calculations for Cu^{2+} compounds*. Hyperfine Interactions **176**, 9–13 (2007).
- [Hase93] Masashi Hase, Ichiro Terasaki and Kunimitsu Uchinokura. *Observation of the spin-Peierls transition in linear Cu^{2+} (spin-1/2) chains in an inorganic compound $CuGeO_3$* . Phys. Rev. Lett. **70**, 3651–3654 (1993).
- [He06] Y. He, T. S. Nunner, P. J. Hirschfeld and H.-P. Cheng. *Local Electronic Structure of $Bi_2Sr_2CaCu_2O_8$ near Oxygen Dopants: A Window on the High- T_c Pairing Mechanism*. Phys. Rev. Lett. **96**, 197002 (2006).
- [He08] Y. He, S. Graser, P. J. Hirschfeld and H.-P. Cheng. *Supermodulation in the atomic structure of the superconductor $Bi_2Sr_2CaCu_2O_{8+x}$ from ab initio calculations*. Phys. Rev. B **77**, 220507 (2008).
- [Hellmann37] H. Hellmann. *Einführung in die Quantenchemie*. Leipzig: Franz Deuticke (1937).
- [Hemberger05] J. Hemberger, M. Hoinkis, M. Klemm, M. Sing, R. Claessen, S. Horn and A. Loidl. *Heat capacity of the quantum magnet $TiOCl$* . Phys. Rev. B **72**, 012420 (2005).
- [Hettler99] Matthias H. Hettler and P. J. Hirschfeld. *Scattering by impurity-induced order-parameter “holes” in d-wave superconductors*. Phys. Rev. B **59**, 9606–9610 (1999).

- [Hirsch85a] J. E. Hirsch. *Attractive Interaction and Pairing in Fermion Systems with Strong On-Site Repulsion*. Phys. Rev. Lett. **54**, 1317–1320 (1985).
- [Hirsch85b] J. E. Hirsch. *Two-dimensional Hubbard model: Numerical simulation study*. Phys. Rev. B **31**, 4403–4419 (1985).
- [Hohenberg64] P. Hohenberg and W. Kohn. *Inhomogeneous Electron Gas*. Phys. Rev. **136**, B864–B871 (1964).
- [Hoinkis05] M. Hoinkis, M. Sing, J. Schäfer, M. Klemm, S. Horn, H. Benthien, E. Jeckelmann, T. Saha-Dasgupta, L. Pisani, R. Valentí and R. Claessen. *Electronic structure of the spin- $\frac{1}{2}$ quantum magnet $TiOCl$* . Phys. Rev. B **72**, 125127 (2005).
- [Howald01] C. Howald, P. Fournier and A. Kapitulnik. *Inherent inhomogeneities in tunneling spectra of $Bi_2Sr_2CaCu_2O_{8-x}$ crystals in the superconducting state*. Phys. Rev. B **64**, 100504 (2001).
- [Hubbard63] J. Hubbard. *Electron Correlations in Narrow Energy Bands*. Proceedings of the Royal Society of London. Series A, Mathematical and Physical Sciences **276**, 238–257 (1963).
- [Hubbard64] J. Hubbard. *Electron correlations in narrow energy bands. II. The degenerate band case*. Proc. R. Soc. Lond. A **277**, 237–259 (1964).
- [Imada98] Masatoshi Imada, Atsushi Fujimori and Yoshinori Tokura. *Metal-insulator transitions*. Rev. Mod. Phys. **70**, 1039–1263 (1998).
- [Isobe96] Masahiko Isobe and Yutaka Ueda. *Magnetic Susceptibility of Quasi-One-Dimensional Compound $\alpha-NaV_2O_5$ – Possible Spin-Peierls Compound with High Critical Temperature of 34 K*. Journal of the Physical Society of Japan **65**, 1178–1181 (1996).
- [Johnston09] S. Johnston, F. Vernay and T. P. Devereaux. *Impact of an oxygen dopant in $Bi_2Sr_2CaCu_2O_{8+\delta}$* . EPL (Europhysics Letters) **86**, 37007 (2009).
- [Kamerlingh Onnes11] H. Kamerlingh Onnes. *Further experiments with liquid helium. C. On the change of electric resistance of pure metals at very low temperatures, etc. IV. The resistance of pure mercury at helium temperatures*. Comm. Phys. Lab. Univ. Leiden **120b** (1911).
- [Kanamori59] J. Kanamori. *Superexchange interaction and symmetry properties of electron orbitals*. J. Phys. Chem. Solids **10**, 87 (1959).

-
- [Kancharla07] S. S. Kancharla and E. Dagotto. *Correlated Insulated Phase Suggests Bond Order between Band and Mott Insulators in Two Dimensions*. Phys. Rev. Lett. **98**, 016402 (2007).
- [Kataev03] V. Kataev, J. Baier, A. Möller, L. Jongen, G. Meyer and A. Freimuth. *Orbital order in the low-dimensional quantum spin system TiOCl probed by ESR*. Phys. Rev. B **68**, 140405 (2003).
- [Kim95] Y. C. Kim, J. R. Thompson, J. G. Ossandon, D. K. Christen and M. Paranthaman. *Equilibrium superconducting properties of grain-aligned HgBa₂Ca₂Cu₃O_{8+δ}*. Phys. Rev. B **51**, 11767–11772 (1995).
- [Kinoda03] G. Kinoda, T. Hasegawa, S. Nakao, T. Hanaguri, K. Kitazawa, K. Shimizu, J. Shimoyama and K. Kishio. *Observations of electronic inhomogeneity in heavily Pb-doped Bi₂Sr₂CaCu₂O_y single crystals by scanning tunneling microscopy*. Phys. Rev. B **67**, 224509 (2003).
- [Kivelson03] S. A. Kivelson, I. P. Bindloss, E. Fradkin, V. Oganesyan, J. M. Tranquada, A. Kapitulnik and C. Howald. *How to detect fluctuating stripes in the high-temperature superconductors*. Rev. Mod. Phys. **75**, 1201–1241 (2003).
- [Koepernik99] Klaus Koepernik and Helmut Eschrig. *Full-potential nonorthogonal local-orbital minimum-basis band-structure scheme*. Phys. Rev. B **59**, 1743–1757 (1999).
- [Kohn65] W. Kohn and L. J. Sham. *Self-Consistent Equations Including Exchange and Correlation Effects*. Phys. Rev. **140**, A1133–A1138 (1965).
- [Kohno07] Masanori Kohno, Oleg A. Starykh and Balents Leon. *Spinons and triplons in spatially anisotropic frustrated antiferromagnets*. Nature Physics **3**, 790–795 (2007).
- [Kotliar88] Gabriel Kotliar and Jialin Liu. *Superexchange mechanism and d-wave superconductivity*. Phys. Rev. B **38**, 5142–5145 (1988).
- [Kresse96] G. Kresse and J. Furthmüller. *Efficiency of ab-initio total energy calculations for metals and semiconductors using a plane-wave basis set*. Computational Materials Science **6**, 15 – 50 (1996).
- [Krüger] N. Krüger. Private communication.

- [Krüger10] N. Krüger, S. Belz, F. Schossau, A. A. Haghighirad, P. T. Cong, B. Wolf, S. Gottlieb-Schoenmeyer, F. Ritter and W. Assmus. *Stable Phases of the $Cs_2CuCl_{4-x}Br_x$ Mixed Systems*. *Crystal Growth & Design* **10**, 4456–4462 (2010).
- [Kugel82] Kliment I. Kugel and D. I. Khomskii. *The Jahn-Teller effect and magnetism: transition metal compounds*. *Soviet Physics Uspekhi* **25**, 231 (1982).
- [Kuntscher06] C. A. Kuntscher, S. Frank, A. Pashkin, M. Hoinkis, M. Klemm, M. Sing, S. Horn and R. Claessen. *Possible pressure-induced insulator-to-metal transition in low-dimensional $TiOCl$* . *Phys. Rev. B* **74**, 184402 (2006).
- [Laasonen91] Kari Laasonen, Roberto Car, Changyol Lee and David Vanderbilt. *Implementation of ultrasoft pseudopotentials in ab initio molecular dynamics*. *Phys. Rev. B* **43**, 6796–6799 (1991).
- [Lang02] K. M. Lang, V. Madhavan, J. E. Hoffman, E. W. Hudson, H. Eisaki, S. Uchida and J. C. Davis. *Imaging the granular structure of high- T_c superconductivity in underdoped $Bi_2Sr_2CaCu_2O_{8+\delta}$* . *Nature* **415**, 412–416 (2002).
- [Langreth83] David C. Langreth and M. J. Mehl. *Beyond the local-density approximation in calculations of ground-state electronic properties*. *Phys. Rev. B* **28**, 1809–1834 (1983).
- [Lee06] Patrick A. Lee, Naoto Nagaosa and Xiao-Gang Wen. *Doping a Mott insulator: Physics of high-temperature superconductivity*. *Rev. Mod. Phys.* **78**, 17–85 (2006).
- [Lee10] Hunpyo Lee, Yu-Zhong Zhang, Harald O. Jeschke, Roser Valentí and Hartmut Monien. *Dynamical Cluster Approximation Study of the Anisotropic Two-Orbital Hubbard Model*. *Phys. Rev. Lett.* **104**, 026402 (2010).
- [Lemmens04] P. Lemmens, K. Y. Choi, G. Caimi, L. Degiorgi, N. N. Kovaleva, A. Seidel and F. C. Chou. *Giant phonon softening in the pseudo-gap phase of the quantum spin system $TiOCl$* . *Phys. Rev. B* **70**, 134429 (2004).
- [Liang88] J. K. Liang, S. S. Xie, G. C. Che, J. Q. Huang, Y. L. Zhang and Z. X. Zhao. *Crystal structure and superconductivity of $Bi_2Sr_2CaCu_2O_8$ compound*. *Mod. Phys. Lett. B* **2**, 483 (1988).

-
- [Lichtenstein98] A. I. Lichtenstein and M. I. Katsnelson. *Ab initio calculations of quasiparticle band structure in correlated systems: LDA++ approach*. Phys. Rev. B **57**, 6884–6895 (1998).
- [Lieb68] Elliott H. Lieb and F. Y. Wu. *Absence of Mott Transition in an Exact Solution of the Short-Range, One-Band Model in One Dimension*. Phys. Rev. Lett. **20**, 1445–1448 (1968).
- [Lindgren86] I. Lindgren and J. Morrison. *Atomic Many-Body Theory*. Springer-Verlag, Berlin (1986).
- [Madsen05] G. K. H. Madsen and P. Novák. *Charge order in magnetite. An LDA+U study*. EPL (Europhysics Letters) **69**, 777 (2005).
- [Maeda88] Hiroshi Maeda, Yoshiaki Tanaka, Masao Fukutomi and Toshihisa Asano. *A New High- T_c Oxide Superconductor without a Rare Earth Element*. Japanese Journal of Applied Physics **27**, L209–L210 (1988).
- [Mahan81] Gerald D. Mahan. *Many-Particle Physics*. Plenum Press, New York (1981).
- [Maitra07] Tulika Maitra and Roser Valentí. *Orbital Order in ZnV_2O_4* . Phys. Rev. Lett. **99**, 126401 (2007).
- [Markiewicz05] R. S. Markiewicz, S. Sahrakorpi, M. Lindroos, Hsin Lin and A. Bansil. *One-band tight-binding model parametrization of the high- T_c cuprates including the effect of k_z dispersion*. Phys. Rev. B **72**, 054519 (2005).
- [Martin88] S. Martin, A. T. Fiory, R. M. Fleming, L. F. Schneemeyer and J. V. Waszczak. *Temperature Dependence of the Resistivity Tensor in Superconducting $Bi_2Sr_{2.2}Ca_{0.8}Cu_2O_8$ Crystals*. Phys. Rev. Lett. **60**, 2194–2197 (1988).
- [Maška07] Maciej M. Maška, Żaneta Śledź, Katarzyna Czajka and Marcin Mierzejewski. *Inhomogeneity-Induced Enhancement of the Pairing Interaction in Cuprate Superconductors*. Phys. Rev. Lett. **99**, 147006 (2007).
- [Matsubara56] Takeo Matsubara and Hirotsugu Matsuda. *A Lattice Model of Liquid Helium, I*. Progress of Theoretical Physics **16**, 569–582 (1956).

- [Mattheiss87] L. F. Mattheiss. *Electronic band properties and superconductivity in $La_{2-y}X_yCuO_4$* . Phys. Rev. Lett. **58**, 1028–1030 (1987).
- [McElroy05] K. McElroy, Jinho Lee, J. A. Slezak, D.-H. Lee, H. Eisaki, S. Uchida and J. C. Davis. *Atomic-Scale Sources and Mechanism of Nanoscale Electronic Disorder in $Bi_2Sr_2CaCu_2O_{8+\delta}$* . Science **309**, 1048–1052 (2005).
- [Medici09a] Luca de' Medici, S. R. Hassan, Massimo Capone and Xi Dai. *Orbital-Selective Mott Transition out of Band Degeneracy Lifting*. Phys. Rev. Lett. **102**, 126401 (2009).
- [Medici09b] Luca de' Medici, Xin Wang, Massimo Capone and Andrew J. Millis. *Correlation strength, gaps, and particle-hole asymmetry in high- T_c cuprates: A dynamical mean field study of the three-band copper-oxide model*. Phys. Rev. B **80**, 054501 (2009).
- [Misguich05] G. Misguich and C. Lhuillier. *Frustrated spin systems*, chapter Two-dimensional quantum antiferromagnets, pages 229–307. World-Scientific (2005).
- [Miyake86] K. Miyake, S. Schmitt-Rink and C. M. Varma. *Spin-fluctuation-mediated even-parity pairing in heavy-fermion superconductors*. Phys. Rev. B **34**, 6554–6556 (1986).
- [Moriya00] T. Moriya and K. Ueda. *Spin fluctuations and high temperature superconductivity*. Advances in Physics **49**, 555–606 (2000).
- [Morosin60] B. Morosin and E. C. Lingafelter. *The crystal structure of cesium tetrabromocuprate(II)*. Acta Crystallographica **13**, 807–809 (1960).
- [Mott49] N. F. Mott. *The basis of the theory of electron metals, with special reference to the transition metals*. Proc. Phys. Soc. London, Ser. A **62**, 416 (1949).
- [Mott56] N.F. Mott. *On the transition to metallic condition in semiconductors*. Canadian Journal of Physics **34**, 1356 (1956).
- [Mott61] N. F. Mott. *The transition to the metallic state*. Phil. Mag. **6**, 287–309 (1961).
- [Mott90] N. F. Mott. *Metal-Insulator Transitions*. Taylor and Francis, London/Philadelphia (1990).

-
- [Müller-Hartmann02] E. Müller-Hartmann and A. Reischl. *Derivation of effective spin models from a three band model for CuO_2 -planes*. Eur. Phys. J. B **28**, 173–183 (2002).
- [Nunner05] Tamara S. Nunner, Brian M. Andersen, Ashot Melikyan and P. J. Hirschfeld. *Dopant-Modulated Pair Interaction in Cuprate Superconductors*. Phys. Rev. Lett. **95**, 177003 (2005).
- [Ono] T. Ono. Private communication.
- [Ono03] T. Ono, H. Tanaka, H. Aruga Katori, F. Ishikawa, H. Mitamura and T. Goto. *Magnetization plateau in the frustrated quantum spin system Cs_2CuBr_4* . Phys. Rev. B **67**, 104431 (2003).
- [Ono04] T. Ono, H. Tanaka, O. Kolomyets, H. Mitamura, T. Goto, K. Nakajima, A. Oosawa, Y. Koike, K. Kakurai, J. Klenke, P. Smeibidle and M. Meißner. *Magnetization plateaux of the $S = 1/2$ two-dimensional frustrated antiferromagnet Cs_2CuBr_4* . Journal of Physics: Condensed Matter **16**, S773 (2004).
- [Ono05] Toshio Ono, Hidekazu Tanaka, O. Kolomyets, Hiroyuki Mitamura, Fumihiko Ishikawa, Tsuneaki Goto, Kenji Nakajima, Akira Oosawa, Yoshihiro Koike, Kazuhisa Kakurai, J. Klenke, P. Smeibidle, M. Meißner, R. Coldea, A. D. Tennant and J. Ollivier. *Field-Induced Phase Transitions Driven by Quantum Fluctuation in $S = 1/2$ Anisotropic Triangular Antiferromagnet Cs_2CuBr_4* . Progress of Theoretical Physics Supplement **159**, 217–221 (2005).
- [Pan01] S. H. Pan, J. P. O’Neal, R. L. Badzey, C. Chamon, H. Ding, J. R. Engelbrecht, Z. Wang, H. Eisaki, S. Uchida, A. K. Gupta, K.-W. Ng, E. W. Hudson, K. M. Lang and J. C. Davis. *Microscopic electronic inhomogeneity in the high- T_c superconductor $\text{Bi}_2\text{Sr}_2\text{CaCu}_2\text{O}_{8+x}$* . Nature **413**, 282–285 (2001).
- [Pauling29] Linus Pauling. *The principle determining the structure of complex ionic crystals*. Journal of the American Chemical Society **51**, 1010–1026 (1929).
- [Pavarini01] E. Pavarini, I. Dasgupta, T. Saha-Dasgupta, O. Jepsen and O. K. Andersen. *Band-Structure Trend in Hole-Doped Cuprates and Correlation with T_{cmax}* . Phys. Rev. Lett. **87**, 047003 (2001).

- [Perdew81] J. P. Perdew and Alex Zunger. *Self-interaction correction to density-functional approximations for many-electron systems*. Phys. Rev. B **23**, 5048–5079 (1981).
- [Perdew86] John P. Perdew and Wang Yue. *Accurate and simple density functional for the electronic exchange energy: Generalized gradient approximation*. Phys. Rev. B **33**, 8800–8802 (1986).
- [Perdew92] John P. Perdew and Yue Wang. *Accurate and simple analytic representation of the electron-gas correlation energy*. Phys. Rev. B **45**, 13244–13249 (1992).
- [Perdew96] John P. Perdew, Kieron Burke and Matthias Ernzerhof. *Generalized Gradient Approximation Made Simple*. Phys. Rev. Lett. **77**, 3865–3868 (1996).
- [Perdew08] John P. Perdew, Adrienn Ruzsinszky, Gábor I. Csonka, Oleg A. Vydrov, Gustavo E. Scuseria, Lucian A. Constantin, Xiaolan Zhou and Kieron Burke. *Restoring the Density-Gradient Expansion for Exchange in Solids and Surfaces*. Phys. Rev. Lett. **100**, 136406 (2008).
- [Phillips03] J. C. Phillips, A. Saxena and A. R. Bishop. *Pseudogaps, dopants, and strong disorder in cuprate high-temperature superconductors*. Reports on Progress in Physics **66**, 2111 (2003).
- [Pickett89] Warren E. Pickett. *Electronic structure of the high-temperature oxide superconductors*. Rev. Mod. Phys. **61**, 433–512 (1989).
- [Pruschke95] Th. Pruschke, M. Jarrell and J. K. Freericks. *Anomalous normal-state properties of high- T_c superconductors: intrinsic properties of strongly correlated electron systems?* Advances in Physics **44**, 187–210 (1995).
- [Pulay69] P. Pulay. *Ab initio calculation of force constants and equilibrium geometries in polyatomic molecules. I. Theor. Mol. Phys.* **17**, 197–204 (1969).
- [Radtke94] R. J. Radtke and M. R. Norman. *Relation of extended Van Hove singularities to high-temperature superconductivity within strong-coupling theory*. Phys. Rev. B **50**, 9554–9560 (1994).

-
- [Radu05] T. Radu, H. Wilhelm, V. Yushankhai, D. Kovrizhin, R. Coldea, Z. Tyliczynski, T. Lühmann and F. Steglich. *Bose-Einstein Condensation of Magnons in Cs_2CuCl_4* . Phys. Rev. Lett. **95**, 127202 (2005).
- [Rosner99] Helge Rosner. *Electronic Structure and exchange Integrals of low-dimensional cuprates*. Ph.D. thesis, Technische Universität Dresden (1999).
- [Rückamp05] R. Rückamp, J. Baier, M. Kriener, M. W. Haverkort, T. Lorenz, G. S. Uhrig, L. Jongen, A. Möller, G. Meyer and M. Grüninger. *Zero-Field Incommensurate Spin-Peierls Phase with Interchain Frustration in $TiOCl$* . Phys. Rev. Lett. **95**, 097203 (2005).
- [Ruckenstein87] Andrei E. Ruckenstein, Peter J. Hirschfeld and J. Appel. *Mean-field theory of high- T_c superconductivity: The superexchange mechanism*. Phys. Rev. B **36**, 857–860 (1987).
- [Saha-Dasgupta04] T. Saha-Dasgupta, R. Valentí, H. Rosner and C. Gros. *$TiOCl$, an orbital-ordered system?* EPL (Europhysics Letters) **67**, 63 (2004).
- [Scalapino86] D. J. Scalapino, E. Loh and J. E. Hirsch. *d -wave pairing near a spin-density-wave instability*. Phys. Rev. B **34**, 8190–8192 (1986).
- [Scalapino95] D. J. Scalapino. *The case for $d_{x^2-y^2}$ pairing in the cuprate superconductors*. Physics Reports **250**, 329–365 (1995).
- [Seidel03] Alexander Seidel, Chris A. Marianetti, F. C. Chou, Gerbrand Ceder and Patrick A. Lee. *$S = \frac{1}{2}$ chains and spin-Peierls transition in $TiOCl$* . Phys. Rev. B **67**, 020405 (2003).
- [Shnirman99] Alexander Shnirman, İnanç Adagideli, Paul M. Goldbart and Ali Yazdani. *Resonant states and order-parameter suppression near pointlike impurities in d -wave superconductors*. Phys. Rev. B **60**, 7517–7522 (1999).
- [Sing11] M. Sing, S. Glawion, M. Schlachter, M. R. Scholz, K. Goß, J. Heidler, G. Berner and R. Claessen. *Photoemission of a Doped Mott Insulator: Spectral Weight Transfer and a Qualitative Mott-Hubbard Description*. Phys. Rev. Lett. **106**, 056403 (2011).
- [Singh91] D. J. Singh and W. E. Pickett. *Gradient-corrected density-functional studies of $CaCuO_2$* . Phys. Rev. B **44**, 7715–7717 (1991).

- [Starykh07] Oleg A. Starykh and Leon Balents. *Ordering in Spatially Anisotropic Triangular Antiferromagnets*. Phys. Rev. Lett. **98**, 077205 (2007).
- [Starykh10] Oleg A. Starykh, Hosho Katsura and Leon Balents. *Extreme sensitivity of a frustrated quantum magnet: Cs_2CuCl_4* . Phys. Rev. B **82**, 014421 (2010).
- [Steglich79] F. Steglich, J. Aarts, C. D. Bredl, W. Lieke, D. Meschede, W. Franz and H. Schäfer. *Superconductivity in the Presence of Strong Pauli Paramagnetism: $CeCu_2Si_2$* . Phys. Rev. Lett. **43**, 1892–1896 (1979).
- [Sugano70] Satoru Sugano, Yukito Tanabe and Hiroshi Kamimura. *Multiplets of transition-metal ions in crystals*. Academic Press, New York and London (1970).
- [Takahashi77] M. Takahashi. *Half-filled Hubbard model at low temperature*. Journal of Physics C: Solid State Physics **10**, 1289 (1977).
- [Takimoto02] T. Takimoto, T. Hotta, T. Maehira and K. Ueda. *Spin-fluctuation-induced superconductivity controlled by orbital fluctuation*. Journal of Physics: Condensed Matter **14**, L369 (2002).
- [Terakura84] K. Terakura, T. Oguchi, A. R. Williams and J. Kübler. *Band theory of insulating transition-metal monoxides: Band-structure calculations*. Phys. Rev. B **30**, 4734–4747 (1984).
- [Thomas27] L. H. Thomas. *The calculation of atomic fields*. Proc. Cambridge Phil. Soc. **23** (5), 542–548 (1927).
- [Timusk99] Tom Timusk and Bryan Statt. *The pseudogap in high-temperature superconductors: an experimental survey*. Reports on Progress in Physics **62**, 61 (1999).
- [Tokiwa06] Y. Tokiwa, T. Radu, R. Coldea, H. Wilhelm, Z. Tylczynski and F. Steglich. *Magnetic phase transitions in the two-dimensional frustrated quantum antiferromagnet Cs_2CuCl_4* . Phys. Rev. B **73**, 134414 (2006).
- [Tranquada95] J. M. Tranquada, B. J. Sternlieb, J. D. Axe, Y. Nakamura and S. Uchida. *Evidence for stripe correlations of spins and holes in copper oxide superconductors*. Nature **375**, 561–563 (1995).

-
- [Tsuei00] C. C. Tsuei and J. R. Kirtley. *Pairing symmetry in cuprate superconductors*. Rev. Mod. Phys. **72**, 969 (2000).
- [Tsujii07] H. Tsujii, C. R. Rotundu, T. Ono, H. Tanaka, B. Andraka, K. Ingersent and Y. Takano. *Thermodynamics of the up-up-down phase of the $S = \frac{1}{2}$ triangular-lattice antiferromagnet Cs_2CuBr_4* . Phys. Rev. B **76**, 060406 (2007).
- [Veillette05] M. Y. Veillette, A. J. A. James and F. H. L. Essler. *Spin dynamics of the quasi-two-dimensional spin- $\frac{1}{2}$ quantum magnet Cs_2CuCl_4* . Phys. Rev. B **72**, 134429 (2005).
- [Veillette06] M. Y. Veillette and J. T. Chalker. *Commensurate and incommensurate ground states of Cs_2CuCl_4 in a magnetic field*. Phys. Rev. B **74**, 052402 (2006).
- [Weihong99] Zheng Weihong, Ross H. McKenzie and Rajiv R. P. Singh. *Phase diagram for a class of spin- $\frac{1}{2}$ Heisenberg models interpolating between the square-lattice, the triangular-lattice, and the linear-chain limits*. Phys. Rev. B **59**, 14367–14375 (1999).
- [Wen11] Hai-Hu Wen and Shiliang Li. *Materials and Novel Superconductivity in Iron Pnictide Superconductors*. Annual Review of Condensed Matter Physics **2**, 121–140 (2011).
- [Wimmer81] E. Wimmer, H. Krakauer, M. Weinert and A. J. Freeman. *Full-potential self-consistent linearized-augmented-plane-wave method for calculating the electronic structure of molecules and surfaces: O_2 molecule*. Phys. Rev. B **24**, 864–875 (1981).
- [Wu06] Zhigang Wu and R. E. Cohen. *More accurate generalized gradient approximation for solids*. Phys. Rev. B **73**, 235116 (2006).
- [Yamanaka98] Shoji Yamanaka, Ken ichi Hotehama and Hitoshi Kawaji. *Superconductivity at 25.5 K in electron-doped layered hafnium nitride*. Nature **392**, 580–582 (1998).
- [Zhang88] F. C. Zhang and T. M. Rice. *Effective Hamiltonian for the superconducting Cu oxides*. Phys. Rev. B **37**, 3759–3761 (1988).
- [Zhang05] Yu Zhong Zhang, Peter Fulde, Peter Thalmeier and Alexander Yaresko. *Charge Ordering in the Spinels AlV_2O_4 and LiV_2O_4* . Journal of the Physical Society of Japan **74**, 2153–2156 (2005).

- [Zhang08a] Yu-Zhong Zhang, Harald O. Jeschke and Roser Valentí. *Microscopic model for transitions from Mott to spin-Peierls insulator in TiOCl*. Phys. Rev. B **78**, 205104 (2008).
- [Zhang08b] Yu-Zhong Zhang, Harald O. Jeschke and Roser Valentí. *Two Pressure-Induced Transitions in TiOCl: Mott Insulator to Anisotropic Metal*. Phys. Rev. Lett. **101**, 136406 (2008).
- [Zhang10] Yu-Zhong Zhang, Kateryna Foyevtsova, Harald O. Jeschke, Martin U. Schmidt and Roser Valentí. *Can the Mott Insulator TiOCl be Metallized by Doping? A First-Principles Study*. Phys. Rev. Lett. **104**, 146402 (2010).
- [Zheng05] Weihong Zheng, Rajiv R. P. Singh, Ross H. McKenzie and Radu Coldea. *Temperature dependence of the magnetic susceptibility for triangular-lattice antiferromagnets with spatially anisotropic exchange constants*. Phys. Rev. B **71**, 134422 (2005).

Acknowledgements

The completion of this work would not be possible without the help of many people whom I would like to acknowledge below. First of all, I am grateful to my PhD adviser Prof. Dr. Roser Valentí for giving me the opportunity to work on the research projects of my PhD thesis in her group. With Roser's support and guidance, I've been able to gather rich experience on DFT calculations, dealing with interesting physics of strongly correlated materials; besides that, I greatly appreciate her encouragement to go beyond the DFT and be open to learning many-body methods, what I really enjoyed a lot and what eventually broadened the scope of my thesis.

My DFT study on the frustrated antiferromagnets Cs_2CuCl_4 and Cs_2CuBr_4 has benefited from numerous discussions with [in alphabetical order] Dr. Harald Jeschke, Dr. Ingo Opahle and Dr. Yuzhong Zhang. Special thanks go to Harald for creating a tight-binding code that was very helpful in parameterizing TB models for Cs_2CuCl_4 , Cs_2CuBr_4 and, especially, $\text{Bi}_2\text{Sr}_2\text{CaCu}_2\text{O}_{8+\delta}$, to Ingo for performing structural relaxations of Cs_2CuCl_4 and Cs_2CuBr_4 and helping me to get started with the FPLO code and to Yuzhong for introducing the PAW code to me and for performing exact diagonalization calculations. I should gratefully mention the comprehensive investigations on TiOCl carried out by Yuzhong, Harald and Roser, which I used as a basis for the analysis of the microscopic model of the Na-doped TiOCl. Also, I would like to thank Prof. Dr. Peter Hirschfeld from the University of Florida for involving me into the exciting research on the inhomogeneities in $\text{Bi}_2\text{Sr}_2\text{CaCu}_2\text{O}_{8+\delta}$ and Dr. Siegfried Graser from the University of Augsburg, our collaborator, for his assistance with the RPA calculations.

It has been a pleasure to work in a friendly atmosphere of our research group, for what I would like to thank all my present and former colleagues and the secretary Frau Maripola Kolokotsa. Many thanks to Johannes Ferber for the careful proofreading of the thesis manuscript and for the German translation of the abstract.

I gratefully acknowledge the Deutsche Forschungsgemeinschaft for financial support through the SFB/TRR 49 program.

Curriculum Vitae

Kateryna Foyevtsova (Tykhanska)

Birth: October 16th, 1983 in Moscow

Citizenship: Ukrainian

Marital status: married



Education:

01/2007 - present PhD student [a German Research Foundation (DFG) position] in the group of Prof. Valentí, ITP, J. W. Goethe-Universität Frankfurt am Main. Doctoral thesis title: *"Investigation of the microscopic behavior of Mott insulators by means of the DFT and many-body methods"*.

09/2004 - 05/2006 Graduate student at the Minnesota State University, MN, USA. The degree of Master of Science received in 05/2006; Master thesis title: *"Magnetic properties of intermediate-valence and heavy fermion materials"*, under supervision of Dr. Igor Kogoutiuk. GPA=4.0.

09/2000 - 06/2004 Undergraduate student at the Lviv National Polytechnic University (Lviv, Ukraine), Department of electrophysics and semiconductor electronics; Bachelor degree received.

Teaching experience:

- Four semesters as a Physics lab instructor at the Minnesota State University for undergraduate students.
- Preparation of exercises and tutoring for the "Advanced solid state physics" course at the Frankfurt University (in English).
- Tutoring for "Thermodynamical physics and statistical mechanics" course at the Frankfurt University (in English).

Publications:

- [1] P. T. Cong, B. Wolf, M. de Souza, N. Krüger, A. A. Haghighirad, S. Gottlieb-Schoenmeyer, F. Ritter, W. Assmus, I. Opahle, K. Foyevtsova, H. O. Jeschke, R. Valentí, L. Wiehl and M. Lang. *Distinct magnetic regimes through site-selective atom substitution in the frustrated quantum antiferromagnet $Cs_2CuCl_{4-x}Br_x$* . Phys. Rev. B **83**, 064425 (2011).
- [2] Kateryna Foyevtsova, Ingo Opahle, Yu-Zhong Zhang, Harald O. Jeschke and Roser Valentí. *Determination of effective microscopic models for the frustrated antiferromagnets Cs_2CuCl_4 and Cs_2CuBr_4 by density functional methods*. Phys. Rev. B **83**, 125126 (2011).
- [3] Kateryna Foyevtsova, H. C. Kandpal, Harald O. Jeschke, S. Graser, H.-P. Cheng, Roser Valentí and P. J. Hirschfeld. *Modulation of pairing interaction in $Bi_2Sr_2CaCu_2O_{8+\delta}$ by an O dopant: a density functional theory study*. Phys. Rev. B **82**, 054514 (2010).
- [4] Yu-Zhong Zhang, Kateryna Foyevtsova, Harald O. Jeschke, Martin U. Schmid and Roser Valentí. *Can the Mott Insulator $TiOCl$ be Metallized by Doping? A First-Principles Study*. Phys. Rev. Lett. **104**, 146402 (2010).
- [5] Kateryna Foyevtsova, Roser Valentí and P. J. Hirschfeld. *Effect of dopant atoms on local superexchange in cuprate superconductors: a perturbative treatment*. Phys. Rev. B **79**, 144424 (2009).
- [6] K. Foyevtsova, Y. Zhang, H. O. Jeschke and Roser Valentí. *First principles perspective on the microscopic model for Cs_2CuCl_4 and Cs_2CuBr_4* . J. of Physics: Conf. Ser. **145**, 012038 (2009).